

AEROSPACE RESEARCH IN BULGARIA

Volume 25, Sofia, 2013
Space Research and Technology Institute
Bulgarian Academy of Sciences

Editorial Board

Prof. Garo Mardirossian (*Editor-in-Chief*)
Chief Assistant Lyudmila Todorieva (*English Language Editor*)
Tsveta Srebrova, MS (*Technical Editor*)

Acad. Valeri Bondour – Russia
Prof. Gerassimos Papadopoulos – Greece
Prof. Stefano Tinti – Italy
Prof. Rupert Gertzler – Germany

Corr. Member Filip Filipov
Corr. Member Petar Velinov
Prof. Petar Getsov
Prof. Petko Nenovski
Prof. Eugenia Roumenina
Assoc. Prof. Tania Ivanova
Assoc. Prof. Lachezar Filipov
Assoc. Prof. Stefan Chapkunov
Assoc. Prof. Dimitar Teodossiev

Address

AEROSPACE RESEARCH IN BULGARIA
Space Research and Technology Institute
bl. 1, *Acad. G. Bonchev* St., Sofia 1113, Bulgaria

e-mail: journal@space.bas.bg

Pre-Publication Processing
Tsveta Srebrova

© Space Research and Technology Institute – Bulgarian Academy of Sciences

ISSN 1313 – 0927

Aerospace Research in Bulgaria

25

Sofia, 2013

Contents

1. *Dimitar Dimitrov*
ANALYTICAL COMPUTATION OF TWO INTEGRALS, APPEARING
IN THE THEORY OF ELLIPTICAL ACCRETION DISCS.
I. SOLVING OF THE AUXILIARY INTEGRALS, EMERGING DURING THEIR
DERIVATIONS. 5
2. *Dimitar Dimitrov*
ANALYTICAL COMPUTATION OF TWO INTEGRALS, APPEARING
IN THE THEORY OF ELLIPTICAL ACCRETION DISCS. II. SOLVING OF SOME
AUXILIARY INTEGRALS, CONTAINING LOGARITHMIC FUNCTIONS INTO
THEIR INTEGRANDS. 35
3. *Peter Velinov, Simeon Asenovski, Lachezar Mateev,
Eduard Vashenyuk, Aleksander Mishev*
INVESTIGATION OF MIDDLE ATMOSPHERE IONIZATION DURING
GLE 70 EVENT FROM DECEMBER 2006 BY MEANS OF CORIMIA
MODEL AND NORMALIZED CR SPECTRA. 62
4. *Maria Abunina, Anatoly Abunin, Anatoly Belov, Sergey Gaidash,
Yordan Tassev, Peter Velinov, Lachezar Mateev, Peter Tonev*
GEOEFFECTIVITY OF SOLAR CORONAL HOLES WITH
DIFFERENT MAGNETIC FIELD POLARITY. 70
5. *Tsvetan Dachev, Nikolay Bankov, Borislav Tomov,
Yury Matviichuk, Plamen Dimitrov*
SPACE RADIATION PECULIARITIES IN THE EXTRA VEHICULAR
ENVIRONMENT OF THE INTERNATIONAL SPACE STATION (ISS). 78
6. *Tsvetan Dachev, Borislav Tomov, Yury Matviichuk,
Plamen Dimitrov, Nikolay Bankov, Vladislav Petrov, Viacheslav
Shurshakov, Olga Ivanova, Donat-Peter Häder, Michael Lebert,
Martin Schuster, Günter Reitz, Gerda Horneck, Ondrej Ploc*
PRELIMINARY RESULTS FOR THE RADIATION ENVIRONMENT
OBSERVED BY RD3-B3 RADIOMETER-DOSIMETER INSIDE BION- M № 1
SPACECRAFT. 109

7. Tatjana Zenchenko, Malina Jordanova, Lilia Poskotinova, Anna Medvedeva, Todor Uzunov, Alexandra Alenikova, Tamara Breus	
SYNCHRONIZATION OF HEART RATES AND GEOMAGNETIC FIELD VARIATIONS: A PILOT STUDY.	125
8. Lachezar Filchev	
DETECTION AND ASSESSMENT OF ABIOTIC STRESS OF CONIFEROUS LANDSCAPES CAUSED BY URANIUM MINING (USING HYPERSPECTRAL EO-1/HYPERION DATA).	138
9. Vassil Vassilev	
CROP INVESTIGATION USING HIGH-RESOLUTION WORLDVIEW-1 AND QUICKBIRD-2 SATELLITE IMAGES ON A TEST SITE IN BULGARIA.	154
10. Vassil Vassilev	
CROP MONITORING USING SPOT-VGT NDVIs S10 TIME-SERIES PRODUCT FOR THE ARABLE LAND OF BULGARIA.	172
11. Vanya Naydenova, Stefan Stamenov	
LANDFORM CLASSIFICATION USING ASTER GDEM AND OPTICAL HIGH RESOLUTION SATELLITE IMAGES OF SOFIA CITY DISTRICT.	183
12. Maria Dimitrova, Iva Ivanova, Mariana Zaharinova, Roumen Nedkov	
APPLICATION OF AEROSPACE METHODS FOR MONITORING OF FOREST FIRES AND EVALUATION OF BURNED AREA IN HASKOVO REGION IN THE SUMMER OF 2011.	194
13. Peter Getzov, Zoia Hubenova, Dimitar Yordanov, Wiliam Popov	
MODELING OF THE HUMAN – OPERATOR IN A COMPLEX SYSTEM FUNCTIONING UNDER EXTREME CONDITIONS.	206
14. Peter Petkov, Elisaveta Alexandrova	
NEW CONSTRUCTION KU-BAND ANTENNA WITH IMPROVED RADIATION DIAGRAM FOR SATELLITE BROADCASTING RECEIVING EARTH STATION.	228
15. Zhivko Zhelezov, Roumen Nedkov, Dimitar Teodosiev, Maria Bivolarska, Neven Georgiev, Ivo Lilov, Georgi Chamov, Spaska Yaneva	
FUNCTIONAL TESTING OF THE CAMERA WITH ACTUATOR FOR THE EXPERIMENTAL DETERMINATION OF THE POLARIZATION OF LIGHT BY MEASURING THE STOKES PARAMETERS.	239
 <u>In memoriam</u>	
80TH ANNIVERSARY OF THE BIRTH AND 10TH DEATH ANNIVERSARY OF ACAD. DIMITAR MISHEV.	254

С Ъ Д Ъ Р Ж А Н И Е

1. **Димитър Димитров**
АНАЛИТИЧНО ПРЕСМЯТАНЕ НА ДВА ИНТЕГРАЛА, ВЪЗНИКВАЩИ
В ТЕОРИЯТА НА ЕЛИПТИЧНИТЕ АКРЕЦИОННИ ДИСКОВЕ.
I. РЕШАВАНЕ НА СПОМАГАТЕЛНИТЕ ИНТЕГРАЛИ, ПОЯВЯВАЩИ СЕ
ПРИ ТЯХНОТО ИЗЧИСЛЯВАНЕ. 5
2. **Димитър Димитров**
АНАЛИТИЧНО ПРЕСМЯТАНЕ НА ДВА ИНТЕГРАЛА, ВЪЗНИКВАЩИ
В ТЕОРИЯТА НА ЕЛИПТИЧНИТЕ АКРЕЦИОННИ ДИСКОВЕ.
II. РЕШАВАНЕ НА НЯКОИ СПОМАГАТЕЛНИТЕ ИНТЕГРАЛИ, СЪДЪРЖАЩИ
ЛОГАРИТМИЧНИ ФУНКЦИИ В СВОИТЕ ИНТЕГРАНДИ. 35
3. **Петър Велинов, Симеон Асеновски, Лъчезар Матеев,
Едуард Вашинюк, Александър Мишев**
ИЗСЛЕДВАНЕ НА ЙОНИЗАЦИЯТА В СРЕДНАТА АТМОСФЕРА
ПО ВРЕМЕ НА СЪБИТИЕТО GLE 70 ОТ ДЕКЕМВРИ 2006 ПОСРЕДСТВОМ
МОДЕЛА CORIMIA И НОРМАЛИЗИРАНЕ НА СПЕКТЪРА НА
КОСМИЧЕСКИТЕ ЛЪЧИ. 62
4. **Мария Абунина, Анатолий Абунин, Анатолий Белов,
Сергей Гайдаш, Йордан Тасев, Петър Велинов,
Лъчезар Матеев, Петър Тонев**
ГЕОЕФЕКТИВНОСТЪ СЪЛНЕЧНИХ КОРОНАЛНИХ ДЪР
С РАЗЛИЧНОЙ ПОЛЯРНОСТЮ МАГНИТНОГО ПОЛЯ. 70
5. **Цветан Дачев, Николай Банков, Борислав Томов,
Юрий Матвийчук, Пламен Димитров**
ОСОБЕНОСТИ НА КОСМИЧЕСКАТА РАДИАЦИЯ В ОБКРЪЖАВАЩОТО
ПРОСТРАНСТВО НА МЕЖДУНАРОДНАТА КОСМИЧЕСКА СТАНЦИЯ
(МКС). 78
6. **Цветан Дачев, Борислав Томов, Юрий Матвийчук,
Пламен Димитров, Николай Банков, Владислав Петров,
Вячеслав Шуриаков, Олга Иванова, Донат-Петер Хедър,
Михаел Леберт, Мартин Шустер, Гюнтер Райтц,
Герда Хорнек, Ондреж Плоц**
ПРЕДВАРИТЕЛНИ РЕЗУЛТАТИ ЗА РАДИАЦИОННАТА ОБСТАНОВКА
НАБЛЮДАВАНА С ДОЗИМЕТЪРА-РАДИОМЕТЪРА RD3-B3
НА СПЪТНИКА BION-M № 1. 109
7. **Татяна Зенченко, Малина Йорданова, Лилия Поскотинова,
Анна Медведева, Тодор Узунов, Александра Аленкова,
Тамара Бреус**
СИНХРОНИЗАЦИЯ НА ВАРИАБИЛНОСТИТЕ НА СЪРДЕЧНИЯ РИТЪМ
И ГЕОМАГНИТНОТО ПОЛЕ: ПИЛОТНО ПРОУЧВАНЕ. 125

- 8. *Лъчезар Филчев***
 ОТКРИВАНЕ И ОЦЕНКА НА АБИОТИЧЕН СТРЕС, ПРИЧИНЕН ОТ
 УРАНОДОБИВ, В ИГЛОЛИСТНИ ЛАНДШАФТИ (С ИЗПОЛЗВАНЕ НА
 СПЪТНИКОВИ СПЕКТРОМЕТРИЧНИ ДАННИ ОТ EO-1/HYPERION). 138
- 9. *Васил Василев***
 АНАЛИЗ НА ЗЕМЕДЕЛСКИТЕ КУЛТУРИ ПО СПЪТНИКОВИ ИЗОБРАЖЕНИЯ
 СЪС СВРЪХ-ВИСОКА ПРОСТРАНСТВЕНА РАЗДЕЛИТЕЛНА СПОСОБНОСТ
 ОТ WORLDVIEW-1 И QUICKBIRD-2 ЗА ТЕСТОВИ УЧАСТЪК НА
 ТЕРИТОРИЯТА НА БЪЛГАРИЯ. 154
- 10. *Васил Василев***
 МОНИТОРИНГ НА ЗЕМЕДЕЛСКИТЕ КУЛТУРИ ПО ВРЕМЕВИ СЕРИИ
 ОТ ВЕГЕТАЦИОНЕН ПРОДУКТ SPOT-VGT NDVI_s S10 ВЪРХУ
 ОБРАБОТВАЕМАТА ТЕРИТОРИЯ НА Р. БЪЛГАРИЯ. 172
- 11. *Ваня Найденова, Стефан Стаменов***
 КЛАСИФИКАЦИЯ НА ФОРМИТЕ НА ЗЕМНАТА ПОВЪРХНОСТ С
 ИЗПОЛЗВАНЕ НА ЦИФРОВ МОДЕЛ НА РЕЛЕФА ASTER GDEM И
 САТЕЛИТНИ ИЗОБРАЖЕНИЯ С ВИСОКА ПРОСТРАНСТВЕНА
 РАЗДЕЛИТЕЛНА СПОСОБНОСТ ЗА РАЙОНА НА ОБЛАСТ СОФИЯ ГРАД. . . . 183
- 12. *Мария Димитрова, Ива Иванова, Мариана Захарина,
 Румен Недков***
 ПРИЛОЖЕНИЕ НА АЕРОКОСМИЧЕСКИТЕ МЕТОДИ ЗА
 ПРОСЛЕДЯВАНЕ НА ГОРСКИ И ПОЛСКИ ПОЖАРИ И ОЦЕНКА НА
 ИЗГОРЕЛИТЕ ПЛОЩИ В ОБЛАСТ ХАСКОВО ПРЕЗ ЛЯТОТО НА 2011 Г. 194
- 13. *Петър Гецов, Зоя Хубенова, Димитър Йорданов,
 Вилям Попов***
 МОДЕЛИРАНЕ НА ЧОВОКА – ОПЕРАТОР В СЛОЖНА СИСТЕМА,
 ФУНКЦИОНИРАЩА В ЕКСТРЕМНИ УСЛОВИЯ. 206
- 14. *Петър Петков, Елисавета Александрова***
 НОВА КОНСТРУКЦИЯ НА АНТЕНА ЗА ПРИЕМНА СТАНЦИЯ
 ЗА СПЪТНИКОВО ТЕЛЕВИЗИОННО РАЗПРЪСКВАНЕ
 В КУ-ОБХВАТА С ПОДОБРЕНА ДИАГРАМА НА ИЗЛЪЧВАНЕ. 228
- 15. *Живко Железов, Румен Недков, Димитър Теодосиев,
 Мария Биволарска, Невен Георгиев, Иво Лилов,
 Георги Чамов, Спаска Янева***
 ФУНКЦИОНАЛНО ТЕСТВАНЕ НА КАМЕРА СЪС ЗАДВИЖВАНЕ ЗА
 ЕКСПЕРИМЕНТАЛНО ОПРЕДЕЛЯНЕ НА ПОЛЯРИЗАЦИЯТА НА
 СВЕТЛИНАТА ЧРЕЗ ИЗМЕРВАНЕ НА ПАРАМЕТРИТЕ НА СТОКС. 239
- In memoriam***
 80 ГОДИНИ ОТ РОЖДЕНИЕТО И 10 ГОДИНИ ОТ СМЪРТТА
 НА АКАД. ДИМИТЪР МИШЕВ. 254

ANALYTICAL COMPUTATION OF TWO INTEGRALS, APPEARING IN THE THEORY OF ELLIPTICAL ACCRETION DISCS. I. SOLVING OF THE AUXILIARY INTEGRALS, EMERGING DURING THEIR DERIVATIONS

Dimitar Dimitrov

*Space Research and Technology Institute – Bulgarian Academy of Sciences
e-mail: dim@mail.space.bas.bg*

Abstract

The present work is a part of an extended analytical investigation of the dynamical equation, determining the spatial structure of the **stationary** elliptical accretion discs, according to the model of Lyubarskij et al. [1]. In the mathematical description of the problem are used as parameters the eccentricity $\mathbf{e}(\mathbf{u})$ of the particle orbits, and its derivative $\dot{\mathbf{e}}(\mathbf{u}) \equiv d\mathbf{e}(\mathbf{u})/d\mathbf{u}$, where $\mathbf{u} \equiv \ln(\mathbf{p})$, and \mathbf{p} is the focal parameter of the considered orbit. During the process of simplification of that equation, there arises

the necessity of analytical evaluations of integrals of the following types: $\mathbf{A}_i(\mathbf{e}, \dot{\mathbf{e}}) \equiv \int_0^{2\pi} (\mathbf{I} + \mathbf{e}\cos\varphi)^{-i} d\varphi$,

$(i = 1, \dots, 5)$, $\mathbf{J}_k(\mathbf{e}, \dot{\mathbf{e}}) \equiv \int_0^{2\pi} (\mathbf{I} + \mathbf{e}\cos\varphi)^{-1} [\mathbf{I} + (\mathbf{e} - \dot{\mathbf{e}})\cos\varphi]^{-k} d\varphi$ and $\mathbf{H}_k(\mathbf{e}, \dot{\mathbf{e}}) \equiv \int_0^{2\pi} (\mathbf{I} + \mathbf{e}\cos\varphi)^{-k} \times$

$\times [\mathbf{I} + (\mathbf{e} - \dot{\mathbf{e}})\cos\varphi]^{-1} d\varphi$, ($k = 1, \dots, 4$). In these formulas φ is the azimuthal angle, over which the averaging is taken. The approach in solving of the task is, in fact, recursive. At first, we evaluate the integrals with the smallest \mathbf{i} and \mathbf{k} (i.e., \mathbf{i} and \mathbf{k} equal to unity). After then, we go to the next steps, gradually increasing the integer powers \mathbf{i} or \mathbf{k} , until achieving the designated values 5 or 4, correspondingly. A special attention is devoted to these values of $\mathbf{e}(\mathbf{u})$ and $\dot{\mathbf{e}}(\mathbf{u})$ (and their difference $\mathbf{e}(\mathbf{u}) - \dot{\mathbf{e}}(\mathbf{u})$), which, eventually, may cause divergences in the intermediate or the final expressions. It is shown that although such troubles arise, they can be overcome by means of a **direct** substitution of the “peculiar” values of $\mathbf{e}(\mathbf{u})$ and/or $\dot{\mathbf{e}}(\mathbf{u})$ into the integrals, and after then performing the calculations. Even if the denominators in the final results appear factors equal to zero (due to the nullifications of $\mathbf{e}(\mathbf{u})$, $\dot{\mathbf{e}}(\mathbf{u})$ or $\mathbf{e}(\mathbf{u}) - \dot{\mathbf{e}}(\mathbf{u})$), the expressions are not divergent, as we have proved, using the L’Hospital’s rule for resolving of indeterminacies of the type 0/0. All the analytical estimations of the above written integrals are performed under the restrictions

$|e(u)| < 1$, $|\dot{e}(u)| < 1$ and $|e(u) - \dot{e}(u)| < 1$. They are imposed by the physical reasons, in view of the application of these solutions into the adopted theory of the elliptical accretion discs.

1. Introduction

We have considered some simplifications of the dynamical equation, governing the structure of the elliptical accretion discs in the model of Lyubarskij et al. [1]. The results are already published in a series of papers ([2], [3] and [4]; see also the references therein). In the course of this work, we have introduced seven integrals, which are functions of the eccentricities $e(u)$ of the particle orbits in the accretion disc, their derivatives $\dot{e}(u) \equiv de(u)/du$ and the power n into the viscosity law $\eta = \beta \Sigma^n$. Further we explain the use of the introduced notations. Here u is defined to be the logarithm of the focal parameter p of the corresponding ellipse, representing the considered particle orbit: $u \equiv \ln(p)$. We remind that in the considered model of Lyubarskij et al. [1], all elliptical trajectories in the accretion flow are such, that the major axes of the ellipses lie on the same line (assumed to be the abscissa on which lie the periastrons and apoastrons of the all trajectories). This simplification (introduced “by hands”) allows to derive a dynamical equation for the particles of the disc, which is a second order ordinary differential equation [1]. Such a situation is more favorable, if we try to apply an analytical approach for solving of this problem. The picture of the dynamics of the elliptical accretion discs becomes much more complicated in the opposite (more general) case, when the ellipses of the orbits have apse lines, which are not necessarily in line with each other. Then the dynamics of the disc is described by partial differential equations, as it has been shown in the investigation of Ogilvie [5]. Our working out of the model of Lyubarskij et al. [1] is stimulated in the first place namely by the above mentioned simplifying circumstance, allowing more favorable possibilities to solve the problem by purely analytical methods. Though the considered case may have less usefulness with respect to the really observed discs. That is to say, elliptical discs with orbits sharing a common longitude of the periastron are rare situations among the objects of the kind eccentric accretion discs. It is worth to note that while the orbital eccentricity $e(u)$ and its derivative $\dot{e}(u) \equiv de(u)/du$ are functions of the focal parameter p ($u \equiv \ln(p)$), the power n does not depend on u . This means that n is a fixed constant through the whole disc, while the elongation of the particle orbits may vary for the different parts of the disc. In particular, for the *outer* parts

the periastron of the elliptical orbits may have positive (negative) values of the abscissa, but at the same time in the *inner* parts of the accretion disc, such values may take negative (positive) meanings, respectively. As it has been written above, the accepted in [1] viscosity law is $\eta = \beta \Sigma^n$ (where β is a constant). The viscosity parameter η will depend on the spatial coordinates r and φ (where r is the length of the radius-vector, measured from the center of the compact object, accreting the matter; φ is the azimuthal angle) only through the surface density of the disc $\Sigma = \Sigma(r, \varphi)$.

During the process of simplification of the dynamical equation of the elliptical accretion discs (derived by Lyubarskij et al. [1], we have introduced seven auxiliary integrals, which appear because of the azimuthal-angle averaging of the task. These integrals are functions of $e(u)$, $\dot{e}(u)$ and n , and are defined in the following manner ([2], [3] and [4]):

$$(1) \quad \mathbf{I}_0(e, \dot{e}, n) \equiv \int_0^{2\pi} (1 + e \cos \varphi)^{n-3} [1 + (e - \dot{e}) \cos \varphi]^{-(n+1)} d\varphi,$$

$$(2) \quad \mathbf{I}_{0+}(e, \dot{e}, n) \equiv \int_0^{2\pi} (1 + e \cos \varphi)^{n-2} [1 + (e - \dot{e}) \cos \varphi]^{-(n+2)} d\varphi,$$

$$(3) \quad \mathbf{I}_j(e, \dot{e}, n) \equiv \int_0^{2\pi} (\cos \varphi)^j (1 + e \cos \varphi)^{n-2} [1 + (e - \dot{e}) \cos \varphi]^{-(n+1)} d\varphi; \quad \mathbf{j} = 0, 1, 2, 3, 4.$$

We remind here, that we consider *a particular* case of the elliptical accretion discs, developed by Lyubarskij et al. [1]: namely, stationary flows. Moreover, there are some additional limitations, imposed for every elliptical orbit in the disc, on the eccentricity $e(u)$ and its derivative $\dot{e}(u) \equiv de(u)/du$. These are the inequalities: $|e(u)| < 1$, $|\dot{e}(u)| < 1$ and $|e(u) - \dot{e}(u)| < 1$, valid for every value $u \equiv \ln(p)$ in the disc. Mathematically viewed, these conditions ensure that the integrals (1) – (3) are well behaving, because the denominators are always strongly positive and, correspondingly, do not cause singularities. From a physical point of view, possible nullifications of the denominators in the definitions (1) – (3) might be connected with the emerging of shock waves in the disc, leading, in own turn, to spiral density waves [1]. Such phenomena *a priori* are not considered by this model. The discussed circumstance is clearly reflected in the expressions for the denominators of the metric tensor and the related quantities (see the Appendices in paper [1]).

In the above cited earlier investigations [2], [3] and [4], we have interested in the establishing of the linear relations between the integrals (1) – (3), in order to eliminate them from the dynamical equation of the

accretion flow. This is in a correspondence with our approach to simplify analytically the equation and, eventually, to reveal its mathematical structure and physical implications by purely analytical manners. And only after that to apply, if it is unavoidable, the numerical computations. Leaving aside the integral $\mathbf{I}_3(e, \dot{e}, n)$, we have shown that four of the other integrals (1) – (3) may be expressed through linear combinations of the integrals $\mathbf{I}_0-(e, \dot{e}, n)$ and $\mathbf{I}_{0+}(e, \dot{e}, n)$. So that, to proceed further, we need to investigate whether the last two integrals are linearly independent functions with respect to the variables $e(u)$ and $\dot{e}(u)$, or not. We remark here that the power n in the viscosity law $\eta = \beta \Sigma^n$ is a fixed quantity throughout the entire elliptical accretion disc. When we state that n is a parameter, entering as an independent variable in the list of arguments of the integrals (1) – (3), etc., we subtend that we, in fact, consider a family of an infinite number of discs. Every with own fixed value of the power n . Saying that n varies, we bear in mind that such a variation of n is not over the spatial coordinates in the disc, but from one model to other model (with different n); i.e., n does not depend on $\mathbf{u} \equiv \ln(\mathbf{p})$. This situation, of course, simplifies the differentiation with respect to $e(u)$ or $\dot{e}(u)$ of variety kinds of expressions, like $(1 + e \cos \varphi)^n$, $[1 + (e - \dot{e}) \cos \varphi]^n$, etc. But there are some cases, when we need of the derivatives with respect to n . Then, according to the well known differentiating rule from the analysis $d(a^x)/dx = a^x \ln(a)$ (where a does not depend on x), as we shall see later, in the integrands of the considered integrals will appear factors of the type $\ln(1 + e \cos \varphi)$ and $\ln[1 + (e - \dot{e}) \cos \varphi]$. This complicates the analytical computation of the integrals, because we did not successfully find any expressions about them in the accessible for us mathematical reference books, manuals, guides and handbooks. The reason for differentiating with respect to the power n is the following. During the process of verification of linear dependence/independence of the integrals $\mathbf{I}_0-(e, \dot{e}, n)$ and $\mathbf{I}_{0+}(e, \dot{e}, n)$, there appear terms containing into their denominators factors like $(n - 1)$, $(n - 2)$, etc., which implies suspicions of divergences, if we try to use the final results for some integer values of n . Of course, we are able to perform the evaluation of the considered expressions in a separate manner for these “peculiar” integer values of n and obtain nonsingular results for this special cases. Such a possibility is guaranteed by the form of the initial expressions (namely, the integrals of the type (1) – (3) and the other integrals, originating from them), which we try to evaluate analytically. They are obviously not singular for these “problematic” integer values of n . But from

physical reasons, there is not motivation to assume the existence of such “special” selection of some integer n , and we expect that the pointed out property to be reflected into the mathematical formulas. More strictly speaking, we suspect that the divergences, appearing because of the nullification of the denominators for some integer n , may be overcome by means of the L’Hospital’s rule for resolving of indeterminacies of the type $0/0$. Such an additional checking of the results for the above mentioned “problematic” integer values of the power n has two reasons: (i) the transition through these integer values of n is continuous. That is to say, the direct computation of the analytically evaluated integrals gives the same results as in the case, when the limit transition to the “problematic” integer n is used into the “singular” formulas. If the L’Hospital’s rule may be applied, of course! There are two L’Hospital’s rules: one helps us to evaluate indeterminacies of the type $0/0$ and the other – for the type ∞/∞ . In our further exposition we shall use only the first theorem of L’Hospital. For this reason, let us formulate (in order to make things clear) the first variant of these rules. The proof of these statements can be found in many textbooks on differential calculus, and we shall not cite them in our references. Because the variables, which describe the accretion disc model, are real numbers, the formulation of the first L’Hospital’s rule will be restricted to this case. Let us have a point x_0 (in our application, this may be a concrete value of $e(u)$, $\dot{e}(u)$, $e(u) - \dot{e}(u)$ or n). Let us be fulfilled the following conditions: (i) functions $f(x)$ and $g(x)$ are defined and continuous in some interval around x_0 ; (ii) both these functions approach zero, when x approaches x_0 :

$\lim_{x \rightarrow x_0} f(x) = \lim_{x \rightarrow x_0} g(x) = 0$; (iii) the derivatives $f'(x) \equiv df(x)/dx$ and $g'(x) \equiv$

$\equiv dg(x)/dx$ in that interval (except, may be, at the point x_0) exist; (iv) these derivatives do not simultaneously vanish for $x \neq x_0$; (v) there also exists the limit

$\lim_{x \rightarrow x_0} [f'(x)/g'(x)]$.

$x \rightarrow x_0$

Then, under these circumstances, the first L’Hospital’s rule states that

$\lim_{x \rightarrow x_0} [f(x)/g(x)] = \lim_{x \rightarrow x_0} [f'(x)/g'(x)]$. In what follows, when arise the need

$x \rightarrow x_0$

$x \rightarrow x_0$

of application of the L’Hospital’s rule, the points (i) – (v) must be checked for their validity. If some of them are not obvious, we shall give a detailed proof of the correctness of these conditions. It may occur, that the rule has to

be applied several times successively, in order to be achieved the reasonable final result.

The establishing of the linear dependence/independence of the integrals $\mathbf{I}_0(e, \dot{e}, n)$ and $\mathbf{I}_{0+}(e, \dot{e}, n)$ follows the standard way – computing the Wronski determinant and evaluation of the domains in the space of variables, where it is equal (or not equal) to zero. In the course of this procedure, which we intend to perform in a purely analytical manner, without using numerical methods, we arrive to the problem of the analytical solving of two integrals. Like the definitions (1) – (3), they are also functions of $e(u)$, $\dot{e}(u)$ and the power n :

$$(4) \quad \mathbf{I}_{0,-4,+1}(e, \dot{e}, n) \equiv \int_0^{2\pi} (1 + e \cos \varphi)^{n-4} [1 + (e - \dot{e}) \cos \varphi]^{-(n+1)} d\varphi ,$$

$$(5) \quad \mathbf{I}_{0,-2,+3}(e, \dot{e}, n) \equiv \int_0^{2\pi} (1 + e \cos \varphi)^{n-2} [1 + (e - \dot{e}) \cos \varphi]^{-(n+3)} d\varphi .$$

The appearance of such expressions is a consequence of the differentiation of $\mathbf{I}_0(e, \dot{e}, n)$ and $\mathbf{I}_{0+}(e, \dot{e}, n)$, in order to write the Wronski determinant. In turn, the computation of the integrals (4) and (5) requires a preliminary analytical evaluation of some auxiliary integrals, also functions of $e(u)$, $\dot{e}(u)$ and n . We divide them into two groups, whether their integrands include (or not include) as factors the logarithms $\ln(1 + e \cos \varphi)$ and $\ln[1 + (e - \dot{e}) \cos \varphi]$.

2. Analytical computation of the auxiliary integrals, which do not contain logarithmic functions

2.1. Evaluation of integrals of the type $\mathbf{A}_i(e, \dot{e}) \equiv \int_0^{2\pi} [1 + (e - \dot{e}) \cos \varphi]^{-i} d\varphi$

In the present subsection we calculate integrals with integrands which are *negative integer* powers of the expression $[1 + (e - \dot{e}) \cos \varphi]$. As already mentioned above, we investigate the model of elliptical accretion discs of Lyubarskij et al. [1] under three restrictions, imposed *a priori* on the eccentricity $e = e(u)$, its derivative $\dot{e}(u) \equiv de(u)/du$ and the difference $e(u) - \dot{e}(u)$. They must be fulfilled for all parts of the accretion flow, i.e., for all $u \equiv \ln(p)$. Particularly, $|e(u) - \dot{e}(u)| < 1$, which ensure that $[1 + (e - \dot{e}) \cos \varphi]$ never vanishes for all values of the azimuthal angle φ ($0 \leq \varphi \leq 2\pi$). With this remark, we are able to evaluate, without any complications, the integrals $\mathbf{A}_i(e, \dot{e})$, defined through the relation:

$$(6) \quad \mathbf{A}_i(e, \dot{e}) \equiv \int_0^{2\pi} [1 + (e - \dot{e})\cos\varphi]^{-i} d\varphi, \quad \mathbf{i} - \text{non-negative integer.}$$

Actually, we shall need of analytical expressions for $\mathbf{A}_i(e, \dot{e})$, when $\mathbf{i} = 1, 2, 3, 4$ and 5 . Note that these functions do not depend on the power $n!$ According to formulas **858.525** and **858.535** from the tables of Dwight [6], we are able immediately to give the analytical expressions for $\mathbf{A}_1(e, \dot{e})$ and $\mathbf{A}_2(e, \dot{e})$, respectively:

$$(7) \quad \mathbf{A}_1(e, \dot{e}) \equiv \int_0^{2\pi} [1 + (e - \dot{e})\cos\varphi]^{-1} d\varphi = 2\pi [1 - (e - \dot{e})^2]^{-1/2},$$

$$(8) \quad \mathbf{A}_2(e, \dot{e}) \equiv \int_0^{2\pi} [1 + (e - \dot{e})\cos\varphi]^{-2} d\varphi = 2\pi [1 - (e - \dot{e})^2]^{-3/2}.$$

Further we observe that for a *fixed* value $n = 3$, the integral $\mathbf{I}_0.(e, \dot{e}, n = 3)$ coincides with the function $\mathbf{A}_4(e, \dot{e})$ (see the definition (1) for $\mathbf{I}_0.(e, \dot{e}, n)$):

$$(9) \quad \begin{aligned} \mathbf{A}_4(e, \dot{e}) &\equiv \int_0^{2\pi} [1 + (e - \dot{e})\cos\varphi]^{-4} d\varphi \equiv \mathbf{I}_0.(e, \dot{e}, n = 3) = \\ &= \pi[2 + 3(e - \dot{e})^2] [1 - (e - \dot{e})^2]^{-7/2}. \end{aligned}$$

The later equality in the above relation follows from formula (6h) from paper [7], where we have already given the analytical solutions of the integrals (1) – (3) for *integer* values of the power n ($n = -1, 0, 1, 2, 3$). The evaluation of the auxiliary integral $\mathbf{A}_3(e, \dot{e})$ requires some additional efforts:

$$(10) \quad \begin{aligned} \mathbf{A}_3(e, \dot{e}) &\equiv \int_0^{2\pi} [1 + (e - \dot{e})\cos\varphi]^{-3} d\varphi = \int_0^{2\pi} \{ [1 + (e - \dot{e})\cos\varphi] - (e - \dot{e})\cos\varphi \} \times \\ &\times [1 + (e - \dot{e})\cos\varphi]^{-3} d\varphi = \int_0^{2\pi} [1 + (e - \dot{e})\cos\varphi]^{-2} d\varphi - \\ &- (e - \dot{e}) \int_0^{2\pi} \cos\varphi [1 + (e - \dot{e})\cos\varphi]^{-3} d\varphi = 2\pi [1 - (e - \dot{e})^2]^{-3/2} - \\ &- (e - \dot{e}) \int_0^{2\pi} \cos\varphi [1 + (e - \dot{e})\cos\varphi]^{-3} d\varphi, \end{aligned}$$

where we have used the mentioned above result (8). To evaluate further the right-hand side of the equality (10), we integrate by parts:

$$(11) \quad \mathbf{A}_3(e, \dot{e}) = 2\pi [1 - (e - \dot{e})^2]^{-3/2} - (e - \dot{e}) \int_0^{2\pi} [1 + (e - \dot{e})\cos\varphi]^{-3} d(\sin\varphi) =$$

$$\begin{aligned}
&= 2\pi [1 - (e - \dot{e})^2]^{-3/2} + 3(e - \dot{e}) \int_0^{2\pi} (1 - \cos^2\varphi)[1 + (e - \dot{e})\cos\varphi]^{-4} d\varphi = \\
&= 2\pi [1 - (e - \dot{e})^2]^{-3/2} + 3(e - \dot{e}) \int_0^{2\pi} [1 + (e - \dot{e})\cos\varphi]^{-4} d\varphi + \\
&+ 3 \int_0^{2\pi} \{[1 - (e - \dot{e})^2\cos^2\varphi] - 1\} [1 + (e - \dot{e})\cos\varphi]^{-4} d\varphi = 2\pi [1 - (e - \dot{e})^2]^{-3/2} + \\
&+ 3(e - \dot{e})^2 \mathbf{A}_4(e, \dot{e}) + 3 \int_0^{2\pi} [1 - (e - \dot{e})\cos\varphi][1 + (e - \dot{e})\cos\varphi]^{-3} d\varphi - \\
&- 3 \int_0^{2\pi} [1 + (e - \dot{e})\cos\varphi]^{-4} d\varphi = 2\pi [1 - (e - \dot{e})^2]^{-3/2} + 3(e - \dot{e})^2 \mathbf{A}_4(e, \dot{e}) + 3\mathbf{A}_3(e, \dot{e}) - \\
&- 3(e - \dot{e}) \int_0^{2\pi} \cos\varphi [1 + (e - \dot{e})\cos\varphi]^{-3} d\varphi - 3\mathbf{A}_4(e, \dot{e}) .
\end{aligned}$$

Consequently, we have about the unknown function $\mathbf{A}_3(e, \dot{e})$ that:

$$\begin{aligned}
(12) \quad &- 2\mathbf{A}_3(e, \dot{e}) = 2\pi [1 - (e - \dot{e})^2]^{-3/2} + 3[(e - \dot{e})^2 - 1]\mathbf{A}_4(e, \dot{e}) - \\
&- 3(e - \dot{e}) \int_0^{2\pi} \cos\varphi [1 + (e - \dot{e})\cos\varphi]^{-3} d\varphi .
\end{aligned}$$

We can again use the equality (10), but now to write it into a form more appropriate for comparison with (12):

$$(13) \quad - 2\mathbf{A}_3(e, \dot{e}) = - 4\pi [1 - (e - \dot{e})^2]^{-3/2} + 2(e - \dot{e}) \int_0^{2\pi} \cos\varphi [1 + (e - \dot{e})\cos\varphi]^{-3} d\varphi .$$

Equating of the right-hand-sides of (12) and (13) enables us to compute the unknown integral. Strictly speaking, this is the integral $\mathbf{I}_1(e, \dot{e}, n = 2)$ (see the definition (3) for $\mathbf{j} = 1$ and $n = 2$):

$$\begin{aligned}
(14) \quad &5(e - \dot{e}) \int_0^{2\pi} \cos\varphi [1 + (e - \dot{e})\cos\varphi]^{-3} d\varphi \equiv 5(e - \dot{e})\mathbf{I}_1(e, \dot{e}, n = 2) = \\
&= 6\pi [1 - (e - \dot{e})^2]^{-3/2} - 3[1 - (e - \dot{e})^2]\mathbf{A}_4(e, \dot{e}) .
\end{aligned}$$

Dividing this result by (- 5) and replacing it into the right side of the relation (10), we obtain the expression for the unknown function $\mathbf{A}_3(e, \dot{e})$:

$$\begin{aligned}
(15) \quad &\mathbf{A}_3(e, \dot{e}) = 2\pi [1 - (e - \dot{e})^2]^{-3/2} - (6\pi/5)[1 - (e - \dot{e})^2]^{-3/2} + \\
&+ (3\pi/5)[1 - (e - \dot{e})^2][2 + 3(e - \dot{e})^2][1 - (e - \dot{e})^2]^{-7/2} ,
\end{aligned}$$

where we have applied the already computed expression (9) for $\mathbf{A}_4(e, \dot{e})$.
Finally:

$$(16) \quad \mathbf{A}_3(e, \dot{e}) \equiv \int_0^{2\pi} [1 + (e - \dot{e})\cos\varphi]^{-3} d\varphi = (4\pi/5)[1 - (e - \dot{e})^2]^{-3/2} + \\ + (3\pi/5)[2 + 3(e - \dot{e})^2][1 - (e - \dot{e})^2]^{-5/2} \equiv (\pi/5)[10 + 5(e - \dot{e})^2][1 - (e - \dot{e})^2]^{-5/2} \equiv \\ \equiv \pi[2 + (e - \dot{e})^2][1 - (e - \dot{e})^2]^{-5/2}.$$

Of course, we are able to use the equation (14) for obtaining the analytical solution of the integral $\mathbf{I}_1(e, \dot{e}, n = 2)$:

$$(17) \quad \mathbf{I}_1(e, \dot{e}, n = 2) \equiv \int_0^{2\pi} \cos\varphi [1 + (e - \dot{e})\cos\varphi]^{-3} d\varphi = [5(e - \dot{e})]^{-1} \{6\pi[1 - (e - \dot{e})^2]^{-3/2} - \\ - 3\pi[1 - (e - \dot{e})^2][2 + 3(e - \dot{e})^2][1 - (e - \dot{e})^2]^{-7/2}\} = -3\pi(e - \dot{e})[1 - (e - \dot{e})^2]^{-5/2}.$$

This is already derived expression (paper [7], formula (5b)). We rewrite it only to underline the consistency of our computation with the earlier evaluations. Let us now set about the analytical computation of the integral $\mathbf{A}_5(e, \dot{e})$. We shall proceed in the following manner: we begin with a transformation of the already evaluated integral $\mathbf{A}_4(e, \dot{e})$, which leads to an integration by parts. The later operation will require differentiation with respect to φ (φ is the azimuthal angle, which in our case is the integration variable) of the quantity $[1 + (e - \dot{e})\cos\varphi]^{-4}$. As a consequence, in the integrand of the one of the terms appears the factor $[1 + (e - \dot{e})\cos\varphi]^{-5}$, generating, as the final result, the integral $\mathbf{A}_5(e, \dot{e})$, which we are seeking for.

$$(18) \quad \mathbf{A}_4(e, \dot{e}) \equiv \int_0^{2\pi} [1 + (e - \dot{e})\cos\varphi]^{-4} d\varphi = \int_0^{2\pi} [1 + (e - \dot{e})\cos\varphi][1 + (e - \dot{e})\cos\varphi]^{-4} d\varphi - \\ - (e - \dot{e}) \int_0^{2\pi} [1 + (e - \dot{e})\cos\varphi]^{-4} d(\sin\varphi) = \int_0^{2\pi} [1 + (e - \dot{e})\cos\varphi]^{-3} d\varphi - \\ - (e - \dot{e}) \{ \sin\varphi [1 + (e - \dot{e})\cos\varphi]^{-4} \Big|_0^{2\pi} - 4(e - \dot{e}) \int_0^{2\pi} \sin^2\varphi [1 + (e - \dot{e})\cos\varphi]^{-5} d\varphi \} = \\ = \mathbf{A}_3(e, \dot{e}) + 4(e - \dot{e})^2 \int_0^{2\pi} (1 - \cos^2\varphi)[1 + (e - \dot{e})\cos\varphi]^{-5} d\varphi = \mathbf{A}_3(e, \dot{e}) + \\ + 4(e - \dot{e})^2 \int_0^{2\pi} [1 + (e - \dot{e})\cos\varphi]^{-5} d\varphi + 4 \int_0^{2\pi} \{ [1 - (e - \dot{e})^2 \cos^2\varphi] - 1 \} [1 + (e - \dot{e})\cos\varphi]^{-5} d\varphi = \\ = \mathbf{A}_3(e, \dot{e}) + 4(e - \dot{e})^2 \mathbf{A}_5(e, \dot{e}) + 4 \int_0^{2\pi} [1 - (e - \dot{e})\cos\varphi][1 + (e - \dot{e})\cos\varphi][1 + (e - \dot{e})\cos\varphi]^{-5} d\varphi -$$

$$\begin{aligned}
& -4 \int_0^{2\pi} [1 + (e - \dot{e})\cos\varphi]^{-5} d\varphi = \mathbf{A}_3(e, \dot{e}) - 4[1 - (e - \dot{e})^2] \mathbf{A}_5(e, \dot{e}) + 4\mathbf{A}_4(e, \dot{e}) - \\
& -4 \int_0^{2\pi} \{[1 + (e - \dot{e})\cos\varphi] - 1\} [1 + (e - \dot{e})\cos\varphi]^{-4} d\varphi = \mathbf{A}_3(e, \dot{e}) + 4\mathbf{A}_4(e, \dot{e}) - \\
& -4[1 - (e - \dot{e})^2] \mathbf{A}_5(e, \dot{e}) - 4\mathbf{A}_3(e, \dot{e}) + 4\mathbf{A}_4(e, \dot{e}) = \\
& = -3\mathbf{A}_3(e, \dot{e}) + 8\mathbf{A}_4(e, \dot{e}) - 4[1 - (e - \dot{e})^2] \mathbf{A}_5(e, \dot{e}).
\end{aligned}$$

The above result enables us to express $\mathbf{A}_5(e, \dot{e})$ by means of $\mathbf{A}_3(e, \dot{e})$ and $\mathbf{A}_4(e, \dot{e})$, and applying the relations (15) and (9), respectively, to write the final form for this integral:

$$\begin{aligned}
(19) \quad \mathbf{A}_5(e, \dot{e}) & \equiv \int_0^{2\pi} [1 + (e - \dot{e})\cos\varphi]^{-5} d\varphi = \{4[1 - (e - \dot{e})^2]\}^{-1} [-3\mathbf{A}_3(e, \dot{e}) + 7\mathbf{A}_4(e, \dot{e})] = \\
& = \{4[1 - (e - \dot{e})^2]\}^{-1} \{-3\pi[2 + (e - \dot{e})^2][1 - (e - \dot{e})^2]^{-5/2} + \\
& + 7\pi[2 + 3(e - \dot{e})^2][1 - (e - \dot{e})^2]^{-7/2}\} = (\pi/4)[1 - (e - \dot{e})^2]^{-9/2} [8 + 24(e - \dot{e})^2 + \\
& + 3(e - \dot{e})^4] \equiv \\
& \equiv (\pi/4)(8 + 24e^2 + 3e^4 - 48e\dot{e} - 12e^3\dot{e} + 24\dot{e}^2 + 18e^2\dot{e}^2 - 12e\dot{e}^3 + 3\dot{e}^4)[1 - (e - \dot{e})^2]^{-9/2}.
\end{aligned}$$

With a view to a further use, we also write the expressions for the integrals $\mathbf{A}_i(e, \dot{e})$, ($i = 1, \dots, 5$), when $\dot{\mathbf{e}}(\mathbf{u}) = \mathbf{0}$. Geometrically, this situation corresponds to the case, when all particles have orbits with some (constant) eccentricity throughout the considered accretion disc. According to the formulas (7), (8), (16), (9) and (19), we have, respectively:

$$(20) \quad \mathbf{A}_1(e, 0) \equiv \int_0^{2\pi} (1 + e\cos\varphi)^{-1} d\varphi = 2\pi (1 - e^2)^{-1/2},$$

$$(21) \quad \mathbf{A}_2(e, 0) \equiv \int_0^{2\pi} (1 + e\cos\varphi)^{-2} d\varphi = 2\pi (1 - e^2)^{-3/2},$$

$$(22) \quad \mathbf{A}_3(e, 0) \equiv \int_0^{2\pi} (1 + e\cos\varphi)^{-3} d\varphi = \pi(2 + e^2)(1 - e^2)^{-5/2},$$

$$(23) \quad \mathbf{A}_4(e, 0) \equiv \int_0^{2\pi} (1 + e\cos\varphi)^{-4} d\varphi = \pi(2 + 3e^2)(1 - e^2)^{-7/2},$$

$$(24) \quad \mathbf{A}_5(e, 0) \equiv \int_0^{2\pi} (1 + e\cos\varphi)^{-5} d\varphi = (\pi/4)(8 + 24e^2 + 3e^4)(1 - e^2)^{-9/2}.$$

2.2. Evaluation of integrals of the type

$$\mathbf{J}_i(e, \dot{e}) \equiv \int_0^{2\pi} (1 + e \cos \varphi)^{-1} [1 + (e - \dot{e}) \cos \varphi]^{-i} d\varphi$$

The noteworthy for these integrals, which are also functions only of the variables $e(u)$ and $\dot{e}(u)$, is that their denominators are products of the multipliers $(1 + e \cos \varphi)$ and $[1 + (e - \dot{e}) \cos \varphi]$. The first of them always presents in the denominator in power one, while the later is risen to a power i . We shall be interested in values of i equal to 1, 2, 3 and 4.

$$\begin{aligned} (25) \quad \mathbf{J}_1(e, \dot{e}) &\equiv \int_0^{2\pi} (1 + e \cos \varphi)^{-1} [1 + (e - \dot{e}) \cos \varphi]^{-1} d\varphi = \int_0^{2\pi} [(1 + e \cos \varphi) - e \cos \varphi] \times \\ &\times (1 + e \cos \varphi)^{-1} [1 + (e - \dot{e}) \cos \varphi]^{-1} d\varphi = \int_0^{2\pi} [1 + (e - \dot{e}) \cos \varphi]^{-1} d\varphi - \\ &- [e/(e - \dot{e})] \int_0^{2\pi} \{ [1 + (e - \dot{e}) \cos \varphi] - 1 \} (1 + e \cos \varphi)^{-1} [1 + (e - \dot{e}) \cos \varphi]^{-1} d\varphi = \\ &= 2\pi [1 - (e - \dot{e})^2]^{-1/2} - [e/(e - \dot{e})] \int_0^{2\pi} (1 + e \cos \varphi)^{-1} d\varphi + \\ &+ [e/(e - \dot{e})] \int_0^{2\pi} (1 + e \cos \varphi)^{-1} [1 + (e - \dot{e}) \cos \varphi]^{-1} d\varphi = \\ &= 2\pi [1 - (e - \dot{e})^2]^{-1/2} - 2\pi [e/(e - \dot{e})] (1 - e^2)^{-1/2} + [e/(e - \dot{e})] \mathbf{J}_1(e, \dot{e}). \end{aligned}$$

Here we have used formula **858.525** from Dwight [6], which, in turn, implies the relations (7) and (20), applied above. Consequently, equation (25) gives that:

$$(26) \quad \{1 - [e/(e - \dot{e})]\} \mathbf{J}_1(e, \dot{e}) \equiv [-\dot{e}/(e - \dot{e})] \mathbf{J}_1(e, \dot{e}) = 2\pi [1 - (e - \dot{e})^2]^{-1/2} - 2\pi [e/(e - \dot{e})] (1 - e^2)^{-1/2}.$$

After multiplication by $[-(e - \dot{e})/\dot{e}]$, we obtain the following result for the integral $\mathbf{J}_1(e, \dot{e})$:

$$(27) \quad \mathbf{J}_1(e, \dot{e}) \equiv \int_0^{2\pi} (1 + e \cos \varphi)^{-1} [1 + (e - \dot{e}) \cos \varphi]^{-1} d\varphi = (2\pi/\dot{e}) \{ e(1 - e^2)^{-1/2} - (e - \dot{e}) [1 - (e - \dot{e})^2]^{-1/2} \}.$$

Two circumstances must be pointed out, concerning the validity of this formula:

(i) We have supposed that $(e - \dot{e}) \neq 0$. If it is not the case, then from the definition (25) it follows that $\mathbf{J}_1(e, \dot{e} = e) = \mathbf{A}_1(e, 0) = 2\pi(1 - e^2)^{-1/2}$ (see the solution (20)). But for $e(u) = \dot{e}(u)$, equation (27) gives the *same* result, i.e., it is valid also for the case $e(u) - \dot{e}(u) = 0$, and the limitation $e(u) - \dot{e}(u) \neq 0$ makes no sense.

(ii) In the relation (27) $\dot{e}(u)$ must not be equal to zero. Of course, if we *directly* set into the definition (25) $\dot{e}(u) = 0$, we easily find that:

$$(28) \quad \mathbf{J}_1(e, \dot{e} = 0) \equiv \int_0^{2\pi} (1 + e \cos \varphi)^{-2} d\varphi = \mathbf{A}_2(e, 0) = 2\pi(1 - e^2)^{-3/2},$$

From the other hand, we have the availability to apply in (27) the L'Hospital's rule, in order to evaluate the right-hand-side of this expression, when $\dot{e}(u)$ approaches zero. In particular, it is fulfilled the condition:

$$(29) \quad \lim_{\dot{e}(u) \rightarrow 0} \{e(1 - e^2)^{-1/2} - (e - \dot{e})[1 - (e - \dot{e})^2]^{-1/2}\} = 0.$$

Further, computation of the derivative with respect to \dot{e} of the difference into the curly brackets gives (after taking the limit $\dot{e} \rightarrow 0$):

$$(30) \quad \begin{aligned} \lim_{\dot{e}(u) \rightarrow 0} \partial/\partial \dot{e} \{e(1 - e^2)^{-1/2} - (e - \dot{e})[1 - (e - \dot{e})^2]^{-1/2}\} = \\ = \lim_{\dot{e}(u) \rightarrow 0} \{[1 - (e - \dot{e})^2]^{-1/2} + (e - \dot{e})^2[1 - (e - \dot{e})^2]^{-3/2}\} = (1 - e^2)^{-3/2}. \end{aligned}$$

Consequently, the above result (30) implies that the L'Hospital's rule, when applied to (27), leads to the same result (28), derived by a *direct* substitution $\dot{e}(u) = 0$ into the original formula for the integral $\mathbf{J}_1(e, \dot{e})$. In that sense, we shall use the expression (27) without checking whether $\dot{e}(u) \neq 0$ or not, having in mind that the L'Hospital's rule ensures a continuous transition through the point $\dot{e}(u) = 0$.

$$(31) \quad \begin{aligned} \mathbf{J}_2(e, \dot{e}) \equiv \int_0^{2\pi} (1 + e \cos \varphi)^{-1} [1 + (e - \dot{e}) \cos \varphi]^{-2} d\varphi = \int_0^{2\pi} [(1 + e \cos \varphi) - e \cos \varphi] \times \\ \times (1 + e \cos \varphi)^{-1} [1 + (e - \dot{e}) \cos \varphi]^{-2} d\varphi = \int_0^{2\pi} [1 + (e - \dot{e}) \cos \varphi]^{-2} d\varphi - \\ - [e/(e - \dot{e})] \int_0^{2\pi} \{[1 + (e - \dot{e}) \cos \varphi] - 1\} (1 + e \cos \varphi)^{-1} [1 + (e - \dot{e}) \cos \varphi]^{-2} d\varphi = \end{aligned}$$

$$\begin{aligned}
&= 2\pi[1 - (e - \dot{e})^2]^{-3/2} - [e/(e - \dot{e})] \int_0^{2\pi} (1 + e\cos\varphi)^{-1} [1 + (e - \dot{e})\cos\varphi]^{-1} d\varphi + \\
&+ [e/(e - \dot{e})] \int_0^{2\pi} (1 + e\cos\varphi)^{-1} [1 + (e - \dot{e})\cos\varphi]^{-2} d\varphi = \\
&= 2\pi[1 - (e - \dot{e})^2]^{-3/2} - [e/(e - \dot{e})] \mathbf{J}_1(e, \dot{e}) + [e/(e - \dot{e})] \mathbf{J}_2(e, \dot{e}).
\end{aligned}$$

Here we again have used formula **858.535** from Dwight [6] (see also the expression (8) for $\mathbf{A}_2(e, \dot{e})$ above) and the definition (25) for the integral (25). The equation (31) enables us to write an explicit form for $\mathbf{J}_2(e, \dot{e})$:

$$(32) \quad -[e/(e - \dot{e})] \mathbf{J}_2(e, \dot{e}) = 2\pi[1 - (e - \dot{e})^2]^{-3/2} - [e/(e - \dot{e})] \mathbf{J}_1(e, \dot{e}),$$

or, after dividing by $[-\dot{e}/(e - \dot{e})]$ (under the condition $\dot{e}(u) \neq 0$), we obtain:

$$(33) \quad \mathbf{J}_2(e, \dot{e}) = -2\pi [(e - \dot{e})/\dot{e}] [1 - (e - \dot{e})^2]^{-3/2} + (e/\dot{e}) \mathbf{J}_1(e, \dot{e}).$$

We are in a position to apply the result (27) for the integral $\mathbf{J}_1(e, \dot{e})$, having in mind the two remarks, which we have already done about the cases $e(u) - \dot{e}(u) = 0$ and $\dot{e}(u) = 0$:

$$\begin{aligned}
(34) \quad \mathbf{J}_2(e, \dot{e}) &\equiv \int_0^{2\pi} (1 + e\cos\varphi)^{-1} [1 + (e - \dot{e})\cos\varphi]^{-2} d\varphi = -2\pi [(e - \dot{e})/\dot{e}] [1 - (e - \dot{e})^2]^{-3/2} - \\
&- 2\pi [e(e - \dot{e})/\dot{e}^2] [1 - (e - \dot{e})^2]^{-1/2} + 2\pi(e^2/\dot{e}^2)(1 - e^2)^{-1/2} \equiv \\
&\equiv -2\pi(e - \dot{e})\dot{e}^{-2} [1 - (e - \dot{e})^2]^{-3/2} (e - e^3 + \dot{e} + 2e^2\dot{e} - e\dot{e}^2) + 2\pi(e^2/\dot{e}^2)(1 - e^2)^{-1/2}.
\end{aligned}$$

Like the case, considering the integral $\mathbf{J}_1(e, \dot{e})$, we again strike with the problem of the applicability of the expression (34) in the general situation. Namely, when $e(u) - \dot{e}(u) = 0$ and /or $\dot{e}(u) = 0$.

(i) If the supposition $e(u) - \dot{e}(u) \neq 0$ is not valid, then from the definition (31) for the integral $\mathbf{J}_2(e, \dot{e})$ it *directly* follows that $\mathbf{J}_2(e, \dot{e} = e) = \mathbf{A}_1(e, 0) = 2\pi (1 - e^2)^{-1/2}$ (see (20)). It is evident that for $e(u) = \dot{e}(u)$, the expression (34) gives the same result. Although, during the derivation of (34), it was supposed that $e(u) - \dot{e}(u) \neq 0$, in the final result about $\mathbf{J}_2(e, \dot{e})$ this limitation is not leading to any singular effects.

(ii) Also, in the relation (34) $\dot{e}(u)$ *must not vanish*. To avoid this constraint, we may directly set $\dot{e}(u) = 0$ in the definition (31). The integral is not singular and is already evaluated. Concretely:

$$(35) \quad \mathbf{J}_2(e, \dot{e} = 0) \equiv \int_0^{2\pi} (1 + e\cos\varphi)^{-3} d\varphi \equiv \mathbf{A}_3(e, 0) = \pi(2 + e^2)(1 - e^2)^{-5/2}.$$

We, of course, are able to ask whether the limit transition $\dot{e}(u) \rightarrow 0$ in the formula (34) will make sense, giving the above result (35). The supposition can be checked by applying **two** times of the L'Hospital's rule/theorem. To do the proof in a more compact manner, let us rewrite the final result (34) into the following form:

$$(36) \quad \mathbf{J}_2(e, \dot{e}) = 2\pi \dot{e}^{-2} (1 - e^2)^{-1/2} \mathbf{B}(e, \dot{e}),$$

where the function $\mathbf{B}(e, \dot{e})$, according to (34), is defined as:

$$(37) \quad \mathbf{B}(e, \dot{e}) \equiv [1 - (e - \dot{e})^2]^{-3/2} \{ e^2 [1 - (e - \dot{e})^2]^{3/2} + (-e^2 + e^4 - 3e^3\dot{e} + \dot{e}^2 + 3e^2\dot{e}^2 - e\dot{e}^3)(1 - e^2)^{1/2} \}.$$

It is easily seen that $\mathbf{B}(e, \dot{e} = 0) = 0$. The other conditions, needed for the applicability of the L'Hospital's rule with respect to the relations (34) and (36), when $\dot{e}(u) \rightarrow 0$, are obviously fulfilled. The first partial derivative of $\mathbf{B}(e, \dot{e})$ with respect to the variable $\dot{e}(u)$ is:

$$(38) \quad \begin{aligned} \partial \mathbf{B}(e, \dot{e}) / \partial \dot{e} &= (1 - e^2)^{1/2} [1 - (e - \dot{e})^2]^{-5/2} \dot{e} (2 + e^2 - 2e\dot{e} + \dot{e}^2) \equiv \\ &\equiv (1 - e^2)^{1/2} [1 - (e - \dot{e})^2]^{-5/2} \dot{e} [2 + (e - \dot{e})^2]. \end{aligned}$$

Obviously, the partial derivative $\partial \mathbf{B}(e, \dot{e}) / \partial \dot{e}$ vanishes for $\dot{e}(u) = 0$. We again see that the partial derivative with respect to $\dot{e}(u)$ of the denominator in (36) is $2\dot{e}(1 - e^2)$ and also vanishes for $\dot{e}(u) = 0$. Nevertheless, the last circumstance does not cause troubles, when the transition $\dot{e}(u) \rightarrow 0$ is performed. The availability of the factor $\dot{e}(u)$ both in the dominator and the denominator enables us to *cancel out* it, and the expression becomes free from the singularity at $\dot{e}(u) = 0$. In such a way, the needed condition (v) in the formulation of the L'Hospital's theorem (given in chapter **2.1.** above) is successfully fulfilled, and the transition $\dot{e}(u) \rightarrow 0$ does not generate a singularity. Therefore:

$$(39) \quad \begin{aligned} \mathbf{J}_2(e, \dot{e} = 0) &= \lim_{\dot{e}(u) \rightarrow 0} \{ 2\pi [\partial \mathbf{B}(e, \dot{e}) / \partial \dot{e}] / \partial [e^2(1 - e^2)^{1/2}] / \partial \dot{e} \} = \\ &= \lim_{\dot{e}(u) \rightarrow 0} \{ 2\pi (1 - e^2)^{1/2} \dot{e} (2 + e^2 - 2e\dot{e} + \dot{e}^2) / \{ [2\dot{e} [1 - (e - \dot{e})^2]^{5/2} (1 - e^2)^{1/2}] \} \} = \\ &= \pi (2 + e^2) (1 - e^2)^{-5/2}. \end{aligned}$$

This result is the same as the relation (35), where is used a *direct* method for computation of the case $\dot{e}(u) = 0$, without the application of any continuum transitions to this special point $\dot{e}(u) = 0$. Consequently, we are

able to use the formula (34) also for values $\dot{e}(u) = 0$, keeping in mind that the singularity may be overcome by means of the L'Hospital's rule.

$$\begin{aligned}
(40) \quad \mathbf{J}_3(e, \dot{e}) &\equiv \int_0^{2\pi} (1 + e \cos \varphi)^{-1} [1 + (e - \dot{e}) \cos \varphi]^{-3} d\varphi = \int_0^{2\pi} [(1 + e \cos \varphi) - e \cos \varphi] \times \\
&\times (1 + e \cos \varphi)^{-1} [1 + (e - \dot{e}) \cos \varphi]^{-3} d\varphi = \int_0^{2\pi} [1 + (e - \dot{e}) \cos \varphi]^{-3} d\varphi - \\
&- [e/(e - \dot{e})] \int_0^{2\pi} \{ [1 + (e - \dot{e}) \cos \varphi] - 1 \} (1 + e \cos \varphi)^{-1} [1 + (e - \dot{e}) \cos \varphi]^{-3} d\varphi = \\
&= \mathbf{A}_3(e, \dot{e}) - [e/(e - \dot{e})] \int_0^{2\pi} (1 + e \cos \varphi)^{-1} [1 + (e - \dot{e}) \cos \varphi]^{-2} d\varphi + \\
&+ [e/(e - \dot{e})] \int_0^{2\pi} (1 + e \cos \varphi)^{-1} [1 + (e - \dot{e}) \cos \varphi]^{-3} d\varphi = \\
&= \mathbf{A}_3(e, \dot{e}) - [e/(e - \dot{e})] \mathbf{J}_2(e, \dot{e}) + [e/(e - \dot{e})] \mathbf{J}_3(e, \dot{e}).
\end{aligned}$$

Transferring the unknown function $\mathbf{J}_3(e, \dot{e})$ into the left-hand-side, we obtain:

$$(41) \quad [1 - e/(e - \dot{e})] \mathbf{J}_3(e, \dot{e}) \equiv - [e/(e - \dot{e})] \mathbf{J}_3(e, \dot{e}) = \mathbf{A}_3(e, \dot{e}) - [e/(e - \dot{e})] \mathbf{J}_2(e, \dot{e}).$$

During the present derivation, we are supposing that both $\dot{e}(u) \neq 0$ and $e(u) - \dot{e}(u) \neq 0$. In agreement with this suggestion, we rewrite the above relation as:

$$\begin{aligned}
(42) \quad \mathbf{J}_3(e, \dot{e}) &= - [(e - \dot{e})/\dot{e}] \mathbf{A}_3(e, \dot{e}) + (e/\dot{e}) \mathbf{J}_2(e, \dot{e}) = -\pi(e - \dot{e}) [2 + (e - \dot{e})^2] \dot{e}^{-1} \times \\
&\times [1 - (e - \dot{e})^2]^{-5/2} - 2\pi e (e - \dot{e}) (e - e^3 + 2e^2 \dot{e} - e \dot{e}^2) \dot{e}^{-3} [1 - (e - \dot{e})^2]^{-3/2} + \\
&+ 2\pi e^3 \dot{e}^{-3} (1 - e^2)^{-1/2} = \\
&= -\pi(e - \dot{e}) \dot{e}^{-3} [1 - (e - \dot{e})^2]^{-5/2} (2e^2 - 4e^4 + 2e^6 + 2e \dot{e} + 6e^3 \dot{e} - 8e^5 \dot{e} + 2\dot{e}^2 + e^2 \dot{e}^2 + \\
&+ 12e^4 \dot{e}^2 - 4e \dot{e}^3 - 8e^3 \dot{e}^3 + \dot{e}^4 + 2e^2 \dot{e}^4) + 2\pi e^3 \dot{e}^{-3} (1 - e^2)^{-1/2}.
\end{aligned}$$

We again strike with the problem concerning the validity of the expression (42). If we set into the definition (40) $e(u) = \dot{e}(u)$ (i.e., $e(u) - \dot{e}(u) = 0$), the *direct* computation of the integral $\mathbf{J}_3(e, \dot{e} = e)$ leads to the following simple result (taking into account the equality (20)):

$$(43) \quad \mathbf{J}_3(e, \dot{e} = e) \equiv \int_0^{2\pi} (1 + e \cos \varphi)^{-1} d\varphi = \mathbf{A}_1(e, 0) = 2\pi (1 - e^2)^{-1/2}.$$

The same answer gives equation (42), if the equality $e(u) - \dot{e}(u) = 0$ is set into it. Therefore, the established analytical evaluation (42) for the integral $\mathbf{J}_3(e, \dot{e})$ may be used also in the case when $e(u) - \dot{e}(u) = 0$. This

reasoning remains valid even if $e(u) = \dot{e}(u) = 0$, under the condition that $e^3(u)$ and $\dot{e}^3(u)$ are preliminary cancelled out in the last term $2\pi e^3 \dot{e}^{-3} (1 - e^2)^{-1/2}$ of the expression (42). Then the result is trivial: $\mathbf{J}_3(0,0) = 2\pi$. Like the previous two cases about the integrals $\mathbf{J}_1(e,\dot{e})$ and $\mathbf{J}_2(e,\dot{e})$, the special case $\dot{e}(u) = 0$ can be resolved by means of a *direct* substitution of this constraint into the definition of the integral $\mathbf{J}_3(e,\dot{e} = 0)$:

$$(44) \quad \mathbf{J}_3(e,\dot{e} = 0) \equiv \int_0^{2\pi} (1 + e \cos \varphi)^{-4} d\varphi = \mathbf{A}_4(e,0) = \pi (2 + 3e^2)(1 - e^2)^{-7/2}.$$

Here we have applied the evaluation (23) of the function $\mathbf{A}_4(e,0)$. It may be checked, that in the limit $\dot{e}(u) \rightarrow 0$, the expression (42) gives a result that coincides with the last term of the equality (43). For this purpose, the L'Hospital's rule must be come into use again. We shall not perform these tedious calculations in the present paper, which are essentially of the same character, as in the cases of the integrals $\mathbf{J}_1(e,\dot{e})$ and $\mathbf{J}_2(e,\dot{e})$, considered under the transition $\dot{e}(u) \rightarrow 0$. We shall only mention, that such a transition gives a continuous result, when is applied to the relation (42). The same approach will be put into use under the computation of the integral $\mathbf{J}_4(e,\dot{e})$, to which we are now going on.

$$(45) \quad \mathbf{J}_4(e,\dot{e}) \equiv \int_0^{2\pi} (1 + e \cos \varphi)^{-1} [1 + (e - \dot{e}) \cos \varphi]^{-4} d\varphi = \int_0^{2\pi} [(1 + e \cos \varphi) - e \cos \varphi] \times \\ \times (1 + e \cos \varphi)^{-1} [1 + (e - \dot{e}) \cos \varphi]^{-4} d\varphi = \int_0^{2\pi} [1 + (e - \dot{e}) \cos \varphi]^{-4} d\varphi - \\ - [e/(e - \dot{e})] \int_0^{2\pi} \{ [1 + (e - \dot{e}) \cos \varphi] - 1 \} (1 + e \cos \varphi)^{-1} [1 + (e - \dot{e}) \cos \varphi]^{-4} d\varphi = \\ = \mathbf{A}_4(e,\dot{e}) - [e/(e - \dot{e})] \int_0^{2\pi} (1 + e \cos \varphi)^{-1} [1 + (e - \dot{e}) \cos \varphi]^{-3} d\varphi + \\ + [e/(e - \dot{e})] \int_0^{2\pi} (1 + e \cos \varphi)^{-1} [1 + (e - \dot{e}) \cos \varphi]^{-4} d\varphi = \\ = \mathbf{A}_4(e,\dot{e}) - [e/(e - \dot{e})] \mathbf{J}_3(e,\dot{e}) + [e/(e - \dot{e})] \mathbf{J}_4(e,\dot{e}).$$

We have applied above the definitions (9), (40) and the first equality/identity in (45). Supposing that both $\dot{e}(u) \neq 0$ and $e(u) - \dot{e}(u) \neq 0$, we proceed further to evaluate the integral $\mathbf{J}_4(e,\dot{e})$ through the already computed functions of $e(u)$ and $\dot{e}(u)$ $\mathbf{A}_4(e,\dot{e})$ and $\mathbf{J}_3(e,\dot{e})$:

$$(46) \quad [1 - e/(e - \dot{e})]\mathbf{J}_4(e, \dot{e}) \equiv - [\dot{e}/(e - \dot{e})]\mathbf{J}_4(e, \dot{e}) = \mathbf{A}_4(e, \dot{e}) - [e/(e - \dot{e})]\mathbf{J}_3(e, \dot{e}).$$

Consequently, on the basis of the relations (9) for $\mathbf{A}_4(e, \dot{e})$ and (42) for $\mathbf{J}_3(e, \dot{e})$, we obtain the final expression for $\mathbf{J}_4(e, \dot{e})$ in an explicit form in terms of $e(u)$ and $\dot{e}(u)$:

$$(47) \quad \mathbf{J}_4(e, \dot{e}) \equiv \int_0^{2\pi} (1 + e \cos \varphi)^{-1} [1 + (e - \dot{e}) \cos \varphi]^{-4} d\varphi = - [(e - \dot{e})/\dot{e}]\mathbf{A}_4(e, \dot{e}) + (e/\dot{e})\mathbf{J}_3(e, \dot{e}) =$$

$$= - (e - \dot{e})[2 + 3(e - \dot{e})^2]\dot{e}^{-1}[1 - (e - \dot{e})^2]^{-7/2} - \pi e(e - \dot{e})(2e^2 - 4e^4 + 2e^6 + 2e\dot{e} +$$

$$+ 6e^3\dot{e} - 8e^5\dot{e} + 2\dot{e}^2 + e^2\dot{e}^2 + 12e^4\dot{e}^2 - 4e\dot{e}^3 - 8e^3\dot{e}^3 + \dot{e}^4 + 2e^2\dot{e}^4)\dot{e}^{-4}[1 - (e - \dot{e})^2]^{-5/2} +$$

$$+ 2\pi e^4\dot{e}^{-4}(1 - e^2)^{-1/2} \equiv$$

$$\equiv \pi(-2e^4 + 6e^6 - 6e^8 + 2e^{10} - 14e^5\dot{e} + 28e^7\dot{e} - 14e^9\dot{e} + 7e^4\dot{e}^2 - 49e^6\dot{e}^2 + 42e^8\dot{e}^2 +$$

$$+ 35e^5\dot{e}^3 - 70e^7\dot{e}^3 + 2\dot{e}^4 + 8e^2\dot{e}^4 + 70e^6\dot{e}^4 - 10e\dot{e}^5 - 14e^3\dot{e}^5 - 42e^5\dot{e}^5 + 3\dot{e}^6 + 7e^2\dot{e}^6 +$$

$$+ 14e^4\dot{e}^6 - e\dot{e}^7 - 2e^3\dot{e}^7) + 2\pi e^4\dot{e}^{-4}(1 - e^2)^{-1/2}.$$

Although the above expression is derived under the restriction $e(u) - \dot{e}(u) \neq 0$, it makes sense even if $e(u) - \dot{e}(u) = 0$. In the last case, the relation (47) shows that:

$$(48) \quad \mathbf{J}_4(e, \dot{e} = e) = 2\pi e^4 \dot{e}^{-4} (1 - e^2)^{-1/2} = 2\pi (1 - e^2)^{-1/2},$$

because, obviously, the first two terms in the right-hand-side are equal to zero for $e(u) - \dot{e}(u) = 0$, and remains only the last term, where $e(u)/\dot{e}(u) = 1$. Of course, the integral $\mathbf{J}_4(e, \dot{e} = e)$ may be *directly* computed by setting $e(u) = \dot{e}(u)$ into its definition (45):

$$(49) \quad \mathbf{J}_4(e, \dot{e} = e) \equiv \int_0^{2\pi} (1 + e \cos \varphi)^{-1} d\varphi = \mathbf{A}_1(e, 0) = 2\pi (1 - e^2)^{-1/2},$$

where we have again used the relation (20). The two expressions (48) and (49) coincide, and, therefore, the restriction $e(u) - \dot{e}(u) \neq 0$ for the solution (47) can be removed. This conclusion continues to be valid even if $\dot{e}(u) = 0$. Concerning the general case $\dot{e}(u) = 0$, the definition (45) also *directly* enables us to evaluate the wanted function $\mathbf{J}_4(e, 0)$, namely:

$$(50) \quad \mathbf{J}_4(e, 0) \equiv \int_0^{2\pi} (1 + e \cos \varphi)^{-5} d\varphi \equiv \mathbf{A}_5(e, 0) = (\pi/4)(8 + 24e^2 + 3e^4)(1 - e^2)^{-9/2},$$

where we have applied the relation (24). It is possible to check, by means of the L'Hospital's rule for revealing of indeterminacies of the type 0/0, that the passage to the limit $\dot{e}(u) = 0$ in the relation (47) leads to the same result (50). Consequently, such a transition through the point $\dot{e}(u) = 0$ is continuous. Further we shall apply formula (47) also when $\dot{e}(u) = 0$, having in mind that the indeterminacy is overcome preliminary through the

L'Hospital's rule. Like in the previous case for the integral $\mathbf{J}_4(e, \dot{e})$, we shall skip, for reasons of brevity, the proof of the statement that the transition $\dot{e}(u) \rightarrow 0$ in (47) gives the same result as the relation (50).

In conclusion, we note that the considered number of integrals of the type $\mathbf{J}_i(e, \dot{e})$, ($i = 1, 2, 3, 4$), is enough for our consequent applications. They will be made in the forthcoming papers (in particular, paper [8]), devoted to the simplification of the dynamical equation of the accretion discs with elliptical shapes. Summarizing some of the results in this chapter, we mention that for all $i = 1, 2, 3$ and 4 we have $\mathbf{J}_i(e, \dot{e} = 0) = \mathbf{A}_{i+1}(e, \dot{e} = 0)$, and $\mathbf{J}_i(e, \dot{e} = e) = \mathbf{A}_1(e, \dot{e} = 0) = 2\pi(1 - e^2)^{-1/2}$.

2.3. Evaluation of integrals of the type

$$\mathbf{H}_i(e, \dot{e}) \equiv \int_0^{2\pi} (1 + e \cos \varphi)^{-i} [1 + (e - \dot{e}) \cos \varphi]^{-1} d\varphi$$

These auxiliary integrals will be evaluated analytically for values of the power $i = 1, 2, 3$ and 4. Their estimates will be applied, in own turn, for computation of *other* auxiliary integrals, which will be made in subsequent papers. We begin with the most simple of them, namely, the integral $\mathbf{H}_1(e, \dot{e})$:

$$(51) \quad \mathbf{H}_1(e, \dot{e}) \equiv \int_0^{2\pi} (1 + e \cos \varphi)^{-1} [1 + (e - \dot{e}) \cos \varphi]^{-1} d\varphi \equiv \mathbf{J}_1(e, \dot{e}) = \\ = (2\pi/\dot{e}) \{ e(1 - e^2)^{-1/2} - (e - \dot{e}) [1 - (e - \dot{e})^2]^{-1/2} \},$$

where we rewrite formula (27) above. All remarks, which were made about the validity of the estimation (27) for the integral $\mathbf{J}_1(e, \dot{e})$, automatically remain in power also for $\mathbf{H}_1(e, \dot{e})$. The next step is to find the integral $\mathbf{H}_2(e, \dot{e})$ as a function of its arguments $e(u)$ and $\dot{e}(u)$:

$$(52) \quad \mathbf{H}_2(e, \dot{e}) \equiv \int_0^{2\pi} (1 + e \cos \varphi)^{-2} [1 + (e - \dot{e}) \cos \varphi]^{-1} d\varphi = \int_0^{2\pi} \{ [1 + (e - \dot{e}) \cos \varphi] - \\ - (e - \dot{e}) \cos \varphi \} (1 + e \cos \varphi)^{-2} [1 + (e - \dot{e}) \cos \varphi]^{-1} d\varphi = \int_0^{2\pi} (1 + e \cos \varphi)^{-2} d\varphi - \\ - [(e - \dot{e})/e] \int_0^{2\pi} [(1 + e \cos \varphi) - 1] (1 + e \cos \varphi)^{-2} [1 + (e - \dot{e}) \cos \varphi]^{-1} d\varphi = \mathbf{A}_2(e, 0) - \\ - [(e - \dot{e})/e] \int_0^{2\pi} (1 + e \cos \varphi)^{-1} [1 + (e - \dot{e}) \cos \varphi]^{-1} d\varphi + [(e - \dot{e})/e] \int_0^{2\pi} (1 + e \cos \varphi)^{-2} \times \\ \times [1 + (e - \dot{e}) \cos \varphi]^{-1} d\varphi = \mathbf{A}_2(e, 0) - [(e - \dot{e})/e] \mathbf{H}_1(e, \dot{e}) + [(e - \dot{e})/e] \mathbf{H}_2(e, \dot{e}) =$$

$$= 2\pi(1 - e^2)^{-3/2} - 2\pi(e - \dot{e})\dot{e}^{-1}(1 - e^2)^{-1/2} + 2\pi(e - \dot{e})^2 e^{-1}\dot{e}^{-1}[1 - (e - \dot{e})^2]^{-1/2} + [(e - \dot{e})/e]\mathbf{H}_2(e, \dot{e}),$$

where we have applied the above already established results (21) and (51) $\mathbf{A}_2(e, 0)$ and $\mathbf{H}_1(e, \dot{e})$, respectively. Therefore, the equation (52) ensures the following solution for the wanted function $\mathbf{H}_2(e, \dot{e})$:

$$(53) \quad [1 - (e - \dot{e})/e]\mathbf{H}_2(e, \dot{e}) \equiv (\dot{e}/e)\mathbf{H}_2(e, \dot{e}) = 2\pi\{e\dot{e}[1 - (e - \dot{e})^2]^{1/2} - e(e - \dot{e})(1 - e^2) \times [1 - (e - \dot{e})^2]^{1/2} + (e - \dot{e})^2(1 - e^2)^{3/2}\}e^{-1}\dot{e}^{-1}(1 - e^2)^{-3/2}[1 - (e - \dot{e})^2]^{-1/2}.$$

After multiplying the both sides of this relation by $e(u)/\dot{e}(u)$, we obtain the final analytical expression for the integral $\mathbf{H}_2(e, \dot{e})$:

$$(54) \quad \mathbf{H}_2(e, \dot{e}) = 2\pi\{(e - \dot{e})^2(1 - e^2)^{3/2} + (-e^2 + e^4 + 2e\dot{e} - e^3\dot{e})[1 - (e - \dot{e})^2]^{1/2}\}\dot{e}^{-2} \times (1 - e^2)^{-3/2}[1 - (e - \dot{e})^2]^{-1/2}.$$

Of course, this result is derived under the assumptions that $[e(u) \neq 0] \cap [\dot{e}(u) \neq 0]$. It can be rewritten also into the form:

$$(55) \quad \mathbf{H}_2(e, \dot{e}) \equiv \int_0^{2\pi} (1 + e\cos\varphi)^{-2} [1 + (e - \dot{e})\cos\varphi]^{-1} d\varphi = (2\pi/\dot{e}^2)\{(e - \dot{e})^2[1 - (e - \dot{e})^2]^{-1/2} + (-e^2 + e^4 + 2e\dot{e} - e^3\dot{e})(1 - e^2)^{-3/2}\}.$$

Obviously, the formulas (54) and (55) have nonsingular meaning for $e(u) = 0$ (preserving the restriction $\dot{e}(u) \neq 0$), namely:

$$(56) \quad \mathbf{H}_2(0, \dot{e}) = (2\pi/\dot{e}^2)[\dot{e}^2(1 - \dot{e}^2)^{-1/2} + 0] \equiv 2\pi(1 - \dot{e}^2)^{-1/2}.$$

A *direct* computation for the case $e(u) = 0$ (with $\dot{e}(u) \neq 0$) for the integral $\mathbf{H}_2(e=0, \dot{e})$ shows that:

$$(57) \quad \mathbf{H}_2(0, \dot{e}) \equiv \int_0^{2\pi} (1 - \dot{e}\cos\varphi)^{-1} d\varphi = 2\pi(1 - \dot{e}^2)^{-1/2},$$

which coincides with (56). Here we have again used formula **858.525** from Dwight [6]. Of course, there is not problem to apply the expressions (56) and (57) when $\dot{e}(u) = 0$. They both give the right answer $\mathbf{H}_2(0, 0) = 2\pi$.

With respect to the general case $\dot{e}(u) = 0$ (when $e(u)$ does not need to be equal to zero), it may be noted that the expression in the curly brackets in (55) approaches zero, when $\dot{e}(u)$ also approaches zero:

$$(58) \quad \lim_{\dot{e}(u) \rightarrow 0} \{(e - \dot{e})^2[1 - (e - \dot{e})^2]^{-1/2} + (-e^2 + e^4 + 2e\dot{e} - e^3\dot{e})(1 - e^2)^{-3/2}\} = e^2(1 - e^2)^{-1/2} - e^2(1 - e^2)(1 - e^2)^{-3/2} = 0.$$

It is easily verified, that the other conditions for the applicability of the L'Hospital's theorem are also fulfilled. Consequently, we are in a position to apply the L'Hospital's rule with regard to the right-hand-side of the relation (55), in order to overcome the indeterminacy of the type 0/0, when $\dot{e}(u) = 0$. In that approach, we have to evaluate the limit transition:

$$(59) \quad \lim_{\dot{e}(u) \rightarrow 0} \partial/\partial \dot{e} \{ (e - \dot{e})^2 [1 - (e - \dot{e})^2]^{-1/2} + (-e^2 + e^4 + 2e\dot{e} - e^3\dot{e})(1 - e^2)^{-3/2} \} = \\ = \lim_{\dot{e}(u) \rightarrow 0} \{ -2(e - \dot{e}) [1 - (e - \dot{e})^2]^{-1/2} - (e - \dot{e})^3 [1 - (e - \dot{e})^2]^{-3/2} + \\ + (2e - e^3)(1 - e^2)^{-3/2} \} = -2e(1 - e^2)^{-1/2} - e^3(1 - e^2)^{-3/2} + \\ + (2e - e^3)(1 - e^2)^{-3/2} = 0.$$

The computation of the expression (55) in the limit $\dot{e}(u) \rightarrow 0$ again strikes with the problem of evaluating of an indeterminacy of the type 0/0. To solve the task, we shall use for a second time the L'Hospital's rule. The premises to do this are available. In particular, we see that:

$$(60) \quad \lim_{\dot{e}(u) \rightarrow 0} \partial/\partial \dot{e} \{ -2(e - \dot{e}) [1 - (e - \dot{e})^2]^{-1/2} - (e - \dot{e})^3 [1 - (e - \dot{e})^2]^{-3/2} + \\ + (2e - e^3)(1 - e^2)^{-3/2} \} = \lim_{\dot{e}(u) \rightarrow 0} \{ 2 [1 - (e - \dot{e})^2]^{-1/2} + 2(e - \dot{e})^2 [1 - (e - \dot{e})^2]^{-3/2} + \\ + 3(e - \dot{e})^2 [1 - (e - \dot{e})^2]^{-3/2} + 3(e - \dot{e})^4 [1 - (e - \dot{e})^2]^{-5/2} \} = \\ = 2(1 - e^2)^{-1/2} + 5e^2(1 - e^2)^{-3/2} + 3e^4(1 - e^2)^{-5/2} = (2 + e^2)(1 - e^2)^{-5/2}.$$

Consequently, the twice recurrent application of the L'Hospital's rule with respect to the right-hand-side of the equation (55), leads to the following result, when $\dot{e}(u)$ approaches zero value:

$$(61) \quad \mathbf{H}_2(e, 0) = \lim_{\dot{e}(u) \rightarrow 0} \{ (2\pi/\dot{e}^2) \{ (e - \dot{e})^2 [1 - (e - \dot{e})^2]^{-1/2} + \\ + (-e^2 + e^4 + 2e\dot{e} - e^3\dot{e})(1 - e^2)^{-3/2} \} \} = \pi(2 + e^2)(1 - e^2)^{-5/2}.$$

From the other hand, the *direct* calculation for $\dot{e}(u) = 0$ leads to (according to the relation (22)):

$$(62) \quad \mathbf{H}_2(e, 0) \equiv \int_0^{2\pi} (1 + e \cos \varphi)^{-3} d\varphi \equiv \mathbf{A}_3(e, 0) = \pi(2 + e^2)(1 - e^2)^{-5/2},$$

which coincides with the previous equality (61). In this connection, we note that the transition $\dot{e}(u) \rightarrow 0$ in (54) and (55) is continuous. That is to say, when we use the later two formulas for $\dot{e}(u) = 0$, we shall subattend the meaning $\pi(2 + e^2)(1 - e^2)^{-5/2}$. Now it is trivial to evaluate $\mathbf{H}_2(e, \dot{e})$ when both $e(u) = 0$ and $\dot{e}(u) = 0$:

$$(63) \quad \mathbf{H}_2(0,0) \equiv \int_0^{2\pi} d\varphi = 2\pi.$$

The same result follows if we set in (56) $\dot{e}(u) = 0$, or if we set in (61) $e(u) = 0$. This implies that there is not matter the order of the performing of the transitions $e(u) \rightarrow 0$ or $\dot{e}(u) \rightarrow 0$. The next integral, of the considered in the present paragraph type, is $\mathbf{H}_3(e,\dot{e})$:

$$(64) \quad \begin{aligned} \mathbf{H}_3(e,\dot{e}) &\equiv \int_0^{2\pi} (1 + e\cos\varphi)^{-3} [1 + (e - \dot{e})\cos\varphi]^{-1} d\varphi = \int_0^{2\pi} \{ [1 + (e - \dot{e})\cos\varphi] - \\ &- (e - \dot{e})\cos\varphi \} (1 + e\cos\varphi)^{-3} [1 + (e - \dot{e})\cos\varphi]^{-1} d\varphi = \int_0^{2\pi} (1 + e\cos\varphi)^{-3} d\varphi - \\ &- [(e - \dot{e})/e] \int_0^{2\pi} [(1 + e\cos\varphi) - 1] (1 + e\cos\varphi)^{-3} [1 + (e - \dot{e})\cos\varphi]^{-1} d\varphi = \mathbf{A}_3(e,0) - \\ &- [(e - \dot{e})/e] \int_0^{2\pi} (1 + e\cos\varphi)^{-2} [1 + (e - \dot{e})\cos\varphi]^{-1} d\varphi + [(e - \dot{e})/e] \int_0^{2\pi} (1 + e\cos\varphi)^{-3} \times \\ &\times [1 + (e - \dot{e})\cos\varphi]^{-1} d\varphi = \mathbf{A}_3(e,0) - [(e - \dot{e})/e] \mathbf{H}_2(e,\dot{e}) + [(e - \dot{e})/e] \mathbf{H}_3(e,\dot{e}). \end{aligned}$$

After taking into account the expressions (22) and (55) for $\mathbf{A}_3(e,0)$ and $\mathbf{H}_2(e,\dot{e})$, respectively, the unknown function $\mathbf{H}_3(e,\dot{e})$ may be find in an explicit form:

$$(65) \quad \begin{aligned} [1 - (e - \dot{e})/e] \mathbf{H}_3(e,\dot{e}) &\equiv (\dot{e}/e) \mathbf{H}_3(e,\dot{e}) = \pi(2 + e^2)(1 - e^2)^{-5/2} - \\ &- 2\pi(e - \dot{e})^3 e^{-1} \dot{e}^{-2} [1 - (e - \dot{e})^2]^{-1/2} - \\ &- 2\pi(e - \dot{e})(-e^2 + e^4 + 2e\dot{e} - e^3\dot{e}) e^{-1} \dot{e}^{-2} (1 - e^2)^{-3/2}. \end{aligned}$$

After multiplying this equation by $e(u)/\dot{e}(u)$ and some other simplifications, we obtain:

$$(66) \quad \begin{aligned} \mathbf{H}_3(e,\dot{e}) &\equiv \int_0^{2\pi} (1 + e\cos\varphi)^{-3} [1 + (e - \dot{e})\cos\varphi]^{-1} d\varphi = \pi e(2e^2 - 4e^4 + 2e^6 - 6e\dot{e} + \\ &+ 10e^3\dot{e} - 4e^5\dot{e} + 6e^2\dot{e}^2 - 5e^2\dot{e}^2 + 2e^4\dot{e}^2) \dot{e}^{-3} (1 - e^2)^{-5/2} - \\ &- 2\pi(e - \dot{e})^2 \dot{e}^{-3} [1 - (e - \dot{e})^2]^{-1/2} \equiv \\ &\equiv \pi \{ (2e^3 - 4e^5 + 2e^7 - 6e^2\dot{e} + 10e^4\dot{e} - 4e^6\dot{e} + 6e\dot{e}^2 - 5e^3\dot{e}^2 + 2e^5\dot{e}^2) [1 - (e - \dot{e})^2]^{1/2} - \\ &- 2(e - \dot{e})^3 (1 - e^2)^{5/2} \} \dot{e}^{-3} (1 - e^2)^{-5/2} [1 - (e - \dot{e})^2]^{-1/2}. \end{aligned}$$

It is evident from the above derivation, that the solution (66) is determined under the suggestion that both $e(u) \neq 0$ and $\dot{e}(u) \neq 0$. The first restriction $e(u) \neq 0$ may be eliminated, if we note that the right-hand-side of (66) makes sense even if we set into it $e(u) = 0$, preserving the other condition $\dot{e}(u) \neq 0$:

$$(67) \quad \mathbf{H}_3(0, \dot{e}) \equiv \int_0^{2\pi} (1 - \dot{e} \cos \varphi)^{-1} d\varphi = 2\pi \dot{e}^3 \dot{e}^{-3} (1 - \dot{e}^2)^{-1/2} \equiv 2\pi (1 - \dot{e}^2)^{-1/2}.$$

Of course, the non-vanishing of $\dot{e}(u)$ ensures the possibility to cancel out the factor $\dot{e}^3(u)$, which presents into the nominator and the denominator of the above quotient. The same result may be established, if we set *directly* $e(u) = 0$ into the definition (64) of the integral $\mathbf{H}_3(e, \dot{e})$, and apply the already known relation (20) for the integral $\mathbf{A}_1(\dot{e}, 0)$:

$$(68) \quad \mathbf{H}_3(0, \dot{e}) \equiv \int_0^{2\pi} (1 - \dot{e} \cos \varphi)^{-1} d\varphi \equiv \mathbf{A}_1(\dot{e}, 0) = 2\pi (1 - \dot{e}^2)^{-1/2}.$$

In this manner, we conclude that the introduced during the derivation of equation (66), restriction $e(u) \neq 0$ is not burdensome. The final result (66) nevertheless gives the right answer, if we formally set into it the ‘‘peculiar’’ value $e(u) = 0$. A little more difficult is the problem concerning the other restriction $\dot{e}(u) \neq 0$. To consider this case in a compact form, let us introduce the notation $\mathbf{C}(e, \dot{e})$ about the term into the curly brackets in the relation (66):

$$(69) \quad \mathbf{C}(e, \dot{e}) \equiv (2e^3 - 4e^5 + 2e^7 - 6e^2\dot{e} + 10e^4\dot{e} - 4e^6\dot{e} + 6e\dot{e}^2 - 5e^3\dot{e}^2 + 2e^5\dot{e}^2) \times \\ \times [1 - (e - \dot{e})^2]^{1/2} - 2(e - \dot{e})^3(1 - e^2)^{5/2}.$$

Then we rewrite (66) into the following way:

$$(70) \quad \mathbf{H}_3(e, \dot{e}) = \pi \mathbf{C}(e, \dot{e}) \dot{e}^{-3} (1 - e^2)^{-5/2} [1 - (e - \dot{e})^2]^{-1/2}.$$

Temporally we disregard the factor $\pi(1 - e^2)^{-5/2} [1 - (e - \dot{e})^2]^{-1/2}$, which does not cause troubles for $\dot{e}(u) = 0$, and concentrate on the quotient $\mathbf{C}(e, \dot{e})/\dot{e}^3$. If the later has a reasonable meaning under the limit transition $\dot{e}(u) \rightarrow 0$, then the total product (70) is also defined – it is evaluated simply by multiplication with $\pi(1 - e^2)^{-3}$. Obviously, for $\dot{e}(u) = 0$, we have $\mathbf{C}(e, 0) = 0$, and the other conditions for applying of the L’Hospital’s theorem (when $\dot{e}(u) \rightarrow 0$) are fulfilled too. Computation of the limit $\lim_{\dot{e}(u) \rightarrow 0} \partial \mathbf{C}(e, \dot{e})/\partial \dot{e}$ gives a zero result:

$$\dot{e}(u) \rightarrow 0$$

$$(71) \quad \lim_{\dot{e}(u) \rightarrow 0} \partial \mathbf{C}(e, \dot{e})/\partial \dot{e} = \lim_{\dot{e}(u) \rightarrow 0} \{(-6e^2 + 10e^4 - 4e^6 + 12e\dot{e} - 10e^3\dot{e} + 4e^5\dot{e})[1 - (e - \dot{e})^2]^{1/2} + \\ + (2e^3 - 4e^5 + 2e^7 - 6e^2\dot{e} + 10e^4\dot{e} - 4e^6\dot{e} + 6e\dot{e}^2 - 5e^3\dot{e}^2 + 2e^5\dot{e}^2)(e - \dot{e}) \times \\ \times [1 - (e - \dot{e})^2]^{-1/2} + 6(e - \dot{e})^2(1 - e^2)^{5/2}\} = (-6e^2 + 10e^4 - 4e^6)(1 - e^2)^{1/2} + \\ + e(2e^3 - 4e^5 + 2e^7)(1 - e^2)^{-1/2} + 6e^2(1 - e^2)^{5/2} \equiv 0.$$

The derivative of the denominator with respect to $\dot{e}(u)$ is $3\dot{e}^2(u)$, which approaches zero, when $\dot{e}(u) \rightarrow 0$. The conditions for application of the L’Hospital’s rule for computation of $\lim_{\dot{e}(u) \rightarrow 0} [(1/3\dot{e}^2)\partial \mathbf{C}(e, \dot{e})/\partial \dot{e}]$ are again

available, and we have:

$$\begin{aligned}
(72) \quad \lim_{\dot{e}(u) \rightarrow 0} \partial^2 \mathbf{C}(e, \dot{e}) / \partial \dot{e}^2 &= \lim_{\dot{e}(u) \rightarrow 0} \{ (12e - 10e^3 + 4e^5) [1 - (e - \dot{e})^2]^{1/2} + (-6e^2 + 10e^4 - 4e^6 + \\
&+ 12e\dot{e} - 10e^3\dot{e} + 4e^5\dot{e})(e - \dot{e}) [1 - (e - \dot{e})^2]^{-1/2} + (-8e^3 + 14e^5 - 6e^7 + 24e^2\dot{e} - \\
&- 30e^4\dot{e} + 12e^6\dot{e} - 18e\dot{e}^2 + 15e^3\dot{e}^2 - 6e^5\dot{e}^2) [1 - (e - \dot{e})^2]^{-1/2} - (2e^4 - 4e^6 + 2e^8 - \\
&- 8e^3\dot{e} + 14e^5\dot{e} - 6e^7\dot{e} + 12e^2\dot{e}^2 - 15e^4\dot{e}^2 + 6e^6\dot{e}^2 - 6e\dot{e}^3 + 5e^3\dot{e}^3 - 2e^5\dot{e}^3)(e - \dot{e}) \times \\
&\times [1 - (e - \dot{e})^2]^{-3/2} - 12(e - \dot{e})(1 - e^2)^{5/2} \} = \\
&= \lim_{\dot{e}(u) \rightarrow 0} \{ (12e - 48e^3 + 72e^5 - 48e^7 + 12e^9 + 90e^2\dot{e} - 198e^4\dot{e} + 156e^6\dot{e} - 48e^8\dot{e} - 54e\dot{e}^2 + \\
&+ 225e^3\dot{e}^2 - 198e^5\dot{e}^2 + 72e^7\dot{e}^2 - 132e^2\dot{e}^3 + 120e^4\dot{e}^3 - 48e^6\dot{e}^3 + 36e\dot{e}^4 - 30e^3\dot{e}^4 + \\
&+ 12e^5\dot{e}^4) [1 - (e - \dot{e})^2]^{-3/2} - 12(e - \dot{e})(1 - e^2)^{5/2} \} = (12e - 48e^3 + 72e^5 - 48e^7 + \\
&+ 12e^9 - 12e + 48e^3 - 72e^5 + 48e^7 - 12e^9)(1 - e^2)^{-3/2} \equiv 0.
\end{aligned}$$

Now we are in a position to use the L'Hospital's rule for a third time during the procedure of the evaluation of the solution (66) under the transition $\dot{e}(u) \rightarrow 0$. Skipping some of the tedious intermediate algebraic computations, we can write:

$$\begin{aligned}
(73) \quad \lim_{\dot{e}(u) \rightarrow 0} \partial^3 \mathbf{C}(e, \dot{e}) / \partial \dot{e}^3 &= (12e - 48e^3 + 72e^5 - 48e^7 + 12e^9)(1 - e^2)^{-5/2} + (90e^2 - 198e^4 + \\
&+ 156e^6 - 48e^8)(1 - e^2)^{-3/2} + 12(1 - e^2)^{5/2} = 6(1 - e^2)^2(2 + 3e^2).
\end{aligned}$$

This time we obtain a non-zero result, and more importantly, $\partial^3(\dot{e}^3) / \partial \dot{e}^3 = 6 \neq 0$. Having also in mind, that for the first factor in the expression (70) we have:

$$\begin{aligned}
(74) \quad \lim_{\dot{e}(u) \rightarrow 0} \{ \pi(1 - e^2)^{-5/2} [1 - (e - \dot{e})^2]^{-1/2} \} &= \pi(1 - e^2)^{-3},
\end{aligned}$$

finally, we are able to summarize the following result:

$$\begin{aligned}
(75) \quad \lim_{\dot{e}(u) \rightarrow 0} \mathbf{H}_3(e, \dot{e}) &= \lim_{\dot{e}(u) \rightarrow 0} \{ \pi \mathbf{C}(e, \dot{e}) \dot{e}^{-3} (1 - e^2)^{-5/2} [1 - (e - \dot{e})^2]^{-1/2} \} = \\
&= \pi(2 + 3e^2)(1 - e^2)^{-7/2}.
\end{aligned}$$

There is not a problem to evaluate *directly* the integral $\mathbf{H}_3(e, \dot{e})$ for the special case $\dot{e}(u) = 0$ without making any transition to this value into an expression of the type (66) (or (70), respectively), which is obtained under the preliminary elimination of this case. Therefore, the direct substitution $\dot{e}(u) = 0$ into the definition (66) leads to (taking into account the already known result (23) for $\mathbf{A}_4(e, 0)$):

$$(76) \quad \mathbf{H}_3(e, 0) \equiv \int_0^{2\pi} (1 + e \cos \varphi)^{-4} d\varphi \equiv \mathbf{A}_4(e, 0) = \pi(2 + 3e^2)(1 - e^2)^{-7/2}.$$

The coincidence of the right-hand-side of the formulas (75) and (76) implies that the analytical evaluation (66) for the integral $\mathbf{H}_3(e, \dot{e})$ ensures a *continuous* transition through the “peculiar” value $\dot{e}(u) = 0$. Namely, this property of the analytical derivation (66) will be implicitly understood, when it will be used in the applications. Without specifying whether $\dot{e}(u)$ is equal to zero or not. The same remark concerns the situation $e(u) = 0$ or $e(u) \neq 0$, and also the combination $[e(u) = 0] \cap [e(u) \neq 0]$. In the later, all established above expressions give the right value $\mathbf{H}_3(0, 0) = 2\pi$.

The next integral $\mathbf{H}_4(e, \dot{e})$, which we shall try to compute analytically, is the last in the series of integrals of the type, considered in the present subsection. In particular, this is stipulated by the circumstance that, in fact, this is the integral $\mathbf{I}_{n-2, n+3}(e, \dot{e}, n = -2)$ for the concrete value power $n = -2$. We apply here a notation, which will be put in use in forthcoming papers, where we shall adopt another system of designations for the considered integrals. This integral $\mathbf{H}_4(e, \dot{e})$ participates in an explicit form into the Wronski determinant, establishing the linear dependence/independence between the integrals $\mathbf{I}_{0-}(e, \dot{e}, n)$ and $\mathbf{I}_{0+}(e, \dot{e}, n)$.

$$\begin{aligned}
(77) \quad \mathbf{H}_4(e, \dot{e}) &\equiv \mathbf{I}_{n-2, n+3}(e, \dot{e}, n = -2) \equiv \int_0^{2\pi} (1 + e \cos \varphi)^{-4} [1 + (e - \dot{e}) \cos \varphi]^{-1} d\varphi = \\
&= \int_0^{2\pi} \{ [1 + (e - \dot{e}) \cos \varphi] - (e - \dot{e}) \cos \varphi \} (1 + e \cos \varphi)^{-4} [1 + (e - \dot{e}) \cos \varphi]^{-1} d\varphi = \\
&= \int_0^{2\pi} (1 + e \cos \varphi)^{-4} d\varphi - [(e - \dot{e})/e] \int_0^{2\pi} [(1 + e \cos \varphi) - 1] (1 + e \cos \varphi)^{-4} \times \\
&\quad \times [1 + (e - \dot{e}) \cos \varphi]^{-1} d\varphi = \mathbf{A}_4(e, 0) - [(e - \dot{e})/e] \int_0^{2\pi} (1 + e \cos \varphi)^{-3} \times \\
&\quad \times [1 + (e - \dot{e}) \cos \varphi]^{-1} d\varphi + [(e - \dot{e})/e] \int_0^{2\pi} (1 + e \cos \varphi)^{-4} [1 + (e - \dot{e}) \cos \varphi]^{-1} d\varphi = \\
&= \mathbf{A}_4(e, 0) - [(e - \dot{e})/e] \mathbf{H}_3(e, \dot{e}) + [(e - \dot{e})/e] \mathbf{H}_4(e, \dot{e}).
\end{aligned}$$

Taking into account the expressions (23) and (66) for $\mathbf{A}_4(e, 0)$ and $\mathbf{H}_3(e, \dot{e})$, respectively, we are able to resolve the above equation (77) with respect to the unknown function $\mathbf{H}_4(e, \dot{e})$ of the variables $e(u)$ and $\dot{e}(u)$. We transfer $\mathbf{H}_4(e, \dot{e})$ into the left-hand side, and taking notice of the of the equality:

$$(78) \quad [1 - (e - \dot{e})/e] \mathbf{H}_4(e, \dot{e}) \equiv (\dot{e}/e) \mathbf{H}_4(e, \dot{e}),$$

we write the following analytical solution:

$$\begin{aligned}
(79) \quad \mathbf{H}_4(e, \dot{e}) &\equiv \mathbf{I}_{n-2, n+3}(e, \dot{e}, n = -2) \equiv \int_0^{2\pi} (1 + e \cos \varphi)^{-4} [1 + (e - \dot{e}) \cos \varphi]^{-1} d\varphi = \\
&= \pi e \dot{e}^2 (2 + 3e^2) \dot{e}^{-3} (1 - e^2)^{-7/2} - \pi \dot{e}^{-4} (1 - e^2)^{-5/2} [1 - (e - \dot{e})^2]^{-1/2} \{ (e - \dot{e}) (2e^3 - \\
&- 4e^5 + 2e^7 - 6e^2 \dot{e} + 10e^4 \dot{e} - 4e^6 \dot{e} + 6e \dot{e}^2 - 5e^3 \dot{e}^2 + 2e^5 \dot{e}^3) [1 - (e - \dot{e})^2]^{1/2} - \\
&- 2(e - \dot{e})^4 (1 - e^2)^{5/2} \} = \pi \dot{e}^{-4} (1 - e^2)^{-7/2} [1 - (e - \dot{e})^2]^{-1/2} \{ (2e \dot{e}^3 + 3e^3 \dot{e}^3) \times \\
&\times [1 - (e - \dot{e})^2]^{1/2} - (2e^4 - 6e^6 + 6e^8 - 2e^{10} - 8e^3 \dot{e} + 22e^5 \dot{e} - 20e^7 \dot{e} + 6e^9 \dot{e} + 12e^2 \dot{e}^2 - \\
&- 27e^4 \dot{e}^2 + 21e^6 \dot{e}^2 - 6e^8 \dot{e}^2 - 6e \dot{e}^3 + 11e^3 \dot{e}^3 - 7e^5 \dot{e}^3 + 2e^7 \dot{e}^3) [1 - (e - \dot{e})^2]^{1/2} + \\
&+ 2(e - \dot{e})^4 (1 - e^2)^{7/2} \} = \pi \dot{e}^{-4} (1 - e^2)^{-7/2} [1 - (e - \dot{e})^2]^{-1/2} \{ (-2e^4 + 6e^6 - 6e^8 + \\
&+ 2e^{10} + 8e^3 \dot{e} - 22e^5 \dot{e} + 20e^7 \dot{e} - 6e^9 \dot{e} - 12e^2 \dot{e}^2 + 27e^4 \dot{e}^2 - 21e^6 \dot{e}^2 + 6e^8 \dot{e}^2 + 8e \dot{e}^3 - \\
&- 8e^3 \dot{e}^3 + 7e^5 \dot{e}^3 - 2e^7 \dot{e}^3) [1 - (e - \dot{e})^2]^{1/2} + 2(e - \dot{e})^4 (1 - e^2)^{7/2} \} \equiv \\
&\equiv \pi \dot{e}^{-4} (1 - e^2)^{-7/2} (-2e^4 + 6e^6 - 6e^8 + 2e^{10} + 8e^3 \dot{e} - 22e^5 \dot{e} + 20e^7 \dot{e} - 6e^9 \dot{e} - \\
&- 12e^2 \dot{e}^2 + 27e^4 \dot{e}^2 - 21e^6 \dot{e}^2 + 6e^8 \dot{e}^2 + 8e \dot{e}^3 - 8e^3 \dot{e}^3 + 7e^5 \dot{e}^3 - 2e^7 \dot{e}^3) + \\
&+ 2\pi (e - \dot{e})^4 \dot{e}^{-4} [1 - (e - \dot{e})^2]^{-1/2}.
\end{aligned}$$

Like the previous computations, this solution (79) is derived under the assumptions $[e(u) \neq 0] \cap [\dot{e}(u) \neq 0]$. But nevertheless, it has a definite meaning for $e(u) = 0$. Namely (under a preserving of the restriction $\dot{e}(u) \neq 0$):

$$(80) \quad \mathbf{H}_4(0, \dot{e}) = 2\pi \dot{e}^4 (1 - \dot{e}^2)^{-1/2} \dot{e}^{-4} \equiv 2\pi (1 - \dot{e}^2)^{-1/2}.$$

A *direct* computation (by means of a *direct* substitution $e(u) = 0$ into the definition (77) of the integral $\mathbf{H}_4(e, \dot{e})$) gives the same result as (80):

$$(81) \quad \mathbf{H}_4(0, \dot{e}) \equiv \int_0^{2\pi} (1 - \dot{e} \cos \varphi)^{-1} d\varphi \equiv \mathbf{A}_1(\dot{e}, 0) = 2\pi (1 - \dot{e}^2)^{-1/2};$$

(see formula (20) for $\mathbf{A}_1(e, 0)$).

Therefore, because the evaluation (81) **does not require** the avoiding of the value $e(u) \neq 0$, we conclude that this restriction is not a factor, which hinders to apply formula (79) in this case. The consideration of the other situation $\dot{e}(u) \neq 0$ requires a more complex treatment, in order to reveal the behaviour of the result (79) under the transition $\dot{e}(u) \rightarrow 0$. Having in mind our experience with the previous such problems, we shall try to explore again the L'Hospital's rule. It is appropriate to put to use *the before* the **last** expression in the right-hand-side of (79), because the two summands in the **last** expression of (79) **do not separately** satisfy the conditions (ii) and (v) in the formulation of the L'Hospital's theorem. Concretely: nullification of the limit $\lim f(e, \dot{e})$ and existing

$$\dot{e}(u) \rightarrow 0$$

of the limit $\lim [f'(e, \dot{e})/g'(e, \dot{e})]$. In view of that, we define the function

$$\dot{e}(u) \rightarrow 0$$

$\mathbf{D}(e, \dot{e})$ as follows:

$$(82) \quad \mathbf{D}(e, \dot{e}) \equiv (-2e^4 + 6e^6 - 6e^8 + 2e^{10} + 8e^3\dot{e} - 22e^5\dot{e} + 20e^7\dot{e} - 6e^9\dot{e} - 12e^2\dot{e}^2 + 27e^4\dot{e}^2 - 21e^6\dot{e}^2 + 6e^8\dot{e}^2 + 8e\dot{e}^3 - 8e^3\dot{e}^3 + 7e^5\dot{e}^3 - 2e^7\dot{e}^3)[1 - (e - \dot{e})^2]^{1/2} + 2(e - \dot{e})^4(1 - e^2)^{7/2}.$$

This definition enables us to rewrite the solution (79) in a more compact form:

$$(83) \quad \mathbf{H}_4(e, \dot{e}) \equiv \pi \mathbf{D}(e, \dot{e}) \dot{e}^{-4} (1 - e^2)^{-7/2} [1 - (e - \dot{e})^2]^{-1/2}.$$

Because

$$(84) \quad \lim_{\dot{e}(u) \rightarrow 0} \{ \pi (1 - e^2)^{-7/2} [1 - (e - \dot{e})^2]^{-1/2} \} = \pi (1 - e^2)^{-4},$$

we, as in the previous consideration of $\mathbf{H}_3(e, \dot{e})$, temporally disregard the factor $\pi (1 - e^2)^{-7/2} [1 - (e - \dot{e})^2]^{-1/2}$, and concentrate on the quotient $\mathbf{D}(e, \dot{e})/\dot{e}^4$ under the limit transition $\dot{e}(u) \rightarrow 0$. Obviously:

$$(85) \quad \begin{aligned} \mathbf{D}(e, 0) &= (-2e^4 + 6e^6 - 6e^8 + 2e^{10})(1 - e^2)^{1/2} + 2e^4(1 - e^2)^{7/2} = \\ &= -2e^4(1 - 3e^2 + 3e^4 - e^6)(1 - e^2)^{1/2} + 2e^4(1 - e^2)^{7/2} = \\ &= -2e^4(1 - e^2)^3(1 - e^2)^{1/2} + 2e^4(1 - e^2)^{7/2}, \end{aligned}$$

which is a premise to make use of the L'Hospital's rule, in order to investigate if the expression (79) or, equivalently, (83) are well behaved, when $\dot{e}(u)$ approaches zero. We shall not enter in details of the needed (to some extent) tedious algebraic and differential calculations, and only give here some of the final results. For example, it may be shown that:

$$(86) \quad \lim_{\dot{e}(u) \rightarrow 0} \frac{\partial \mathbf{D}(e, \dot{e})}{\partial \dot{e}} = \lim_{\dot{e}(u) \rightarrow 0} \frac{\partial^2 \mathbf{D}(e, \dot{e})}{\partial \dot{e}^2} = \lim_{\dot{e}(u) \rightarrow 0} \frac{\partial^3 \mathbf{D}(e, \dot{e})}{\partial \dot{e}^3} = 0.$$

The above nullifications are essential conditions (among the others, of course!) to apply the L'Hospital's rule several times by turns. Finally, taking the limit $\dot{e}(u) \rightarrow 0$ after the fourth differentiation:

$$(87) \quad \lim_{\dot{e}(u) \rightarrow 0} \frac{\partial^4 \mathbf{D}(e, \dot{e})}{\partial \dot{e}^4} = 6(8 + 24e^2 + 3e^4)(1 - e^2)^{-1/2},$$

we obtain a non-zero result. In view of the fact that the fourth derivative $\partial^4(\dot{e}^4)/\partial \dot{e}^4 = 24 \neq 0$, and taking into account the temporally disregarded factor (84), we arrive to the following conclusion:

$$(88) \quad \begin{aligned} \lim_{\dot{e}(u) \rightarrow 0} \mathbf{H}_4(e, \dot{e}) &= \lim_{\dot{e}(u) \rightarrow 0} \{ \pi \mathbf{D}(e, \dot{e}) \dot{e}^{-4} (1 - e^2)^{-7/2} [1 - (e - \dot{e})^2]^{-1/2} \} = \\ &= (6\pi/24)(8 + 24e^2 + 3e^4)(1 - e^2)^{-7/2} (1 - e^2)^{-1/2} (1 - e^2)^{-1/2} = \\ &= (\pi/4)(8 + 24e^2 + 3e^4)(1 - e^2)^{-9/2}. \end{aligned}$$

A *direct* computation, based on the substitution $\dot{e}(u) = 0$ into the definition (79), leads to an equivalent to (88) final expression. That is to say, the evaluation procedure does not include in the intermediate calculations terms, containing the factor $\dot{e}(u)$ into their denominators. And, consequently, they do not suffer from a “peculiar” behaviour, when $\dot{e}(u)$ approaches zero. The integral $\mathbf{H}_4(e, \dot{e})$ becomes for $\dot{e}(u) = 0$ an already known function of $e(u)$:

$$(89) \quad \mathbf{H}_4(e, 0) \equiv \int_0^{2\pi} (1 + e \cos \varphi)^{-5} d\varphi \equiv \mathbf{A}_5(e, 0) = (\pi/4)(8 + 24e^2 + 3e^4)(1 - e^2)^{-9/2},$$

where we have put into use the estimation (24). Like the previous considered cases, the conclusion which follows, implies that under the limit transition $\dot{e}(u) \rightarrow 0$, the solution (79) preserves its meaning and passes through the “divergence” point $\dot{e}(u) = 0$ in a continuous manner. Evidently, when both $e(u)$ and $\dot{e}(u)$ vanish simultaneously, the already derived expressions give the “right” answer $\mathbf{H}_4(0, 0) = 2\pi$, in spite of the order by which $e(u)$ and $\dot{e}(u)$ attain their zero values.

3. Conclusions

The basic goal, which we intend to do in this paper, is to compute, by an analytical way, expressions for certain type integrals. They will be used in the forthcoming investigations of the dynamical equation of the elliptical accretion discs ([1], [2]). More precisely speaking, the integrands of these functions of the eccentricity $e(u)$ of the particle orbits, and their derivatives $\dot{e}(u) \equiv \partial e(u)/\partial u$. They contain into their denominators factors (or products of them) of the type $(1 + e \cos \varphi)^i$ or $[1 + (e - \dot{e}) \cos \varphi]^j$. The powers \mathbf{i} and \mathbf{j} may take integer values 1, 2, 3, 4, 5 and so on. We stress that the considered integrals do not include into their nominators factors other than unity. Therefore, the integers \mathbf{i} and \mathbf{j} are always positive. Of course, we have limited us to a minimum set of numbers of these powers - such, which will be enough, in view of the future applications of the analytical solutions for these integrals. Although there is not (at least an obvious) doubt, that the used in the present paper (essentially recurrent) approach for analytical evaluations of the integrals $\mathbf{A}_i(e, \dot{e})$, $\mathbf{J}_i(e, \dot{e})$ and $\mathbf{H}_i(e, \dot{e})$, ($\mathbf{i} = 1, 2, 3, \dots$), may be extended for arbitrary integers \mathbf{i} , we do not solve this general problem. That is to say, we do not try to obtain any common expressions for each of these functions of $e(u)$ and $\dot{e}(u)$, valid for *arbitrary* powers $\mathbf{i} = 1, 2, 3, \dots$. This would be an extended mathematical task, which would be beyond the

scope of our efforts to analyze a concrete physical problem – the dynamical equation of the *stationary* elliptical accretion discs.

An essential peculiarity, which occurs for almost all the calculations of the above mentioned integrals, is that in the intermediate results appear terms, which may be divergent for some values of $e(u)$, $\dot{e}(u)$ or the difference $e(u) - \dot{e}(u)$. In the final expressions, representing the final solutions of the integrals, these peculiarities may present *or* not present. These indeterminacies can be overcome by means of *direct* substitutions of the above noted “peculiar” meanings into the initial definitions of $\mathbf{A}_i(e, \dot{e})$, $\mathbf{J}_i(e, \dot{e})$ and $\mathbf{H}_i(e, \dot{e})$, ($i = 1, 2, 3, \dots$), and then performing the integration. As a rule, this procedure is more easily fulfilled, and, fortunately, does not involve, at any stage of the calculations, the considered type of peculiarity. As it becomes evident, after the comparison of the two solutions, we strike with the following two situations:

(i) The final result for the expression, obtained through the “peculiar” intermediate terms, does not involve similar “peculiar” terms. Consequently, it is “regular” with respect to the substitution into it of the “singular” $e(u)$ and $\dot{e}(u)$. It is remarkable that the two ways (with singular intermediate terms and *direct* computation, without passing through such singular terms) give identical expressions. This is, of course, a favorable property, because there is not a necessity to point out the method, by which the considered formula is obtained.

(ii) The final result for the expression, obtained through the “peculiar” intermediate terms, retains its indeterminacy for the considered (caused by the divergent intermediate terms), “peculiar” values of $e(u)$ or/and $\dot{e}(u)$. Then, it turns out that it is possible, by the use of the L’Hospital’s rule, to reveal these indeterminacies of the type 0/0. Again, it is worthy to note that the evaluated in this way (by means of the limit transitions $e(u) \rightarrow 0$, or/and $\dot{e}(u) \rightarrow 0$) expressions coincide with those, computed through the *direct* substitution of the “problem” values of $e(u)$ and $\dot{e}(u)$ into the integrals, which we want to evaluate analytically. Such a continuous transition enables us to use into the applications the derived formulas, without to specify the path by which they are established. And also **not to worry** whether the applications of the above computed analytical expressions for the integrals $\mathbf{A}_i(e, \dot{e})$, ($i = 1, \dots, 5$), $\mathbf{J}_k(e, \dot{e})$ and $\mathbf{H}_k(e, \dot{e})$, ($k = 1, \dots, 4$) do introduce any type their own divergence into the evaluated (more complex) composite expressions, of which they are parts.

References

1. Lyubarskiy, Yu. E., K. A. Postnov, M. E. Prokhorov. Eccentric accretion discs., Monthly Not. Royal Astron. Soc., 266, 1994, № 2, pp. 583–596.
2. Dimitrov, D. One possible simplification of the dynamical equation governing the evolution of elliptical accretion discs., Aerospace research in Bulgaria, 17, 2003, pp. 17–22.
3. Dimitrov, D. V. Thin viscous elliptical accretion discs with orbits sharing a common longitude of periastron. V. Linear relations between azimuthal-angle averaged factors in the dynamical equation., Aerospace Research in Bulgaria, 24, 2010, (in print).
4. Dimitrov, D. V. Thin viscous elliptical accretion discs with orbits sharing a common longitude of periastron. VI. simplification of the dynamical equation., Aerospace Research in Bulgaria, 25, 2010, (in print).
5. Ogilvie, G. I. Non-linear fluid dynamics of eccentric discs., Monthly Notices Royal Astron. Soc., 325, 2001, № 1, pp. 231–248.
6. Dwight, H. B. Tables of integrals and other mathematical data., Fourth edition, New York, MacMillan company, 1961.
7. Dimitrov, D. V. Thin viscous elliptical accretion discs with orbits sharing a common longitude of periastron. I. Dynamical equation for integer values of the powers in the viscosity law., Aerospace Research in Bulgaria, 19, 2006, pp.16–28.
8. Dimitrov, D. V. Thin viscous elliptical accretion discs with orbits sharing a common longitude of periastron. VII. Do we have a truncation of the chain of linear relations between the integrals, entering into the dynamical equation?, Aerospace research in Bulgaria, (in preparation).

АНАЛИТИЧНО ПРЕСМЯТАНЕ НА ДВА ИНТЕГРАЛА, ВЪЗНИКВАЩИ В ТЕОРИЯТА НА ЕЛИПТИЧНИТЕ АКРЕЦИОННИ ДИСКОВЕ. I. РЕШАВАНЕ НА СПОМАГАТЕЛНИТЕ ИНТЕГРАЛИ, ПОЯВЯВАЩИ СЕ ПРИ ТЯХНОТО ИЗЧИСЛЯВАНЕ

Д. Димитров

Резюме

Настоящата работа е част от едно обширно аналитично изследване на динамичното уравнение, определящо пространствената структура на *стационарните* елиптични акреционни дискове, съгласно модела на Любарски и др. [1]. При математическото описание на задачата са използвани като параметри ексцентрицитета $e(u)$ на орбитите на частиците и неговата производна $\dot{e}(u) \equiv de(u)/du$, където

$u \equiv \ln(p)$, p е фокалният параметър на разглежданата орбита. В течение на процеса на опростяване на това уравнение, възниква необходимостта от

аналитично оценяване на интеграли от следните типове: $A_i(e, \dot{e}) = \int_0^{2\pi} (1 + e \cos \varphi)^{-i} d\varphi$,

$(i = 1, \dots, 5)$, $J_k(e, \dot{e}) = \int_0^{2\pi} (1 + e \cos \varphi)^{-1} [1 + (e - \dot{e}) \cos \varphi]^{-k} d\varphi$ и $H_k(e, \dot{e}) = \int_0^{2\pi} (1 + e \cos \varphi)^{-k} [1 + (e - \dot{e}) \cos \varphi]^{-1} d\varphi$, ($k = 1, \dots, 4$). В тези формули φ е

азимуталният ъгъл, върху който е извършено усредняването. Подходът при решаването на задачата е, фактически, рекурсивен. Най-напред ние оценяваме интегралите за най-малките стойности на i и k (т.е., i и k равни на единица). След това ние преминаваме към следващите стъпки, постепенно увеличавайки целочислените степени i или k , докато се достигнат указаните стойности 5 или 4, съответно. Специално внимание е посветено на тези значеия на $e(u)$ и $\dot{e}(u)$ (и тяхната разлика $e(u) - \dot{e}(u)$), които евентуално могат да причинят разходимости в промеждутъчните или крайните изрази. Показано е, въпреки възникването на такива затруднения, че те могат да бъдат преодоляни посредством прякото заместване на “особените” стойности на $e(u)$ и/или $\dot{e}(u)$ в интегралите, като чак след това се извършват изчисленията. Даже ако в знаменателите на крайните резултати се появяват множители равни на нула (в следствие на анулиранията на $e(u)$, $\dot{e}(u)$ или $e(u) - \dot{e}(u)$), изразите не са разходящи, както ние сме доказали, използвайки правилото на Лъопитал за разрешаване на неопределености от вида $0/0$. Всички аналитични оценки на горенаписаните интеграли са извършени при ограниченията $|e(u)| < 1$, $|\dot{e}(u)| < 1$ и $|e(u) - \dot{e}(u)| < 1$. Те са наложени поради физически съображения, с оглед на прилагането на тези решения във възприетата теория на елиптичните акреционни дискове.

**ANALYTICAL COMPUTATION OF TWO INTEGRALS,
 APPEARING IN THE THEORY OF ELLIPTICAL ACCRETION
 DISCS. II. SOLVING OF SOME AUXILIARY INTEGRALS,
 CONTAINING LOGARITHMIC FUNCTIONS
 INTO THEIR INTEGRANDS**

Dimitar Dimitrov

*Space Research and Technology Institute – Bulgarian Academy of Sciences
 e-mail: dim@mail.space.bas.bg*

Abstract

This paper is a part of the investigations, dealing with the mathematical structure of the stationary elliptical accretion discs in the model of Lyubarskij et al. [1], i.e., discs for which all the apse lines of the particle orbits are in line with each other. The main point of the adopted approach is to find linear relations between the integrals, entering into the dynamical equation for these objects. They will enable us to eliminate these complicate (and, generally speaking, unknown analytically) functions of the eccentricity $\mathbf{e}(\mathbf{u})$ and its derivative $\dot{\mathbf{e}}(\mathbf{u}) \equiv d\mathbf{e}(\mathbf{u})/d\mathbf{u}$ of the individual orbits. Here $\mathbf{u} \equiv \ln(\mathbf{p})$, where \mathbf{p} is the focal parameter of the corresponding accretion disc particle orbit. During the process of realization of this program, we strike with the necessity to find analytical evaluations for two kinds of integrals:

$$L_i(\mathbf{e}, \dot{\mathbf{e}}) \equiv \int_0^{2\pi} [\ln(1 + e \cos \varphi)] (1 + e \cos \varphi)^{-1} [1 + (e - \dot{e}) \cos \varphi]^{-i} d\varphi, \quad (i = 0, \dots, 3), \text{ and } K_j(\mathbf{e}, \dot{\mathbf{e}}) \equiv \int_0^{2\pi} [\ln(1 + e \cos \varphi)] \times$$

$\times [1 + (e - \dot{e}) \cos \varphi]^{-j} d\varphi, \quad (j = 1, \dots, 5)$. In the present investigation we find recurrence relations, allowing us to compute the integrals $L_i(\mathbf{e}, \dot{\mathbf{e}})$, ($i = 1, 2, 3$), under the condition that the integrals $L_{i-1}(\mathbf{e}, \dot{\mathbf{e}})$ and $K_i(\mathbf{e}, \dot{\mathbf{e}})$ are already known. Conversely, computations of the integrals $K_j(\mathbf{e}, \dot{\mathbf{e}})$, ($j = 1, \dots, 5$), through the recurrence dependences do not require the knowledge of the analytical solutions of the integrals $L_i(\mathbf{e}, \dot{\mathbf{e}})$, ($i = 0, \dots, 3$). In view of the fact that the integrals $L_0(\mathbf{e})$ (it does not depend on $\dot{\mathbf{e}}(\mathbf{u})$) and $K_1(\mathbf{e}, \dot{\mathbf{e}})$ serve as “starting--points” into the corresponding recurrence relations, we have find analytical expressions for them. The solution of the full set of analytical evaluations of $L_i(\mathbf{e}, \dot{\mathbf{e}})$, ($i = 1, 2, 3$), and $K_j(\mathbf{e}, \dot{\mathbf{e}})$, ($j = 2, \dots, 5$), will be given elsewhere [7].

1. Introduction

The present paper continues a series of investigations, devoted to the simplification of the dynamical equation of the elliptical accretion discs. Especially, the considerations are constrained to a specific model, developed by Lyubarskij et al. [1]. The essential property of this model is that the all elliptical particle orbits are sharing a common longitude of periastron. The other restriction, which we impose on the adopted elaboration, is that the accretion flow is *stationary*. That is why, the dynamical equation, with which we are dealing, governs the *stationary* space structure of the disc. We remind that the particle orbits at different parts of the disc, may have different eccentricities $e(u)$, respectively. Here with the variable u we denote the logarithm of the focal parameter p of the corresponding elliptical orbit: $u \equiv \ln(p)$. Also we shall often use the notation $\dot{e}(u) \equiv de(u)/du$ for the first ordinary derivative of the eccentricity $e(u)$ with respect to u . The way we proceed, to reveal the mathematical structure of the above mentioned equation, is to eliminate certain definite integrals over the azimuthal angle φ . They are functions of $e(u)$, $\dot{e}(u)$ and the power n in the viscosity law $\eta = \beta \Sigma^n$ (β is a constant, η is the viscosity and Σ is the surface density of the accretion disc). The procedure of reducing of the number of these integrals, by means of establishing of linear relations between them, is described and applied in earlier papers ([2], [3] and the references therein). Until now, the question: if three of these functions $\mathbf{I}_3(e, \dot{e}, n)$, $\mathbf{I}_0_-(e, \dot{e}, n)$ and $\mathbf{I}_0_+(e, \dot{e}, n)$ are linearly independent **or** not, still remains open (for definitions of these three integrals see [2] and [3]). The standard method to check which of these two alternative cases is available, is to compute the corresponding Wronskian. The procedure includes evaluation of some derivatives with respect to $e(u)$ or $\dot{e}(u)$ of the above mentioned integrals. In turn, this leads to appearing of two new integrals, for which we also have to find analytical solutions. In the course of realizing of this computational scheme, we, at first, must have available analytical expressions of given auxiliary integrals. In the preceding paper [4], we have given the solutions of such integrals, when their integrands do not include logarithmic functions of $e(u)$ or $\dot{e}(u)$. The present investigation deals just with this complementary case. It will be seen from the following exposition, that such integrals arise, when we obtain formulas, containing into their denominators factors, vanishing for some integer values of the power n . But from a physical point of view, we do not expect that the integer numbers n have “special” meanings in the considered accretion disc theory. And it is reasonable to check the “problem” formulas

for their behaviour, when n approaches the “singular” value. It turns out, that the corresponding nominators also tend to zero, “compensating” the divergent (at the first glance) character of the analytical expression. As usual, it is instructive to apply in this situation the L’Hospital’s rule for resolving of indeterminacies of the type $0/0$. In turn, similar computational scheme implies the necessity of finding the partial derivatives with respect to the power n . More specifically, for the considered by us integrals, we shall compute derivatives like:

$$(1) \quad \partial[(1 + e \cos \varphi)^n] / \partial n = n \ln(1 + e \cos \varphi),$$

according to the well-known rules from the differential calculus. In the above formula we take into account that the eccentricity $e(u)$ (or the difference $e(u) - \dot{e}(u)$, which may stand in the place of $e(u)$) and the azimuthal angle φ do not depend on n . Of course, the considered model of elliptical accretion discs [1] keeps fixed the power n (i.e., the viscosity law $\eta = \beta \Sigma^n$ remains valid throughout the entire disc) for every concrete accretion disc. The mathematical variability of n in the equality (1) should be supposed physically as a change/transition from one accretion flow (with a given fixed power n) to another accretion flow (with other, also fixed, but a little different value of n).

2. Integrands, including as a factor logarithmic function

The available handbooks, which we had considered, in order to find already computed analytical expressions for the integrals, representing an interest for us, do not give a direct answer to the task. We do not strike *only* with the incompleteness of the lists of the cited formulas, but also with the need to obtain evaluations of the integrals, which are valid for special choices (i.e., restrictions on the domains) of the parameter space, characterizing them. Probably, the specialization of the considered by us problem, leads to two possible situations:

(i) The integrals, for which we are seeking, are too “specialized”, in view of the circumstance that the considered problem also treats too “narrow” aspects of the physical/mathematical theory. Correspondingly, such solutions of the integrals remain, as a rule, out of the attention of the compilers of the reference books, containing mathematical formulas.

(ii) In the other, generating difficulties case, the analytical expressions are very complicated formulas. Then, if even these solutions are found, they may not be included in many handbooks, for reasons of their extended form. The later property is, in particular, stipulated by the aspiration of the

calculators to resolve these integrals in the most general case of the domain of variables.

Dealing with the problems of the types (i) and/or (ii), we have to overcome these troubles by performing our own computations of the considered integrals. Fortunately, we were able to find an analytical evaluation of an integral, which may serve as an initial starting-point for our further advance. In the reference handbook of Prudnikov et al. [4] is given the following formula for the analytical solution of the integral (formula on page 545; note that the integration is from 0 to π , not from 0 to 2π !):

$$(2) \quad \int_0^{\pi} [\ln(1 - 2a\cos\varphi + a^2)](1 - 2b\cos\varphi + b^2)^{-1} d\varphi =$$

$$= \left\{ \begin{array}{l} 2\pi |1 - b^2|^{-1} \ln(1 - ab^{\pm 1}); \\ 2\pi |1 - b^2|^{-1} \ln|a - b^{\pm 1}|; \end{array} \right. \left\{ \begin{array}{l} |b| < 1 \\ |b| > 1 \end{array} \right. , \left. \begin{array}{l} |a| \leq 1 \\ |a| > 1 \end{array} \right\} ,$$

or

$$\left\{ \begin{array}{l} 2\pi |1 - b^2|^{-1} \ln|a - b^{\pm 1}|; \end{array} \right. \left\{ \begin{array}{l} |b| < 1 \\ |b| > 1 \end{array} \right. , \left. \begin{array}{l} |a| > 1 \end{array} \right\} .$$

For further use of the above formula, we shall express the parameters a and b by means of the eccentricity $e(u)$ and its derivative $\dot{e}(u)$ in a way, depending on the kind of the integral, which we intend to evaluate. At first glance, the existence of four possible branches in the right-hand-side of the relation (2), leads to the suspicion that the solutions, which are based on (2), are lacking of uniqueness. We shall see later, that in our applications all the four solutions are, in fact, *identical*. That is to say, the branching in our case makes no sense. We also stress that the eccentricity $e(u)$, its derivative $\dot{e}(u)$ and, correspondingly, their difference $e(u) - \dot{e}(u)$ are real functions of u . In turn, the parameters a and b , expressed in terms of $e(u)$ and $\dot{e}(u)$, are also real quantities. Taking into account that we resolve the task under the conditions of satisfying the inequalities $|e(u)| < 1$, $|\dot{e}(u)| < 1$ and $|e(u) - \dot{e}(u)| < 1$, we could conclude that the integral into the left-hand-side of the equality (2) is a real function on $e(u)$ and $\dot{e}(u)$. Without any singular behaviour in the pointed out domain of these variables.

Our main goal in the present paper is to compute analytically the following two kinds of integrals:

$$(3) \quad \mathbf{L}_i(e, \dot{e}) \equiv \int_0^{2\pi} [\ln(1 + e \cos \varphi)] (1 + e \cos \varphi)^{-1} [1 + (e - \dot{e}) \cos \varphi]^{-i} d\varphi ; \quad \mathbf{i} = 0, \dots, 3 ,$$

$$(4) \quad \mathbf{K}_j(e, \dot{e}) \equiv \int_0^{2\pi} [\ln(1 + e \cos \varphi)] [1 + (e - \dot{e}) \cos \varphi]^{-j} d\varphi ; \quad \mathbf{j} = 1, \dots, 5 .$$

The above integrals resemble to the integrals:

$$(5) \quad \mathbf{A}_i(e, \dot{e}) \equiv \int_0^{2\pi} [1 + (e - \dot{e}) \cos \varphi]^{-i} d\varphi ; \quad \mathbf{i} = 1, \dots, 5 ,$$

$$(6) \quad \mathbf{J}_j(e, \dot{e}) \equiv \int_0^{2\pi} (1 + e \cos \varphi)^{-1} [1 + (e - \dot{e}) \cos \varphi]^{-j} d\varphi ; \quad \mathbf{j} = 1, \dots, 4 ,$$

$$(7) \quad \mathbf{H}_j(e, \dot{e}) \equiv \int_0^{2\pi} (1 + e \cos \varphi)^{-j} [1 + (e - \dot{e}) \cos \varphi]^{-1} d\varphi ; \quad \mathbf{j} = 1, \dots, 4 ,$$

in the sense, that in the denominators of the integrands encounter as factors certain powers of the quantities $(1 + e \cos \varphi)$ or $[1 + (e - \dot{e}) \cos \varphi]$. But for the first system of integrals (3) & (4), the nominators are equal to the logarithmic function $\ln(1 + e \cos \varphi)$, instead to unity. The later circumstance essentially complicates the analytical evaluations of $\mathbf{L}_i(e, \dot{e})$, ($\mathbf{i} = 0, \dots, 3$) and $\mathbf{K}_j(e, \dot{e})$, ($\mathbf{j} = 1, \dots, 5$), in comparison with the corresponding computations of the integrals $\mathbf{A}_i(e, \dot{e})$, ($\mathbf{i} = 1, \dots, 5$), $\mathbf{J}_j(e, \dot{e})$ and $\mathbf{H}_j(e, \dot{e})$, ($\mathbf{j} = 1, \dots, 4$), which were done in an earlier paper [4]. Of course, the selection of the powers of the factors $(1 + e \cos \varphi)$ and $[1 + (e - \dot{e}) \cos \varphi]$ into the definitions (3) and (4), is predetermined by the necessity of the applications of the analytical solutions for our own future developments. That is to say, like the situation with $\mathbf{A}_i(e, \dot{e})$, $\mathbf{J}_j(e, \dot{e})$ and $\mathbf{H}_j(e, \dot{e})$, the integrals $\mathbf{L}_i(e, \dot{e})$ and $\mathbf{K}_j(e, \dot{e})$, in principle, may be evaluated analytically for arbitrary non-negative integers \mathbf{i} or \mathbf{j} , by the means, which we shall use in the present paper. But we shall limit us further only to the necessary minimum of computations. These will be based on the application of the relation (2), and in connection with this, we make the following *important remark*. We do not trace back the derivation of the formula (2) and accept to trust the adduced solution of the Prudnikov et al. [5]. To preserve us from any possible incorrectness of this formula, we further check the derived analytical expressions also by means of *numerical* computations for a dense enough lattice of values of $e(u)$ and $\dot{e}(u)$. Both in the *open* interval $(-1.0; +1.0)$, taking also into account that $|e(u) - \dot{e}(u)| < 1$. Speaking in advance, we note that there is not doubt in the validity of the relation (2), because the discrepancies between the analytical and numerical evaluations (based on

the formula (2)) are of the order $10^{-11} - 10^{-13}$ – the accuracy of the numerical computations itself.

2.1. Recurrence relations for the integrals of the type

$$\mathbf{L}_i(e, \dot{e}) \equiv \int_0^{2\pi} [\ln(1 + e \cos \varphi)] (1 + e \cos \varphi)^{-1} [1 + (e - \dot{e}) \cos \varphi]^{-i} d\varphi$$

We shall establish in this chapter a number of relations between the integrals given by the definitions (3) and (4), which will enable us to evaluate in an explicit analytical form these integrals as functions of the eccentricity $e(u)$ and its derivative $\dot{e}(u) \equiv de(u)/du$. Actually, these formulas will be recurrence relations for the first kind of integrals, namely, $\mathbf{L}_i(e, \dot{e})$, ($i = 0, \dots, 3$). They will include also integrals of the type $\mathbf{K}_j(e, \dot{e})$, ($j = 1, \dots, 5$), which, at the present stage of the computations, *are still unknown* functions of $e(u)$ and $\dot{e}(u)$. Later we shall find another recurrence relations about $\mathbf{K}_j(e, \dot{e})$, ($j = 1, \dots, 5$), that refer *only* to this kind of integrals. As a final result, this will give us an opportunity to calculate in an explicit form the integrals $\mathbf{K}_j(e, \dot{e})$, ($j = 1, \dots, 5$). Returning back to the recurrence relations for $\mathbf{L}_i(e, \dot{e})$, ($i = 0, \dots, 3$), derived below in the present chapter, we finally are in a position to write explicitly the analytical solutions for the integrals $\mathbf{L}_i(e, \dot{e})$, ($i = 0, \dots, 3$).

We begin with the remark that $\mathbf{L}_0(e)$ is a function only of the eccentricity $e(u)$, but not of its derivative $\dot{e}(u)$:

$$(8) \quad \mathbf{L}_0(e) \equiv \int_0^{2\pi} [\ln(1 + e \cos \varphi)] (1 + e \cos \varphi)^{-1} d\varphi.$$

To the end of the present chapter, we shall suppose that $e(u) \neq 0$ and $\dot{e}(u) \neq 0$. The evaluations of $\mathbf{L}_1(e, \dot{e})$, $\mathbf{L}_2(e, \dot{e})$ and $\mathbf{L}_3(e, \dot{e})$ for these particular values of their arguments are more appropriate to be given, when the full expressions for them are already available. According to the definitions (3) and (4), we have:

$$(9) \quad \begin{aligned} \mathbf{L}_3(e, \dot{e}) &\equiv \int_0^{2\pi} [\ln(1 + e \cos \varphi)] (1 + e \cos \varphi)^{-1} [1 + (e - \dot{e}) \cos \varphi]^{-3} d\varphi = \\ &= \int_0^{2\pi} \{ [1 + (e - \dot{e}) \cos \varphi] - (e - \dot{e}) \cos \varphi \} [\ln(1 + e \cos \varphi)] (1 + e \cos \varphi)^{-1} \times \\ &\times [1 + (e - \dot{e}) \cos \varphi]^{-3} d\varphi = \int_0^{2\pi} [\ln(1 + e \cos \varphi)] (1 + e \cos \varphi)^{-1} [1 + (e - \dot{e}) \cos \varphi]^{-2} d\varphi - \end{aligned}$$

$$\begin{aligned}
& - [(e - \dot{e})/e] \int_0^{2\pi} [(1 + e \cos \varphi) - 1] [\ln(1 + e \cos \varphi)] (1 + e \cos \varphi)^{-1} [1 + (e - \dot{e}) \cos \varphi]^{-3} d\varphi = \\
& = \mathbf{L}_2(e, \dot{e}) - [(e - \dot{e})/e] \int_0^{2\pi} [\ln(1 + e \cos \varphi)] [1 + (e - \dot{e}) \cos \varphi]^{-3} d\varphi + \\
& + [(e - \dot{e})/e] \int_0^{2\pi} [\ln(1 + e \cos \varphi)] (1 + e \cos \varphi)^{-1} [1 + (e - \dot{e}) \cos \varphi]^{-3} d\varphi = \\
& = \mathbf{L}_2(e, \dot{e}) - [(e - \dot{e})/e] \mathbf{K}_3(e, \dot{e}) + [(e - \dot{e})/e] \mathbf{L}_3(e, \dot{e}).
\end{aligned}$$

Therefore, transferring the last term $[(e - \dot{e})/e] \mathbf{L}_3(e, \dot{e})$ into the right-hand-side, we obtain that:

$$(10) \quad \{1 - [(e - \dot{e})/e]\} \mathbf{L}_3(e, \dot{e}) \equiv (\dot{e}/e) \mathbf{L}_3(e, \dot{e}) = \mathbf{L}_2(e, \dot{e}) - [(e - \dot{e})/e] \mathbf{K}_3(e, \dot{e}),$$

or, multiplying by e/\dot{e} :

$$(11) \quad \mathbf{L}_3(e, \dot{e}) = (e/\dot{e}) \mathbf{L}_2(e, \dot{e}) - [(e - \dot{e})/\dot{e}] \mathbf{K}_3(e, \dot{e}).$$

By the exactly analogous way, we may derive recurrence relations for the integrals $\mathbf{L}_2(e, \dot{e})$ and $\mathbf{L}_1(e, \dot{e})$. We simply write here the final results:

$$\begin{aligned}
(12) \quad \mathbf{L}_2(e, \dot{e}) & \equiv \int_0^{2\pi} [\ln(1 + e \cos \varphi)] (1 + e \cos \varphi)^{-1} [1 + (e - \dot{e}) \cos \varphi]^{-2} d\varphi = \\
& = (e/\dot{e}) \mathbf{L}_1(e, \dot{e}) - [(e - \dot{e})/\dot{e}] \mathbf{K}_2(e, \dot{e}),
\end{aligned}$$

$$\begin{aligned}
(13) \quad \mathbf{L}_1(e, \dot{e}) & \equiv \int_0^{2\pi} [\ln(1 + e \cos \varphi)] (1 + e \cos \varphi)^{-1} [1 + (e - \dot{e}) \cos \varphi]^{-1} d\varphi = \\
& = (e/\dot{e}) \mathbf{L}_0(e, \dot{e}) - [(e - \dot{e})/\dot{e}] \mathbf{K}_1(e, \dot{e}).
\end{aligned}$$

We call to mind, that the above formulas are deduced under the assumptions that $e(u) \neq 0$ and $\dot{e}(u) \neq 0$. Obviously, the equations (11), (12) and (13) are useful if $\mathbf{K}_1(e, \dot{e})$, $\mathbf{K}_2(e, \dot{e})$ and $\mathbf{K}_3(e, \dot{e})$ are already known functions of $e(u)$ and $\dot{e}(u)$.

2.2. Analytical computation of the integral

$$\mathbf{L}_0(e) \equiv \int_0^{2\pi} [\ln(1 + e \cos \varphi)] (1 + e \cos \varphi)^{-1} d\varphi$$

For our present purposes we shall transform the left-hand-side of the formula (2) (given by Prudnikov et al. [5]) in the following way:

$$(14) \quad \int_0^{\pi} [\ln(1 - 2a \cos \varphi + a^2)] (1 - 2b \cos \varphi + b^2)^{-1} d\varphi =$$

$$(22) \quad b_{II} = (a^2 + 1 + 1 - a^2)/(2a) \equiv 1/a.$$

The existence of the above equalities means that we *have to consider two cases*: $b_I = a$ and $b_{II} = 1/a$. However, let us examine at first, how the restriction $|e(u)| < 1$ imposes itself other restrictions over the variables a and b . We have that, according to the substitution (15):

$$(23) \quad -2a = e + ea^2,$$

which implies a quadratic equation for a :

$$(24) \quad ea^2 + 2a + e = 0.$$

Solving with respect to a this quadratic equation, we obtain:

$$(25) \quad a_{1,2} = [-2 \pm (4 - 4e^2)^{1/2}]/(2e) = [-1 \pm (1 - e^2)^{1/2}]/e.$$

We have to investigate the following *four* situations:

(i) **solution** $a_1 = [-1 + (1 - e^2)^{1/2}]/e$; $|a_1| = |-1 + (1 - e^2)^{1/2}|/|e| < 1$. This implies that:

$$(26) \quad |-1 + (1 - e^2)^{1/2}| < |e|.$$

Because $|e| < 1$, we can write $0 < 1 - e^2 < 1$, or $(1 - e^2)^{1/2} < 1$.

Further we have:

$-1 + (1 - e^2)^{1/2} < 0$, which means that $|-1 + (1 - e^2)^{1/2}| = 1 - (1 - e^2)^{1/2}$.

Consequently, from the inequality (26) follows that: $0 < 1 - (1 - e^2)^{1/2} < |e|$.

Therefore:

$0 < 1 - |e| < (1 - e^2)^{1/2}$. Raising into square will give:

$$(27) \quad 1 + e^2 - 2|e| < 1 - e^2 \Rightarrow 2e^2 < 2|e| \Rightarrow e^2 < |e| \Rightarrow |e| < 1.$$

The above chain of inequalities means that we do not arrive at a contradiction. That is to say, this case (i) is admissible.

(ii) **solution** $a_1 = [-1 + (1 - e^2)^{1/2}]/e$; $|a_1| = |-1 + (1 - e^2)^{1/2}|/|e| > 1$. This implies that:

$$(28) \quad |-1 + (1 - e^2)^{1/2}| > |e|.$$

Because $|e| < 1$, we can write $e^2 < 1$, or $0 < 1 - e^2 < 1$, and $(1 - e^2)^{1/2} < 1$.

Further we have: $-1 + (1 - e^2)^{1/2} < 0$, which means that $|-1 + (1 - e^2)^{1/2}| = 1 - (1 - e^2)^{1/2}$. We shall substitute the later equality into the inequality (28). Unlike the previous case (i), now the sign of the inequality (28) is changed in comparison with (26). This will introduce a radical change in our conclusions. According to (28), we write $[0 < 1 - (1 - e^2)^{1/2}] \cap [1 - (1 - e^2)^{1/2} > |e|]$, or $[0 < 1 - |e|] \cap [1 - |e| > (1 - e^2)^{1/2}]$. Raising into square will give:

(29) $1 + e^2 - 2|e| > 1 - e^2 \Rightarrow 2e^2 > 2|e| \Rightarrow e^2 > |e| \Rightarrow |e| > 1$.

We derive a contradiction, because, by hypothesis, $|e| < 1$. That is to say, the considered case (ii) is not permitted!

(iii) **solution** $a_2 = [-1 - (1 - e^2)^{1/2}]/e$; $|a_2| = |-1 - (1 - e^2)^{1/2}|/|e| < 1$. This implies that:

$$(30) \quad |-1 - (1 - e^2)^{1/2}| \equiv 1 + (1 - e^2)^{1/2} < |e|.$$

This relation may be immediately rewritten as:

$$(31) \quad 0 < 1 - |e| < -(1 - e^2)^{1/2} < 0.$$

It turns out that must be fulfilled simultaneously *two* inequalities about the difference $1 - |e|$:

$$(33) \quad (1 - |e| > 0) \cap (1 - |e| < 0).$$

i.e., we obtain a contradiction. Therefore, the considered case (iii) is not permitted!

(iv) **solution** $a_2 = [-1 - (1 - e^2)^{1/2}]/e$; $|a_2| = |-1 - (1 - e^2)^{1/2}|/|e| > 1$. This implies that:

$$(34) \quad |-1 - (1 - e^2)^{1/2}| \equiv 1 + (1 - e^2)^{1/2} > |e|,$$

$$(35) \quad 1 - |e| > -(1 - e^2)^{1/2} \Rightarrow 1 - |e| > 0 > -(1 - e^2)^{1/2}.$$

Correspondingly, in this case (iv) we do not strike with a contradiction.

To summarize the conclusions from the considered above four possible opportunities, we shortly say that, under the restriction $|e(u)| < 1$:

1) The solution of the quadratic equation (24) $a_1 = [-1 + (1 - e^2)^{1/2}]/e$ is in agreement with this restriction only if $|a| < 1$;

2) The solution of the quadratic equation (24) $a_2 = [-1 - (1 - e^2)^{1/2}]/e$ is in agreement with this restriction only if $|a| > 1$.

The situation is illustrated graphically in Figure 1 (a) and (b).

Because of the symmetry, given by the equalities (15), the same conclusions are valid for the coefficient b , where we have to consider the quadratic equation

$$(36) \quad eb^2 + 2b + e = 0,$$

instead of the equation (24).

3) The solution of the quadratic equation (36) $b_1 = [-1 + (1 - e^2)^{1/2}]/e$ is in agreement with the restriction $|e(u)| < 1$ only if $|b| < 1$;

4) The solution of the quadratic equation (36) $b_2 = [-1 - (1 - e^2)^{1/2}]/e$ is in agreement with the restriction $|e(u)| < 1$ only if $|b| > 1$.

We must not confuse the roots b_I and b_{II} with the roots b_1 and b_2 !

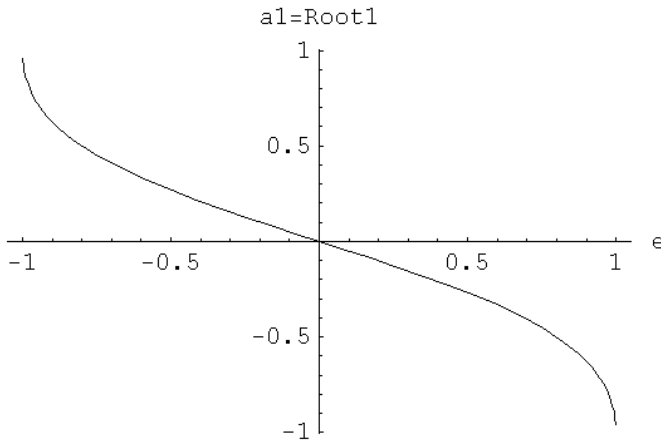
Having in mind the above preliminary remarks, we now return to the investigation of the equation (19).

Case I: $b = a$. Subcase 1: $|b| = |a| < 1$.

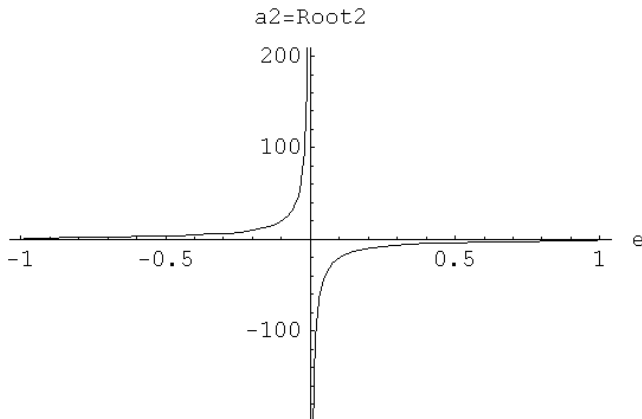
According to the deductions 1) and 3), $a_1 = b_1 = [-1 + (1 - e^2)^{1/2}]/e$.

Then, in view of the formula (16):

$$(37) \quad \int_0^\pi [\ln(1 + e \cos \varphi)](1 + e \cos \varphi)^{-1} d\varphi = -\pi \{\ln[1 + (a_1)^2]\}(1 - e^2)^{-1/2} + 2\pi[1 + (a_1)^2][1 - (a_1)^2]^{-1} \ln[1 - (a_1)^2].$$



a) Case (i): $|a_1| = |-1 + (1 - e^2)^{1/2}|/|e| < 1$.



b) Case (iv): $|a_2| = |-1 - (1 - e^2)^{1/2}|/|e| > 1$.

Fig.1. Solutions of the quadratic equation (24) $ea^2 + 2a + e = 0$

We compute the following auxiliary expressions:

$$(38) \quad 1 + (a_1)^2 = 1 + (1/e^2)[1 + 1 - e^2 - 2(1 - e^2)^{1/2}] = (2/e^2)[1 - (1 - e^2)^{1/2}] > 0,$$

$$(39) \quad 1 - (a_1)^2 = 1 - (1/e^2)[1 + 1 - e^2 - 2(1 - e^2)^{1/2}] = (1/e^2)[e^2 - 2 + e^2 + 2(1 - e^2)^{1/2}] = \\ = (2/e^2)[e^2 - 1 + (1 - e^2)^{1/2}][1 + (1 - e^2)^{1/2}][1 + (1 - e^2)^{1/2}]^{-1} = \\ = 2e^2(1 - e^2)^{1/2}/\{e^2[1 + (1 - e^2)^{1/2}]\} \equiv 2(1 - e^2)^{1/2}/[1 + (1 - e^2)^{1/2}].$$

Consequently, we have:

$$(40) \quad 0 < 1 - (a_1)^2 = 2(1 - e^2)^{1/2}/[1 + (1 - e^2)^{1/2}] < 1.$$

$$(41) \quad \int_0^{\pi} [\ln(1 + e\cos\varphi)](1 + e\cos\varphi)^{-1} d\varphi = \mathbf{solution\ 1} \equiv \\ \equiv -\pi(1 - e^2)^{-1/2} \ln\{(1/e^2)[2 - 2(1 - e^2)^{1/2}]\} + \\ + 2\pi(2/e^2)[1 - (1 - e^2)^{1/2}][1 + (1 - e^2)^{1/2}][2(1 - e^2)^{1/2}]^{-1} \times \\ \times \ln\{2(1 - e^2)^{1/2}/[1 + (1 - e^2)^{1/2}]\} = -\pi(1 - e^2)^{-1/2} \ln\{(1/e^2)[2 - 2(1 - e^2)^{1/2}]\} + \\ + 2\pi(1 - e^2)^{-1/2} \ln\{2(1 - e^2)^{1/2}/[1 + (1 - e^2)^{1/2}]\} = \pi(1 - e^2)^{-1/2} \ln\{4e^2(1 - e^2) \times \\ \times \{2[1 - (1 - e^2)^{1/2}][1 + (1 - e^2)^{1/2}][1 + (1 - e^2)^{1/2}]\}^{-1}\} = \\ = \pi(1 - e^2)^{-1/2} \ln\{2e^2(1 - e^2)\{(1 - 1 + e^2)[1 + (1 - e^2)^{1/2}]\}^{-1}\}.$$

Finally, we are able to write for this case:

$$(42) \quad \int_0^{\pi} [\ln(1 + e\cos\varphi)](1 + e\cos\varphi)^{-1} d\varphi = \mathbf{solution\ 1} \equiv \\ \equiv \pi(1 - e^2)^{-1/2} \ln\{2(1 - e^2)[1 + (1 - e^2)^{1/2}]^{-1}\} \equiv \\ \equiv -\pi(1 - e^2)^{-1/2} \ln\{[1 + (1 - e^2)^{1/2}][2(1 - e^2)]^{-1}\}.$$

Case I: $b = a$. Subcase 2: $|b| = |a| > 1$.

According to the deductions 2) and 4), $a_2 = b_2 = [-1 - (1 - e^2)^{1/2}]/e$.

Then, in view of the formula (16):

$$(43) \quad \int_0^{\pi} [\ln(1 + e\cos\varphi)](1 + e\cos\varphi)^{-1} d\varphi = -\pi(1 - e^2)^{-1/2} \ln[1 + (a_2)^2] + \\ + 2\pi[1 + (a_2)^2][1 - (a_2)^2]^{-1} \ln|a_2 - 1/a_2|.$$

We compute the following auxiliary expressions:

$$(44) \quad 1 + (a_2)^2 = 1 + (1/e^2)[1 + 1 - e^2 + 2(1 - e^2)^{1/2}] = (2/e^2)[1 + (1 - e^2)^{1/2}],$$

$$(45) \quad 1 - (a_2)^2 = 1 - (1/e^2)[1 + 1 - e^2 + 2(1 - e^2)^{1/2}] = (1/e^2)[e^2 - 2 + e^2 - 2(1 - e^2)^{1/2}] = \\ = (2/e^2)[e^2 - 1 - (1 - e^2)^{1/2}][1 - (1 - e^2)^{1/2}][1 - (1 - e^2)^{1/2}]^{-1} = \\ = -2(1 - e^2)^{1/2}[1 - (1 - e^2)^{1/2}]^{-1} < 0,$$

$$(46) \quad |a_2 - 1/a_2| = |[a_2^2 - 1]/a_2| = |(a_2)^2 - 1|/|a_2| = [(a_2)^2 - 1]/|a_2| = \\ = 2|e|(1 - e^2)^{1/2}[1 + (1 - e^2)^{1/2}]^{-1}[1 - (1 - e^2)^{1/2}]^{-1} = \\ = 2|e|(1 - e^2)^{1/2}(1 - 1 + e^2)^{-1} = 2(1 - e^2)^{1/2}/|e|.$$

The derivation of the equality (46) takes into account the last inequality in (45), according to which $(a_2)^2 - 1 > 0$, implying that $|(a_2)^2 - 1| = (a_2)^2 - 1$. Therefore, in the present subcase we can write:

$$(47) \quad \int_0^{\pi} [\ln(1 + \operatorname{ecos}\varphi)](1 + \operatorname{ecos}\varphi)^{-1} d\varphi = \mathbf{solution\ 2} \equiv \\ \equiv -\pi(1 - e^2)^{-1/2} \ln\{(2/e^2)[1 + (1 - e^2)^{1/2}]\} + \pi(1 - e^2)^{-1/2} \ln[4(1 - e^2)/e^2] = \\ = -\pi(1 - e^2)^{-1/2} \ln\{2e^2[1 + (1 - e^2)^{1/2}]/[4e^2(1 - e^2)]\} = \\ = -\pi(1 - e^2)^{-1/2} \ln\{[1 + (1 - e^2)^{1/2}][2(1 - e^2)]^{-1}\} = \mathbf{solution\ 1}.$$

We see that the both subcases give the same analytical solutions for the integral that we are resolving!

Case II: $b = 1/a$. Subcase 3: $|b| = |1/a| < 1$.

According to the deductions 2) and 3), $a = a_2 = [-1 - (1 - e^2)^{1/2}]/e$ and $b = b_1 = [-1 + (1 - e^2)^{1/2}]/e$. Then, applying formula (16):

$$(48) \quad \int_0^{\pi} [\ln(1 + \operatorname{ecos}\varphi)](1 + \operatorname{ecos}\varphi)^{-1} d\varphi = \mathbf{solution\ 3} \equiv -\pi(1 - e^2)^{-1/2} \ln[1 + (a_2)^2] + \\ + 2\pi[1 + (b_1)^2]|1 - (b_1)^2|^{-1} \ln|a_2 - b_1|.$$

Note that $b_1 = (1/e)[-1 + (1 - e^2)^{1/2}][1 + (1 - e^2)^{1/2}][1 + (1 - e^2)^{1/2}]^{-1} = (1/e)(1 - e^2 - 1)[1 + (1 - e^2)^{1/2}]^{-1} = e[-1 - (1 - e^2)^{1/2}]^{-1} = 1/(a_2)$, i.e., $b_1 = 1/(a_2)$. This result once again affirms the consistency of our calculations. We shall use the already computed expressions (38) and (39) for $1 + (a_1)^2$ and $1 - (a_1)^2$, respectively, because

$$1 + (b_1)^2 = 1 + (a_1)^2 \quad \text{and} \quad |1 - (b_1)^2| = |1 - (a_1)^2|.$$

Moreover:

$$(49) \quad |a_2 - b_1| = |a_2 - 1/(a_2)|.$$

After these remarks, we have:

$$(50) \quad \int_0^{\pi} [\ln(1 + \operatorname{ecos}\varphi)](1 + \operatorname{ecos}\varphi)^{-1} d\varphi = \mathbf{solution\ 3} \equiv \\ = -\pi(1 - e^2)^{-1/2} \ln\{(2/e^2)[1 + (1 - e^2)^{1/2}]\} + 2\pi\{2[1 - (1 - e^2)^{1/2}][1 + (1 - e^2)^{1/2}] \times \\ \times [2e^2(1 - e^2)^{1/2}]^{-1} \ln[2(1 - e^2)^{1/2}|e|^{-1}]\} = -\pi(1 - e^2)^{-1/2} \ln\{(2/e^2)[1 + (1 - e^2)^{1/2}]\} + \\ + \pi(1 - e^2)^{-1/2} [(1 - 1 + e^2)/e^2] \ln[4(1 - e^2)/e^2] = \\ = -\pi(1 - e^2)^{-1/2} \ln\{[1 + (1 - e^2)^{1/2}][2(1 - e^2)]^{-1}\} = \mathbf{solution\ 1}.$$

We again have a coincidence with the earlier evaluations of the considered integral.

Let us to proceed to the last remaining case in formula (16).

Case II: $b = 1/a$. Subcase 4: $|b| = 1/|a| > 1$.

According to the deductions 1) and 4), we have $a = a_1 = (1/e)[-1 + (1 - e^2)^{1/2}]$ and $b = b_2 = (1/e)[-1 - (1 - e^2)^{1/2}]$. Note that $b_2 = (1/e)[-1 - (1 - e^2)^{1/2}][1 - (1 - e^2)^{1/2}] \times [1 - (1 - e^2)^{1/2}]^{-1} = (-1/e)(1 - 1 + e^2)[1 - (1 - e^2)^{1/2}]^{-1} = e[-1 + (1 - e^2)^{1/2}]^{-1} = 1/a_1$, i.e., $b_2 = 1/a_1$. This result once again affirms the consistency of our calculations.

$$(51) \quad \int_0^{\pi} [\ln(1 + e \cos \varphi)](1 + e \cos \varphi)^{-1} d\varphi = \text{solution 4} \equiv -\pi(1 - e^2)^{-1/2} \ln[1 + (a_1)^2] + 2\pi[1 + (b_2)^2]|1 - (b_2)^2|^{-1} \ln|1 - a_1/b_2|.$$

Taking into account that $1 + (b_2)^2 = 1 + (a_2)^2$ (see equality (44)) and $|1 - (b_2)^2| = |1 - (a_2)^2| = 2(1 - e^2)^{1/2}[1 - (1 - e^2)^{1/2}]^{-1}$ (see equality (45)), and also $(1 - a_1/b_2) = [1 - (a_1)^2] = 2(1 - e^2)^{1/2}[1 + (1 - e^2)^{1/2}]^{-1}$, we find that in this subcase:

$$(52) \quad \int_0^{\pi} [\ln(1 + e \cos \varphi)](1 + e \cos \varphi)^{-1} d\varphi = \text{solution 4} \equiv \\ \equiv -\pi(1 - e^2)^{-1/2} \ln\{(2/e^2)[1 - (1 - e^2)^{1/2}]\} + 2\pi\{2[1 + (1 - e^2)^{1/2}][1 - (1 - e^2)^{1/2}] \times \\ \times [2e^2(1 - e^2)^{1/2}]^{-1} \ln\{2(1 - e^2)^{1/2}[1 + (1 - e^2)^{1/2}]^{-1}\} = \\ = -\pi(1 - e^2)^{-1/2} \ln\{(2/e^2)[1 - (1 - e^2)^{1/2}]\} + \\ + \pi(1 - e^2)^{-1/2} [(1 - 1 + e^2)/e^2] \ln\{4(1 - e^2)[1 + (1 - e^2)^{1/2}]^{-2}\} = \\ = -\pi(1 - e^2)^{-1/2} \ln\{2[1 - (1 - e^2)^{1/2}][1 + (1 - e^2)^{1/2}][1 + (1 - e^2)^{1/2}][4e^2(1 - e^2)]^{-1}\} = \\ = -\pi(1 - e^2)^{-1/2} \ln\{(1 - 1 + e^2)[1 + (1 - e^2)^{1/2}][2e^2(1 - e^2)]^{-1}\} = \\ = -\pi(1 - e^2)^{-1/2} \ln\{[1 + (1 - e^2)^{1/2}][2(1 - e^2)]^{-1}\} = \text{solution 1}.$$

The final conclusion is that for all cases/subcases we obtain identical results. It is also easily checked, that the extension of the interval of integration over the azimuthal angle φ from $[0, \pi]$ to $[0, 2\pi]$, simply leads to a multiplying of the results by a factor of two. Therefore:

$$(53) \quad \mathbf{L}_0(e) \equiv \int_0^{2\pi} [\ln(1 + e \cos \varphi)](1 + e \cos \varphi)^{-1} d\varphi = \\ = -2\pi(1 - e^2)^{-1/2} \ln\{[1 + (1 - e^2)^{1/2}][2(1 - e^2)]^{-1}\}.$$

It must be emphasized that the above derivations are performed under the condition $e(u) \neq 0$. But the direct computation for $\mathbf{L}_0(0)$ gives a zero value, because for this case $\ln(1 + e \cos \varphi) \equiv 0$. The same evaluation follows also from the formula (53), though it was established under non-zero values of the eccentricity $e(u)$. Consequently, we are able to apply the evaluation (53) for $\mathbf{L}_0(e)$ for arbitrary values of $e(u)$ belonging to the open interval $(-1.0; +1.0)$.

2. 3. Analytical computation of the integral

$$\mathbf{K}_1(e, \dot{e}) \equiv \int_0^{2\pi} [\ln(1 + e \cos \varphi)] [1 + (e - \dot{e}) \cos \varphi]^{-1} d\varphi$$

First of all, we note that the integral $\mathbf{K}_0(e)$, which does not depend on the derivative $\dot{e}(u) \equiv de(u)/du$, is already calculated in [6]. According to formula **865.44** in this handbook of formulas, we have:

$$(54) \quad \mathbf{K}_0(e) \equiv \int_0^{2\pi} \ln(1 + e \cos \varphi) d\varphi = 2\pi \ln\{[1 + (1 - e^2)^{1/2}]/2\}.$$

Our main purpose in the present chapter is to find analytical evaluations for the integrals $\mathbf{K}_i(e, \dot{e})$, ($i = 1, \dots, 5$), given by the definition (4). For this reason, we rewrite formula (2) into the following, more suitable form (see also the relation (14)):

$$(55) \quad \int_0^{\pi} [\ln(1 - 2a \cos \varphi + a^2)] (1 - 2b \cos \varphi + b^2)^{-1} d\varphi =$$

$$= (1 + b^2)^{-1} [\ln(1 + a^2)] \int_0^{\pi} \{1 - [2b/(1 + b^2)] \cos \varphi\}^{-1} d\varphi +$$

$$+ (1 + b^2)^{-1} \int_0^{\pi} \{\ln\{1 - [2a/(1 + a^2)] \cos \varphi\}\} \{1 - [2b/(1 + b^2)] \cos \varphi\}^{-1} d\varphi =$$

$$= (1 + b^2)^{-1} [\ln(1 + a^2)] \int_0^{\pi} [1 + (e - \dot{e}) \cos \varphi]^{-1} d\varphi +$$

$$+ (1 + b^2)^{-1} \int_0^{\pi} [\ln(1 + e \cos \varphi)] [1 + (e - \dot{e}) \cos \varphi]^{-1} d\varphi.$$

We have used above the two substitutions:

$$(56) \quad -2a/(1 + a^2) = e(u), \quad \text{and}$$

$$(57) \quad -2b/(1 + b^2) = e(u) - \dot{e}(u).$$

We use also the result/formula **858.524** from Dwight [6]:

$$(58) \quad \int_0^{\pi} [1 + (e - \dot{e}) \cos \varphi]^{-1} d\varphi = \pi [1 - (e - \dot{e})^2]^{-1/2}.$$

Therefore:

$$(59) \quad \int_0^{\pi} [\ln(1 - 2a \cos \varphi + a^2)] (1 - 2b \cos \varphi + b^2)^{-1} d\varphi =$$

$$= -\pi [1 - (e - \dot{e})^2]^{-1/2} \ln(1 + a^2) +$$

$$+ \left[\begin{array}{l} 2\pi(1+b^2)|1-b^2|^{-1} \ln|1-ab^{\pm 1}|; \\ \left. \begin{array}{l} |b| < 1 \\ |b| > 1 \end{array} \right\}, |a| \leq 1 \end{array} \right], \quad \text{or} \\ \left[\begin{array}{l} 2\pi(1+b^2)|1-b^2|^{-1} \ln|a-b^{\pm 1}|; \\ \left. \begin{array}{l} |b| < 1 \\ |b| > 1 \end{array} \right\}, |a| > 1 \end{array} \right].$$

The solution of the equation (56) gives two roots:

$$(60) \quad a_1 = [-1 + (1 - e^2)^{1/2}]/e,$$

$$(61) \quad a_2 = [-1 - (1 - e^2)^{1/2}]/e.$$

The solution of the equation (57) also gives two roots:

$$(62) \quad b_1 = \{-1 + [1 - (e - \dot{e})^2]^{1/2}\}/(e - \dot{e}),$$

$$(63) \quad b_2 = \{-1 - [1 - (e - \dot{e})^2]^{1/2}\}/(e - \dot{e}).$$

The restriction $|e(u)| < 1$ implies that $|a_1| < 1$ and $|a_2| > 1$. From the other hand, the restriction $|e(u) - \dot{e}(u)| < 1$ implies that $|b_1| < 1$ and $|b_2| > 1$. Let us find relations between the systems of roots $\{a_1, a_2\}$ and $\{b_1, b_2\}$, respectively. From substitutions (56) and (57) follows that:

$$(64) \quad -2b/(1+b^2) + 2a/(1+a^2) = -\dot{e}(u).$$

Multiplication of this equality by $(1+a^2)(1+b^2)$ leads to a new form of this relation:

$$(65) \quad -2b(1+a^2) + 2a(1+b^2) = -\dot{e}(1+a^2)(1+b^2) \quad <=> \\ <=> \quad -2b - 2ba^2 + 2a + 2ab^2 + \dot{e} + \dot{e}b^2 + \dot{e}a^2 + \dot{e}a^2b^2 = 0.$$

If we consider the variable b as an unknown quantity, the later equality may be regarded as a quadratic equation for b :

$$(66) \quad (\dot{e}a^2 + 2a + \dot{e})b^2 + (-2 - 2a^2)b + (\dot{e}a^2 + 2a + \dot{e}) = 0.$$

Taking into account the equality (56), we compute that:

$$(67) \quad \dot{e}a^2 + 2a + \dot{e} = 2a + \dot{e}(1+a^2) = 2a + \dot{e}(-2a/e) = 2a(1 - \dot{e}/e) = (2a/e)(e - \dot{e}).$$

Moreover:

$$(68) \quad -2 - 2a^2 = -2(1+a^2) = 4a/e.$$

Therefore, the quadratic equation (66) becomes (after dividing by $2a/e$):

$$(69) \quad (e - \dot{e})b^2 + 2b + (e - \dot{e}) = 0.$$

The two roots of this equation are:

$$(70) \quad b_1 = \{-1 + [1 - (e - \dot{e})^2]^{1/2}\}(e - \dot{e})^{-1},$$

$$(71) \quad b_2 = \{-1 - [1 - (e - \dot{e})^2]^{1/2}\}(e - \dot{e})^{-1}.$$

In the opposite case, we also may consider the equation (65) as a quadratic equation for the unknown variable a . Then we obtain the following quadratic equation:

$$(72) \quad (\dot{e}b^2 - 2b + \dot{e})a^2 + (2 + 2b^2)a + (\dot{e}b^2 - 2b + \dot{e}) = 0.$$

We compute that (in view of the equality (57)):

$$(73) \quad \begin{aligned} \dot{e}b^2 - 2b + \dot{e} &= -2b + \dot{e}(1 + b^2) = -2b + \dot{e}[-2b/(e - \dot{e})] = \\ &= [-2b/(e - \dot{e})](\dot{e} + e - \dot{e}) = -2be/(e - \dot{e}). \end{aligned}$$

Moreover:

$$(74) \quad 2 + 2b^2 = 2(1 + b^2) = -4b/(e - \dot{e}).$$

Then, the quadratic equation (72) becomes (after dividing by $-2b/(e - \dot{e})$):

$$(75) \quad ea^2 + 2a + e = 0.$$

The two roots of this equation are:

$$(76) \quad a_1 = [-1 + (1 - e^2)^{1/2}]/e,$$

$$(77) \quad a_2 = [-1 - (1 - e^2)^{1/2}]/e.$$

We stress that the equations (24) and (75) are identical, and, correspondingly, their roots (25) and $\{(76), (77)\}$ coincide. But the situation is different when we compare the quadratic equations (36) and (69). Because, generally speaking, $\dot{e}(u) \neq 0$, we have not coincidence between these relations, and, consequently, their solutions *are not identical*. For this reason, the notations $\{b_1, b_2\}$ in the present chapter must not be confused with the corresponding notations for the roots in the preceding chapter! With this remark, we continue our investigation of the (possible) relations between the two systems of roots $\{a_1, a_2\}$ and $\{b_1, b_2\}$. In general, the solutions of the equations (69) and (75) imply that we have four self-consistent representations of the analytical expression for the integral

$$\mathbf{K}_1(e, \dot{e}) \equiv \int_0^{2\pi} [\ln(1 + e \cos \varphi)][1 + (e - \dot{e}) \cos \varphi]^{-1} d\varphi. \text{ Namely: } \{a_1, b_1\}, \{a_1, b_2\}, \{a_2, b_1\} \text{ and}$$

$\{a_2, b_2\}$. We shall prove now that all these four solutions for $\mathbf{K}_1(e, \dot{e})$ are equivalent! In view of this purpose, we consider the following four cases:

Case I: $a_1 = [-1 + (1 - e^2)^{1/2}]/e$, $b_1 = \{-1 + [1 - (e - \dot{e})^2]^{1/2}\}(e - \dot{e})^{-1}$.

For this case $|a_1| < 1$ and $|b_1| < 1$. We have already computed that $1 + (a_1)^2 = (2/e^2)[1 - (1 - e^2)^{1/2}] > 0$ (see equality (38)). Further we calculate that:

$$(78) \quad 1 + (b_1)^2 = 1 + \{1 + 1 - (e - \dot{e})^2 - 2[1 - (e - \dot{e})^2]^{1/2}\}(e - \dot{e})^{-2} = \\ = 2\{1 - [1 - (e - \dot{e})^2]^{1/2}\}(e - \dot{e})^{-2}.$$

The next evaluation is:

$$(79) \quad |1 - (b_1)^2| = 1 - (b_1)^2 = 1 - \{1 + 1 - (e - \dot{e})^2 - 2[1 - (e - \dot{e})^2]^{1/2}\}(e - \dot{e})^{-2} = \\ = \{(e - \dot{e})^2 - 2 + (e - \dot{e})^2 + 2[1 - (e - \dot{e})^2]^{1/2}\}(e - \dot{e})^{-2} = \\ = 2\{(e - \dot{e})^2 + [1 - (e - \dot{e})^2]^{1/2} - 1\}(e - \dot{e})^{-2}.$$

Further we have:

$$(80) \quad 1 - a_1 b_1 = 1 - [e(e - \dot{e})]^{-1}[-1 + (1 - e^2)^{1/2}]\{-1 + [1 - (e - \dot{e})^2]^{1/2}\} = \\ = [e(e - \dot{e})]^{-1}\{e(e - \dot{e}) - \{1 - [1 - (e - \dot{e})^2]^{1/2} - (1 - e^2)^{1/2} + \\ + (1 - e^2)^{1/2}[1 - (e - \dot{e})^2]^{1/2}\}\}.$$

Having available the above preliminary evaluations, we can write (in accordance to the formula (59)):

$$(81) \quad (1/2)\mathbf{K}_1(e, \dot{e}) \equiv \int_0^\pi [\ln(1 + e \cos \varphi)][1 + (e - \dot{e}) \cos \varphi]^{-1} d\varphi = \text{solution } a_1 b_1 = \\ = -\pi[1 - (e - \dot{e})^2]^{-1/2} \ln\{(2/e^2)[1 - (1 - e^2)^{1/2}]\} - 2\pi[2/(e - \dot{e})^2] \times \\ \times \{1 - [1 - (e - \dot{e})^2]^{1/2}\} [(e - \dot{e})^2/2] \{1 - [1 - (e - \dot{e})^2]^{1/2} - (e - \dot{e})^2\}^{-1} \times \\ \times \ln\{\{e(e - \dot{e}) - 1 + (1 - e^2)^{1/2} + [1 - (e - \dot{e})^2]^{1/2} - (1 - e^2)^{1/2}[1 - (e - \dot{e})^2]^{1/2}\} \times \\ \times [e(e - \dot{e})]^{-1}\} = \\ = -\pi[1 - (e - \dot{e})^2]^{-1/2} \ln\{(2/e^2)[1 - (1 - e^2)^{1/2}]\} - \pi\{1 - [1 - (e - \dot{e})^2]^{1/2}\} \times \\ \times \{1 - [1 - (e - \dot{e})^2]^{1/2} - (e - \dot{e})^2\}^{-1} \ln\{\{e^2(e^2 + \dot{e}^2 - 2e\dot{e}) + 1 + 1 - e^2 + 1 - \\ - (e^2 + \dot{e}^2 - 2e\dot{e}) + (1 - e^2)(1 - e^2 - \dot{e}^2 + 2e\dot{e}) - 2(e^2 - e\dot{e}) + 2(e^2 - e\dot{e})(1 - e^2)^{1/2} + \\ + 2(e^2 - e\dot{e})[1 - (e - \dot{e})^2]^{1/2} - 2(e^2 - e\dot{e})(1 - e^2)^{1/2}[1 - (e - \dot{e})^2]^{1/2} - 2(1 - e^2)^{1/2} - \\ - 2[1 - (e - \dot{e})^2]^{1/2} + 2(1 - e^2)^{1/2}[1 - (e - \dot{e})^2]^{1/2} + 2(1 - e^2)^{1/2}[1 - (e - \dot{e})^2]^{1/2} - \\ - 2[1 - (e - \dot{e})^2]^{1/2} + 2e^2[1 - (e - \dot{e})^2]^{1/2} - 2(1 - e^2)^{1/2} - \\ - 2(1 - e^2)^{1/2}(-e^2 - \dot{e}^2 + 2e\dot{e})\}[e^2(e - \dot{e})^2]^{-1}\}.$$

In the above derivation we have taken into account that the transition of the integration over the azimuthal angle φ from the interval $[0, \pi]$ to the interval $[0, 2\pi]$ gives exactly doubling of the result. That is to say:

$$(82) \quad \mathbf{K}_1(e, \dot{e}) \equiv \int_0^{2\pi} [\ln(1 + e \cos \varphi)][1 + (e - \dot{e}) \cos \varphi]^{-1} d\varphi = \\ = 2 \int_0^\pi [\ln(1 + e \cos \varphi)][1 + (e - \dot{e}) \cos \varphi]^{-1} d\varphi.$$

We also note that we shall use further the following equality:

$$(83) \quad [1 - (e - \dot{e})^2]^{1/2} \{ [1 - (e - \dot{e})^2]^{1/2} - 1 \} = 1 - [1 - (e - \dot{e})^2]^{1/2} - (e - \dot{e})^2,$$

in order to transform the denominator of the second term in the relation (81). In turn, we are able to perform a cancellation with the multiplier $\{-[1 - [1 - (e - \dot{e})^2]^{1/2}]\}$ in the nominator. Combining the two terms into one, we obtain:

$$(84) \quad \begin{aligned} \text{solution } \mathbf{a}_1 \mathbf{b}_1 &= \pi [1 - (e - \dot{e})^2]^{-1/2} \ln \{ e^2 \{ 4 - 6e^2 + 2e^4 + 6e\dot{e} - 4e^3\dot{e} - 2\dot{e}^2 + 2e^2\dot{e}^2 + \\ &+ (-4 + 4e^2 - 6e\dot{e} + 2\dot{e}^2)(1 - e^2)^{1/2} + (-4 + 4e^2 - 2e\dot{e})[1 - (e - \dot{e})^2]^{1/2} + \\ &+ (4 - 2e^2 + 2e\dot{e})(1 - e^2)^{1/2} [1 - (e - \dot{e})^2]^{1/2} \} \{ 2[1 - (1 - e^2)^{1/2}] e^2 (e - \dot{e})^2 \}^{-1} \} = \\ &= \pi [1 - (e - \dot{e})^2]^{-1/2} \ln \{ \{ 2 - 3e^2 + e^4 + 3e\dot{e} - 2e^3\dot{e} - \dot{e}^2 + e^2\dot{e}^2 + \\ &+ (-2 + 2e^2 - 3e\dot{e} + \dot{e}^2)(1 - e^2)^{1/2} + (-2 + 2e^2 - e\dot{e})[1 - (e - \dot{e})^2]^{1/2} + \\ &+ (2 - e^2 + e\dot{e})(1 - e^2)^{1/2} [1 - (e - \dot{e})^2]^{1/2} \} \{ [1 - (1 - e^2)^{1/2}] (e - \dot{e})^2 \}^{-1} \}. \end{aligned}$$

It is interesting to check what will be the behaviour of the above solution under the transition $\dot{e}(u) \rightarrow 0$. We compute that:

$$(85) \quad \begin{aligned} \lim_{\dot{e}(u) \rightarrow 0} \text{solution } \mathbf{a}_1 \mathbf{b}_1 &= \pi (1 - e^2)^{-1/2} \ln \{ [2 - 3e^2 + e^4 + (-2 + 2e^2)(1 - e^2)^{1/2} + \\ &+ (-2 + 2e^2)(1 - e^2)^{1/2} + 2 - e^2 - 2e^2 + e^4] \{ e^2 [1 - (1 - e^2)^{1/2}] \}^{-1} \} = \\ &= \pi (1 - e^2)^{-1/2} \ln \{ 2[2 - 3e^2 + e^4 - 2(1 - e^2)(1 - e^2)^{1/2}] \{ e^2 [1 - (1 - e^2)^{1/2}] \}^{-1} \} = \\ &= \pi (1 - e^2)^{-1/2} \ln \{ 2(1 - e^2)[2 - e^2 - 2(1 - e^2)^{1/2}] \{ e^2 [1 - (1 - e^2)^{1/2}] \}^{-1} \}. \end{aligned}$$

We see that:

$$(86) \quad [1 - (1 - e^2)^{1/2}][1 + (1 - e^2)^{1/2}] = 1 - (1 - e^2) \equiv e^2.$$

Consequently:

$$(87) \quad \begin{aligned} [2 - e^2 - 2(1 - e^2)^{1/2}] \{ e^2 [1 - (1 - e^2)^{1/2}] \}^{-1} &= \\ = [2 - e^2 - 2(1 - e^2)^{1/2}] [1 + (1 - e^2)^{1/2}]^{-1} [1 - (1 - e^2)^{1/2}]^{-2} &= \\ = [2 - e^2 - 2(1 - e^2)^{1/2}] [1 + (1 - e^2)^{1/2}]^{-1} [1 - 2(1 - e^2)^{1/2} + 1 - e^2]^{-1} &= \\ = 1/[1 + (1 - e^2)^{1/2}]. \end{aligned}$$

Substitution of (87) into (85) gives (see equality (42)):

$$(88) \quad \lim_{\dot{e}(u) \rightarrow 0} \text{solution } \mathbf{a}_1 \mathbf{b}_1 = \pi (1 - e^2)^{-1/2} \ln \{ 2(1 - e^2)/[1 + (1 - e^2)^{1/2}] \} = \text{solution } \mathbf{I}.$$

Consequently:

$$(89) \quad \lim_{\dot{e}(u) \rightarrow 0} (1/2)\mathbf{K}_1(e, \dot{e}) = (1/2)\mathbf{L}_0(e),$$

as we expected to be, in order to have an agreement between the definitions (3) and (4).

Case II: $\mathbf{a}_1 = [-1 + (1 - e^2)^{1/2}]/e$, $\mathbf{b}_2 = \{-1 - [1 - (e - \dot{e})^2]^{1/2}\}(e - \dot{e})^{-1}$.

For this case $|a_1| < 1$ and $|b_2| > 1$. We evaluate that:

$$(90) \quad 1 + (b_2)^2 = 1 + \{1 + 1 - (e - \dot{e})^2 + 2[1 - (e - \dot{e})^2]^{1/2}\}(e - \dot{e})^{-2} = \\ = 2\{1 + [1 - (e - \dot{e})^2]^{1/2}\}(e - \dot{e})^{-2},$$

$$(91) \quad |1 - (b_2)^2| \equiv (b_2)^2 - 1 = \{1 + 1 - (e - \dot{e})^2 + 2[1 - (e - \dot{e})^2]^{1/2} - (e - \dot{e})^2\}(e - \dot{e})^{-2} = \\ = 2\{1 - (e - \dot{e})^2 + [1 - (e - \dot{e})^2]^{1/2}\}(e - \dot{e})^{-2} = 2\{[1 - (e - \dot{e})^2]^{1/2}\}^2 + \\ + [1 - (e - \dot{e})^2]^{1/2}\}(e - \dot{e})^{-2} = 2[1 - (e - \dot{e})^2]^{1/2}\{1 + [1 - (e - \dot{e})^2]^{1/2}\}(e - \dot{e})^{-2}.$$

Further we compute:

$$(92) \quad 1 - (a_1/b_2) = 1 - [-1 + (1 - e^2)^{1/2}](e - \dot{e})\{e[-1 - [1 - (e - \dot{e})^2]^{1/2}]\}^{-1} = \\ = \{e + e[1 - (e - \dot{e})^2]^{1/2} - e + e(1 - e^2)^{1/2} + \dot{e} - \dot{e}(1 - e^2)^{1/2}\} \times \\ \times \{e\{1 + [1 - (e - \dot{e})^2]^{1/2}\}\}^{-1} = \\ = \{e(1 - e^2)^{1/2} + e[1 - (e - \dot{e})^2]^{1/2} + \dot{e} - \dot{e}(1 - e^2)^{1/2}\}\{e\{1 + [1 - (e - \dot{e})^2]^{1/2}\}\}^{-1}.$$

$$(93) \quad (1/2)\mathbf{K}_1(e, \dot{e}) = \text{solution } a_1 b_2 = -\pi[1 - (e - \dot{e})^2]^{-1/2} \ln\{(2/e^2)[1 - (1 - e^2)^{1/2}]\} + \\ + 2\pi(e - \dot{e})^2\{1 + [1 - (e - \dot{e})^2]^{1/2}\}\{2(e - \dot{e})^2[1 - (e - \dot{e})^2]^{1/2}\{1 + [1 - (e - \dot{e})^2]^{1/2}\}\}^{-1} \times \\ \times \ln\{e(1 - e^2)^{1/2} + e[1 - (e - \dot{e})^2]^{1/2} + \dot{e} - \dot{e}(1 - e^2)^{1/2}\}\{e\{1 + [1 - (e - \dot{e})^2]^{1/2}\}\}^{-1}\} = \\ = \pi[1 - (e - \dot{e})^2]^{-1/2} \ln\{e^2\{e^2 - e^4 + e^2 - e^2(e^2 + \dot{e}^2 - 2e\dot{e}) + \dot{e}^2 + \dot{e}^2 - e^2\dot{e}^2 + \\ + 2e^2(1 - e^2)^{1/2}[1 - (e - \dot{e})^2]^{1/2} + 2e\dot{e}(1 - e^2)^{1/2} - 2e\dot{e}(1 - e^2) + 2e\dot{e}[1 - (e - \dot{e})^2]^{1/2} - \\ - 2e\dot{e}(1 - e^2)^{1/2}[1 - (e - \dot{e})^2]^{1/2} - 2\dot{e}^2(1 - e^2)^{1/2}\}\{2e^2[1 - (1 - e^2)^{1/2}]\} \times \\ \times \{1 + [1 - (e - \dot{e})^2]^{1/2}\}^2\}^{-1}\} = \\ = \pi[1 - (e - \dot{e})^2]^{-1/2} \ln\{e^2 - e^4 - e\dot{e} + 2e^3\dot{e} + \dot{e}^2 - e^2\dot{e}^2 + (e\dot{e} - \dot{e}^2)(1 - e^2)^{1/2} + \\ + e\dot{e}[1 - (e - \dot{e})^2]^{1/2} + (e^2 - e\dot{e})(1 - e^2)^{1/2}[1 - (e - \dot{e})^2]^{1/2}\}\{[1 - (1 - e^2)^{1/2}]\} \times \\ \times \{1 + [1 - (e - \dot{e})^2]^{1/2}\}^2\}^{-1}\}.$$

In order to simplify the argument of the logarithm, we evaluate its two multipliers:

$$(94) \quad \{[1 - (1 - e^2)^{1/2}]\{1 + [1 - (e - \dot{e})^2]^{1/2}\}^2\}^{-1} = \{1 - [1 - (e - \dot{e})^2]^{1/2}\} \times \\ \times \{[1 - (1 - e^2)^{1/2}]\{1 + [1 - (e - \dot{e})^2]^{1/2}\}\{1 + [1 - (e - \dot{e})^2]^{1/2}\}\}^{-1} \times \\ \times \{1 - [1 - (e - \dot{e})^2]^{1/2}\}^{-1} = \\ = \{1 - [1 - (e - \dot{e})^2]^{1/2}\}\{[1 - (1 - e^2)^{1/2}]\{1 + [1 - (e - \dot{e})^2]^{1/2}\}[1 - 1 + (e - \dot{e})^2]\}^{-1} = \\ = \{1 - [1 - (e - \dot{e})^2]^{1/2}\}\{(e - \dot{e})^2[1 - (1 - e^2)^{1/2}]\{1 + [1 - (e - \dot{e})^2]^{1/2}\}\}^{-1},$$

$$(95) \quad \{1 - [1 - (e - \dot{e})^2]^{1/2}\}\{e^2 - e^4 - e\dot{e} + 2e^3\dot{e} + \dot{e}^2 - e^2\dot{e}^2 + (e\dot{e} - \dot{e}^2)(1 - e^2)^{1/2} + \\ + e\dot{e}[1 - (e - \dot{e})^2]^{1/2} + (e^2 - e\dot{e})(1 - e^2)^{1/2}[1 - (e - \dot{e})^2]^{1/2}\} = (e - \dot{e})^2(1 - e^2 + e\dot{e}) - \\ - (e - \dot{e})^2(1 - e^2 + e\dot{e})(1 - e^2)^{1/2} - (e - \dot{e})^2(1 - e^2)[1 - (e - \dot{e})^2]^{1/2} + \\ + (e - \dot{e})^2(1 - e^2)^{1/2}[1 - (e - \dot{e})^2]^{1/2} = (e - \dot{e})^2\{(1 - e^2 + e\dot{e})[1 - (1 - e^2)^{1/2}] + \\ + (1 - e^2)^{1/2}[1 - (e - \dot{e})^2]^{1/2}[1 - (1 - e^2)^{1/2}]\} = \\ = (e - \dot{e})^2[1 - (1 - e^2)^{1/2}]\{1 - e^2 + e\dot{e} + (1 - e^2)^{1/2}[1 - (e - \dot{e})^2]^{1/2}\}.$$

Substitution of the above results (94) and (95) into (93) gives:

$$(96) \quad (1/2)\mathbf{K}_1(e, \dot{e}) = \text{solution } a_1 b_2 = \pi[1 - (e - \dot{e})^2]^{-1/2} \ln\{(e - \dot{e})^2[1 - (1 - e^2)^{1/2}]\} \times \\ \times \{1 - e^2 + e\dot{e} + (1 - e^2)^{1/2}[1 - (e - \dot{e})^2]^{1/2}\}\{(e - \dot{e})^2[1 - (1 - e^2)^{1/2}]\} \times \\ \times \{1 + [1 - (e - \dot{e})^2]^{1/2}\}\}^{-1}\} = \\ = \pi[1 - (e - \dot{e})^2]^{-1/2} \ln\{[1 - e^2 + e\dot{e} + \\ + (1 - e^2)^{1/2}[1 - (e - \dot{e})^2]^{1/2}]\{1 + [1 - (e - \dot{e})^2]^{1/2}\}^{-1}\}.$$

It is easy to see that the transition $\dot{e}(u) \rightarrow 0$ gives the expected result:

$$(97) \quad \lim_{\dot{e}(u) \rightarrow 0} \text{solution } a_1 b_2 = \lim_{\dot{e}(u) \rightarrow 0} [\pi[1 - (e - \dot{e})^2]^{-1/2} \ln\{[1 - e^2 + e\dot{e} + \\ \dot{e}(u) \rightarrow 0 \quad \dot{e}(u) \rightarrow 0$$

$$\begin{aligned}
& + (1 - e^2)^{1/2} [1 - (e - \dot{e})^2]^{1/2} \{1 + [1 - (e - \dot{e})^2]^{1/2}\}^{-1} \} = \\
& = \pi(1 - e^2)^{-1/2} \ln\{2(1 - e^2)[1 + (1 - e^2)^{1/2}]^{-1}\} = (1/2)\mathbf{L}_0(e).
\end{aligned}$$

There arises the natural question: whether the coincidence of the *solution* $\mathbf{a}_1\mathbf{b}_1$ and the *solution* $\mathbf{a}_1\mathbf{b}_2$ happens only in the limit $\dot{e}(u) \rightarrow 0$, or it is due to the equivalence of these solutions in general? We shall show that the later situation is true. For this purpose, it is enough to check the equality of the arguments of the logarithmic functions. In fact, this means to verify that:

$$\begin{aligned}
(98) \quad & \{1 + [1 - (e - \dot{e})^2]^{1/2}\} \{2 - 3e^2 + e^4 + 3e\dot{e} - 2e^3\dot{e} - \dot{e}^2 + e^2\dot{e}^2 + \\
& + (-2 + 2e^2 - 3e\dot{e} + \dot{e}^2)(1 - e^2)^{1/2} + (-2 + 2e^2 - e\dot{e})[1 - (e - \dot{e})^2]^{1/2} + \\
& + (2 - e^2 + e\dot{e})(1 - e^2)^{1/2} [1 - (e - \dot{e})^2]^{1/2}\} = \\
& = e^2 - e^4 - 3e^2\dot{e} + (-e^2 + e^4 + 2e\dot{e} - 3e^3\dot{e} - \dot{e}^2 + 3e^2\dot{e}^2 - e\dot{e}^3)(1 - e^2)^{1/2} + \\
& + (-e^2 + e^4 + 2e\dot{e} - 2e^3\dot{e} - \dot{e}^2 + e^2\dot{e}^2)[1 - (e - \dot{e})^2]^{1/2} - 2e\dot{e} + 3e^3\dot{e} + e\dot{e}^3 + \dot{e}^2 + \\
& + (e^2 - 2e\dot{e} + \dot{e}^2)(1 - e^2)^{1/2} [1 - (e - \dot{e})^2]^{1/2},
\end{aligned}$$

$$\begin{aligned}
(99) \quad & [1 - (1 - e^2)^{1/2}](e - \dot{e})^2 \{1 - e^2 + e\dot{e} + (1 - e^2)^{1/2} [1 - (e - \dot{e})^2]^{1/2}\} = e^2 - e^4 - 2e\dot{e} + \\
& + 3e^3\dot{e} + \dot{e}^2 - 3e^2\dot{e}^2 + (-e^2 + e^4 + 2e\dot{e} - 3e^3\dot{e} - \dot{e}^2 + 3e^2\dot{e}^2 - e\dot{e}^3)(1 - e^2)^{1/2} + \\
& + (-e^2 + e^4 + 2e\dot{e} - 2e^3\dot{e} - \dot{e}^2 + e^2\dot{e}^2)[1 - (e - \dot{e})^2]^{1/2} + \\
& + (e^2 - 2e\dot{e} + \dot{e}^2)(1 - e^2)^{1/2} [1 - (e - \dot{e})^2]^{1/2}.
\end{aligned}$$

The right-hand-sides of the above two equalities (98) and (99) are equal, which, in turn, after all, implies the equivalence of the *solution* $\mathbf{a}_1\mathbf{b}_1$ (given by formula (84)) and *solution* $\mathbf{a}_1\mathbf{b}_2$ (given by formula (96)).

Case III: $\mathbf{a}_2 = [-1 - (1 - e^2)^{1/2}]/e$, $\mathbf{b}_1 = \{-1 + [1 - (e - \dot{e})^2]^{1/2}\}(e - \dot{e})^{-1}$.

For this case $|a_2| > 1$ and $|b_1| < 1$. We have already computed that $1 + (a_2)^2 = (2/e^2)[1 + (1 - e^2)^{1/2}]$ (see equality (44)), which gives us the opportunity to write the expression (59) into the form:

$$\begin{aligned}
(100) \quad & (1/2)\mathbf{K}_1(e, \dot{e}) \equiv \int_0^\pi [\ln(1 + e\cos\varphi)][1 + (e - \dot{e})\cos\varphi]^{-1} d\varphi = \text{solution } \mathbf{a}_2\mathbf{b}_1 = \\
& = -\pi[1 - (e - \dot{e})^2]^{-1/2} \ln\{(2/e^2)[1 + (1 - e^2)^{1/2}]\} - 2\pi\{1 - [1 - (e - \dot{e})^2]^{1/2}\} \times \\
& \times \{1 - [1 - (e - \dot{e})^2]^{1/2} - (e - \dot{e})^2\}^{-1} \ln|a_2 - b_1| = \\
& = -\pi[1 - (e - \dot{e})^2]^{-1/2} \ln\{(2/e^2)[1 + (1 - e^2)^{1/2}]\} + \pi\{1 - [1 - (e - \dot{e})^2]^{1/2}\} \times \\
& \times \{[1 - (e - \dot{e})^2]^{1/2}\} \{1 - [1 - (e - \dot{e})^2]^{1/2}\}^{-1} \ln(a_2 - b_1)^2 = \\
& = \pi[1 - (e - \dot{e})^2]^{-1/2} \ln\{(e^2/2)(a_2 - b_1)^2 [1 + (1 - e^2)^{1/2}]^{-1}\}.
\end{aligned}$$

We take into account that:

$$(101) \quad [1 + (1 - e^2)^{1/2}]^{-1} = [1 - (1 - e^2)^{1/2}]^2 [1 - (1 - e^2)^{1/2}]^{-1} [1 - (1 - e^2)^{1/2}]^{-1} \times \\
\times [1 + (1 - e^2)^{1/2}]^{-1} = [2 - e^2 - 2(1 - e^2)^{1/2}]e^{-2} [1 - (1 - e^2)^{1/2}]^{-1}.$$

$$\begin{aligned}
(102) \quad & (a_2 - b_1)^2 = \{[-1 - (1 - e^2)^{1/2}]/e - \{-1 + [1 - (e - \dot{e})^2]^{1/2}\}(e - \dot{e})^{-1}\} = \\
& = \{(e - \dot{e})(1 - e^2)^{1/2} + e - \dot{e} - e + e[1 - (e - \dot{e})^2]^{1/2}\}^2 e^{-2} (e - \dot{e})^{-2} = \\
& = \{(e^2 + \dot{e}^2 - 2e\dot{e})(1 - e^2) + \dot{e}^2 + e^2 - e^2(e^2 + \dot{e}^2 - 2e\dot{e}) + (-2e\dot{e} + 2\dot{e}^2)(1 - e^2)^{1/2} + \\
& + (2e^2 - 2e\dot{e})(1 - e^2)^{1/2} [1 - (e - \dot{e})^2]^{1/2} - 2e\dot{e}[1 - (e - \dot{e})^2]^{1/2}\} e^{-2} (e - \dot{e})^{-2} = \\
& = 2\{e^2 - e^4 - e\dot{e} + 2e^3\dot{e} + \dot{e}^2 - e^2\dot{e}^2 - \dot{e}(e - \dot{e})(1 - e^2)^{1/2} +
\end{aligned}$$

$$+ e(e-\dot{e})(1-e^2)^{1/2}[1-(e-\dot{e})^2]^{1/2} - e\dot{e}[1-(e-\dot{e})^2]^{1/2} e^{-2}(e-\dot{e})^{-2}.$$

Having in mind the above intermediate calculations (101) and (102), we are able to rewrite the expression (100) in the following way:

$$(103) \quad (1/2) \mathbf{K}_1(e, \dot{e}) = \text{solution } \mathbf{a}_1 \mathbf{b}_1 = \pi [1 - (e - \dot{e})^2]^{-1/2} \ln \{ 2e^2 [2 - e^2 - 2(1 - e^2)^{1/2} \times \\ \times \{ e^2 - e^4 - e\dot{e} + 2e^3\dot{e} + \dot{e}^2 - e^2\dot{e}^2 - e(e-\dot{e})(1-e^2)^{1/2} + \\ + e(e-\dot{e})(1-e^2)^{1/2} [1 - (e-\dot{e})^2]^{1/2} - e\dot{e}[1 - (e-\dot{e})^2]^{1/2} \} \times \\ \times \{ 2e^2 [1 - (1 - e^2)^{1/2} e^2 (e - \dot{e})^2 \}^{-1} \} = \\ = \pi [1 - (e - \dot{e})^2]^{-1/2} \ln \{ \{ 2 - 3e^2 + e^4 + 3e\dot{e} - 2e^3\dot{e} - \dot{e}^2 + e^2\dot{e}^2 + \\ + (-2 + 2e^2 - 3e\dot{e} + \dot{e}^2)(1 - e^2)^{1/2} + (-2 + 2e^2 - e\dot{e})[1 - (e - \dot{e})^2]^{1/2} + \\ + (2 - e^2 + e\dot{e})(1 - e^2)^{1/2} [1 - (e - \dot{e})^2]^{1/2} \} (e - \dot{e})^{-2} [1 - (1 - e^2)^{1/2}]^{-1} \} = \\ = \text{solution } \mathbf{a}_1 \mathbf{b}_1.$$

To establish the equivalence of the *solution* $\mathbf{a}_2 \mathbf{b}_1$ with the *solution* $\mathbf{a}_1 \mathbf{b}_1$, we have used the result (84).

Case IV: $\mathbf{a}_2 = [-1 - (1 - e^2)^{1/2}] / e$, $\mathbf{b}_2 = \{-1 - [1 - (e - \dot{e})^2]^{1/2}\} (e - \dot{e})^{-1}$.

For this case $|a_2| > 1$ and $|b_2| > 1$. Using the already computed expression for $1 + (a_2)^2$ (equality (44)), we have, according to formula (59), the following solution for the integral $\mathbf{K}_1(e, \dot{e})$:

$$(104) \quad (1/2) \mathbf{K}_1(e, \dot{e}) \equiv \int_0^\pi [\ln(1 + e \cos \varphi)] [1 + (e - \dot{e}) \cos \varphi]^{-1} d\varphi = \text{solution } \mathbf{a}_2 \mathbf{b}_2 = \\ = -\pi [1 - (e - \dot{e})^2]^{-1/2} \ln \{ (2/e^2) [1 + (1 - e^2)^{1/2}] \} + 2\pi [1 - (e - \dot{e})^2]^{-1/2} \times \\ \times \ln |a_2 - 1/b_2| = \pi [1 - (e - \dot{e})^2]^{-1/2} \ln \{ (e^2/2) (a_2 - 1/b_2)^2 [1 + (1 - e^2)^{1/2}]^{-1} \} = \\ = \pi [1 - (e - \dot{e})^2]^{-1/2} \ln \{ (e^2/2) [1 + 1 - e^2 - 2(1 - e^2)^{1/2}] (a_2 - 1/b_2)^2 \times \\ \times [1 - (1 - e^2)^{1/2}]^{-1} [1 - (1 - e^2)^{1/2}]^{-1} [1 + (1 - e^2)^{1/2}]^{-1} \} = \\ = \pi [1 - (e - \dot{e})^2]^{-1/2} \ln \{ (e^2/2) [2 - e^2 - 2(1 - e^2)^{1/2}] (a_2 - 1/b_2)^2 [1 - (1 - e^2)^{1/2}]^{-1} \times \\ \times (1 - 1 + e^2)^{-1} \}.$$

It remains to calculate the multiplier $(a_2 - 1/b_2)^2$, in order to finish the evaluation of the integral $\mathbf{K}_1(e, \dot{e})$ in this last **Case IV**.

$$(105) \quad (a_2 - 1/b_2)^2 = \{ [-1 - (1 - e^2)^{1/2}] / e - (e - \dot{e}) \{-1 - [1 - (e - \dot{e})^2]^{1/2}\}^{-1} \}^2 = \\ = \{ [1 + (1 - e^2)^{1/2}] \{ 1 + [1 - (e - \dot{e})^2]^{1/2} \} - e(e - \dot{e})^2 e^{-2} \{ 1 + [1 - (e - \dot{e})^2]^{1/2} \}^{-2} \}^2 = \\ = \{ 1 - e^2 + e\dot{e} + (1 - e^2)^{1/2} + [1 - (e - \dot{e})^2]^{1/2} + (1 - e^2)^{1/2} [1 - (e - \dot{e})^2]^{1/2} \times \\ \times e^{-2} \{ 1 + [1 - (e - \dot{e})^2]^{1/2} \}^{-2} \}^2 = 2 \{ 2 - 3e^2 + e^4 + 3e\dot{e} - 2e^3\dot{e} - \dot{e}^2 + e^2\dot{e}^2 + \\ + (2 - 2e^2 + 3e\dot{e} - \dot{e}^2)(1 - e^2)^{1/2} + (2 - 2e^2 + e\dot{e})[1 - (e - \dot{e})^2]^{1/2} + \\ + (2 - 2e^2 + e\dot{e})(1 - e^2)^{1/2} [1 - (e - \dot{e})^2]^{1/2} \} e^{-2} \{ 1 + [1 - (e - \dot{e})^2]^{1/2} \}^{-2}.$$

Substitution of the above equality into (104) leads to:

$$(106) \quad (1/2) \mathbf{K}_1(e, \dot{e}) = \text{solution } \mathbf{a}_2 \mathbf{b}_2 = \pi [1 - (e - \dot{e})^2]^{-1/2} \ln \{ 2 [2 - e^2 - 2(1 - e^2)^{1/2} \times \\ \times \{ 1 - [1 - (e - \dot{e})^2]^{1/2} \}^2 \{ 2 - 3e^2 + e^4 + 3e\dot{e} - 2e^3\dot{e} - \dot{e}^2 + e^2\dot{e}^2 + \\ + (2 - 2e^2 + 3e\dot{e} - \dot{e}^2)(1 - e^2)^{1/2} + (2 - 2e^2 + e\dot{e})[1 - (e - \dot{e})^2]^{1/2} + \\ + (2 - 2e^2 + e\dot{e})(1 - e^2)^{1/2} [1 - (e - \dot{e})^2]^{1/2} \} \{ 2e^2 [1 - (1 - e^2)^{1/2}] \times \\ \times \{ 1 + [1 - (e - \dot{e})^2]^{1/2} \}^2 \{ 1 - [1 - (e - \dot{e})^2]^{1/2} \}^2 \}^{-1} \},$$

where we have multiplied *both* the nominator and the denominator of the argument of the logarithm by the *same* multiplier $\{1 - [1 - (e - \dot{e})^2]^{1/2}\}^2$.

We also have the equality:

$$(107) \quad \{1 + [1 - (e - \dot{e})^2]^{1/2}\}^2 \{1 - [1 - (e - \dot{e})^2]^{1/2}\}^2 = [1 - 1 + (e - \dot{e})^2]^2 \equiv (e - \dot{e})^4.$$

After some tedious algebra, we arrive at the final expression for $\mathbf{K}_1(e, \dot{e})$:

$$(108) \quad (1/2)\mathbf{K}_1(e, \dot{e}) = \text{solution } \mathbf{a}_2 \mathbf{b}_2 = \pi [1 - (e - \dot{e})^2]^{-1/2} \ln \{ e^2 (e - \dot{e})^2 \{ 2 - 3e^2 + e^4 + 3e\dot{e} - 2e^3\dot{e} - \dot{e}^2 + e^2\dot{e}^2 + (-2 + 2e^2 - 3e\dot{e} + \dot{e}^2)(1 - e^2)^{1/2} + (-2 + 2e^2 - e\dot{e})[1 - (e - \dot{e})^2]^{1/2} + (2 - e^2 + e\dot{e})(1 - e^2)^{1/2}[1 - (e - \dot{e})^2]^{1/2} \} \times \{ e^2 (e - \dot{e})^4 [1 - (1 - e^2)^{1/2}]^{-1} \} = \text{solution } \mathbf{a}_1 \mathbf{b}_1.$$

In this way, we obtain that for all the possible cases, prescribed by the formula (59) for the different combinations $\{a_i, b_j\}$, ($i, j = 1, 2$) of the roots a_1, a_2, b_1 and b_2 , the solutions for the integral $\mathbf{K}_1(e, \dot{e})$ are equivalent. Of course, it is reasonable to check whether these evaluations remain valid under these values of the variables $e(u)$, $\dot{e}(u)$ and $e(u) - \dot{e}(u)$, when we strike with nullification of some of the denominators in the intermediate calculations. For example, if $e(u) = 0$, we have that:

$$(109) \quad \mathbf{K}_1(0, \dot{e}) \equiv \int_0^{2\pi} [\ln(1)] (1 + \dot{e} \cos \varphi)^{-1} d\varphi = 0.$$

At the same time, from formula (84) (describing the *solution* $\mathbf{a}_1 \mathbf{b}_1$), we may evaluate the factor in the argument of the logarithmic function, which is associated with the “peculiar” behavior under the limit transition $e(u) \rightarrow 0$. Omitting the multiplier $1/(e - \dot{e})^2$, which tends to $1/\dot{e}^2$, when $e(u) \rightarrow 0$, we have to compute the following limit:

$$(110) \quad \lim_{e(u) \rightarrow 0} \{ 2 - 3e^2 + e^4 + 3e\dot{e} - 2e^3\dot{e} - \dot{e}^2 + e^2\dot{e}^2 + (-2 + 2e^2 - 3e\dot{e} + \dot{e}^2)(1 - e^2)^{1/2} + (-2 + 2e^2 - e\dot{e})[1 - (e - \dot{e})^2]^{1/2} + (2 - e^2 + e\dot{e})(1 - e^2)^{1/2}[1 - (e - \dot{e})^2]^{1/2} \times \{ [1 - (1 - e^2)^{1/2}]^{-1} \}.$$

Because for the denominator we have:

$$(111) \quad \lim_{e(u) \rightarrow 0} \{ \partial/\partial e [1 - (1 - e^2)^{1/2}] \} = \lim_{e(u) \rightarrow 0} [e(1 - e^2)^{-1/2}] = 0,$$

$$(112) \quad \lim_{e(u) \rightarrow 0} \{ \partial/\partial e [e(1 - e^2)^{-1/2}] \} = \lim_{e(u) \rightarrow 0} [(1 - e^2)^{-1/2} + e^2(1 - e^2)^{-3/2}] = 1.$$

This means that if we want to evaluate the expression (110) by means of the L’Hospital’s rule, we need to apply it two successive times. It is easily verified that the conditions for such an approach are fulfilled. In fact, we have to calculate the second derivative of the nominator in the equality (110), and than to take the limit $e(u) \rightarrow 0$.

$$\begin{aligned}
(113) \quad & \lim\{\partial^2/\partial e^2\{2-3e^2+e^4+3e\dot{e}-2e^3\dot{e}-\dot{e}^2+e^2\dot{e}^2+ \\
& e(u) \rightarrow 0 \\
& + (-2+2e^2-3e\dot{e}+\dot{e}^2)(1-e^2)^{1/2} + (-2+2e^2-e\dot{e})[1-(e-\dot{e})^2]^{1/2} + \\
& + (2-e^2+e\dot{e})(1-e^2)^{1/2}[1-(e-\dot{e})^2]^{1/2}\} = \lim\{\partial/\partial e\{-6e+4e^3+3\dot{e}-6e^2\dot{e}+ \\
& e(u) \rightarrow 0 \\
& + 2e\dot{e}^2+(4e-3\dot{e})(1-e^2)^{1/2}+(2e-2e^3+3e^2\dot{e}-e\dot{e}^2)(1-e^2)^{-1/2}+ \\
& +(4e-\dot{e})[1-(e-\dot{e})^2]^{1/2}+(2e-2e^3-2\dot{e}+3e^2\dot{e}-e\dot{e}^2)[1-(e-\dot{e})^2]^{-1/2}+ \\
& + (-2e+\dot{e})(1-e^2)^{1/2}[1-(e-\dot{e})^2]^{1/2}+(-2e+e^3-e^2\dot{e})(1-e^2)^{-1/2}\times \\
& \times [1-(e-\dot{e})^2]^{1/2}+(-2e+e^3+2\dot{e}-2e^2\dot{e}+e\dot{e}^2)(1-e^2)^{1/2}[1-(e-\dot{e})^2]^{-1/2}\} = \\
& = \lim\{-6+12e^2-12e\dot{e}+2\dot{e}^2+4(1-e^2)^{1/2}-4(4e-3\dot{e})e(1-e^2)^{-1/2}+ \\
& e(u) \rightarrow 0 \\
& + (2-6e^2+6e\dot{e}-\dot{e}^2)(1-e^2)^{-1/2}+(2e-2e^3+3e^2\dot{e}-e\dot{e}^2)e(1-e^2)^{-3/2}- \\
& - (4e-\dot{e})(e-\dot{e})[1-(e-\dot{e})^2]^{-1/2}+(2-6e^2+6e\dot{e}-\dot{e}^2)[1-(e-\dot{e})^2]^{-1/2}+ \\
& + (2e-2e^3-2\dot{e}+3e^2\dot{e}-e\dot{e}^2)(e-\dot{e})[1-(e-\dot{e})^2]^{-3/2}- \\
& - 2(1-e^2)^{1/2}[1-(e-\dot{e})^2]^{1/2}+(2e-\dot{e})e(1-e^2)^{-1/2}[1-(e-\dot{e})^2]^{1/2}+ \\
& + (2e-\dot{e})(e-\dot{e})(1-e^2)^{1/2}[1-(e-\dot{e})^2]^{-1/2}+ \\
& + (-2+3e^2-2e\dot{e})(1-e^2)^{-1/2}[1-(e-\dot{e})^2]^{1/2}+(-2e+e^3-e^2\dot{e})e(1-e^2)^{-3/2}\times \\
& \times [1-(e-\dot{e})^2]^{1/2}+(-2e+e^3-e^2\dot{e})(e-\dot{e})(1-e^2)^{-1/2}[1-(e-\dot{e})^2]^{-1/2}+ \\
& + (-2+3e^2-4e\dot{e}+\dot{e}^2)(1-e^2)^{1/2}[1-(e-\dot{e})^2]^{-1/2}- \\
& - (-2e+e^3+2\dot{e}-2e^2\dot{e}+e\dot{e}^2)e(1-e^2)^{-1/2}+ \\
& + (-2e+e^3+2\dot{e}-2e^2\dot{e}+e\dot{e}^2)(e-\dot{e})(1-e^2)^{1/2}[1-(e-\dot{e})^2]^{-3/2}\} = \\
& = -6+2\dot{e}^2+4+2-\dot{e}^2+4(1-e^2)^{1/2}-\dot{e}^2(1-e^2)^{-1/2}+(2-\dot{e}^2)(1-e^2)^{-1/2}- \\
& - 2(1-e^2)^{1/2}+\dot{e}^2(1-e^2)^{-1/2}-2(1-e^2)^{1/2}+(-2+\dot{e}^2)(1-e^2)^{-1/2}- \\
& - 2\dot{e}^2(1-e^2)^{-1}(1-e^2)^{-1/2}=\dot{e}^2.
\end{aligned}$$

Consequently (using two times the L'Hospital's rule), we have:

$$\begin{aligned}
(114) \quad & \{ \lim(e-\dot{e})^{-2} \} \lim\{ [1-(1-e^2)^{1/2}]^{-1} \{ 2-3e^2+e^4+3e\dot{e}-2e^3\dot{e}-\dot{e}^2+e^2\dot{e}^2+ \\
& e(u) \rightarrow 0 \quad e(u) \rightarrow 0 \\
& + (-2+2e^2-3e\dot{e}+\dot{e}^2)(1-e^2)^{1/2} + (-2+2e^2-e\dot{e})[1-(e-\dot{e})^2]^{1/2} + \\
& + (2-e^2+e\dot{e})(1-e^2)^{1/2}[1-(e-\dot{e})^2]^{1/2} \} \} = (1/\dot{e}^2)\dot{e}^2 = 1.
\end{aligned}$$

It seems out that the argument of the logarithm in the *solution* a_1b_1 approaches unity, when $e(u) \rightarrow 0$, and, correspondingly, the value of the logarithm approaches zero. This is in agreement with the direct computation of the integral $\mathbf{K}_1(e,\dot{e})$, when $e(u) = 0$ (see equality (109)).

As regards to the situation when $e(u) - \dot{e}(u) = 0$ (this possibility is excluded *a priori* by hypothesis during the calculation of the expression (84)), a *direct* computation of the integral $\mathbf{K}_1(e,\dot{e} = e)$ gives:

$$(115) \quad (1/2) \mathbf{K}_1(e,\dot{e} = e) \equiv \int_0^\pi \ln(1 + e \cos \varphi) d\varphi = \pi \ln\{ [1 + (1 - e^2)^{1/2}] / 2 \}.$$

Here we have used formula 865.44 from Dwight [6], setting in it $a = 1$ and $b = e(u)$, and taking into account that for the all parts of the accretion disc $e(u)$ is less than unity (by absolute value). The transition $e(u) - \dot{e}(u) \rightarrow 0$ may be attained in two ways: (i) by fixing $\dot{e}(u)$ and letting $e(u)$ to

approach $\dot{e}(u)$, and (ii) by fixing $e(u)$ and letting $\dot{e}(u)$ to approach $e(u)$. If we apply these two methods to the expression (84), drawing the correspondingly times the L'Hospital's rule for revealing of indeterminacies of the type $0/0$, we shall obtain a result which is identical to the relation (115). This means that the formula (84) can be useful also in the case when $e(u) - \dot{e}(u) = 0$, despite it was derived under the rejection of the later equality. It is important only to remember that in this "peculiar" case it is necessary to perform the limit transition $e(u) - \dot{e}(u) \rightarrow 0$. This transition gives also a continuous passage of the integral $\mathbf{K}_1(e, \dot{e})$ through the point $e(u) - \dot{e}(u) = 0$. We shall not write here the tedious computations, which prove the above statements. We restrict us only to mention that they are valid, in order to underline that the formula (84) (respectively, *solution $\mathbf{a}_1\mathbf{b}_1$* = *solution $\mathbf{a}_1\mathbf{b}_2$* = *solution $\mathbf{a}_2\mathbf{b}_1$* = *solution $\mathbf{a}_2\mathbf{b}_2$*) is not limited by any restrictions, imposed by the values of the eccentricity $e(u)$ and its derivative $\dot{e}(u) \equiv de(u)/du$. Of course, the quantities $e(u)$ and $\dot{e}(u)$ oneself must obey the three inequalities $|e(u)| < 1$, $|\dot{e}(u)| < 1$ and $|e(u) - \dot{e}(u)| < 1$. They are induced by the properties of the considered elliptical accretion disc model [1], as mentioned earlier. To end this chapter, we write into the final form the analytical expression for the integral $\mathbf{K}_1(e, \dot{e})$. Taking into account that the transition of the integration over the azimuthal angle φ from the interval $[0, \pi]$ to the interval $[0, 2\pi]$ simply leads to a doubling of the result, we are able to give the following analytical formula:

$$(116) \quad \mathbf{K}_1(e, \dot{e}) \equiv \int_0^{2\pi} [\ln(1 + e \cos \varphi)] [1 + (e - \dot{e}) \cos \varphi]^{-1} d\varphi =$$

$$= 2\pi [1 - (e - \dot{e})^2]^{-1/2} \ln \{ \{ 2 - 3e^2 + e^4 + 3e\dot{e} - 2e^3\dot{e} - \dot{e}^2 + e^2\dot{e}^2 +$$

$$+ (-2 + 2e^2 - 3e\dot{e} + \dot{e}^2)(1 - e^2)^{1/2} + (-2 + 2e^2 - e\dot{e})[1 - (e - \dot{e})^2]^{1/2} +$$

$$+ (2 - e^2 + e\dot{e})(1 - e^2)^{1/2}[1 - (e - \dot{e})^2]^{1/2} \} (e - \dot{e})^{-2} [1 - (1 - e^2)^{1/2}]^{-1} \}.$$

3. Conclusions

In the present paper we have moved one step more towards the revealing of the mathematical characteristics of the dynamical equation. The later determines the *spatial* structure of the *stationary* elliptical accretion discs, according to the model of Lyubarskij et al. [1]. More concretely, it is shown, that we are able to perform analytical evaluations of two kinds of integrals, which are functions of the eccentricity $e(u)$ and its derivative $\dot{e}(u) \equiv de(u)/du$. Namely, these are $\mathbf{L}_i(e, \dot{e})$, ($\mathbf{i} = 0, \dots, 3$) and $\mathbf{K}_j(e, \dot{e})$, ($\mathbf{j} = 1, \dots, 5$), defined by the equalities (3) and (4), respectively. It is possible to calculate analytical expressions for the integrals $\mathbf{L}_i(e, \dot{e})$, ($\mathbf{i} = 1, 2, 3$) through

recurrence relations, under the condition that both the lower order (in the sense of the indices \mathbf{i} and \mathbf{j}) integrals $\mathbf{L}_i(e, \dot{e})$ and $\mathbf{K}_j(e, \dot{e})$ are already known. About the computation of the integrals $\mathbf{K}_j(e, \dot{e})$, ($\mathbf{j} = 1, \dots, 5$) the situation is slightly different. There is not need to know the expressions for $\mathbf{L}_i(e, \dot{e})$, ($\mathbf{i} = 0, \dots, 3$), but only these for the other integrals $\mathbf{K}_m(e, \dot{e})$, ($\mathbf{m} = 1, \dots, \mathbf{j} - 1$). In preparation to solve the so mentioned two kinds of integrals, we have computed the “initial” integrals $\mathbf{L}_0(e)$ and $\mathbf{K}_1(e, \dot{e})$, which are recognized to serve as starting points for the established recurrence relations. The complete set of analytical solutions for the integrals $\mathbf{L}_i(e, \dot{e})$, ($\mathbf{i} = 1, 2, 3$) and $\mathbf{K}_j(e, \dot{e})$, ($\mathbf{j} = 2, \dots, 5$) will be expressed in a forthcoming paper [7]. Until now, we have traced out the way to reach the determination of these analytical formulas. As follows from the evaluations of $\mathbf{L}_0(e)$ and $\mathbf{K}_1(e, \dot{e})$, we strike with somewhat tedious calculations of these two integrals. But nevertheless, they lead to the pleasurable conclusion that all possible combinations of the permitted values of the parameters give identical solutions for the integrals $\mathbf{L}_0(e)$ and $\mathbf{K}_1(e, \dot{e})$. This property, i.e., the uniqueness of the solutions, obviously facilitates our task to find the analytical solutions of the integrals $\mathbf{L}_i(e, \dot{e})$, ($\mathbf{i} = 0, \dots, 3$) and $\mathbf{K}_j(e, \dot{e})$, ($\mathbf{j} = 1, \dots, 5$).

References

1. Lyubarskiy, Y u. E., K. A. Postnov, M. E. Prokhorov. Eccentric accretion discs., Monthly Not. Royal Astron. Soc., 266, 1994, № 2, pp. 583–596.
2. Dimitrov, D. V. Thin viscous elliptical accretion discs with orbits sharing a common longitude of periastron. V. Linear relations between azimuthal-angle averaged factors in the dynamical equation., Aerospace Research in Bulgaria, 24, 2012.
3. Dimitrov, D. V. Thin viscous elliptical accretion discs with orbits sharing a common longitude of periastron. VI. Simplification of the dynamical equation., Aerospace Research in Bulgaria, 24, 2012.
4. Dimitrov, D. V. Analytical computation of two integrals, appearing in the theory of elliptical accretion discs. I. Solving of the auxiliary integrals, emerging during their derivations., Aerospace Research in Bulgaria, 25, 2013.
5. Prudnikov, A. P., Y u. A. Brichkov, O. I. Marichev. Integrals and series. Elementary functions, Moscow, “Nauka” publishing house, 1981 (in Russian).
6. Dwight, H. B. Tables of integrals and other mathematical data., Fourth edition, New York, MacMillan company, 1961.
7. Dimitrov, D. V. Analytical computation of two integrals, appearing in the theory of elliptical accretion discs. I. Solving of the full set of auxiliary integrals, containing logarithmic functions into their integrands, Aerospace Research in Bulgaria, 26, 2014, (to appear).

АНАЛИТИЧНО ПРЕСМЯТАНЕ НА ДВА ИНТЕГРАЛА, ВЪЗНИКВАЩИ В ТЕОРИЯТА НА ЕЛИПТИЧНИТЕ АКРЕЦИОННИ ДИСКОВЕ. II. РЕШАВАНЕ НА НЯКОИ СПОМАГАТЕЛНИТЕ ИНТЕГРАЛИ, СЪДЪРЖАЩИ ЛОГАРИТМИЧНИ ФУНКЦИИ В СВОИТЕ ИНТЕГРАНДИ

Д. Димитров

Резюме

Тази статия е част от изследванията, третиращи математическата структура на *стационарните* елиптични акреционни дискове в модела на Любарски и др. [1], т.е., дискове при които всички апсидни линии на орбитите на частиците лежат върху една и съща права линия. Главната отличителна черта на възприетия подход е да се намерят линейни зависимости между интегралите, влизащи в това уравнение. Те ще ни дадат възможност да елиминираме тези сложни (и изобщо казано, неизвестни в аналитичен вид) функции на ексцентрицитета $e(u)$ и неговата производна $\dot{e}(u) \equiv de(u)/du$ на орбитите. Тук $u \equiv \ln(p)$, където p е фокалният параметър на орбитата на съответната частица от акреционния диск. В течение на процеса на реализиране на тази програма, ние се сблъскваме с необходимостта да намерим аналитични оценки за два вида интеграла:

$$L_i(e, \dot{e}) \equiv \int_0^{2\pi} [\ln(1 + e \cos \varphi)] (1 + e \cos \varphi)^{-i} [1 + (e - \dot{e}) \cos \varphi]^{-i} d\varphi, \quad (i = 0, \dots, 3), \text{ and } K_j(e, \dot{e}) \equiv \int_0^{2\pi} [\ln(1 + e \cos \varphi)] \times$$

$\times [1 + (e - \dot{e}) \cos \varphi]^{-j} d\varphi, \quad (j = 1, \dots, 5)$. В настоящето изследване, ние намираме рекурентни съотношения, даващи ни възможност да изчислим интегралите $L_i(e, \dot{e})$, ($i = 1, \dots, 3$) при условие че интегралите $L_{i-1}(e, \dot{e})$ и $K_j(e, \dot{e})$ са вече известни. Обратно, изчисленията на интегралите $K_j(e, \dot{e})$, ($j = 1, \dots, 5$), чрез рекурентни зависимости, *не изискват* знанието на аналитичните решения на интегралите $L_i(e, \dot{e})$, ($i = 0, \dots, 3$). С оглед на факта, че интегралите $L_0(e)$ (той не зависи от $\dot{e}(u)$) и $K_1(e, \dot{e})$ служат като “отправни точки” в съответните рекурентни съотношения, ние сме намерили аналитични изрази за тях. Решаването на пълната система от аналитични оценки за $L_i(e, \dot{e})$, ($i = 1, \dots, 3$), и $K_j(e, \dot{e})$, ($j = 2, \dots, 5$), ще бъде дадено другаде [7].

INVESTIGATION OF MIDDLE ATMOSPHERE IONIZATION DURING GLE 70 EVENT FROM DECEMBER 2006 BY MEANS OF CORIMIA MODEL AND NORMALIZED CR SPECTRA

*Peter Velinov¹, Simeon Asenovski¹, Lachezar Mateev¹,
Eduard Vashenyuk², Aleksander Mishev^{3,4}*

¹*Space Research and Technology Institute – Bulgarian Academy of Sciences*

²*Polar Geophysical Institute – Russian Academy of Sciences, Murmansk*

³*Institute for Nuclear Research and Nuclear Energy – Bulgarian Academy of
Sciences*

⁴*Sodankylä Geophysical Observatory, University of Oulu, Finland*

e-mail: pvelinov@bas.bg

Abstract

The ground level enhancement (GLE) of cosmic rays (CRs) on December of 13, 2006 is one of the biggest GLEs in 23rd cycle (behind GLE 69 from 20 January 2005 only) in minimum phase of solar cycle. The greatest maximum was recorded at Oulu Neutron Monitor Station (92.1 %), i.e. the maximum of GLE70 was recorded at sub-polar stations, which shows that the anisotropy source was located near the equator.

Here we compute in details the ionization effects in the terrestrial middle atmosphere and ionosphere (30-120 km) for various latitudes. The computation of electron production rate profiles $q(h)$ is according the operational model CORIMIA (COsmic Ray Ionization Model for Ionosphere and Atmosphere). This improved CR ionization model is important for investigation of the different space weather effects. The influence of galactic and solar CR is computed with the new version of CORIMIA code, which is with fully operational implementations. The solar CR spectra are taken from recent reconstructions from ground based measurements with neutron monitors. Hence we compute the time evolution of the electron production rates $q(h)$ in the ionosphere and middle atmosphere.

The cosmic rays determine to a great extent the chemistry and electrical parameters in the ionosphere and atmosphere. They create ozonosphere and influence actively the stratosphere ozone processes. But the ozonosphere controls the meteorological solar constant and the thermal regime and dynamics of the lower atmosphere, i.e. the weather and climate processes.

1. Introduction

The relativistic solar energetic particles (SEP) cause an excess of ionization, specifically over the polar caps and sub-polar latitudes, but also over the high middle, respectively low middle latitudes, i.e. the SEP influence has global and planetary character. The cosmic ray induced ionization rate will be estimated from the particle flux using the basic physics of ionization in air, an appropriate atmospheric model and realistic modeling of cascade process in the atmosphere [1, 2]. The detailed study of ion production in the ionosphere and atmosphere is important, because it is related to various environmental processes in the space weather and atmospheric physics and chemistry [3].

The solar cycle 23 (May 1996 - January 2008) have provided altogether 16 GLEs (Ground Level Enhancements) (<http://cosmicrays oulu.fi/GLE.html>), which are some of the largest SEP events in the history of CRs, namely the Bastille day event on 14 July 2000 (GLE 59), Easter event on 15 April 2001 (GLE 60), October-November 2003 Halloween events (GLEs 65, 66 & 67), the enormous GLE 69 on January 20, 2005 and the last event from the cycle on 13 December 2006 (GLE 70). This event occurred during the decline phase of solar cycle 23 in conditions on the Sun and in interplanetary medium appropriate to a solar minimum, however it refers to large events. This event was related to X3.4/2B flare with the coordinates at the Sun S06 W24. The flare was accompanied by radio bursts of types II and IV and by a halo type coronal mass ejection (CME). The GLE 70 on 13.12.2006 during the initial phase showed a large anisotropy [4] and the duration of the event of neutron monitor energies was approximately 5 hours.

The present paper shows the results from CORIMIA (COsmic Ray Ionization Model for Ionosphere and Atmosphere) programme [3, 5, 6] with application to the GLE 70 on December of 13, 2006.

2. Determination of differential spectra of Solar Energetic Particles

The SCR spectra at different moments from the event onset, namely 03:00 UT (initial phase), 04:00 UT (main phase) and 06:00 UT (late phase) are assumed as power law:

$$D(E) = J_0 E^{-\gamma}$$

They are reconstructed on the basis of ground based neutron monitor measurements (www.nmdb.eu) according [7] (see Table 1).

Table 1. Rigidity spectra of SEP assumed for ion rate production during GLE 70 [7]

Time UT	J_0 [$\text{m}^{-2} \text{s}^{-1} \text{sr}^{-1} \text{GV}^{-1}$]	γ
03:00	78550	3.77
04:00	203100	6.75
05:00	181750	7.76

We take experimental spectra from the GLE 70 event on 13 December 2006 [7, 2]. We transform the spectrum $D(R)=KR^{-\gamma}$ in its new form $D(E_k)=K'(E_k)R^{-\gamma}$. The latter is suitable for calculations with CORIMIA model [3]. The measurement units are transformed in the new form as follows: particles/($\text{m}^2 \cdot \text{s} \cdot \text{st} \cdot \text{GV}$) become particles/($\text{cm}^2 \cdot \text{s} \cdot \text{MeV}$) by multiplication with normalizing factor $2\pi/(10^4)$ and application of the formula $E_k=f(R)$ [MeV] [8] where E_k is kinetic energy of the penetrating cosmic rays. For two characteristic points $E_{k1}(R_1)$ and $E_{k2}(R_2)$ at lower and higher energies we calculate spectrum values $D(R_1)$ and $D(R_2)$. Then the following nonlinear system of equations is solved towards K' and gamma':

$$D(R_1) = K' E_{k1}(R_1)^{-\gamma'}$$

$$D(R_2) = K' E_{k2}(R_2)^{-\gamma'}$$

On this way we obtain the new transformed spectrum $D(E_k)=K'(E_k)^{-\gamma'}$. The calculated CR spectra for the case under consideration are presented in Fig. 1.

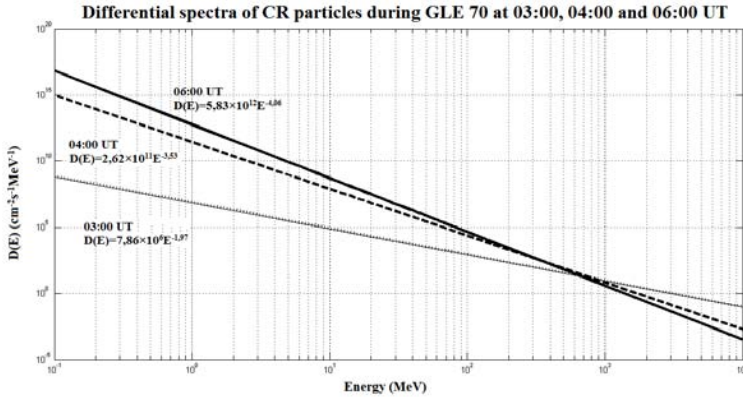


Fig. 1

3. Electron production rate profiles during GLE 70

The ionization production rate during GLE 70 on 13 December 2006 is calculated as a superposition of ion rate due to SEP and to the permanent

flux of GCR. The ionization rate due to GCR is computed considering parameterization based on force field model [9, 10]. The atmospheric simulations are fulfilled considering winter atmospheric profile, which allows a detailed and realistic description of ionization profiles in specific conditions. We apply our operational programme CORIMIA (COsmic Ray Ionization Model for Ionosphere and Atmosphere). In the final version of the applied model an approximation in 5 characteristic energy intervals of the Bohr–Bethe–Bethe function including charge decrease interval is used. For the first time we present these quantitative and qualitative appreciations of the SCR fluxes impact from these Solar Particle Events (SPE) on the ionosphere and middle atmosphere (30–120 km). Unlike the cases of galactic cosmic rays (GCR), SCR differential spectra vary essentially in time during the course of the investigated event. Also SCR fluxes differ from one another for different events. The profiles behavior is explained taking into account the structure of the CORIMIA programme.

The production rate is computed for different rigidity cut-offs, namely 1 GV, 3 GV and 5 GV corresponding to sub-polar and polar latitude, high middle, and respectively low middle latitudes. The obtained production rate at 1 GV rigidity cut-off is presented on Fig. 2. Accordingly, the ion production rate is plotted on Fig. 3 for 3 GV rigidity cutoff and Fig. 4 for 5 GV rigidity cut-off. As was expected the maximal effect is observed at polar and sub-polar regions (Fig. 2).

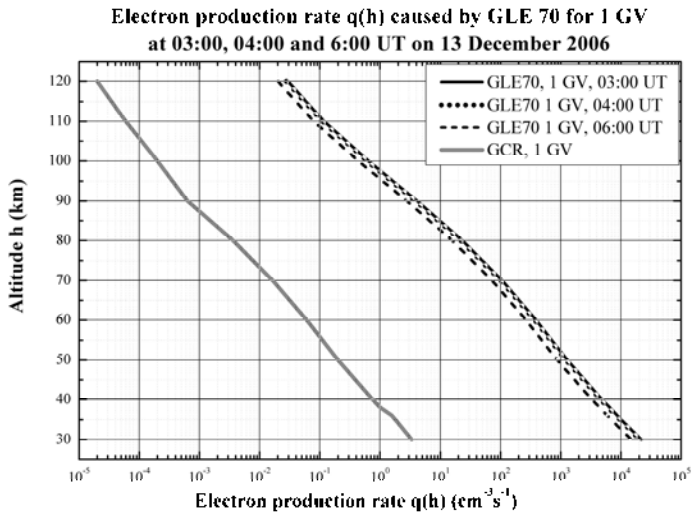


Fig. 2

**Electron production rate $q(h)$ caused by GLE 70 for 3 GV
at 03:00, 04:00 and 6:00 UT on 13 December 2006**

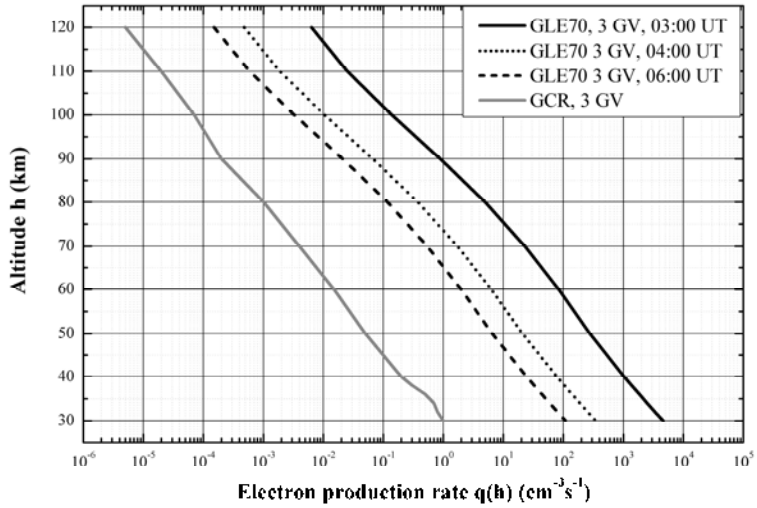


Fig. 3

**Electron production rate $q(h)$ caused by GLE 70 for 5 GV
at 03:00, 04:00 and 6:00 UT on 13 December 2006**

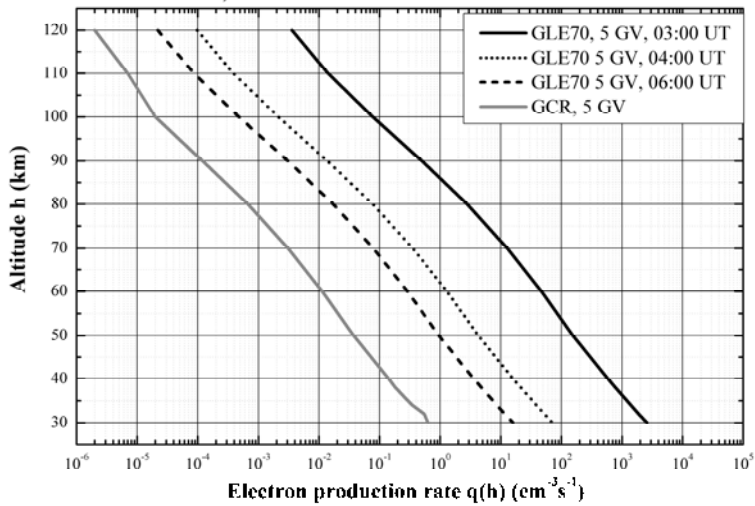


Fig. 4

4. Analysis and conclusion

Ground Level Enhancements are more likely to occur when the Sun is very active. The investigated GLE was a maverick. It occurred near solar minimum, but it was a large event by historical standards, with a peak increase exceeding 90% at some stations - f.e. the ground level neutron monitor Oulu, 5 min average, detected count rate increase by 92%.

The obtained results are important for improvement of recent models of cosmic ray induced ionization and the studies of solar-terrestrial influences and space weather. The cosmic rays determine to a great extent the chemistry and electrical parameters in the ionosphere and atmosphere. They create ozonosphere and influence actively the stratosphere ozone processes. But the ozonosphere controls the meteorological solar constant and the thermal regime and dynamics of the lower atmosphere, i.e. the weather and climate processes. This hypothesis of the solar-terrestrial relationships shows the way to a solution of the key problems of the solar-terrestrial influences.

Acknowledgements: One of the authors (S.A.) is supported under contract: № BG051PO001-3.3.06 0051.

References

1. M i s h e v, A., P. I. Y. V e l i n o v. Atmosphere Ionization Due to Cosmic Ray Protons Estimated with CORSIKA Code Simulations. C.R. Acad. bulg. Sci., 60, 3, 225-230.
C.R. Acad. bulg. Sci. 60, 2007, 3, 225-230.
2. M i s h e v, A., P. I. Y. V e l i n o v, A Maverick GLE 70 in Solar Minimum. Calculations of Enhanced Ionization in the Atmosphere Due to Relativistic Solar Energetic Particles. C.R. Acad. bulg. Sci., 66, 10, 1457-1462.
3. V e l i n o v, P. I. Y., S. A s e n o v s k i, K. K u d e l a, J. L a s t o v I c k a, L. M a t e e v, A. M i s h e v, P. T o n e v, Impact of Cosmic Rays and Solar Energetic Particles on the Earth's Environment. J. Space Weather Space Clim. 3, 2013, A14, 1-17.
4. B u e t I k o f e r, R., E. O. F l u e c k I g e r, L. D e s o r g h e r, M. R. M o s e r, B. P i r a r d, The solar cosmic ray ground-level enhancements on 20 January 2005 and 13 December 2006. Adv. Space Res. 43, 499-503, 2009.
5. A s e n o v s k i, S., P. I. Y. V e l i n o v, L. M a t e e v. Ionization of Solar Cosmic Rays in Ionosphere and Middle Atmosphere Simulated by CORIMIA Programme. C.R. Acad. bulg. Sci., 66, 2, 235-242. C.R. Acad. bulg. Sci. Sci. 66, 2013, 2, 235-242.

6. A s e n o v s k i, S., P. I. Y. V e l i n o v, L. M a t e e v. Determination of the Spectra and Ionization of Anomalous Cosmic Rays in Polar Atmosphere, C.R. Acad. bulg. Sci., 66, 6, 2013, 865-870.
7. V a s h e n y u k, E. V., Y u. V. B a l a b i n, J. P e r e z - P e r a z a, A. G a l l e g o s - C r u z, L. I. M i r o s h n i c h e n k o. Some features of relativistic particles at the Sun in the solar cycles 21-23, Adv. Space Res., 38, 411-417, 2006.
8. V e l i n o v, P. I. Y., G. N e s t o r o v, L. I. D o r m a n, 1974. Cosmic Ray Influence on the Ionosphere and on Radiowave Propagation. Publishing House of Bulgarian Academy of Sciences, Sofia, 312 p.
9. U s o s k i n, I., G. K o v a l t s o v. Cosmic ray induced ionization in the atmosphere: Full modeling and practical applications, J. Geophys.Res., 111, D21206, doi:10.1029/2006JD007150, 2006.
10. M c C r a c k e n, K. G., F. M c D o n a l d, J. B e e r, G. R a i s b e c k, F. Y i o u. A phenomenological study of the long-term cosmic ray modulation, J. Geophys. Res. 109, 2004, A12103, doi:10.1029/2004JA010685.

ИЗСЛЕДВАНЕ НА ЙОНИЗАЦИЯТА В СРЕДНАТА АТМОСФЕРА ПО ВРЕМЕ НА СЪБИТИЕТО GLE 70 ОТ ДЕКЕМВРИ 2006 ПОСРЕДСТВОМ МОДЕЛА CORIMIA И НОРМАЛИЗИРАНЕ НА СПЕКТЪРА НА КОСМИЧЕСКИТЕ ЛЪЧИ

П. Велинов, С. Асеновски, Л. Матеев, Е. Вашинюк, А. Мишев

Резюме

Събитието GLE (Ground Level Enhancement) на Космическите лъчи (CRs) от 13 декември, 2006 год. е едно от най-мощните събития за изминалия 23-ти слънчев цикъл (единствено предходното събитие GLE 69 от 20 Януари, 2005 е по-мощно от него). Най-големият максимум (92.1 %) беше регистриран от неутронния монитор в Оулу (Oulu Neutron Monitor Station), тоест максимума на GLE 70 беше регистриран от суб-полярна станция, което показва, че анизотропният източник е локализиран в близост до екватора.

Тук ние детайлно изчисляваме йонизационните ефекти в средната атмосфера и йоносфера (30-120 км) за различни геомагнитни ширини, като въздействието на галактичните космически лъчи (GCR) и слънчевите енергетични частици (SEP) са представени отделно. Тези изчисления са направени посредством операционния модел CORIMIA (COsmic Ray Ionization Model for Ionosphere and Atmosphere), чрез

който значително се увеличават възможностите ни за изследване на различни проявления на космическото време. Спектрите на слънчевите енергетични частици са получени при реконструкции на експериментални данни от неутронни монитори. Чрез използване на различни спектри изместени във времето за потока от слънчеви енергетични частици, ние сме представили времевата еволюция на електронната продукция $q(h)$.

Съвременните изследвания показват, че космическите лъчи (КЛ) са един от основните фактори в химичните и електрически процеси в атмосферата и йоносферата на Земята. КЛ влияят върху образуването на озона в атмосферата, което директно ги свързва с климатичните процеси.

GEOEFFECTIVITY OF SOLAR CORONAL HOLES WITH DIFFERENT MAGNETIC FIELD POLARITY

*Maria Abunina¹, Anatoly Abunin¹, Anatoly Belov¹, Sergey Gaidash¹,
Yordan Tassev², Peter Velinov², Lachezar Mateev², Peter Tonev²*

¹*Institute for Geomagnetism, Ionosphere and Radiowave Propagation (IZMIRAN),
Russian Academy of Sciences, Troitsk, Moscow Region
e-mails: abunina@izmiran.ru, abunin@izmiran.ru, gaidash@izmiran.ru,
abelov@izmiran.rssi.ru*

²*Space Research and Technology Institute – Bulgarian Academy of Sciences
e-mails: yktassev@bas.bg, pvelinov@bas.bg, lnmateev@bas.bg, ptonev@bas.bg*

Abstract

The coronal holes (CH) are sources of high-speed flows of solar wind, and, in its turn, are one of the main sources of geomagnetic disturbances. The coronal holes differ very much one from another and their geoeffectivity varies in a wide range. In this paper we implement a study to answer the question how the coronal holes characterized by different location on the Sun and by their polarity influence the geomagnetic activity. We considere several tens of coronal holes observed in a few recent years, and separate them into groups by the solar latitude and their polarity. A conclusion is made that the trans-equatorial group is the most effective one, and that almost all coronal holes in this group have a negative polarity. Less, but yet sufficiently effective, are the holes of negative polarity at north latitudes and those of positive polarity at south latitudes. The much smaller number of coronal holes of opposite polarity (CH of negative polarity in south hemisphere and CH of positive one in horth hemisphere) are less effective.

1. Introduction

The coronal holes are extended regions in the solar corona where the density and temperature are lower than other places in the corona. The weak, diverging and open magnetic field lines in coronal holes extend radially outward. The high speed path of the solar wind streams out from

coronal holes. The low density of the gas makes this parts of the corona appear dark in extreme-ultraviolet and soft X-ray images of the Sun, as if they were a hole in the corona [1, 2].

The investigation of the coronal holes properties and behavior is connected before all with their effects at the Earth. The studies which are related to the coronal holes positions as well as to the flow, polarity and solar wind [3] velocity are really very important. Some models are developed for prediction of the solar wind from coronal holes [4].

The model is based on the position and the magnitude of the solar coronal holes. Some studies are proposed concerning the quantitative analysis of the quadruple component of the magnetic field [5]. By means of this method the magnetic field poles are determined and therefore the coronal holes behavior as well as their appearance and motion. It is assumed that the coronal holes position follows the magnetic field poles motion. All these and also other investigations consider before all the coronal holes, their behavior and structure or the solar wind from them. But these studies do not connect directly the coronal holes with the geophysical activity.

The goal of the present work is to investigate the geoeffectivity of solar coronal holes in dependence on the polarity of the corresponding magnetic fields.

2. Data and methods

The data base for Forbush-effects and interplanetary disturbances developed in IZMIRAN [6] is used by us in order to chose events in which the coronal holes (*CH*) have influence on the Earth's magnetosphere. 53 events in the period 2011-2012 were chosen, such that a well recognized coronal hole was the source of geoeffectivity in each case. We considered the coronal holes with respect to their polarity and the location on the solar disk. The enumeration and location of the CH we obtained from the site [7], and the polarity was retrieved from data taken from [8].

3. Discussion of the results

We considered 53 events whose sources were coronal holes on Sun. We found 12 coronal holes of negative polarity in the northern solar hemisphere; 16 CH of positive polarity in the southern solar hemisphere; 21 coronal holes crossing the equator (19 of them - of negative polarity, and only 2 – of positive polarity); and 4 untypical coronal holes (3 of them of

negative polarity in the southern hemisphere, and one of positive polarity in the north hemisphere).

Table 1. Average characteristics of the geomagnetic activity and of the interplanetary space in studied events

Location	N	S	C	N/S
Polarity	-	+	-/+	+/-
Number	12	16	21	4
Forbush effect	1.01 ± 0.13	0.81 ± 0.09	1.00 ± 0.10	1.15 ± 0.25
Kp_max	3.83 ± 0.35	3.62 ± 0.23	4.27 ± 0.21	3.16 ± 0.35
Ap_max	29.83 ± 6.27	24.63 ± 3.71	35.52 ± 4.38	17.25 ± 3.75
V_{\max}	547.3 ± 36.4	524.1 ± 15.0	572.6 ± 22.1	498.5 ± 83.9
Dst _{min}	-34.0 ± 4.6	-21.9 ± 3.3	-32.6 ± 3.8	-15.8 ± 2.4

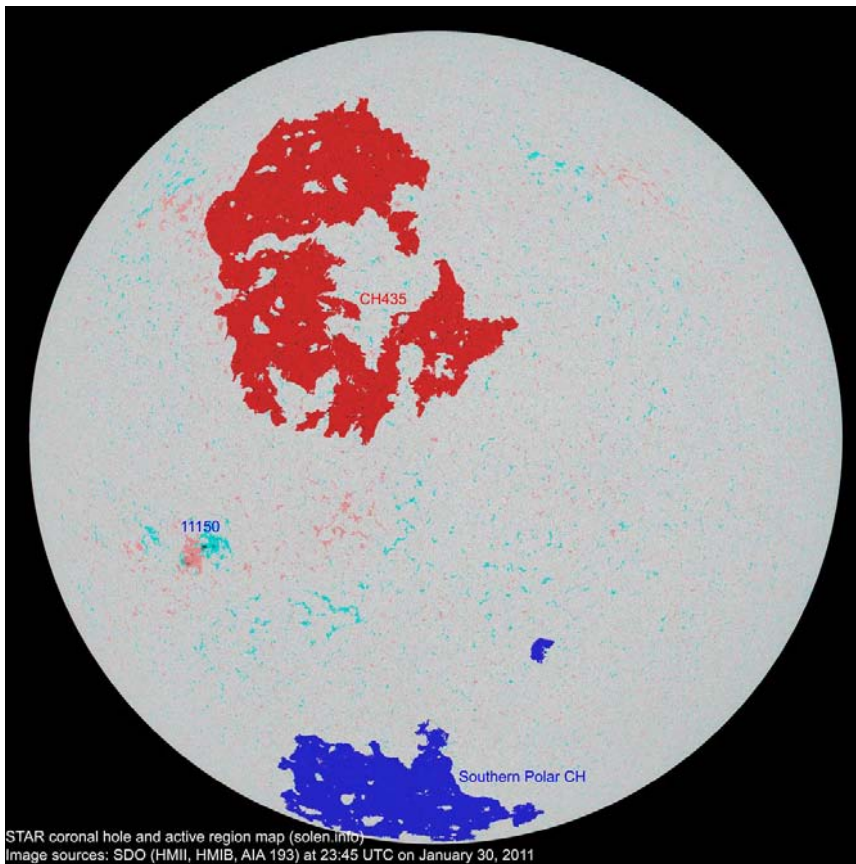


Fig.1. A case of a northern coronal hole of negative polarity of its magnetic field

The coronal hole CH435 demonstrated in Fig.1 passed through the solar central meridian on January 30 - February 1, 2011, and the related geomagnetic effect was observed on the Earth on February 4-8. This hole created a Forbush-effect of magnetude 1.5%, as well as a small geomagnetic storm (Kp-index was 6-, and Dst-index reached -56 nT). The maximal velocity of the solar wind was 647 km/s.

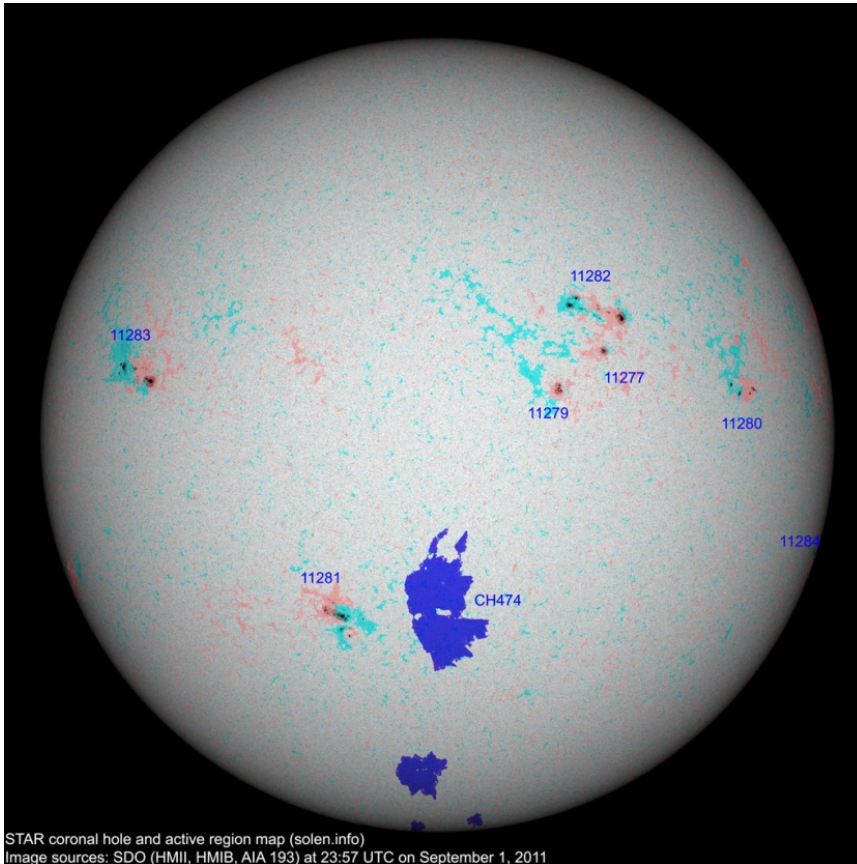


Fig. 2. A case of a southern coronal hole of positive polarity of its magnetic field

The coronal hole CH474, shown in Fig. 2, passed through the solar central meridian on September 1, 2011, and the related geomagnetic effect on the Earth was observed on September 4-8. This hole caused a Forbush-effect of magnetude 0.7%, and was accompanied with a small disturbance of

the geomagnetic field (Kp-index was 3; Dst-index was -20 nT). The maximum velocity of the solar wind was 441 km/s.

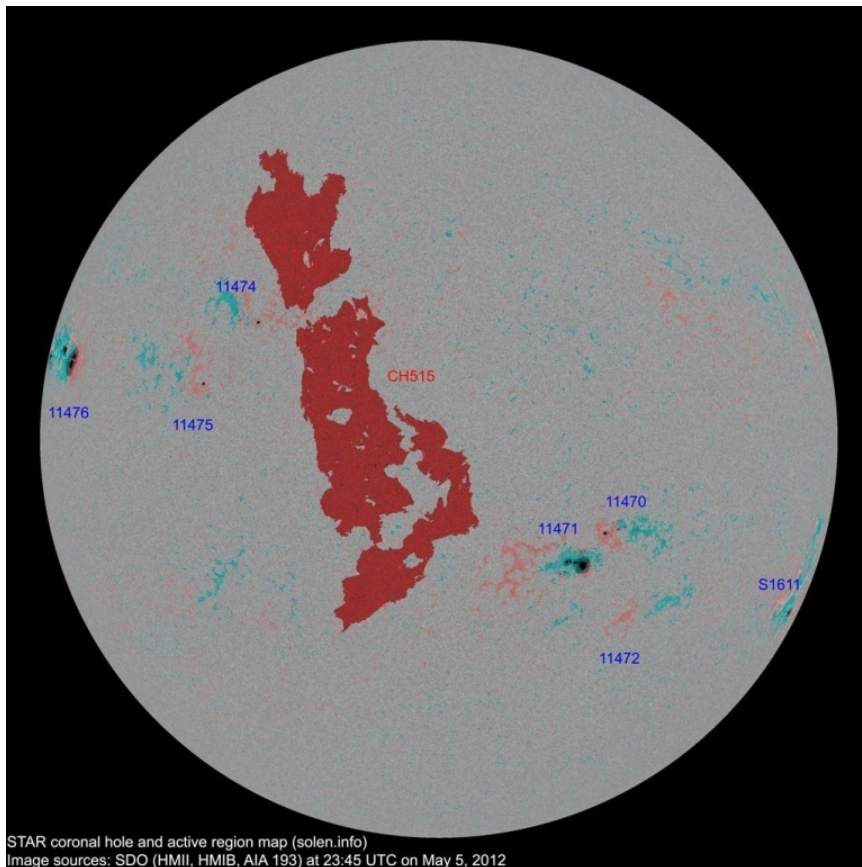


Fig. 3. A case of a trans-equatorial coronal hole of negative polarity of its magnetic field

The coronal hole CH515 demonstrated in Fig. 3 passed through the solar central meridian on May 5-7, 2012, and the related geomagnetic effect was observed on the Earth on May 8-12. This hole created a Forbush-effect of magnitude 1.9%, as well as a small geomagnetic storm (Kp-index was 5-; Dst-index reached -42 nT). The maximum velocity of the solar wind was 638 km/s.

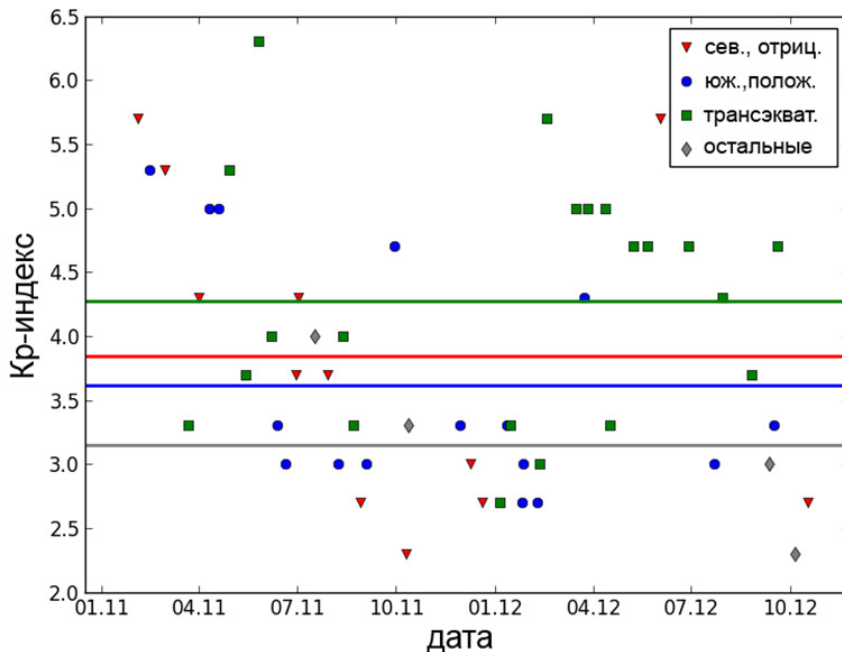


Fig. 4. The average geoeffectivity of the coronal holes in different groups. The horizontal lines correspond to the average value of the Kp index for each group of coronal holes

4. Conclusion

We found that the most geo-effective is the trans-equatorial group, in which almost all coronal wholes are of negative polarity. Our analysis show that less (yet sufficiently) effective are the holes of negative polarity in the northern hemisphere and those of positive polarity in the southern hemisphere. There are very small number of coronal holes of opposite polarity (southern negative, and northern positive); their effectivity is smallest. One has to remember, however, that our study concerns a single solar cycle. We suppose that with the change of sign of the common solar magnetic field opposite results will be obtained.

It is demonstrated, also, that there is no significant difference between the groups considered, with respect to the magnitude of the Forbush-effect. Actually, the intensity of a geomagnetic storm is influenced by the sign of the B_z component of the magnetic field; on the other hand, for the Forbush effect the global interplanetary characteristics, such as the solar

wind velocity, the magnitude of the common magnetic field, and dimensions of the disturbance, etc., are important.

The results obtained can not be considered as absolutely correct, since the statistics is rather limited; its further enhancement is needed. Especially, this is related to untypical coronal holes (negative in the southern solar hemisphere, or positive in northern hemisphere). Our goal is to enlarge the statistics and to improve the results in our future works.

References

1. L a n g, K. R. The Cambridge Encyclopedia of the Sun, Cambridge University Press, Cambridge, UK, 2001, 246 p.
2. L a n g, K. R. Sun, Earth and Sky. Springer-Verlag, Berlin Heidelberg, Germany, 1995.
3. C r o o k e r, N. U. Solar and heliospheric geoeffective disturbances. J. Atmos. Solar-Terr. Phys. 62, 1071–1085, 2000.
4. R o b b i n s, S. J., C. J. Henney, J. W. Harvey. Solar Wind Forecasting with Coronal Holes, Solar Phys., 233, No. 2. doi: 10.1007/s11207-006-0064-y. 2006.
5. S a n d e r s o n, T. R., T. A p p o u r c h a u x, J. T. H o e k s e m a, K. L. H a r v e y. Observations of the Sun's magnetic field during the recent solar maximum. J. Geophys. Res. 108, NO. A1, 1035, doi:10.1029/2002JA009388, 2003.
6. B e l o v, A. V. Forbush effects and their connection with solar, interplanetary and geomagnetic phenomena. Proc. 257-th of the International Astronomical Union. Ed. N. Gopalswamy and D. F. Webb. Ioannina, Greece. Volume 257, 439-450, 2009.
7. http://www.solen.info/solar/coronal_holes.html
8. http://www.solen.info/solar/old_reports/

ГЕОЭФФЕКТИВНОСТЬ СОЛНЕЧНЫХ КОРОНАЛЬНЫХ ДЫР С РАЗЛИЧНОЙ ПОЛЯРНОСТЬЮ МАГНИТНОГО ПОЛЯ

*М. Абунина, А. Абунин, А. Белов, С. Гайдаш, Й. Тасев,
П. Велинов, Л. Матеев, П. Тонев*

Аннотация

Корональные дыры являются источником высокоскоростных потоков солнечного ветра, которые в свою очередь являются одной из главных причин геомагнитных возмущений. Корональные дыры весьма разнообразны и их геоэффективность меняется в широких

пределах. В данной работе мы попытались исследовать, как влияют на геомагнитную обстановку корональные дыры с различным положением на Солнце и с различной полярностью магнитного поля. Мы рассмотрели несколько десятков корональных дыр, наблюдавшихся в последние годы, и разделили их на группы по гелиошироте и полярности. Наиболее эффективной оказалась трасэкваториальная группа, почти все корональные дыры из этой группы имели отрицательную полярность. Менее, но тоже достаточно эффективными оказались дыры с отрицательной полярностью на севере и с положительной – на юге. Немногочисленные корональные дыры с противоположными полярностями (отрицательные на юге и положительные на севере) были менее эффективными.

SPACE RADIATION PECULIARITIES IN THE EXTRA VEHICULAR ENVIRONMENT OF THE INTERNATIONAL SPACE STATION (ISS)

***Tsvetan Dachev, Nikolay Bankov, Borislav Tomov,
Yury Matviichuk, Plamen Dimitrov***

*Space Research and Technology Institute – Bulgarian Academy of Sciences
e-mail: tdachev@bas.bg*

Abstract

The space weather and the connected with it ionizing radiation were recognized as a one of the main health concern to the International Space Station (ISS) crew. Estimation the effects of radiation on humans in ISS requires at first order accurate knowledge of the accumulated by them absorbed dose rates, which depend of the global space radiation distribution and the local variations generated by the 3D surrounding shielding distribution. The R3DE (Radiation Risks Radiometer-Dosimeter (R3D) for the EXPOSE-E platform on the European Technological Exposure Facility (EuTEF) worked successfully outside of the European Columbus module between February 2008 and September 2009. Very similar instrument named R3DR for the EXPOSE-R platform worked outside Russian Zvezda module of ISS between March 2009 and August 2010. Both are Liulin type, Bulgarian build miniature spectrometers-dosimeters. They accumulated about 5 million measurements of the flux and absorbed dose rate with 10 seconds resolution behind less than 0.41 g cm^{-2} shielding, which is very similar to the Russian and American space suits [1-3] average shielding. That is why all obtained data can be interpreted as possible doses during Extra Vehicular Activities (EVA) of the cosmonauts and astronauts. The paper first analyses the obtained long-term results in the different radiation environments of: Galactic Cosmic Rays (GCR), inner radiation belt trapped protons in the region of the South Atlantic Anomaly (SAA) and outer radiation belt (ORB) relativistic electrons. The large data base was used for development of an empirical model for calculation of the absorbed dose rates in the extra vehicular environment of ISS at 359 km altitude. The model approximate the averaged in a grid empirical dose rate values to predict the values at required from the user geographical point, station orbit or area in geographic coordinate system. Further in the paper it is presented an intercomparison between predicted by the model dose rate values and data collected by the R3DE/R instruments and NASA Tissue Equivalent Proportional Counter (TEPC) during real cosmonauts and astronauts EVA in

the 2008-2010 time interval including large relativistic electrons doses during the magnetosphere enhancement in April 2010. The model was also used to be predicted the accumulated along the orbit of ISS galactic cosmic rays and inner radiation belt dose for 1 orbit (1.5 hours) and 4 consequent orbits (6 hours), which is the usual EVA continuation in dependence by the longitude of the ascending node of ISS. These predictions of the model could be used by space agencies medical and other not specialized in the radiobiology support staff for first approach in the ISS EVA time and space planning.

1. Introduction

The radiation field around the ISS is complex, composed by galactic cosmic rays (GCR), trapped radiation of the Earth radiation belts, solar energetic particles, albedo particles from Earth's atmosphere and secondary radiation produced in the shielding materials of the spacecraft and in biological objects.

1.1. Galactic cosmic rays

The dominant radiation component in near Earth space environment are the galactic cosmic rays (GCR) modulated by the solar activity. The GCR are charged particles that originate from sources beyond our solar system. They are thought to be accelerated at the highly energetic sources like neutron star, black holes and supernovae within our Galaxy. GCR are the most penetrating of the major types of ionizing radiation. The distribution of GCR is believed to be isotropic throughout interstellar space. The energies of GCR particles range from several tens up to 10^{12} MeV nucleon⁻¹. The GCR spectrum consists of 98% protons and heavier ions (baryon component) and 2% electrons and positrons (lepton component). The baryon component is composed of 87% protons, 12% helium ions (alpha particles) and 1% heavy ions [4]. Highly energetic particles in the heavy ion component, typically referred to as high Z and energy (HZE) particles, play a particularly important role in space dosimetry (Benton and Benton, 2001). HZE particles, especially iron, possess high-LET and are highly penetrating, giving them a large potential for radiobiological damage [5]. Up to 1 GeV, the flux and spectra of GCR particles are strongly influenced by the solar activity and hence shows modulation which is anti-correlated with solar activity.

1.2. Trapped radiation belts

Radiation belts are the regions of high concentration of the energetic electrons and protons trapped within the Earth's magnetosphere. There are

two distinct belts of toroidal shape surrounding Earth where the high energy charged particles get trapped in the Earth's magnetic field. Energetic ions and electrons within the Earth's radiation belts pose a hazard to both astronauts and spacecraft. The inner radiation belt, located between about 0.1 to 2 Earth radii, consists of both electrons with energies up to 10 MeV and protons with energies up to ~ 100 MeV. The outer radiation belt (ORB) starts from about 4 Earth radii and extends to about 9-10 Earth radii in the anti-sun direction. The outer belt mostly consists of electrons whose energy is not larger than 10 MeV. The electron flux may cause problems for components located outside a spacecraft (e.g. solar cell degradation). They do not have enough energy to penetrate a heavily shielded spacecraft such as the ISS wall, but may deliver large additional doses to astronauts during extra vehicular activity [6-8]. The main absorbed dose inside the ISS is contributed by the protons of the inner radiation belt. The South-Atlantic Anomaly (SAA) is an area where the radiation belt comes closer to the Earth surface owing to a displacement of the magnetic dipole axes from the Earth's center. The daily average SAA doses reported by Reitz et al. (2005) [9] inside of the ISS vary in the range $74\text{-}215 \mu\text{Gy d}^{-1}$ for the absorbed dose rates and in the range $130\text{-}258 \mu\text{Sv d}^{-1}$ for the averaged equivalent daily dose rates.

1.3. Solar Energetic Particles (SEP)

The SEP are mainly produced by solar flares, sudden sporadic eruptions of the chromosphere of the Sun. High fluxes of charged particles (mostly protons, some electrons and helium and heavier ions) with energies up to several GeV are emitted by processes of acceleration outside the Sun. The time profile of a typical SEP starts off with a rapid exponential increase in flux, reaching a peak in minutes to hours. The energy emitted lies between 15 and $500 \text{ MeV nucleon}^{-1}$ and the intensity can reach $10^4 \text{ cm}^{-2} \text{ s}^{-1} \text{ sr}^{-1}$. Electrons with energies of ~ 0.5 to 1 MeV arrive at Moon, usually traveling along interplanetary field lines, within tens of minutes to tens of hours. Protons with energies of 20 to 80 MeV arrive within a few to ~ 10 hours, although some high energy protons can arrive in as little as 20 minutes. SEP are relatively rare and occur most often during the solar maximum phase of the 11-year solar cycle. In the years of maximum solar activity up to 10 flares can occur, during the years of minimum solar activity only one event can be observed on average

The radiation field at a location, either outside or inside the spacecraft is affected both by the shielding and surrounding materials [10-12]. Dose characteristics in LEO depend also on many other parameters such as the solar cycle phase, spacecraft orbit parameters, helio and geophysical parameters.

Recently the radiation environment inside and outside of ISS has been studied with various arrangements of radiation detectors. The paper first analyses the obtained long-term results in the different radiation environments of: Galactic Cosmic Rays (GCR), inner radiation belt trapped protons in the region of the South Atlantic Anomaly (SAA) and outer radiation belt (ORB) relativistic electrons. The dose rates and fluxes was measured in 2008-2009 by the R3DE active dosimeter, mounted in EXPOSE-E facility outside the Columbus module of ISS and by the R3DR active dosimeter in EXPOSE-R facility outside the Russian Zvezda module of the ISS.

2. Instrumentation



Fig. 1. External view of R3DE instrument. R3DR instrument is with very similar external view

The (Radiation Risks Radiometer-Dosimeter (R3D) R3DE and R3DR instruments (Figure 1) are successors of the Liulin-E094 instrument, which was part of the experiment Dosimetric Mapping-E094 headed by Dr. G. Reitz that was placed in the US Laboratory Module of the ISS as a part of Human Research Facility of Expedition Two Mission 5A.1 in May-August, 2001 [9, 13-17].

The experiments with the R3DE/R spectrometers were performed after successful participations to ESA Announcements of Opportunities, led by German colleagues Gerda Horneck [18] and Donat-P. Häder. The spectrometers were mutually developed with the colleagues from the University in Erlangen, Germany [32, 33]. The R3DE instrument for the EXPOSE-E facility on the European Technological Exposure Facility (EuTEF) worked outside of the European Columbus module of the ISS between 20th of February 2008 and 1st of September 2009 with 10 seconds resolution behind less than 0.4 g.cm⁻² shielding.

The R3DR spectrometer was launched inside of the EXPOSE-R

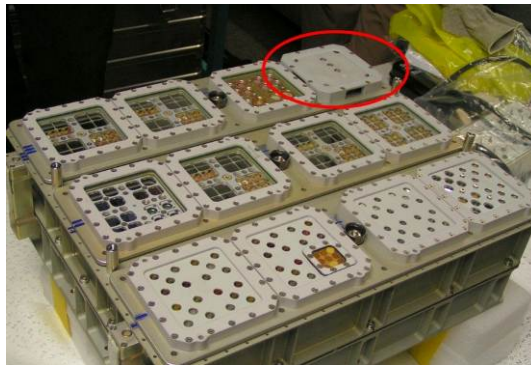


Fig. 2. External view of the EXPOSE-R facility. The R3DR instrument was situated inside of the red oval. EXPOSE-E facility was with very similar external view

facility (Figure 2) to the ISS in December 2008 and was mounted at the outside platform of Russian Zvezda module of the ISS. The first data were received on March 11, 2009. Until 27th of January 2011 the instrument worked almost permanently with 10 seconds resolution.

The exact mounting locations of the both instruments are seen in Figure 3. The Figure is discussed comprehensively in the data analysis part of the paper.

R3DE/R instruments was a low mass, small dimensions automatic devices that measures solar radiation in 4 channels and ionizing radiation in 256 channels. The 4 solar UV and visible radiations photodiodes are seen in the center of the Figure 1, while the silicon detector is behind the aluminum box of the instrument; that is why is not seen in the picture. It is situated above the 4 photodiodes. They are Liulin type energy deposition

spectrometers [13] (Dachev et al., 2002). The four optical channels use 4 photodiodes with enhanced sensitivity in the following ultraviolet (UV) and visible ranges: UV-A (315-400 nm), UV-B (280-315 nm), UV-C (<280 nm) and Photosynthetic Active Radiation (PAR) (400-700 nm). They are constructed as filter dosimeters and measure the solar UV irradiance in W/m^2 . Additional measurements of the temperature of UV photodiodes are performed for more precise UV irradiance assessments. The size of the aluminum box of the R3DR instrument is 76 x 76 x 34 mm.

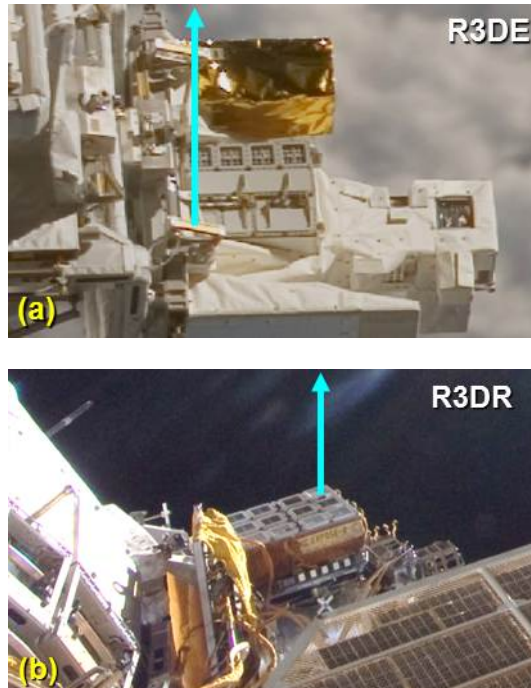


Fig. 3. Real photographs of the mounting positions of the EXPOSE-E/R facilities. The bases of the arrows show the exact places of R3DE/R instruments

The block diagram of the instruments is shown in Figure 4. Two microprocessors control the ionizing and the solar radiation circuitry, respectively, and the data are transmitted by standard serial interface of RS422 type through the EXPOSE-E/R facilities to the telemetry of Columbus module or Russian segment of the ISS. The photodiodes and the silicon detector are placed close to the preamplifiers to keep the noise level low. The signals from the solar radiation channels and the temperature

sensor are digitized by a 12 bit A/D converter. The analysis of these data is performed by the University of Erlangen, Germany (<http://www.zellbio.nat.unierlangen.de/forschung/lebert/index.shtml>).

The ionizing radiation is monitored using a semiconductor PIN diode detector (2 cm² area and 0.3 mm thick). Its signal is digitized by a 12 bit fast A/D converter after passing a charge-sensitive preamplifier. The deposited energies (doses) are determined by a pulse height analysis

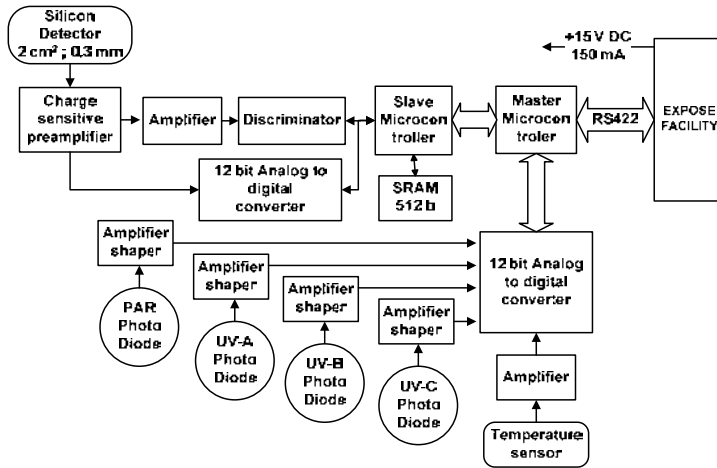


Fig. 4. Block diagram of the R3DE/R instruments

technique and then passed to a discriminator. The amplitudes of the pulses $A[V]$ are transformed into digital signals, which are sorted into 256 channels by a multi-channel analyzer. At every exposure time interval one energy deposition spectrum is collected. The energy channel number 256 accumulates all pulses with amplitudes higher than the maximal level of the spectrometer of 20.83 MeV. The methods for characterization of the type of incoming space radiation are described in (Dachev, 2009).

The “System international (SI)” determination of the dose is used, in order to calculate the doses absorbed in the silicon detector. SI determines that the dose is the energy in Joules deposited in one kilogram. The following equation is used:

$$(1) \quad D[Gy] = K \sum_{i=1}^{256} (EL_i i)[J] / MD[kg]$$

where K is a coefficient, MD - the mass of the solid state detector in [kg] and EL_i is the energy loss in Joules in channel i . The energy in MeV is proportional to the amplitude A of the pulse and the coefficient depends on the used preamplifier and sensitivity.

$$EL_i [MeV] = A[V] / 0.24[V / MeV] \cdot 0.24[V / MeV]$$

The construction of the R3DE/R boxes consists of 1.0 mm thick aluminum shielding in front of the detector. The total shielding of the detector is formed by additional internal constructive shielding of 0.1 mm copper and 0.2 mm plastic material. The total external and internal shielding before the detector of R3DR device is 0.41 g cm^{-2} . The calculated stopping energy of normally incident particles to the detector is 0.78 MeV for electrons and 15.8 MeV for protons [19]. This means that only protons and electrons with energies higher than the above mentioned could reach the detector.

3. Data analysis

3.1. Global distribution

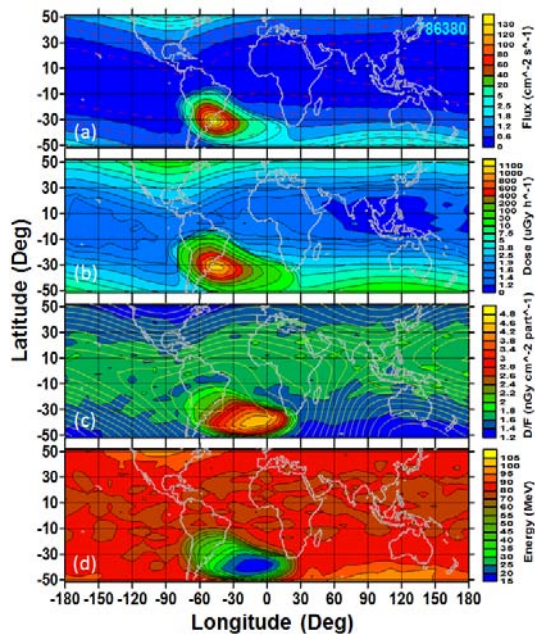


Fig. 5. Global distribution of the R3DE dose rate, flux, D/F ratio and incident energy data in the period 21 October 2008-24 February 2009

Figure 5 presents the global view on the R3DE dose rate, flux and energy data for the time period between 21/10/2008 and 24/02/2009. The ISS altitude for this period varies between 364 and 375 km. The first 2 panels contain 786380 measurements of the flux in the upper panel and of the absorbed dose rate in the panel below. On the Figure 5a except the global map of the flux the isolines of the L value [20, 21] at the altitude of the ISS are also presented with red dashed lines. It is seen that the lines of equal flux in the north and south high latitude regions follow very well the L-shell isolines as expected. The place and area of the South Atlantic Magnetic Anomaly (SAA) is well seen by the last close isoline of 0.26 Gauss on Figure 5c. Because of relative low magnetic field strength in the SAA the protons in the inner radiation belt penetrated deeper in the upper atmosphere and reach the altitude of the station forming large maximums of the flux and dose respectively. Both the flux and dose rate maximums was displaced from the magnetic field minimum in South-East direction, while the dose rate maximum goes even further to the same direction.

On the Figure 5c the global distribution of the dose to flux ratio (D/F) in $\text{nGy cm}^{-2} \text{ particle}^{-1}$ is presented. 247277 measurement points was used. D/F ratios larger than $1 \text{ nGy cm}^{-2} \text{ particle}^{-1}$ was selected and plotted. It is seen that the ratio form a maximum with D/F value greater than $4 \text{ nGy cm}^{-2} \text{ particle}^{-1}$ in the South-East edge of the anomaly. The global distribution of the calculated from the D/F ratio incident energy of the arriving to the detector inner radiation belt protons [22, 30] (Heffner, 1971; Dachev, 2009) was presented at the Figure 4d and as expected form a minimum at the places of the dose to flux ratio maximum in the Figure 4c. The center of the 15-20 MeV protons maximum is with coordinates 15°W , 38°S . This result is controversial than the AP-8 MIN [23, 24] predictions, which show the place of the maximum almost at same latitude but at about 38° west longitude.

The GCR dose and flux global distribution is presented in the Figures 5a and 5b with all areas outside the SAA region. It forms wide minimum close to the geomagnetic equator and rise toward the magnetic poles in both hemispheres (For more information please look Fig.6). For the regions outside the SAA the calculated values for the dose to flux ratio and for the incident energies presented in the Figures 5c and 5d are not valid because of the small statistics in the spectra.

3.2. R3DE/R data comparison

Figure 6 presents in 2 panels the dose rate (black (dark blue) points) and flux data (gray (sky blue) points) obtained in the 10-20 April 2009 time

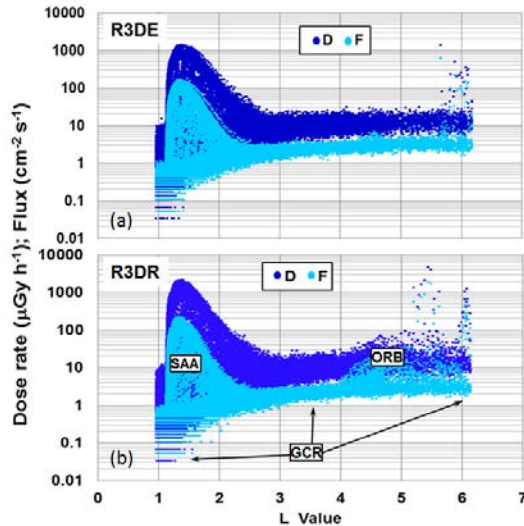


Fig. 6. Comparison of the dose rate and flux data measured with 10 s resolution by the R3DE/R instruments in the period 10-20 April 2009

interval as measured with 10 s resolution by the R3DE/R instruments. The bottom panel (Figure 6b) contains data from the R3DR instrument, while the top panel (Figure 6a) contain data from the R3DE instrument.

Three different radiation sources are easily distinguished visually from the data presented in both panels. The major amount of measurements with more than 7000 points per day is concentrated in the zone of GCR, which is seen as area with many points in the lower part of the panels in L-values range between 0.9 and 6.2. The covered dose rate range is between 0.03 and 15-20 $\mu\text{Gy h}^{-1}$. The lowest rates are close to the magnetic equator ($L < 1.5$), while the highest are at high latitudes ($L > 4$) equatorwards from both magnetic poles.

The maximum of the inner radiation belt protons observed in the region of the SAA is seen in the left side of the panels with dose rates between 10 and 1250 $\mu\text{Gy h}^{-1}$ from R3DR instrument (Figure 6b), while the

maximum from R3DE instrument is smaller and reach $1100 \mu\text{Gy h}^{-1}$ (Figure 6a).

The reason of R3DR SAA dose rates being higher than the R3DE dose rates is seen in Figure 3. The 2 photographs on Figure 3 presented the surrounding of the R3DE and R3DR instruments on ISS. As mentioned before, R3DE was located at the top of the EuTEF platform outside the European Columbus module.

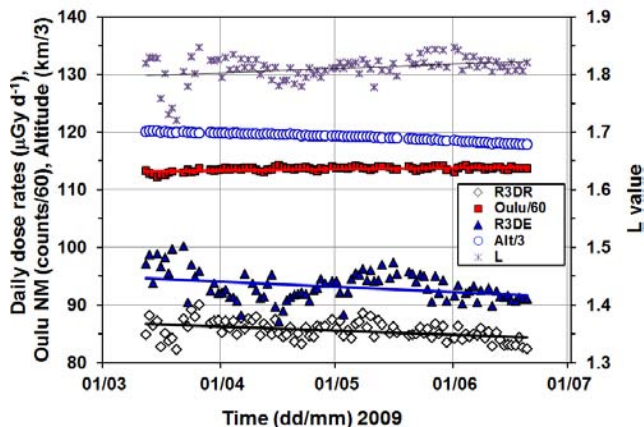


Fig. 7. Comparison of the daily GCR dose rates measured simultaneously by the R3DE/R instruments in 2009

In Figure 3a, the lower end of the heavy arrows pointing “up” (along the Earth radius) in the R3DE photograph shows the exact place of the instrument. It is seen that it was surrounded by different constructive elements of the EuTEF platform and Columbus module, which produced additional shielding of the instrument against the SAA flux of 30-100 MeV protons. The R3DR position presented in Figure 3b shows that this instrument was far from the Zvezda module at the end of the EXPOSE-R facility and was practically shielded only from below.

The wide maximum observed on Figure 6b for L-values between 3.5 and 6.2 was connected with the registration of rare sporadic relativistic electrons precipitations (REP) generated in the outer radiation belt [25, 6-8]. Here the R3DR maximum of dose rate reached value of about $5000 \mu\text{Gy h}^{-1}$. This large dose is deposited by electrons with energies above 0.78 MeV. The R3DE ORB maximum was also lower and “thinner” than the R3DR maximum. The reason was same as the described above for the SAA maximum.

Figure 7 presents the result of comparison of the daily CGR dose rates for the period between 12 March and 20 June 2009 as measured by the R3DE/R instruments. The daily GCR dose rate was obtained by averaging of 5000-8200 measurements per day (7024 in average) with 10 s resolution at all latitudes in the altitudinal range 353-361 km above the Earth. Both data sets are situated in the bottom of the Figure and follow slowly decreasing with time trend, which can be associated with the decreasing altitude of the ISS from 360 down to 353 km. This trend is in opposite direction than the expected increase of the GCR dose rates with the increase of the Oulu Neutron monitor (NM) count rate shown with quadrats above the two dose rates curves. The Oulu NM count rate increase because of the decrease of solar activity in the end of the 23rd solar cycle. The decreasing solar activity leads to decrease of the amount and speed of solar wind and respectively decrease of the embedded magnetic field strength, which couldn't deflect effectively the GCR entering in the solar system.

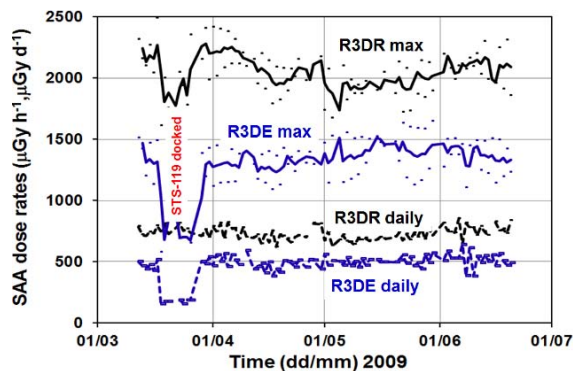


Fig. 8. Comparison of the daily SAA dose rates measured simultaneously by the R3DE/R instruments in 2009

The shapes of the dose rate curves are also strongly affected by the L value of the place where the averaged values was obtained. This is well seen when a comparison is made between the mean L curve in the top of the Figure 7 with the two daily dose rate curves in the bottom. L values are presented according to the right scale of the Figure. As expected there is almost positive correlation between them.

The difference between R3DE and R3DR dose rate data is about 10 $\mu\text{Gy d}^{-1}$ during the whole period of about 3 months. Relatively small part of this difference is produced by the additional dose rate produced by secondary particles in the heavily shielded R3DE instrument but another

mechanism have to be found to be described the difference. This will be subject of another more precise investigation with use of theoretical models.

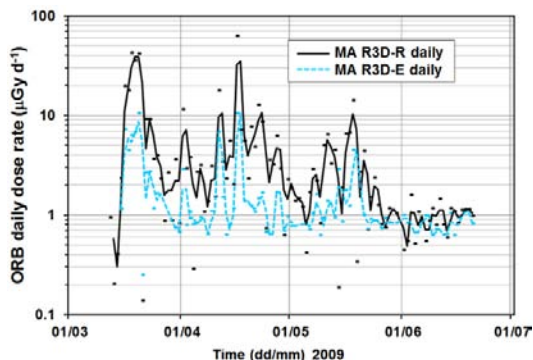


Fig. 9. Comparison of the daily ORB dose rates measured simultaneously by the R3DE/R instruments in 2009

In the bottom part of Figure 8 are shown the average daily dose rates obtained in the region of the SAA as measured by the R3DE/R instruments. The daily SAA dose rate was obtained by averaging of 400-500 measurements per day with 10 s resolution at all latitudes in the altitudinal range 357-361 km above the earth. In the top part of the figure the maximal observed per each day dose rates in $\mu\text{Gy h}^{-1}$ are presented. It is well seen that both curves of hourly and daily dose rates obtained by R3DR instrument are higher than the R3DE dose rates for the whole time interval between 12 March and 20 June 2009. The reason was already discussed in the presentation of Figure 6.

The strong depletion in the maximum dose rates in the left side of the Fig. 8 was generated by the additional shielding, which USA Space Shuttle 78 tons body on his mission STS-119 provided to both instruments when it was docked with the ISS (Dachev et al., 2011a).

Figure 9 shows moving averaged dose rates inside the ORB as measured by the R3DE/R instruments. The daily, average ORB dose rate over the whole period from R3DR is $4.9 \mu\text{Gy d}^{-1}$, while the daily, average ORB dose rate over the whole period from R3DE is about 3 times smaller - $1.7 \mu\text{Gy d}^{-1}$. The reason for the smaller dose rates measured by R3DE instrument is same as already described for the SAA dose rates.

Table 1. Comparison of the hourly and daily dose rates measured simultaneously by the R3DE/R instruments in 2009

SAA parameter	Average R3DR	Average R3DE	Comments
Hourly averaged absorbed dose rate (>500 meas. per day) ($\mu\text{Gy h}^{-1}$)	352	296	R3DR > R3DE
Daily averaged absorbed dose rate (in Si) ($\mu\text{Gy d}^{-1}$)	537	426	R3DR > R3DE
GCR parameter	Average R3DR	Average R3DE	Comments
Hourly averaged absorbed dose rate (>6000 meas. per day) ($\mu\text{Gy h}^{-1}$)	3.39	3.79	R3DE > R3DR
Daily averaged absorbed dose rate (in Si) ($\mu\text{Gy d}^{-1}$)	81.40	91.10	R3DE > R3DR
ORB parameter	Average R3DR	Average R3DE	Comments
Hourly averaged absorbed dose rate (no limit) ($\mu\text{Gy h}^{-1}$)	98.0	42.0	R3DR > R3DE
Daily averaged absorbed dose rate (in Si) ($\mu\text{Gy d}^{-1}$)	76.0	8.6	R3DR > R3DE

Table 1 summarizes the results of the observations made simultaneously by the R3DE/R instruments on ISS in 2009. The table practically presented by numbers the observations presented on Figures 6-10.

3.3. Empirical model for calculation of the absorbed dose rates in the extra vehicular environment of ISS at 359 km altitude

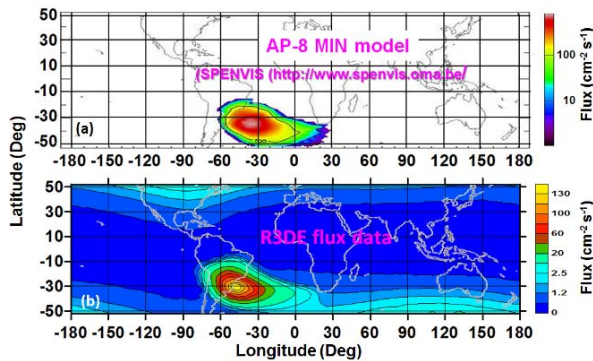


Fig. 10. Comparison of the global distribution of the R3DE flux data in the period 21 October 2008-24 February 2009 with the AP-8 MIN model

Figure 10 presents comparison of the global distribution of the R3DE flux data in the period 21 October 2008-24 February 2009 with the AP-8 MIN model. Figure 10b presented same data as shown in the Figure 5a. Figure 10a was created using the available in SPENVIS

(<http://www.spervis.oma.be/>) AP-8 MIN model [23] (Vette, 1991). The model is calculated for the epoch of 1970, for the minimum of the solar activity at altitude of 359 km and for protons with energy larger than 15.8 MeV. It is seen that the external oval of the data and the model are similar but the coordinates of the R3DE SAA was at -50° west longitude - 30° south latitude. These values are in comparison with AP-8 MIN moved with -12° (0.3° per year) to the west and with 2° (0.05° per year) to the north and coincided relatively well with the values obtained by [16] Wilson et al., (2007). Another big difference between the model and the experimental data is seen for the value of the flux central location. The predicted by the model values were much higher than the observed. This can be explained by the fact that the R3DE SAA flux data are obtained in the end of the 2008 and beginning of 2009, which was in the period of extremely low solar activity not observed before and respectively not included in the AP-8 MIN model.

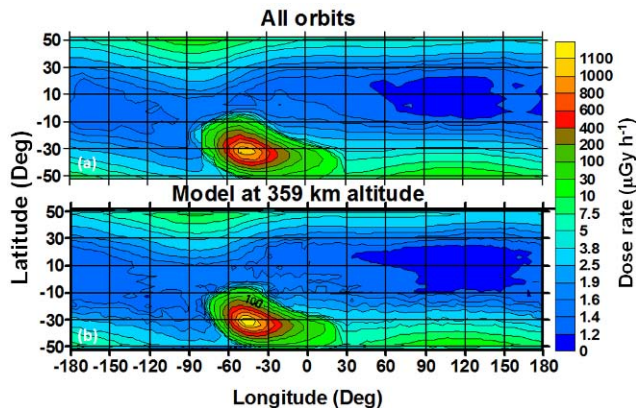


Fig. 11. Comparison of the global distribution of the R3DE dose rate data in the period 21 October 2008-24 February 2009 with the predicted by the empirical model data

The large data base obtained by the R3DE instrument was used for development of an empirical model for calculation of the absorbed dose rates from GCR and inner radiation belt protons in the extra vehicular environment of ISS at 359 km altitude. The model approximate the averaged in a grid empirical dose rate values to predict the values at required from the user geographical point, station orbit or area in geographic coordinate system [27]. The model is valid for the location of R3DE instrument outside the ISS at the EXPOSE-E platform behind 0.41 g cm^{-2} shielding. These predictions of the model could be used by space agencies

medical and other not specialized in the radiobiology support staff only for first rough approach in the ISS EVA time and space planning.

Figure 11 contains 2 panels. In the upper panel (Figure 11a) the global distribution of the R3DE averaged dose rates (in $\mu\text{Gy h}^{-1}$) data obtained in the period 21 October 2008-24 February 2009 was presented, while the lower panel (Figure 11b) presented the result of the calculated by the model global distribution of the dose rates. It is seen that both pictures are very similar and this verify that the model predicted well the dose rates in the areas of predominated inner belt energetic proton of the SAA region and areas of predominated GCR outside SAA in equatorial, middle and high latitudes.

The empirical model is available online from the following 2 links: http://www.stil.bas.bg/dwp/R3DE_POINT_model.zip and http://www.stil.bas.bg/dwp/R3DE_ORBIT_model.zip. Both links allowed

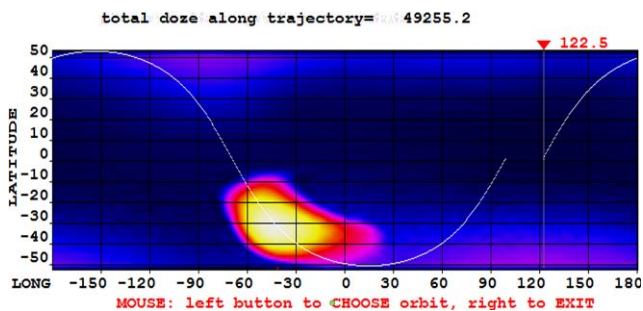


Fig. 12. Example of the graphical output from the “ORBIT” model for an orbit with ascending node equal to 122.5°

the possible user of the model to obtain for each model a compressed (ZIP) application (exe file), which directly in the computer of the user perform the calculation and present the result. The first link is for the so named “POINT” model, which calculated and presented the dose rate result (in $\mu\text{Gy h}^{-1}$) for a point with geographic coordinates inside of the set of coordinates with following limits: $-52^\circ < \text{Latitude} < 52^\circ$, $-180^\circ < \text{Longitude} < 180^\circ$. To calculate the dose it is necessary the obtained value to divide by 360.

The second link is for the so named “ORBIT” model, which calculated and presented the summarized dose rate results (in $\mu\text{Gy h}^{-1}$) along an orbit of the ISS, which ascending node is in the limit of -

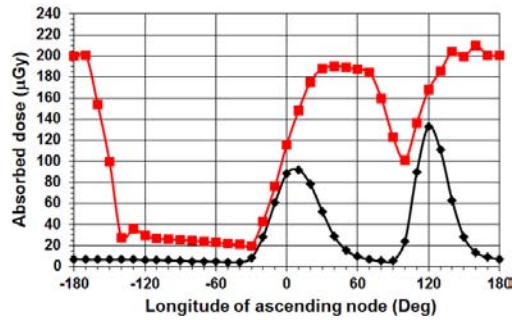


Fig. 13. Predicted by the model accumulated along the orbit absorbed dose for 1 orbit (~1.5 hours) (curve with diamonds) and 4 consecutive orbits (~6 hours) (curve with squares)

$180^{\circ} < \text{Longitude} < 180^{\circ}$. The step along the orbit is equal to 10 sec and is same as the R3DE time interval for 1 measurement.

Figure 12 presented one example of the graphical output from the “ORBIT” model for an ISS orbit with ascending node equal to 122.5° . The ascending node can be choosing by the user with movement of one arrow in the program and with pushing of the left mouse button. In the upper part after the label “total dose along trajectory” the calculated summarized dose rate is shown. To calculate the dose it is necessary the obtained value to divide by 360. Except the graphical output the model created automatically (in the directory where the model is) a text file with the following name “ORB_DOZ.TXT”. The file contains 4 columns: Lat. (deg), Long. (deg), Dose rate ($\mu\text{Gy h}^{-1}$) and the Accumulated till the moment dose rate ($\mu\text{Gy h}^{-1}$). If you use the model please reference Bankov et al. 2010, available online at <http://www.stil.bas.bg/FSR2009/pap144.pdf>

Figure 13 presents the predicted by the model accumulated along the orbit absorbed dose for 1 orbit (~1.5 hours) (curve with diamonds) and 4 consequent orbits (~6 hours) (curve with squares). The model was run with a longitudinal step of 10° for both cases. It is seen that for 1 orbit case the most dangerous ascending node is this crossing the equator at 120° East longitude when a total accumulated dose along the orbit of $139 \mu\text{Gy}$ is predicted. The 4 orbit case was chosen because usual EVA duration is about 6 hours, i.e. 4 orbits. The most dangerous ascending node for this case is this crossing the equator in the interval 140° East longitude to 170° West longitude when a total accumulated doses of about $200 \mu\text{Gy}$ are predicted.

3.4. Analysis of data collected by different instruments during real cosmonauts and astronauts EVA in the 2009-2010

3.4.1. Analysis of the dose rates and doses obtained during EVA2 of Expedition 18 on March 10, 2009. Example with predominant SAA crossings

Figure 14 purposes was: first to show the dose rate dynamics observed by R3DE and NASA TEPC

http://www.nasa.gov/mission_pages/station/research/experiments/TEPC.html

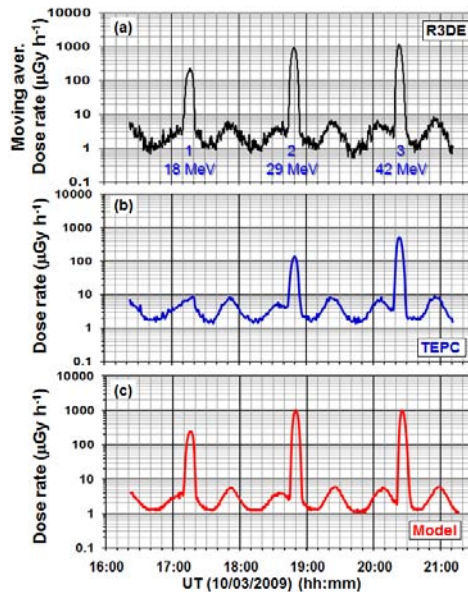


Fig. 14. The dose rate dynamics observed by R3DE and NASA TEPC during the EVA 2 of Expedition 18 on March 10, 2009 between 16:22 and 21:11 for 4 h and 49 m. Measured data was compared with the model predictions

during the EVA 2 of Expedition 18 on March 10, 2009 between 16:22 and 21:11 for 4 h and 49 m and second to compare the measured with R3DE instrument dose rates with the predicted by the model values.

Figure 15 supported the observations made on Figure 14 with actual information of the ground tracks of the ISS orbit during the EVA over the global maps of the R3DE measured dose rate and energy presented previously on Figure 5. The orbit numbers (1, 2 and 3) shown in Figure 14a correspond to the numbers on Figure 15a. Also the measured values of the

proton energy are shown, which according to Figure 15b increased from orbit number 1 to orbit number 3.

On Figure 14a the moving average (with period of 6 points (1 minute

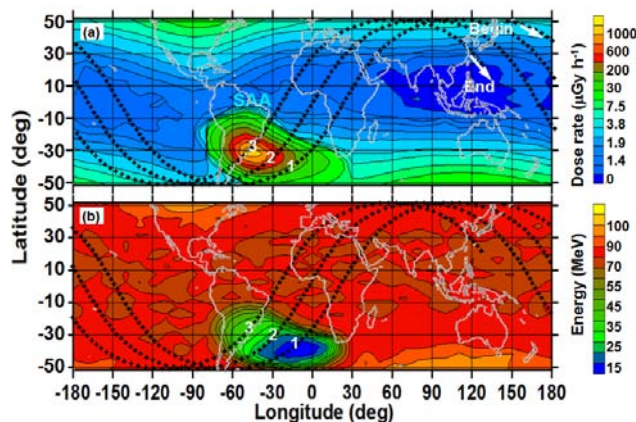


Fig. 15. Global maps of the R3DE measured dose rate and energy with the ground tracks of the ISS during the EVA shown on Figure 14. The numbers (1,2 and 3) in the region of the SAA corresponded to the number of SAA crossings seen on Figure 14

resolution)) of the dose rate measured by R3DE outside ISS behind less than 0.41 g cm^{-2} is presented. The labels on Figure 14a present the measured at the detector of the R3DE proton energy at the positions of the maximums, while Figure 15b presented the global map and it is identical to the Figure 5d. Very similar data with 1 minute resolution were plotted on Figure 14b, but from NASA TEPC situated inside ISS at physical location “SM-327”. Data were taken by [http://cdaweb.gsfc.nasa.gov/ server](http://cdaweb.gsfc.nasa.gov/server) [28]. Unfortunately we haven’t found what is the exact shielding of the TEPC at that location, but we consider that the shielding is much higher than the R3DE shielding. On Figure 14c were presented the calculated by the empirical model dose rates along the orbits of ISS. It is necessary to be mentioned that the 3 curves on Figure 14 coincided relatively very well by values and shape.

The 3 main maximums seen on figures 14a and 14b were created during the ISS crossings of the inner radiation belt high energy proton zone in the region of the SAA. R3DE dose rates maximums reached about $1000 \text{ } \mu\text{Gy h}^{-1}$ for orbits 2 and 3 and only $250 \text{ } \mu\text{Gy h}^{-1}$ for orbit number 1. The TEPC SAA maximums for orbits 2 and 3 are much smaller, while the SAA maximum for orbit 1 was completely missing. This feature can be explained by the R3DE measured proton energies shown on Figure 14a and on Figure 15b where the proton energy for orbit number 1 at the detector of

the R3DE was the smallest of all 3 and reach only 18 MeV. This proton energy wasn't enough for penetration of the larger shielding at the TEPC location inside ISS and that is why the maximum there is missing.

The maximums, which reached up to $9.5 \mu\text{Gy h}^{-1}$ in R3DE and TEPC data on Figure 14a and 14b are connected with the crossings at high latitude GCR regions in the both hemispheres, while the local minimums with dose rates around $1 \mu\text{Gy h}^{-1}$ and below correspond to the magnetic equator crossings. It is remarkable that the GCR TEPC dose rate data were always higher than the R3DE dose rates. Part of this higher exposition can be attributed to the additional dose rate created by secondary particles generated in the ISS walls. Another part is connected with the fact that TEPC having smaller sensitivity ($1 \mu\text{Gy h}^{-1}$) than R3DE overestimate the dose rates.

Table 2 presents the statistics for the total accumulated doses during the EVA2 of Expedition 18 on March 10, 2009 between 16:22 and 21:11 for 4 h and 49 m. Also the results of the separation of the doses accumulated by two different radiation sources – protons in the inner radiation belt, seen in the region of SAA, and GCR at low and high latitudes outside SAA are shown. The values for the R3DE and model doses were obtained using the

Table 2. Statistics of the measured and predicted doses in different locations during the EVA2 of Expedition 18 on March 10, 2009

Parameter	R3DE	TEPC	Model	Comments
Total accumulated absorbed dose (μGy)/equivalent dose (μSv) during the EVA	191/268	72/154	187	R3DE > TEPC
SAA accumulated absorbed dose (μGy)/equivalent dose (μSv) during the EVA	180/241	56/97	176	R3DE > TEPC
GCR accumulated absorbed dose (μGy)/equivalent dose (μSv) during the EVA	11/27	16/57	11	TEPC > R3DE

same periods along the orbit of ISS as the available information for the “Dominant radiation source at given time” in the <http://cdaweb.gsfc.nasa.gov/> server files. The R3DE ambient dose equivalent rates are calculated using the procedure described in [29].

The analysis of the Table 2 shows: 1) The SAA absorbed and equivalent doses predominate in the total doses for both instruments and the

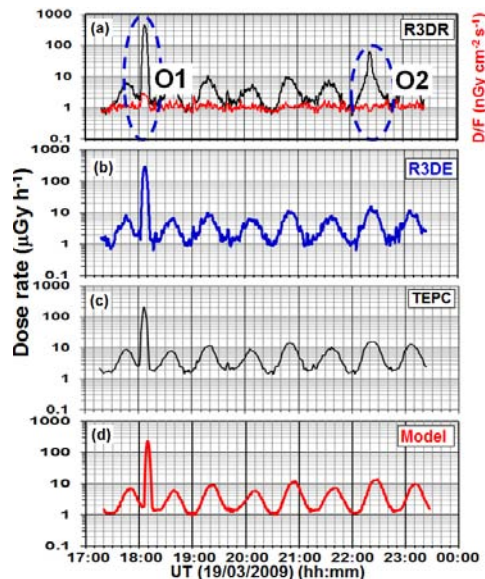


Fig. 16. The dose rate dynamics observed by R3DR, R3DE and NASA TEPC during the EVA 1 of STS-119 on March 19, 2009 between 17:16 and 23:23 for 6 h and 7 m. Measured data was compared with the model predictions

model; 2) The R3DE SAA absorbed doses were about 3 times higher than the TEPC doses because of the much smaller shielding of the R3DE detector; 3) The TEPC GCR absorbed and equivalent doses were higher than the R3DE doses. The possible reasons were discussed earlier; 4) There was a very good coincidence between the measured by the R3DE and predicted by the model doses.

3.4.2. Analysis of the dose rates and doses obtained during EVA 1 of STS-119 on March 19, 2009. Example with mixed SAA and outer radiation belt (ORB) relativistic electron precipitation (REP) crossings

Figures 16 and 17 form another pair of very similar content to the Figures 14 and 15. The 3D background of Figure 17 is identical to Figure 4 of Dachev et al., 2012b and presents the geographical distribution of the data for the period 01 April – 07 May 2010 when intensive REP was observed in the outer radiation belt region. The geographic longitude and latitude are on the X and Y axes, respectively. The white (white blue) curves represent equal McIlwain's L-parameter values [20, 21] (McIlwain, 1961;

Heynderickx et al., 1996) at the altitude of the ISS. The closed line in the eastern Hemisphere represents $L = 1$. Other open lines rise with values 1.5, 2.5, 3.5 and 4.5 from the equator toward the poles. The dose rate is in the 3rd dimension and the values are color coded by the logarithmic scale bar shown at the right side of the graphic. The dose rate values presented are obtained by averaging of the rough data in longitude/latitude squares 1° in size.

The REP regions were parts of the ORB and are seen in both hemispheres as bands of high dose rate values in the range $3.5 < L < 4.5$. The GCR dose rate values are also well seen in Fig. 17 as enhanced bands with values between 0.5 and $10 \mu\text{Gy h}^{-1}$ equatorwards from the REP bands.

The averaged L value distributions of the dose rates of the three major radiation sources are as follows: (1) GCR minimum average dose rate value is about $1 \mu\text{Gy h}^{-1}$ at $L = 1$. It rises up to $10\text{--}11 \mu\text{Gy h}^{-1}$ at $L = 4$ and stays at this value up to $L = 6.14$; (2) SAA dose rates are about $22 \mu\text{Gy h}^{-1}$ at $L = 1.1$. They rise sharply to a value of $600 \mu\text{Gy h}^{-1}$ at $L = 1.4$ and then slowly decrease to a value of $20 \mu\text{Gy h}^{-1}$ at $L = 2.8$; (3) ORB dose rates are at a value of $18 \mu\text{Gy h}^{-1}$ at $L = 3.15$, rise up to a value of $500 \mu\text{Gy h}^{-1}$ at $L = 4$ and then decrease down to a value of $80 \mu\text{Gy h}^{-1}$ at $L = 6.14$.

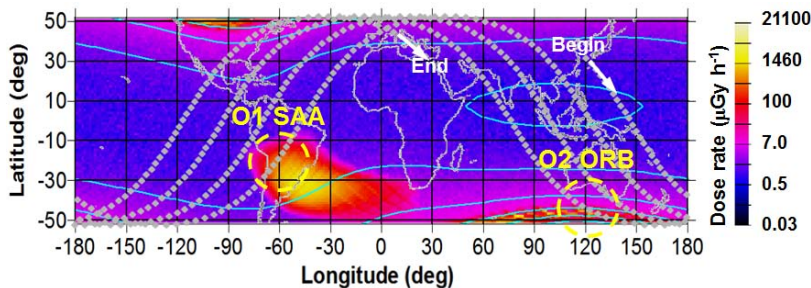


Fig. 17. Global maps of the R3DR measured dose rate with the ground tracks of the ISS during the EVA shown on Figure 16. The labels O1 and O2 corresponded to the number of SAA orbit crossings seen on Figure 16. The white (white blue) curves represent equal L -parameter values. South and north ORB regions are situated at $4.5 < L < 3.5$

Figure 16 is composed with similar dose rate dynamics observations as on Figure 14 but during the EVA 1 of STS-119 on March 19, 2009 between 17:16 and 23:23 for 6 h and 7 m. Here also is added the data obtained by the R3DR instrument. The maximum labeled with O1 is seen by all 3 instruments and by the model because it is formed during the crossings of the SAA South-West regions. Its dose rate is highest ($\sim 400 \mu\text{Gy h}^{-1}$) in

the R3DR data, which was less shielded than R3DR and TEPC instruments. The lowest dose rate is observed by the TEPC being inside ISS. The maximum labeled with O2 was seen only by the less shielded R3DR instrument. The maximum is formed inside of the South Hemisphere ORB region and the predominated radiation source in it was relativistic electrons with energies above 0.78 MeV. To prove this consideration on Figure 16a except the dose rate the dose to flux ratio is plotted. It is seen that the ratio in the O1 maximum is with values 2-3 nGy cm⁻² per particle, which is typical for protons with energies 30-50 MeV [30, 22] (Dachev, 2009; Heffner, 1971). The D/F values in the O2 maximum are less than 1 nGy cm⁻² per particle, which proved that predominant radiation source was from electrons [30, 22].

Table 3. Statistics of the measured and predicted doses in different locations during the EVA 1 of STS-119 on March 19, 2009 between 17:16 and 23:23 for 6 h and 7 m

Parameter	R3DR	R3DE	TEPC	Model
Total accumulated absorbed dose (μGy)/equivalent dose (μSv) during the EVA	57	45	47/142	37
SAA accumulated absorbed dose (μGy)/equivalent dose (μSv) during the EVA	32	23	16/28	14
GCR accumulated absorbed dose (μGy)/equivalent dose (μSv) during the EVA	18.6	22	31/114	23
ORB accumulated absorbed dose (μGy)/equivalent dose (μSv) during the EVA	5.2	0	0/0	0

Table 3 presented the statistics for the total accumulated doses during the EVA 1 of STS-119 on March 19, 2009 between 17:16 and 23:23 for 6 h and 7 m. Also the results of the separation of the doses accumulated by 2 different radiation sources – protons in the inner radiation belt, seen in the region of SAA and GCR at low and high latitudes outside SAA are shown. The values for the R3DE and model doses were obtained using the same periods along the orbit of ISS as the available information for the “Dominant radiation source at given time” in the <http://cdaweb.gsfc.nasa.gov/> server files.

The analysis of the Table 3 shows: 1) The GCR absorbed and equivalent doses predominate in the total doses for TEPC and the model; 2) The R3DR and R3DE SAA absorbed doses were higher than the TEPC

doses because of the much smaller shielding of their detectors; as expected there is a very good coincidence between the measured by the R3DE and the predicted by the model doses. The coincidence between the measured by the R3DR and predicted by the model doses is fair.

3.4.3. Analysis of the dose rates and doses obtained during EVA 1 of STS-131 on April 9, 2010. Example with predominant ORB REP crossings

The Space shuttle Discovery on the mission STS-131 docked with ISS at 07:44 UTC on 7th of April 2010 and undocked at 12:52 UTC on 17th of April 2010

http://www.nasa.gov/mission_pages/shuttle/shuttlemissions/sts131/launch/131_mission_overview.html. During the STS-131 mission on ISS 3 EVA were performed by the NASA astronauts Rick Mastracchio and Clayton Anderson on 9, 11 and 13 April 2010.

After the Coronal Mass Ejection (CME) at 09:54 UTC on 3 April 2010, a shock was observed at the ACE spacecraft at 0756 UTC on 5 April, which led to a sudden impulse on Earth at 08:26 UTC. Nevertheless, while

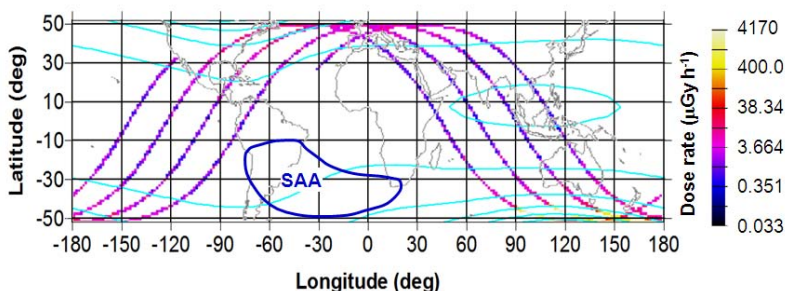


Fig. 18. Gray scale (color) coded dose rates along the trajectory of the ISS during the first EVA on 9th of April 2010. It is seen that the carefully chosen time of the EVA avoid SAA crossings. Highest dose rates are seen in the longitudinal range 90-150° in Southern Hemisphere

the magnetic substorms on 5 and 6 of April were moderate; the second largest in history of GOES fluence of electrons with energy >2 MeV was measured [7]. The R3DR data show a relatively small amount of relativistic electrons on 5 April. The maximum dose rate of 2323 $\mu\text{Gy day}^{-1}$ was reached on 7 April; by 9 April, a dose of 6600 μGy was accumulated. By

the end of the period on 7 May 2010 a total dose of 11,587 μGy was absorbed [7, 8].

Figure 18 presents the ISS trajectory during the EVA 1 on 9 April 2010 on the global map. As in Figure 17 the same L equal values lines are presented. The SAA place and surrounding curve are taken also from Figure 5 and shown here with a heavy line. The dose rate values along the trajectory of ISS are grey scale (color) coded by the logarithmic scale bar shown at the right side in Figure 18. It is seen that the ISS trajectories during the EVA were very carefully chosen by NASA radiologists to avoid crosses of the SAA high dose rates region. The GCR doses outside the relativistic electrons precipitation zones vary between $0.1 \mu\text{Gy h}^{-1}$ at the magnetic equator and $15 \mu\text{Gy h}^{-1}$ at high latitudes. Because of the outer radiation belt enhancement the astronauts were irradiated by the relativistic electrons. As seen they obtained the highest dose rates in the Southern Hemisphere at descending orbits at geographic latitudes above 42° South latitude. Precise analysis of the picture shows that when the trajectories

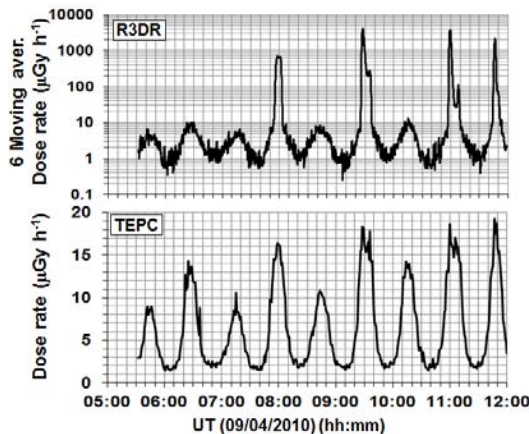


Fig. 19. The dose rate dynamics observed by R3DE and NASA TEPC during the EVA1 of STS-131 on April 9, 2010 between 05:31 and 11:58 UT for 6 h and 27 m

reached $L=3.5$ the color coded dose rates become white, i.e. they reach the maximum ($4170 \mu\text{Gy h}^{-1}$) of the code bar in the right hand side of Figure 18.

Figure 19 presents with usual 2D graphics the same dose rate dynamics as on Figure 18 observed by R3DE and NASA TEPC during the EVA 1 of STS-131 on April 9, 2010. The sinusoidal like meander of minimums and maximums shows the sequence of Northern and Southern Hemisphere crossings through the magnetic equator of the ISS high latitude

regions. Smaller maximums, excluding the last maximum, represented the Northern Hemisphere crossings, while the larger was observed in the Southern Hemisphere. The difference is because maximal L values in Northern Hemisphere are less than these in Southern Hemisphere. Looking precisely on the TEPC data it is possible to be seen that the energetic electrons outside ISS did enhance even the TEPC dose rates with few $\mu\text{Gy h}^{-1}$ and that the small maximums in TEPC data well coincide with much larger maximums in R3DR data. The TEPC dose rate maximums in REP regions can be associated even by direct impact of high energy electrons or with bremsstrahlung on the TEPC detector. Similar is the situation with the dose rate dynamics during other two EVAs on 11 and 13 April.

Figure 19 also presents how and where the TEPC overestimate the GCR dose rates. This is seen well in the minimal dose rates close to the magnetic equator. Here the minimal TEPC values are about $1 \mu\text{Gy h}^{-1}$, while at same places the more sensitive R3DR instrument measured much smaller dose rates reaching $0.25 \mu\text{Gy h}^{-1}$.

Keeping in mind that the average shielding of the space suit [1-3] (Anderson et al. 2003; Benton et al., 2006; Shurshakov et al. 2009) is very similar to the shielding of the R3DR detector we may conclude that a major

Table 4. Estimations of the doses obtained by American astronauts during 3 EVAs on 9th, 11th and 13th of April 2010.

Absorbed doses/Equivalent doses					
R3DR					TEPC (Zapp, 2011)
STS-131 EVA number	UTC from-to	GCR dose Gy/ Sv	ORB dose Gy/ Sv	Total Gy/ Sv	Total = GCR Gy/ Sv
EVA-1 6 h and 27 m	09/04/2010 05:31-11:58	17.6/49	443/443	461/492	41/138
EVA-2 7 h and 26 m	11/04/2010 05:30-12:56	18.6/53	269/269	288/322	49/163
EVA-3 6 h. and 24 m	13/04/2010 06:14-12:36	18.1/56	299/299	318/355	45/144
Total 20 h and 27 m		54.3/158.4	1012/1012	1067/1170	135/445

part of the astronaut's skins were irradiated with similar doses as the measured by R3DR instrument.

Table 4 summarizes the statistics for the 3 EVAs. It is seen that the GCR TEPC absorbed doses are more than 2 times larger than the R3DR doses. The measured by R3DR instrument ORB doses during the 3 EVAs was 443, 269 and 299 μGy respectively. In comparison with TEPC absorbed doses inside ISS the R3DR measured outside absorbed doses are 5-10 times larger for these 6-7 hours during EVAs. The difference for equivalent dose rates is about 2-3 times. (The R3DR ambient dose equivalent rates are calculated using the procedure described in (Spurny and Dachev, 2003).

The astronauts inside ISS collected during the docking with ISS between 7:44 hour on 7th of April and 12:52 at 17th of April 2010 totally 2766 μGy or 6663 μSv according to TEPC data. For the same period R3DR instrument behind 0.41 g cm^{-2} shielding collected much larger doses of 14523 μGy and 18187 μSv . If we will consider that the R3DR measurements during the three EVAs reflected the additional doses collected by the NASA astronauts outside ISS than we find in Table 4 that this is for 20 h and 27 m totally 1067 μGy or an enhancement of 38.6% in comparison to the astronauts being inside ISS. The equivalent additional dose according to R3DR data is 1170 μSv or an enhancement of 17.6%. Although the obtained doses do not pose extreme risks for the astronauts being on EVA they have to be considered as permanently observed source, which requires additional comprehensive investigations.

Conclusions

The paper analyzed the obtained results in the different radiation environments of Galactic Cosmic Rays, inner radiation belt trapped protons in the region of the South Atlantic Anomaly and outer radiation belt relativistic electrons during measurements with the Bulgarian build instruments on ISS. The obtained data was behind less than 0.41 g cm^{-2} shielding, which is very similar to cosmonauts and astronauts space suits shielding. These measurements results can be used by space agencies medical and other not specialized in the radiobiology support staff for first approach in the ISS extra vehicular activity time and space planning.

In conclusion, we would like to mention that the R3DE/R, low mass, dimension and price instruments, proved their ability to characterize the outside ISS radiation environment including the relativistic electron

precipitations. This was achieved mainly with the analysis of the deposited energy spectra, which was obtained at each measurement cycle of 10 s.

The main conclusion of the presented data is that REP events are common on the ISS. Although that the obtained doses do not pose extreme risks for astronauts being on EVA they have to be considered as a permanently observed source, which requires additional comprehensive investigations. An instrumental solution was proposed by Dachev et al., (2011b) where the possible hardware and software solutions for a new Liulin type dosimeter was proposed. New instrument will be able on the base of the analysis of the shape of the deposited energy spectrum and the value of the dose to flux ratio to distinguish the different kind of radiation sources in space as GCR, Inner radiation belt protons and outer radiation belt electrons and to calculate, store and present on display the absorbed and equivalent doses.

Acknowledgements

The authors are thankful to the following colleagues: G. Reitz, G. Horneck from DLR, Germany and D.-P. Häder, M. Lebert, M. Schuster from University of Erlangen, Germany for the cooperation in the development and operation of the R3DE/R instruments.

This work is partially supported by the Bulgarian Academy of Sciences and contract DID 02/8 with Bulgarian Science Fund.

References

- 1 . A n d e r s o n , B. M., et al. Analysis of a Radiation Model of the Shuttle Space Suit, NASA/TP-2003-212158, March 2003.
- 2 . B e n t o n , E.R., et al. (2006) Characterization of the radiation shielding properties of US and Russian EVA suits using passive detectors, Radiation Measurements, 41, 1191 – 1201, 2006.
- 3 . S h u r s h a k o v , V. A., et al. Solar particle events observed on MIR station, Radiat. Measur., 30, (3), 317-325, 1999.
- 4 . S i m p s o n J.A., in: Shapiro M.M. (Ed.) (1983) Composition and origin of cosmic rays, NATO ASI Series C: Mathematical and Physical Sciences. Vol. 107, Reidel, Dordrecht, 1983.
- 5 . K i m , M.-H.Y., et al. (2010) Probabilistic assessment of radiation risk for astronauts in space missions, Acta Astronautica, Volume 68, Issues 7-8, April-May 2011, Pages 747-759, 2010.

- 6 . D a c h e v , Ts. P., et al. Relativistic Electrons High Doses at International Space Station and Foton M2/M3 Satellites, *Adv. Space Res.*, 1433-1440, 2009. doi:10.1016/j.asr.2009.09.023
- 7 . D a c h e v , Ts., et al. Relativistic Electron Fluxes and Dose Rate Variations Observed on the International Space Station, published online in *JASTP*, 2012a. <http://dx.doi.org/10.1016/j.jastp.2012.07.007>
- 8 . D a c h e v , Ts., et al. Relativistic Electron Fluxes and Dose Rate Variations during April-May 2010 Geomagnetic Disturbances in the R3DR Data on ISS, *Adv. Space Res.*, 50, 282-292, 2012b. <http://dx.doi.org/10.1016/j.asr.2012.03.028>
- 9 . R e i t z , G., et al. Space radiation measurements on-board ISS—the DOSMAP experiment, *Radiat Prot Dosimetry*, 116, 374-379, 2005. <http://rpd.oxfordjournals.org/cgi/content/abstract/116/1-4/374>
10. B a d h w a r , G.D., et al. Radiation environment on the MIR orbital station during solar minimum. *Adv. Space. Res.* 22 (4), 501-510, 1998.
11. B e n t o n , E . R . a n d B e n t o n E . V . Space radiation dosimetry in low-Earth orbit and beyond, *Nucl. Instrum. And Methods in Physics Research, B*, 184, (1-2), 255-294, 2001.
12. NCRP. Radiation Protection Guidance for Activities in Low Earth Orbit. Report No. 142, Bethesda, MD, 2002.
13. D a c h e v , Ts., et al. Calibration Results Obtained With Liulin-4 Type Dosimeters, *Adv. Space Res.*, V 30, No 4, 917-925, 2002. doi:10.1016/S0273-1177(02)00411-8
14. D a c h e v , Ts., et al. Observations of the SAA radiation distribution by Liulin-E094 instrument on ISS, *Adv. Space Res.* 37 (9), 1672–1677, 2006.
15. N e a l y , J. E., et al. Pre-engineering spaceflight validation of environmental models and the 2005 HZETRN simulation code, *Adv. Space Res.*, 40, 11, 1593-1610, 2007. doi:10.1016/j.asr.2006.12.030
16. W i l s o n , J. W., et al. Time serial analysis of the induced LEO environment within the ISS 6A, *Adv. Space Res.*, 40, 11, 1562-1570, 2007. doi:10.1016/j.asr.2006.12.030
17. S l a b a , T.C., et al. Statistical Validation of HZETRN as a Function of Vertical Cutoff Rigidity using ISS Measurements, *Adv. Space Res.*, 47, 600-610, 2011. doi:10.1016/j.asr.2010.10.021
18. H o r n e c k , G., et al. Biological experiments on the EXPOSE facility of the International Space Station, *Proceedings of the 2nd European Symposium – Utilisation of the International Space Station*, ESTEC, Noordwijk, 16-18 November 1998, SP-433, pp. 459-468, 1998.
19. B e r g e r , M.J., et al. (2012) Stopping-Power and Range Tables for Electrons, Protons, and Helium Ions,. NIST Standard Reference Database 124, 2012. Available online at: <http://physics.nist.gov/PhysRefData/Star/Text/contents.html>
20. M c I l w a i n , C. E. (1961) Coordinates for mapping the distribution of magnetically trapped particles. *J. Geophys. Res.*, 66, pp. 3681-3691.
21. H e y n d e r i c k x , D., et al. Historical Review of the Different Procedures Used to Compute the L-Parameter. *Radiation Measurements*, 26, 325-331, 1996.
22. H e f f n e r , J., (1971) Nuclear radiation and safety in space, M, Atomizdat, pp. 115, 1971. (in Russian).

23. V e t t e , J. I. The NASA/National Space Science Data Center Trapped Radiation Environment Model Program (1964–1991). NSSDC/WDCR-R&S, 19–29, 1991.
24. H e y n d e r i c k x , D., et al. Calculating Low-Altitude Trapped Particle Fluxes With the NASA Models AP-8 and AE-8, Radiat. Meas., 26, 947-952, 1996.
25. W r e n n , G. L. (2009) Chronology of ‘killer’ electrons: Solar cycles 22 and 23, Journ. Atmos. Solar-Terr. Phys., 71, 1210-1218.
26. D a c h e v , T. P., et al. Space Shuttle drops down the SAA doses on ISS, Adv. Space Res., 47, 2030-2038, 2011a. doi:10.1016/j.asr.2011.01.034
27. B a n k o v , N. G., et al. Simulation model of the radiation dose measured onboard of the ISS, Fundamental Space Research, Supplement of Comptes Rend. Acad. Bulg. Sci., ISBN 987-954-322-409-8, 147-149, 2010. <http://www.stil.bas.bg/FSR2009/pap144.pdf>
28. Z a p , N. (2012) at NASA space Radiation Analysis Group, Johnson Space Center and by ‘Coordinated Data Analysis Web’ at Goddard Space Flight Center, (<http://cdaweb.gsfc.nasa.gov/>, June, 2012).
29. S p u r n y , F. a n d T s . D a c h e v . Long-Term Monitoring of the Onboard Aircraft Exposure Level With a Si-Diode Based Spectrometer, Adv. Space Res., 32, No.1, 53-58, 2003. doi:10.1016/S0273-1177(03)90370-X
30. D a c h e v , T s. P. Characterization of near Earth radiation environment by Liulin type instruments, Adv. Space Res., 44, pp 1441-1449, 2009. doi:10.1016/j.asr.2009.08.007
31. D a c h e v , T s. P. et al. Main Specifications of New Liulin Type Intelligent Crew Personal Dosimeter, Proceedings of Sixth Scientific Conference with International Participation SES, Sofia, 2-4 November 2010, ISSN 13131-3888, 76-82, 2011b. http://www.space.bas.bg/SENS/SES2010/1_SpPh/10.pdf
32. H ä d e r , D. P., et al. R3D-B2 - Measurement of ionizing and solar radiation in open space in the BIOPAN 5 facility outside the FOTON M2 satellite, Adv. Space Res. Volume 43, Issue 8, Pages 1200-1211, 2009. doi:10.1016/j.asr.2009.01.021
33. S t r e b , C., et al. R3D-B, Radiation Risk Radiometer-Dosimeter on Biopan (Foton) and expose on International Space Station, Proceedings of the Second Exo-Astrobiology workshop, Graz, Austria, ESA SP-518, 71-74, November 2002.

ОСОБЕНОСТИ НА КОСМИЧЕСКАТА РАДИАЦИЯ В ОБКРЪЖАВАЩОТО ПРОСТРАНСТВО НА МЕЖДУНАРОДНАТА КОСМИЧЕСКА СТАНЦИЯ (МКС)

Ц. Дачев, Н. Банков, Б. Томов, Ю. Матвийчук, П. Димитров

Резюме

Космическото време и свързаната с него йонизираща радиация се разглеждат като един от основните здравни проблеми на екипажа на Международната космическа станция (МКС). За да се определят радиационните ефекти върху хората е необходимо да се знае:

1) Натрупаната абсорбирана доза, която зависи от нейното глобално разпределение; 2) Локалното 3D разпределение на екраниращите маси. Радиометърът-дозиметърът на радиационния риск R3DE (Radiation Risks Radiometer-Dosimeter (R3D) за платформата EXPOSE-E на установката European Technological Exposure Facility (EuTEF) работи успешно извън европейския модул Columbus от м. февруари 2008 до м. септември 2009 г. Много подобен на него прибор, наречен R3DR, работи успешно в платформата EXPOSE-R извън руският модул „Звезда“ на МКС от м. март 2009 до м. август 2010 г. Двата миниатюрни спектрометри-дозиметри са от типа „Люлин“ и са разработени и изработени в България. Те натрупаха повече от 5 милиона измервания с 10 с. разрешение по време зад защита от 0.41 g cm^{-2} , която е много подобна на средната защита на американските и руските космически скафандри [1-3]. Това ни позволява да интерпретираме получените данни като възможни дози по време на работа на космонавтите извън стените на станцията Extra Vehicular Activities (EVA). В статията първо се анализират получените дългосрочни данни за: 1) Галактическата космическа радиация (GCR); 2) Захванатите във вътрешния радиационен пояс протони в района на южно-атлантическата аномалия (SAA) и 3) Релативистичните електрони във външния радиационен пояс (ORB). Голямата база от данни е използвана за създаването на емпиричен модел за пресмятане на абсорбираната доза в окръжаващата среда на МКС на височина от 359 км. Моделът апроксимира средната мощност на дозата в определена от потребителя: географска точка, орбита на станцията или площ в географска координатна система. В статията са показани сравнения на получените данни от приборите R3DE/R и приборът на NASA Tissue Equivalent Proportional Counter (TEPC) с модела по време на реални EVA на космонавти и астронавти в периода 2008-2010 г. Моделът е използван и за предсказване на акумулираните дози по дължината на орбитата на МКС за 1-ва орбита (1.5 часа) и за 4 последователни орбити (6 часа), което е обичайната продължителност на EVA. Тези предсказания могат да бъдат използвани от медицинския и другия неспециализиран в радиобиологията персонал на космическите агенции за определяне в първо приближение на възможната доза при планиране на времето и мястото на бъдещи EVA.

PRELIMINARY RESULTS FOR THE RADIATION ENVIRONMENT OBSERVED BY RD3-B3 RADIOMETER- DOSIMETER INSIDE BION-M № 1 SPACECRAFT

*Tsvetan Dachev¹, Borislav Tomov¹, Yury Matviichuk¹, Plamen Dimitrov¹
Nikolay Bankov¹, Vladislav Petrov², Viacheslav Shurshakov²,
Olga Ivanova², Donat-Peter Häder³, Michael Lebert⁴,
Martin Schuster⁴, Günter Reitz⁵, Gerda Horneck⁵, Ondrej Ploc⁶*

¹*Space Research and Technology Institute – Bulgarian Academy of Sciences*

²*State Research Center Institute of Biomedical problem – Russian Academy of
Sciences*

³*Neue Str. 9, 91096 Möhrendorf, Germany*

⁴*Friedrich-Alexander-Universität, Institut für Botanik und Pharmazeutische
Biologie, Erlangen, Germany*

⁵*DLR, Institute of Aerospace Medicine, Köln, Germany*

⁶*Nuclear Physics Institute, Czech Academy of Sciences, Prague, Czech Republic
e-mail: tdachev@bas.bg*

Abstract

Space radiation has been monitored using the PД3-B3 (further is used the Latin transcription RD3-B3) spectrometer-dosimeter on board a recent space flight on the Russian recoverable satellite БИОН-M № 1 (further is used the Latin transcription BION-M № 1). The instrument was mounted inside of the satellite in pressurized volume together with biological objects and samples. RD3-B3 instrument is a battery operated version of the spare model of the R3D-B3 instrument developed and built for the ESA BIOPAN-6 facility on Foton M3 satellite flown in September 2007. Cosmic ionizing radiation has been monitored and separated in 256 deposited energy spectra, which were further used for determination of the absorbed dose rate and flux. The report summarizes the first results for the Earth radiation environment at the altitude (253–585 km) of the BION-M № 1 spacecraft.

1. Introduction

The radiation field inside the BION-M № 1 spacecraft is complex, composed of GCRs, trapped radiation of the Earth's radiation belts, possible solar energetic particles, albedo particles from Earth's atmosphere and secondary radiation produced in the shielding materials of the spacecraft and biology objects. Dose characteristics in BION-M № 1 spacecraft also depend on many other parameters such as the spacecraft orbit parameters, solar cycle phase and current helio-and geophysical parameters.

This paper analyses the first results for the radiation environment inside the BION-M № 1 spacecraft generated by different radiation sources, including: Galactic Cosmic Rays (GCRs), IRB trapped protons in the region of the South Atlantic Anomaly (SAA) and outer radiation belt (ORB) relativistic electrons. The satellite was launched on 19 April 2013 at 10:00 UT from the Cosmodrome of Baikonur (Kazakhstan). On 19th of May at 03:12 UT the Landing module of BION-M № 1 successfully touched down at Orenburg region, after 30 days in orbit. <http://biosputnik.imbp.ru/eng/index.html>

1.1. Earth radiation environment at BION-M № 1 spacecraft orbit

1.1.1. Galactic cosmic rays

The dominant radiation component in the ISS radiation environment consists of GCRs modulated by the altitude and geomagnetic coordinates of the space craft. GCRs are charged particles that originate from sources beyond the Solar System. They are thought be accelerated at highly energetic sources such as neutron stars, and supernovae within our Galaxy. GCRs are the most penetrating of the major types of ionizing radiation [1]. The fluxes and spectra of GCR particles show modulation that is anti-correlated with solar activity. The distribution of GCRs is believed to be isotropic throughout interstellar space. The energies of GCR particles range from several tens up to 10^{12} MeV nucleon⁻¹. The GCR spectrum consists of 98% protons and heavier ions (baryon component) and 2% electrons and positrons (lepton component). The baryon component is composed of 87% protons, 12% helium ions (alpha particles) and 1% heavy ions [2]. Highly energetic particles in the heavy ion component, typically referred to as high Z and energy (HZE) particles, play a particularly important role in space dosimetry and strongly affect humans and other biological entities in space

[3]. HZE particles, especially iron, possess high-LET and are highly penetrating, giving them a large potential for inflicting radiobiological damage [4]. The daily average GCR absorbed dose rates measured with the R3DE instrument [5] outside of the ISS at about 360 km altitude vary in the range 77-102 $\mu\text{Gy day}^{-1}$ with an average of 91 $\mu\text{Gy day}^{-1}$. The expected BION-M № 1 dose rates are higher because of the higher altitude.

1.1.2 Trapped radiation belts

Radiation belts are regions with high concentrations of energetic electrons and protons trapped within the Earth's magnetosphere. There are two distinct belts of toroidal shape surrounding Earth where the high energy charged particles get trapped in the Earth's magnetic field. Energetic ions and electrons within the Earth's radiation belts pose a hazard to both astronauts and spacecraft electronics. The inner radiation belt (IRB), located between about 0.1 to 2 Earth radii, consists of electrons with energies up to 10 MeV and protons with energies up to ~ 200 MeV. The South-Atlantic Anomaly (SAA) is an area where the IRB comes closer to the Earth's surface due to a displacement of the magnetic dipole axes from the Earth's center. The daily average SAA absorbed dose rates measured with the R3DE instrument [5] outside of the ISS at about 360 km altitude vary in the range 110-685 $\mu\text{Gy day}^{-1}$ with an average of 426 $\mu\text{Gy day}^{-1}$. The maximum hourly SAA absorbed dose rates reached 1500-1600 $\mu\text{Gy h}^{-1}$. It was found [6] that the docking of the US Space Shuttle with the ISS strongly decreases the SAA doses because of the additional shielding that the 78-ton body of the Shuttle provides against the IRB protons. The expected BION-M № 1 dose rates are higher because of the higher altitude.

The outer radiation belt (ORB) starts from about four Earth radii and extends to about nine to ten Earth radii in the anti-sun direction. The outer belt mostly consists of electrons whose energy is not larger than 10 MeV. Relativistic electron enhancements in the ORB are one of the major manifestations of space weather [7, 8] near Earth's orbit. These enhancements occur mainly after magnetic storms. The electron flux may cause problems for components located outside a spacecraft (e.g., solar cell degradation). ORB electrons do not have enough energy to penetrate a heavily shielded spacecraft such as the ISS wall but may deliver large additional doses to astronauts during EVA [5, 9, 10]. The average ORB dose rate measured with the R3DE [5] outside of the ISS at about 360 km altitude is 8.64 $\mu\text{Gy day}^{-1}$, and ranges between 0.25 and 212 $\mu\text{Gy day}^{-1}$. Rare

sporadic fluxes of relativistic electrons were measured with the R3DR instrument to deliver absorbed doses as high as $20,000 \mu\text{Gy h}^{-1}$. The expected BION-M № 1 dose rates are lower because of the higher shielding inside the BION-M № 1 satellite.

1.1.3 Solar energetic particles (SEP)

The SEP are mainly produced by solar flares, sudden sporadic eruptions of the chromosphere of the Sun. High fluxes of charged particles (mostly protons, some electrons and helium and heavier ions) with energies up to several GeV are emitted by processes of acceleration outside the Sun. It is now generally understood that SEP events arise from coronal mass ejections (CME) from active regions of the solar surface. The CME propagates through interplanetary space carrying along with it the local surface magnetic field frozen into the ejected mass. There is a transition (shock) region between the normal sectored magnetic structure of interplanetary space and the fields frozen into the ejected mass, which forms a transition region (shock) where the interplanetary gas is accelerated forming the SEP. As the accelerated region passes an observation point, the flux intensity is observed to increase dramatically [11]. The time profile of a typical SEP starts off with a rapid exponential increase in flux, reaching a peak in minutes to hours. The energy emitted lies between 15 and 500 MeV nucleon⁻¹ and the intensity can reach $10^4 \text{ cm}^{-2} \text{ s}^{-1} \text{ sr}^{-1}$. Electrons with energies of 0.5 to 1 MeV arrive at the Earth, usually traveling along interplanetary field lines, within tens of minutes to tens of hours. Protons with energies of 20 to 80 MeV arrive within a few to 10 h, although some high energy protons can arrive in as early as 20min. SEP are relatively rare and occur most often during the solar maximum phase of the 11-year solar cycle. In the years of maximum solar activity up to 10 flares can occur, during the years of minimum solar activity only one event can be observed on average [12].

2. Instrumentation

In order to determine and quantify the radiation field outside the Foton M2/M3 satellites a radiation environment spectrometers-dosimeters R3D-B2/B3 were developed by the collaboration of the Bulgarian and German teams and integrated into the Biopan-5/6 facilities [13-15]. Both of them worked successfully during the Foton M2/M3 missions. The RD3-B3

spectrometer-dosimeter used at the BION-M № 1 mission is a battery operated version of the spare model of the R3D-B3 instrument developed and built for the ESA Biopan-6 facility on Foton M3 satellite in September 2007 [10, 16].

The scientific objectives of the RD3-B3 spectrometer-dosimeter were in first order connected with the quantification of the global distribution of the radiation field inside the BION-M № 1 satellite.

Also there was housed other 17 scientific equipment's http://biosputnik.imbp.ru/eng/science_tech.html related to different scientific disciplines. For many of the experiments on board the knowledge of the space radiation properties and the dynamics of the dose accumulation is highly important for the interpretation of the data collected during the mission.

The RD3-B3 instrument is successor of the Liulin-E094 instrument, which was part of the experiment Dosimetric Mapping-E094, headed by Dr. G. Reitz, that was placed in the US Laboratory Module of the ISS as a part of the Human Research Facility of Expedition Two Mission 5A.1 in



Fig. 1. External view of R3DE instrument

May-August, 2001 [17-20].

Figure 1 present the RD3-B3 instrument as situated inside the BION-M № 1 satellite. In the left side of the figure is seen the 2 Lithium-ion battery housing (pl. look below the label), while in the right side is the R3D-B3 instrument. The RD3-B3 instrument is low mass, small dimension automatic devices that measure solar radiation in four channels and ionizing radiation in 256 channels Liulin type energy deposition spectrometer. The four solar UV and visible radiations photodiodes are seen in the left part of the figure. They were active during the flight of BION-M № 1 satellite but

because of the darkness inside the obtained values were equal to zero. The size of the aluminum box of R3D-B3 instruments is with 53x82x28 mm size of the box and 120 g weight [15, 16].

The ionizing radiation is monitored using a semiconductor detector (2 cm² area and 0.3 mm thick). Its signal is digitized by 12 bit fast A/D converter after passing a charge-sensitive preamplifier. The deposited energies (doses) are determined by a pulse height analysis technique and then passed to a discriminator. The amplitudes of the pulses are transformed into digital signals, which are sorted into 256 channels by multi-channel analyzer. At every exposition time interval one energy deposition spectrum is collected. The energy channel number 256 accumulates all pulses with amplitudes higher than the maximal level of the spectrometer of 20.83 MeV. The methods for characterization of the type of incoming space radiation are described by Dachev in [21].

The total external and internal shielding before the detectors of R3D-B3 instrument is not well known but very rough estimations give value of at least 5 g cm⁻² aluminum material. The calculated stopping energy of normally incident particles to the detector of the instrument is 8.5 MeV for electrons and 67.5 MeV for protons [22]. This means that only protons and electrons with energies higher than the above mentioned could reach the detector.

BION-M № 1 is a LEO satellite that orbited the Earth with a period of 89.9 min, an inclination of 63° with respect to the Earth's equator (highly inclined orbit), and with an altitude above the Earth surface in the range 253-585 km. In this study the orbital parameters used were calculated by the software KADR-2 [24].

3. Data analysis and results

3.1. All time dose rate and flux measurements

BION-M № 1 mission took place in the decreasing phase of the 24th solar cycle, and the satellite flew during a period characterized by moderate solar activity. 2 relatively small SEP occurred during the flight of the satellite. The maximum of the first one occurred about midday on 21 April 2013. No real enhancement in the proton flux with energies above 100 MeV was observed in the GOES-13 data. The maximum of the second one http://www.swpc.noaa.gov/ftplibdir/warehouse/2013/2013_plots/proton/20130426_proton.gif occurred at the early morning time on 25 April 2013. In this period BION-M № 1 was in the region of the SAA that is why R3D-B3

instrument was not able to registries it. The geomagnetic field during the period of the BION-M № 1 flight was also at moderate level with a sporadic period with $K_p=5$ in the interval 3:00-6:00 on 26 April 2013.

Ionizing radiation doses and fluxes during the whole monitoring period of the RD3-B3 instrument (16 April to 13 May 2013) are plotted at Fig. 2. The red curves there correspond to the dose rate values, while the blue curves shows the flux rate variations.

Fig. 2 shows two important periods recorded at 1-min resolution. The lowest doses and fluxes in the left part of the figure were obtained after 16:00 UT on 16 of April 2013 when the switching ON of RD3-B3 into the BION-M № 1 satellite occurred. These values are comparable with the natural background radiation with a mean value about $0.1 \mu\text{Gy h}^{-1}$. Few sporadic maxima, which are seen there was generated by the so called “Microphone effect” when the detector produces noise pulses in result of mechanical strikes outside the RD3-R3 instrument.

The recorded maxima in the central and right side part of Fig. 1 were obtained during the crossings of the South-Atlantics magnetic anomaly (SAA) region where the inner radiation belt populated with high-energy protons is encountered. The meander of dose rates between 0.3 and $12 \mu\text{Gy h}^{-1}$ is generated when the satellite crosses the geomagnetic equator

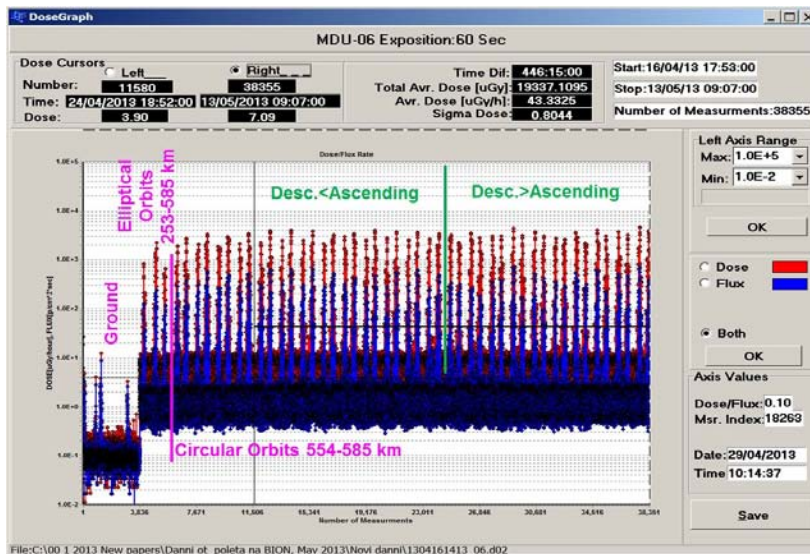


Fig. 2. Ionizing radiation doses and fluxes during the whole monitoring period of the RD3-B3 instrument (16 April to 13 May 2013)

($0.3 \mu\text{Gy h}^{-1}$) and returns back to high latitudes in the polar regions ($12 \mu\text{Gy h}^{-1}$).

Very first part of the in orbit data at figure 2 was recorded when the BION-M № 1 satellite was still in elliptical orbits at altitudes between 253 and 585 km, that is why these SAA crossings maxima are relatively lower than the main part of the data. In the circular orbits data well seen are 2 different periods. First period shows that the descending orbits SAA maxima are lower than the ascending. In the second period this is in reverse. The probable reason for these features is changing in the orientation of the satellite.

3.2. Analysis of the recorded space radiation sources

In Dachev [21] it was shown that the dose from flux and dose to flux dependencies can characterize the type of the predominant radiation source in the Liulin type instruments. The dose to flux dependence is also known as specific dose (SD). Figure 3 is prepared to confirm these features again with the RD3-B3 data and to be analyzed the recorded space radiation sources.

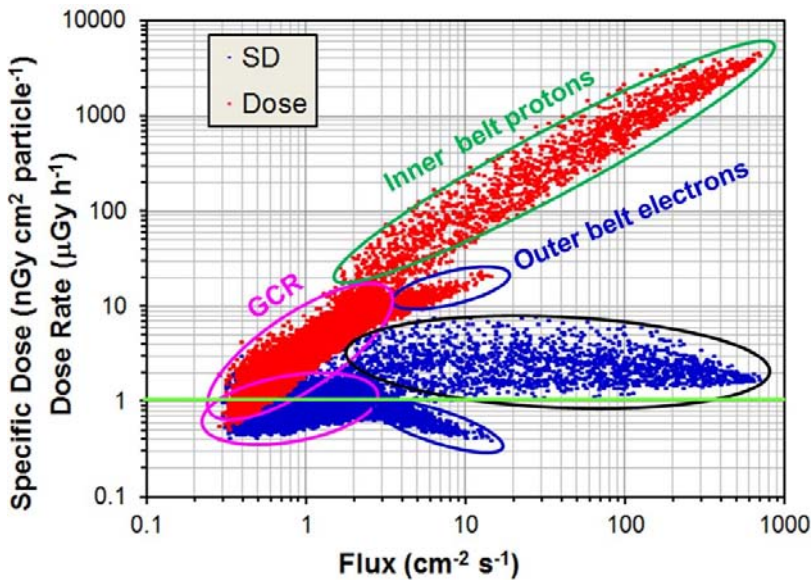


Fig. 3. Characterization of the RD3-B3 predominant radiation sources by the dose rate from flux and specific dose dependencies

The abscissa plots the measured flux in $\text{cm}^{-2} \text{s}^{-1}$, while the ordinate shows

the dose rate in $\mu\text{Gy h}^{-1}$ and specific dose in $\text{nGy cm}^2 \text{ part}^{-1}$ [21, 23] (Heffner, 1971; Dachev, 2009) for the period 23 April - 13 May 2013.

The large amount of red points in the diagonal of the figure is responsible for the dose rate values, which, as expected, are in linear dependence from the flux, while the almost horizontally plotted blue points present the SD values.

Three branches in each graphic are differentiated and they look as a left hand wrist with two fingers. The wrist represents a highly populated part in the diagonal bunch of points: (1) it takes a large amount of the measured points in the range $0.3\text{--}15 \mu\text{Gy h}^{-1}$; (2) for a fixed flux a wide range of doses is observed. These two features could be explained only by the GCR particles, which, being with small statistical relevance and high LET, are able to deposit various doses for fixed flux value. The smallest dose rates ($0.3\text{--}0.4 \mu\text{Gy h}^{-1}$) are observed close to the magnetic equator, while the largest are at high latitudes. In the horizontal graphic this part of the data is represented with a similar large amount of points, which in large scale overlap the dose rate diagonal points.

The “index” finger is in the dose rate range $9\text{--}23 \mu\text{Gy h}^{-1}$. Its representation in the horizontal graphic is a finger extending up to $17 \text{ cm}^{-2} \text{ s}^{-1}$, with SD values below $1 \text{ nGy cm}^2 \text{ part}^{-1}$ (pls. look the green horizontal line). This finger is based on low LET particles and could be formed only by the relativistic electrons [21, 25] (Dachev et al., 2009 and 2012b) in the outer radiation belt. Here because of higher shielding (more than 5 g cm^{-2} aluminum) the relativistic electrons fluxes measured with RD3-R3 instrument are much lower than the presented in the referenced above papers.

The “big” finger in the diagonal graphic has a different source compared to the previous two because it is characterized by a high range of doses for fixed flux but the dose rates are in the range $20\text{--}4300 \mu\text{Gy h}^{-1}$. This amount of points could be formed only by protons from the IRB (The region of South Atlantic Anomaly (SAA)) whose dose depositions depend on the energy. The lower energy protons are depositing higher doses. In the horizontal graphic this finger has a similar form and is situated in the range $1.2\text{--}8.5 \text{ nGy cm}^2 \text{ part}^{-1}$. Both IRB and ORB fingers can be approximated by straight lines. From these approximations we obtain that 1 proton in IRB produces in the Silicon detector on average a dose of 1.4 nGy , while 1 electron in ORB produces a dose of 0.33 nGy , which is in good agreement with Heffner’s formula [23].

Table 1 summarizes the observations presented in figure 3 and gives the statistics of the measured values. In the last 2 columns of table 1 the selecting requirements is presented. The values was obtained in reference with the points distribution presented at figure 3 but the data period is larger and cover the following time interval - 19/04/2013 10:08:59 - 13/05/2013 08:59:39. Also the daily average and total accumulated values are calculated and presented. In 3 columns the averaged coordinates: longitude, latitude and altitude where the values are obtained are presented.

The comparison of the values presented in table 1 with analogical values obtained at International space station (ISS) and reported by Dachev [5] reveal the following results: 1) The obtained at the BION-M № 1 GCR average daily dose rate values ($120 \mu\text{Gy day}^{-1}$) is higher than the measured at ISS ($91.1 \mu\text{Gy day}^{-1}$) because the BION-M № 1 altitude and inclination of the orbit is higher than respectively ISS parameters (360 km altitude and 52° inclination); 2) Same is applicable for the inner radiation belt average daily dose rate values. The ISS value is $426 \mu\text{Gy day}^{-1}$. The BION-M № 1 dose rate increase is more than 2 times and reach $876 \mu\text{Gy day}^{-1}$; 3) As already mentioned the outer radiation belt relativistic electrons dose rate on BION-M № 1 satellite are very small because of large shielding and

Table 1. Statistical data obtained with the RD3-B3 instrument in the period 19/04/2013 10:08:59 - 13/05/2013 08:59:39

Re-gion	Meas. [No] [Day]	Aver. Dose Rate/Flux [Gy h ⁻¹]/ [cm ⁻² s ⁻¹] [Gy day ⁻¹]	Min. Dose Rate/Flux [Gy h ⁻¹]/ [cm ⁻² s ⁻¹] [Gy day ⁻¹]	Max. Dose Rate/Flux [Gy h ⁻¹]/ [cm ⁻² s ⁻¹] [Gy day ⁻¹]	Total Dose Rate/Fluen. [mGy]/ [No part.]	Aver. Alt. [km]	Aver. Lat. [Deg.]	Aver. Long. [Deg.]	Selecting requirements	
									Dose/Flux [Gy h ⁻¹]/ [cm ⁻² s ⁻¹]	SD [nGy cm ² part ⁻¹]
All data	34391	41.03	0.4	4530.12	23.523	561	-0.06	0.08	No	No
	23.883	6.05	0.26	699.8	4159420					
	34401	985	495	1139						
GCR	32407	5.34	0.4	14.99	2.887	561	1.49	2.62	<15	<2
	22.505	1.57	0.26	10.12	1015420					
		120	108	124						
IRB (SAA)	1768	698.3	20.04	4530.12	20.58	566	-24.9	-44.6	>20	>1
	1.228	88.44	1.63	699.8	3127360					
		876	387	1017						
ORB	226	13.61	20.04	22.61	0.051	583	-36.7	17.2	10<D<30 F>5	<0.8
	0.157	6.77	5.0	14.53	30580					
		38	0.0	241						

practically is not comparable with data obtained outside ISS.

3.3. Latitudinal distributions of the data

Figure 4 summarizes the distribution of the obtained dose and flux data and of the calculated SD value in $\text{nGy cm}^2 \text{ part}^{-1}$ against the L value [25]. The dose and flux data show two obvious maxima – one at L values of about 1.3 and another at about 4. The lower L value maximum corresponds to the inner (proton) radiation belt, which is populated mainly by protons with energies from few tens to few hundred MeV. The higher L value maximum corresponds to the outer (electron) radiation belt, which is populated mainly by electrons with energies from hundreds of keV to a few MeV. The large amount of points with low doses and fluxes are obtained at

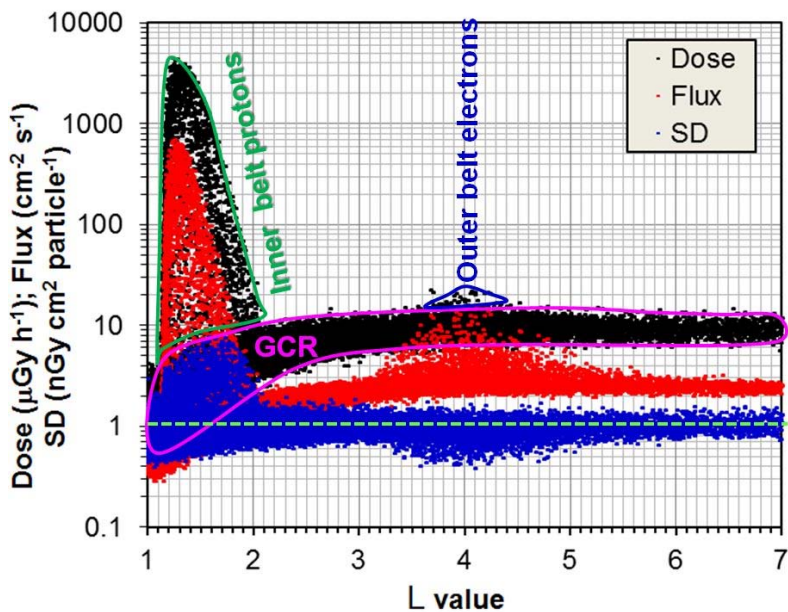


Fig. 4. Distribution of dose and flux and SD data against the L value

low and mid magnetic latitudes outside of the radiation belts and is generated mainly by Galactic cosmic ray (GCR) particles. This radiation shows a “knee” at L value about 2.5–3. The large amount of points close to $1 \text{ nGy cm}^2 \text{ part}^{-1}$ is produced by GCR, which being high LET particles are able to delivery different doses with same flux values. Also the GCR did have very small fluxes and the Heffner’s formula [23] is not applicable for them.

The specific dose value is provisionally divided into two parts – below and above $1 \text{ nGy cm}^2 \text{ part}^{-1}$. According to this value divides the range of doses delivered by electrons below of about $0.7 \text{ nGy cm}^2 \text{ part}^{-1}$ and by protons above $1.12 \text{ nGy cm}^2 \text{ part}^{-1}$. Some more features are seen also in the SD distribution. Points with specific doses at about $1\text{--}2 \text{ nGy cm}^2 \text{ part}^{-1}$ at $L = 1.2$ are generated by protons with energies of a few hundred MeV. Points with specific doses at about $2\text{--}5 \text{ nGy cm}^2 \text{ part}^{-1}$ around $L = 1.7$ are generated by protons with energies below 100 MeV.

Generally the SD variations at BION-M № 1 satellite are with small dynamics in comparison with analogical distributions obtained on Foton-M2/M3 satellites and on ISS [14, 16, 21, 26] with instruments outside the pressurized volume.

Conclusions

This paper analyses the first results for the radiation environment inside the BION-M № 1 spacecraft generated by different radiation sources, including: Galactic Cosmic Rays (GCRs), IRB trapped protons in the region of the South Atlantic Anomaly (SAA) and outer radiation belt (ORB) relativistic electrons. The satellite was launched on 19 April 2013 at 10:00 UT from the Cosmodrome of Baikonur (Kazakhstan).

On 19th of May at 03:12 UT the Landing module of BION-M № 1 successfully touched down at Orenburg region, after 30 days in orbit. <http://biosputnik.imbp.ru/eng/index.html>

The RD3-R3 low mass, dimension and price instrument proved its ability to characterize the radiation environment inside the BION-M № 1 satellite, including the relativistic electron precipitations. This was achieved mainly with the analysis of the deposited energy spectra, obtained at each measurement cycle of 60 s.

The comparison of the values obtained with RD3-R3 instrument with analogical values obtained at International space station (ISS) and reported by Dachev [5] reveal the following results: 1) The obtained at the BION-M № 1 GCR average daily dose rate values ($120 \text{ }\mu\text{Gy day}^{-1}$) is higher than the measured at ISS ($91.1 \text{ }\mu\text{Gy day}^{-1}$) because the BION-M № 1 altitude and inclination of the orbit is higher than respectively ISS parameters (360 km altitude and 52° inclination); 2) Same is applicable for the inner radiation belt average daily dose rate values. The average ISS value is about $250 \text{ }\mu\text{Gy day}^{-1}$. The BION-M № 1 dose rate increase is more than 3 times and reach $876 \text{ }\mu\text{Gy day}^{-1}$; 3) As already mentioned the outer radiation belt

relativistic electrons dose rate on BION-M № 1 satellite are very small because of large shielding and practically is not comparable with data obtained outside ISS.

The obtained first results with the RD3-R3 instrument on BION-M № 1 encouraged us to perform further more comprehensive analysis of the dose rate and flux data.

Acknowledgements

This work was supported financially by the Bulgarian science fund (DID-02). The authors gratefully acknowledge the discussion performed with Victor Benghin.

References

1. M e w a l d t , R . A . 1996. Cosmic rays. In Macmillan Encyclopedia of AU5c Physics, Simon & Schuster Macmillan, New York.
2. S i m p s o n , J . A . 1983. Composition and origin of cosmic rays. In: Shapiro, M.M. (Ed.), NATO ASI Series, Series C Mathematical and Physical Sciences, 107. Reidel, Dordrecht.
3. H o r n e c k , G . 1994. HZE particle effects in space. *Acta Astronaut.* 32:749–755.
4. K i m , M . - H . Y . , A n g e l i s , G . , D e C u c i n o t t a , F . A . 2010. Probabilistic assessment of radiation risk for astronauts in space missions. *Acta Astronautica* 68 (7–8), 747–759.
5. D a c h e v , T s . , H o r n e c k , G . , H ä d e r , D . - P . , L e b e r t , M . , R i c h t e r , P . , S c h u s t e r , M . , D e m e t s , R . 2012a. Time profile of cosmic radiation exposure during the EXPOSE-emission: the R3D instrument. *Journal of Astrobiology* 12 (5), 403–411 <http://eea.spaceflight.esa.int/attachments/spacestations/ID501800a9c26c2.pdf>
6. D a c h e v , T . P . , S e m k o v a , J . , T o m o v , B . , M a t v i i c h u k , Y u . , D i m i t r o v , P l . , K o l e v a , R . , M a l c h e v , S t . , R e i t z , G . , H o r n e c k , G . , D e A n g e l i s , G . , H ä d e r , D . - P . , P e t r o v , V . , S h u r s h a k o v , V . , B e n g h i n , V . , C h e r n y k h , I . , D r o b y s h e v , S . , a n d B a n k o v . N.G. 2011. Space shuttle drops down the SAA doses on ISS. *Adv Space Res.* 11:2030–2038 <http://dx.doi.org/10.1016/j.asr.2011.01.034>.
7. Z h e n g , Y . , L u i , A . T . Y . , L i , X . , F o k , M . - C . Characteristics of 2–6 MeV electrons in the slot region and inner radiation belt. *J. Geophys. Res.* 111, A10204, 2006.
8. W r e n n , G . L . Chronology of ‘relativistic’ electrons: solar cycles 22 and 23. *J. Atmos. Solar-Terr. Phys.* 71, 1210–1218, 2009.

9. Dachev, Ts.P., Tomov, B.T., Matviichuk, Yu.N., Dimitrov, Pl.G., Bankov, N.G., Reitz, G., Horneck, G., Häder, D.-P., Lebert, M., Schuster, M. 2013. Relativistic Electron Fluxes and Dose Rate Variations Observed on the International Space Station. *J. Atmospheric and Solar-Terrestrial Physics* 99, 150-156, <http://dx.doi.org/10.1016/j.jastp.2012.07.007>.
10. Dachev, Ts.P., Tomov, B.T., Matviichuk, Yu.N., Dimitrov, P.G., Bankov, N.G. 2009. Relativistic electrons high doses at international space station and Foton M2/M3 satellites. *Adv. Space Res.*, 1433-1440, <http://dx.doi.org/10.1016/j.asr.2009.09.023>.
11. Mertens, C.J., Wilson, J.W., Blattinig, S.R., Solomon, S.C., Wiltberger, M.J., Kunches, J., Kress, B.T., Murray, J.J. 2007. Space weather nowcasting of atmospheric ionizing radiation for aviation safety, NASA Langley Research Center. Available online at: http://ntrs.nasa.gov/archive/nasa/casi.ntrs.nasa.gov/20070005803_2007005368.pdf
12. Lantos, P., 1993. The Sun and its effects on the terrestrial environment. *Radiation Protection Dosimetry* 48 (1), 27-32.
13. Streb, C., Richter, P., Lebert, M., Dachev, T., Häder, D.-P. 2002. R3D-B, radiation risk radiometer-dosimeter on BIOPAN (Foton) and expose on the International Space Station (ISS). Proceedings of the Second European Workshop on Exo/Astrobiology, Graz, Austria, 16-19 September, (ESA SP-518), 71-74,
14. Häder, D.-P., and Dachev, T.P. 2003. Measurement of solar and cosmic radiation during spaceflight, Kluwer Press, *Surveys in Geophysics*, 24, 229-246.
15. Häder, D.P., Richter, P., Schuster, M., Dachev, Ts., Tomov, B. Dimitrov, P., Matviichuk, Yu., 2009. R3D-B2-Measurement of ionizing and solar radiation in open space in the BIOPAN 5 facility outside the FOTON M2 satellite. *Advances in Space Research: The Official Journal of the Committee on Space Research (COSPAR)* 43 (8), 1200-1211, <http://dx.doi.org/10.1016/j.asr.2009.01.021>.
16. Damasso, M., Dachev, Ts., Falzetta, G., Giardi, M.T., Rea, G., Rea, G., Zanini, A. 2009. The radiation environment observed by Liulin-Photo and R3D-B3 spectrum-dosimeters inside and outside Foton-M3 spacecraft. *Radiat. Meas.* 44 (3), 263-272, <http://dx.doi.org/10.1016/j.radmeas.2009.03.007>.
17. Reitz, G., Beaujean, R., Benton, E., Burmeister, S., Dachev, T., Deme, S. Luszik-Bhadra, M., Olko, P., 2005. Space radiation measurements on-board ISS-The DOSMAP experiment. *Radiation Protection Dosimetry* 116 (1-4), 374-379.

18. Dachev, Ts., Tomov, B., Matviichuk, Yu., Dimitrov, Pl., Lemaire, J., Gregoire, Gh., Cyamukungu, M., Schmitz, H., Fujitaka, K., Uchihori, Y., Kitamura, H., Reitz, G., Beaujean, R., Petrov, V., Shurshakov, V., Benghin, V., Spurny, F. 2002. Calibration results obtained with Liulin-4 type dosimeters. *Advances in Space Research* 30, 917–925 [http://dx.doi.org/10.1016/S0273-1177\(02\)00411-8](http://dx.doi.org/10.1016/S0273-1177(02)00411-8).
19. Nealy, J.E., Cucinotta, F.A., Wilson, J.W., Badavi, F.F., Zapp, N., Dachev, T., Tomov, B.T., Semones, E., Walker, S.A., Angelis, G.De, Blattnig, S.R., Atwell, W. 2007. Preengineering spaceflight validation of environmental models and the 2005 HZETRN simulation code. *Advances in Space Research* 40 (11), 1593–1610, <http://dx.doi.org/10.1016/j.asr.2006.12.030>.
20. Slaba, T.C., Blattnig, S.R., Badavi, F.F., Stoffle, N.N., Rutledge, R.D., Lee, K.T., Zapp, E.N., Dachev, T.P., Tomov, B.T. 2011. Statistical validation of HZETRN as a function of vertical cutoff rigidity using ISS measurements. *Advances in Space Research* 47, 600–610, <http://dx.doi.org/10.1016/j.asr.2010.10.021>.
21. Dachev, Ts.P. 2009. Characterization of near Earth radiation environment by Liulin type instruments. *Advances in Space Research*, 1441–1449, <http://dx.doi.org/10.1016/j.asr.2009.08.007>.
22. Berger, M.J., Coursey, J.S., Zucker, M.A., Chang, J. Stopping-power and range tables for electrons, protons, and helium ions, NIST Standard Reference Database 124, October, <http://www.nist.gov/pml/data/star/index.cfm>, 2013.
23. Heffner, J., Nuclear radiation and safety in space, M, Atomizdat, pp 115, 1971. (in Russian).
24. Galperin, Yu.I., Ponomarev, Yu.N., Sinizin, V.M. 1980. Some Algorithms for Calculation of Geophysical Information along the Orbit of Near Earth Satellites. Report No 544. Space Res. Inst., Moscow (in Russian).
25. McIlwain, C.E. Coordinates for mapping the distribution of magnetically trapped particles. *J. Geophys. Res.* 66, 3681–3691, 1961.
26. Dachev, Ts.P., Tomov, B.T., Matviichuk, Yu.N., Dimitrov, Pl.G., Bankov, N.G., Reitz, G., Horneck, G., Häder, D.-P., Lebert, M., Schuster, M. 2012b. Relativistic electron fluxes and dose rate variations during April–May 2010 geomagnetic disturbances in the R3DR data on ISS. *Advances in Space Research* 50, 282–292 <http://dx.doi.org/10.1016/j.asr.2012.03.028>.

ПРЕДВАРИТЕЛНИ РЕЗУЛТАТИ ЗА РАДИАЦИОННАТА ОБСТАНОВКА НАБЛЮДАВАНА С ДОЗИМЕТЪРА- РАДИОМЕТЪР RD3-B3 НА СПЪТНИКА BION-M № 1

*Ц. Дачев, Б. Томов, Ю. Матвийчук, П. Димитров, Н. Банков,
В. Петров, В. Шуришаков, О. Иванова, Д.-П. Хедър, М. Леберт,
М. Шустер, Г. Райтц, Г. Хорнек, О. Плоц*

Резюме

Космическата радиация е измерена със спектрометъра-дозиметъра РДЗ-БЗ (в статията се използва латинската транскрипция RD3-B3) на борда руския възвращаем спътник БИОН-М № 1 (в статията се използва латинската транскрипция BION-M № 1). Уредът е монтиран във вътрешната част на спътника, заедно с биологични обекти и проби. Приборът RD3-B3 е работеща на батерии версия на резервния модел на прибора R3D-B3, разработен и изработен за платформата на ESA BIOPAN-6 летяла на спътника Foton M3 през септември 2007 година. Космическото йонизиращо лъчение е наблюдавано с 256 канални спектри на погълнатата енергия, които по-нататък се използват за определяне на погълнатата доза и поток. Докладът представя първите резултати за радиационната обстановка на височина (253-585 km) на спътника БИОН-М № 1.

SYNCHRONIZATION OF HEART RATES AND GEOMAGNETIC FIELD VARIATIONS: A PILOT STUDY

**Tatjana Zenchenko^{1,2}, Malina Jordanova³, Lilia Poskotinova⁴,
Anna Medvedeva¹, Todor Uzunov⁵, Alexandra Alenikova⁴, Tamara Breus²**

¹*Institute of Theoretical and Experimental Biophysics, Russian Academy of
Sciences, Pushchino, Russia*

²*Space Research Institute – Russian Academy of Sciences*

³*Space Research and Technology Institute – Bulgarian Academy of Sciences*

⁴*Institute of Environmental Physiology, Ural Branch of Russian Academy of
Sciences, Arkhangelsk, Russia*

⁵*nethelpforums.net, Sofia, Bulgaria
e-mail: mjordan@bas.bg*

Abstract

The project “Heliobiology” (2011 – 2015) reflects the intense interest towards the influence of solar activity on the human health. One of its tasks is to study the putative relationship between geomagnetic activity and the changes of heart rate variability in healthy volunteers.

The paper presents the first results from 5 simultaneous experiments performed in 2013 at 3 different latitudes - Sofia, Moscow and Arkhangelsk. The aim of the experiment is to study the degree of conjugation of the heart rate variability with the variations of the geomagnetic field.

To minimize the experimental bias one and the same hard- and software is applied during the testing. ECG signals are recorder via "KARDI-2"; the software package is "Ecosan-2007", both developed by "Medical Computer Systems", Zelenograd, Russia. The duration of the observations ranged from 60 to 100 minutes. A comparison of the dynamics of the minute variations of the heart rate with the horizontal components of the geomagnetic field vector has revealed a synchronization of the research parameters. Further experiments are planned in the years to come to confirm the results in a larger experimental group.

Introduction

Geomagnetic field is a natural phenomenon. When the Earth was formed 4.5 billion years ago magnetic fields were already present.

Long before the appearance of human species, almost 2 billion years ago, marine magnetotactic bacteria evolved. Magnetotactic bacteria developed membrane-encapsulated nano-particles known as magnetosomes. Magnetosomes allowed and still permit bacteria to orient themselves along the Earth's magnetic field lines in order to migrate to more favorable environments. Magnetosomes are result of Earth's evolution. They contain the iron-oxygen composite, magnetite, and presumed to play a key role in navigation. Magnetosomes are widely speared over various species. Example is the avian magnetic compass, developed 90 million years ago, enabling pigeons to detect magnetic field changes from 20 nT to 0.02 μ T or even lower. To put it short: Geomagnetic sensitivity is phylogenetically widespread. It exists in fishes, major groups of vertebrate animals (chickens, mole rats, etc.), as well as in some mollusks, crustaceans and insects [1] Humans are not an exception.

When humans are concerned the impact of the geomagnetic field (GMF) variations on health is an underexplored area. Studies revealed that geomagnetic variations may causes changes in the normal functioning of the central and vegetative nervous systems, cardiovascular system and cognitive performance [2-7]. It is already accepted that:

- A subset of the human population (10-15%) is not only sensitive but a bona fide hypersensitive and predisposed to adverse health problems due to geomagnetic variations;
- Extremely high as well as extremely low values of geomagnetic activity seem to have opposing health effects;
- Geomagnetic effects are more pronounced at higher magnetic latitudes.

The biological mechanism of geomagnetic variations on human health is not clear. Researchers are trying hard to understand magnetic sensitivity which still remains one of nature's extraordinary secrets. During last decades two theories are widely discussed. According to the first melatonin hypotheses temporal geomagnetic variations are acting as an additional zeitgeber (a temporal synchronizer) for circadian rhythms. The second, Cryptochrome gene hypothesis, considers that changes in the geomagnetic field are mediating stress responses more broadly across the

hypothalamic–pituitary–adrenal axis. To use different wording – in both cases the reactions of biological systems to geomagnetic field variations is supposed to be evident when the main frequencies present in the spectrum of geomagnetic fluctuations is similar to the main frequencies of the physiological processes [8-11]. Despite of the fact that some experimental results supporting the above statement were published recently [12] sufficient amount of experimental data with humans is still lacking. The authors of this paper have already found similar periods in the spectra of the heart rate variations and in the vector components of GMP in the milli hertz frequency range. The periods were not only similar but they appeared and disappeared at one and the same time. The synchronization effect was observed in small group of health volunteers [13-14].

It is well-known that the decreasing of the geographical latitude results in a reduction of the amplitude variations of the magnetic field vector. The aim of this experiment is to study the degree of conjugation of the heart rate variability and the variations of the geomagnetic field at one hand and its dependence on the latitude of the place of observation on the other. To do this, simultaneous monitoring of heart rate variability of healthy volunteers was conducted at three geographic locations.

Methodology

At the very beginning it is necessary to underline that the experiment is difficult and time consuming. It is also connected with lots of ethical principles that have to be respected and were followed strictly, i.e. (a) an informed consent from research participants was obtain before the experiment; (b) the risk of harm to participants was minimized; (c) participants had the right to withdraw from the research; (d) deceptive practices were avoided; and (e) participants anonymity and confidentiality is protected and their real names will not be revealed. In this paper the participants or subjects are marked as No. 1, No. 2 etc.

Subjects are 5 healthy volunteers, women, mean age 39,4 years – 1 in Sofia, 2 in Moscow and 2 in Arkhangelsk.

Locations of the experiment and their latitudes are: Sofia, Bulgaria 42° 40' N 23° 20' E; Moscow, Russia 55° 45' N 37 ° 36' E and Arkhangelsk, Russia 64° 34' N / 40° 32' E.

The procedure is as follows: Monitoring of heart rate activity is performed simultaneously in the 3 locations. The four leads electrocardiogram (ECG) is recorded at rest, in a supine position, after a 10-

minute adaptation. There are specific dietary requirements to be followed 24 hours before the experiments, i.e. exclusion of some types of drugs, natural stimulants, etc.

To minimize any potential bias of the results one and the same device, specified for measuring electrical micro alternation of ECG, Kardi-2, is used. The software package is "Ecosan-2007". Both are developed by "Medical Computer Systems", Zelenograd, Russia. The duration of the observation periods ranged from 60 to 100 minutes.

Parameters used in the analysis are:

- Physiological - the minute values of heart rate (HR);
- Geophysical – the minute values the horizontal components of the geomagnetic field.

Geomagnetic data were derived from 2 geomagnetic stations for each location, i.e.

- For Archangel (64° 34' N / 40° 32' E) data from the geomagnetic stations Sodankyla (SOD, 67.400 26.600) and Nurmijarvi (NUR, 60.500 N, 24.600 E) were used;
- For Moscow (55° 45' N / 37° 36' E) data from the geomagnetic stations Borok (BOX, 58.070 N, 38.230 E) and Kiev (KIV, 50.70 N, 30.30 E) were used;
- For Sofia (42° 40' N / 23° 20' E) data from the geomagnetic stations Panagjurishte (PAG, 42.50 N, 24.20 E) and Surlari (SUA, 44.68 N, 26.25 E) were used.

The INTERMAGNET network (International Real-time Magnetic Observatory Network, http://ottawa.intermagnet.org/Welcom_e.php) listed for free all these data.

The aim of the experiment is to look for synchronized minute variations of the heart rate indices that match the minute variations GMF.

Analysis and Results

MATLAB R2010a software was applied for the analysis. Priorly the calculations the linear trend was excluded from all analyzed time series. To delete a range of high-frequency noise, the constant component of the signal and the linear trend, the records were passed through a band pass filter with a Blackman-Harris window with the values of the lower and upper cut-off frequencies, respectively, 0.025 and 0.95 of the Nyquist frequency.

When physiological parameters are concerned important is not only the presence or absence of a certain period in the signal spectrum, but also

the time of its appearance and disappearance. The records analyzed in these experiments were relatively short – from 60 up to 100 minutes. This does not allow applying the method of spectral-temporal transformation. A more convenient for this case, the method of wavelet transformation (applied in digital signal processing and exploration geophysics) with the basic function of Morlet [15] is used.

To make the comparison of the results easier, large-scale parameters obtained in the wavelet analysis, have been converted into temporary characteristics similar to the period of oscillation in the spectral analysis.

Geomagnetic conditions at the time of observation: The geomagnetic activity was low in the days of the experiments. The values of the three-hour Kp index at the time of the experiments ranged from 0 to 1.7 according ftp://ftp.ngdc.noaa.gov/STP/GEOMAGNETIC_DATA/INDICES/KP_AP

The horizontal components of the GMF at the time of the experiments are presented at Fig. 1. Time series are shown after applying thereto a band pass filter, i.e. bring them to a form suitable for comparison with the physiological data.

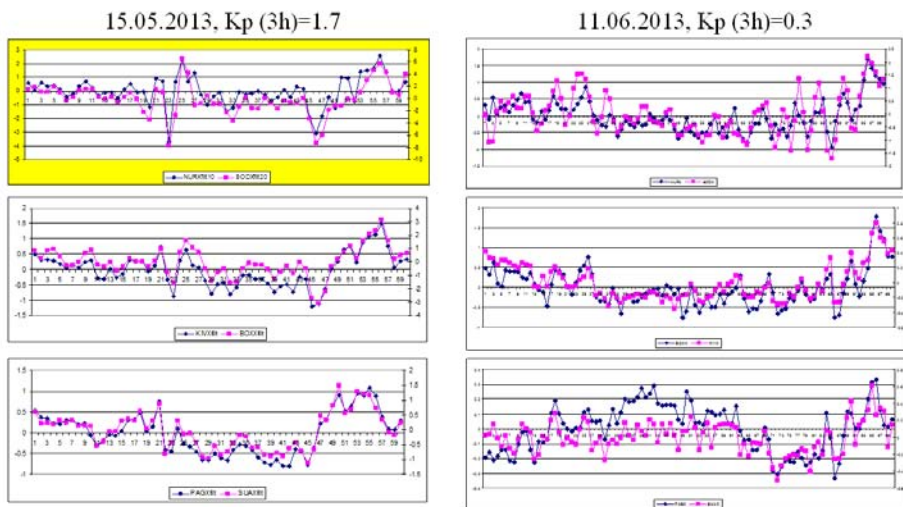


Fig. 1. Comparative dynamics of the horizontal components of the geomagnetic field at the time of one of the synchronous experiments (15.05.2013, 07-08 UT)

The figure reveals that the variations of the horizontal component of the GMF are very close despite of the significant distance between the recording stations. At the same time, the comparison of the GMF variations at different latitudes and the comparison of the magnitude scales show that

the amplitude of the rapid variations decreases with the decreasing latitude, a fact that is in correspondence within the nowadays understanding of the behavior of GMF variations. Such a comparative analysis was performed for all five experiments.

In contrast to the horizontal X-component, the minute variation of the vertical component Z of GMF is highly dependent on the underlying surface at the point of measurement. As the experiments are performed far away from the recording geomagnetic stations, the dynamics of the Z-components cannot be used in the statistical analysis.

Figures 2 and 3 present the results of wavelet analyses of two out of the five experiments.

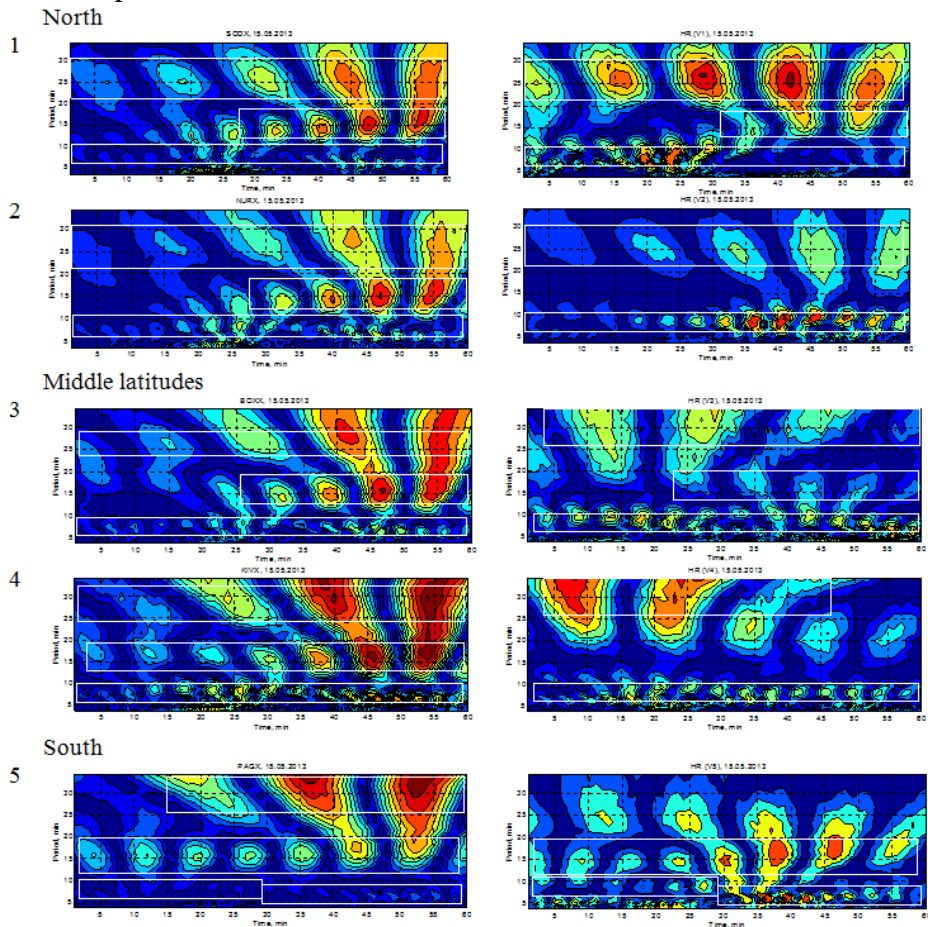


Fig. 2. The wavelet transform of time series of geophysical and physiological data, 15.05.2013

Fig. 2 reveals the results from experiments performed on 15.05.2013, starting at 7 UT. The left column contains the wavelet images of minute variations of GMF. The order of the data is as follows (1) Sodankyla (67.4167° N, 26.5833° E), (2) Nurmijarvi (60.4667° N, 24.8083° E), (3) Borok ($49^{\circ} 51' 0''$ N, $31^{\circ} 34' 0''$ E), (4) Kiev (50.4500° N, 30.5233° E), (5) Panagjurishte (42.5000° N, 24.1833° E), i.e. the latitude is descending. The right column contains images of wavelet time-series of the heart rate data, measured in corresponding latitudes - (1) and (2) are subjects No.1 and No.2 in Arkhangelsk , (3) and (4) – subjects No. 3 and No. 4 in Moscow while No. 5 - in Sofia.

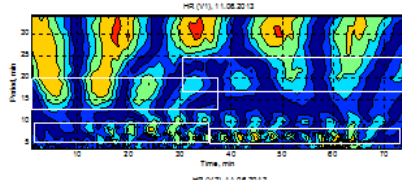
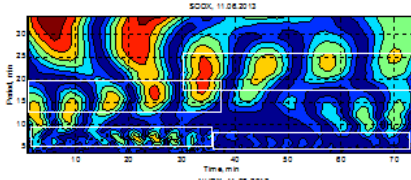
Applying wavelet analyses similarities were searched for in the patterns of variation of GMF and heart rates. No matter whether the geomagnetic data or the heart rates were analyzed, the following requirements were fixed - periods must not be smaller than 3 and not larger than 33. The boundaries of 3 and 33 gave the chance to delete noise and yet to “catch” available periods in the data. The upper level of 33 was chosen as the experimental lines of the physiological measurements in part of the experiments do not exceed 60 minutes. Thus even if there are only 2 periods during an experiment, they will be marked. The upper level 33 also explains why on the Y axes the maximum mark is 35.

The analysis of the five figures in the left column reveals 3 periods in horizontal variations of the components of the GMF – 7-10 minutes, 15 minutes and 25-28 minutes. They are indicated with white rectangles on the figure. The first period (7-10 minutes), although present in all measure, has a lower intensity and is less pronounced in the southern latitude (5). The second one (15 minutes) is observed during all the experiments in the southern latitudes. It is also evident in middle latitudes (parts 1-3) too but with a slight delay - approximately after 30 minutes from the beginning of the experiment. On the contrary, the third period (25-28 minutes), is visible throughout the experiment in northern latitudes (with increasing amplitude to the end of the experiment), while at the southern (5) is exposed as separate perturbations somewhat to the second half of the experiment.

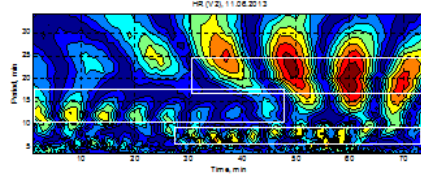
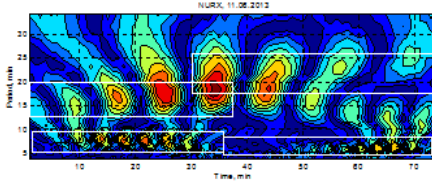
The comparisons of the dynamics of the heart rate variability and the GMF variations have a significant number of matches. Thus, for subjects No. 1-4 wavelet spectra reveals a period 25-27 minutes. Its amplitude is increasing in the second half of the experiment especially in the data of subjects No. 1 and 2, tested in the most northern location, i.e. the dynamic is similar to the variations in the geophysical rows.

North

1

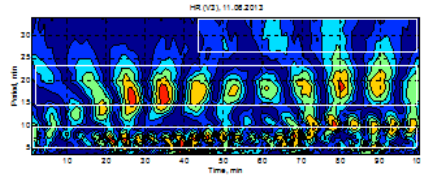
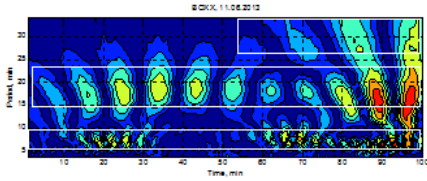


2

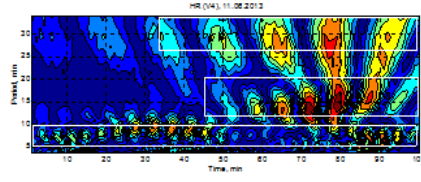
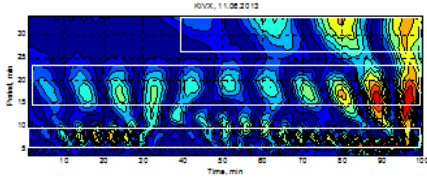


Middle latitudes

3



4



South

5

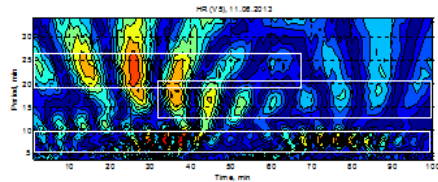
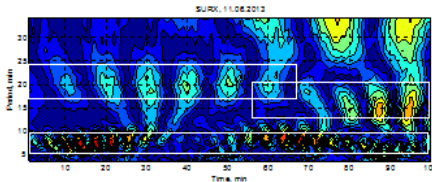


Fig. 3. The wavelet transform of time series of geophysical and physiological data, 11.06.2013

A 15 minutes period is evident in the southern latitudes. It is clearly visible throughout the entire experiment in both physiological and geophysical data. To a larger extent it is also present in the results of subjects No. 1 and 3 in the second half of the experiment and is observed as a decrease in the value of the longer, 27 -minute, period.

A period of 9-10 minutes, rather similar to the 7-10 minutes period revealed in the geophysical series, is detected in the physiological records of all 5 subjects. The fact that the time of the maximum amplitude of this

period is different for different subjects is not a surprise. Even though strong emotional stimuli were excluded from the experimental environment, short-term (1-2 min) changes in the level of heart rate may be result of differences in personalities of the subject participating in the experiment or be provoked from their thoughts.

Figure 3 shows the results of an experiment conducted by 11.06.2013, starting time of the experiment – 7 UT. The dynamics of the horizontal component of the GMF variation is on the right side, while the left side presents the heart rate variability.

The comparative analysis of the different spectral components of the geomagnetic variations at different latitudes discloses that a period of 7-10 minutes, despite of changes in its intensity, is represented in all five wavelet spectra over the entire period of the observation. The same period is shown in all wavelet spectra of the heart rate variations.

Another period that is detected is a 15-20 minutes one. The dynamics of this period is different at different latitudes. It started as a 15 minutes period in the Northern latitude during the first half of the experiment. 30 minutes after the beginning of the experiment it increases to 20-23 minutes. In the middle latitudes (BOXX and KIVX) its value is approximately constant at 17 minutes, while in the South is 20 minutes in the first half and 15 in the second half of the observation. A similar trend is revealed in the variability of the physiological data. The match between the geophysical variability and heart rate variability is rather good in 3 out of 5 subjects tested (No. 1, 3 and 5).

Individual differences between subjects taking part in the experiment could also be detected. For example, heart rate variability of subject No. 4 demonstrates a period of 15 minutes only the second half of the experiment, whereas GMF values in middle latitudes contained a period of 20 minutes during the entire observation period.

The result of the analyses all five experiments are summarized in Table 1.

Table 1

	19.04.2013	15.05.2013	17.05.2013	11.06.2013	13.06.2013
No. 1					
No. 2			No measures		
No. 3					
No. 4					
No. 5	No measures				

The grey color indicates the “full” matches between geophysical data and heart rate data, i.e. the trends, moments of appearance and the end of the periods, changes in the average. Such matches are especially evident in the records of subject No. 3 on Fig. 2 and 3.

The white (no color) color indicates the experiments in which there are small fragments that are not presented simultaneously in both geophysical and physiological data lines, despite of the fact that all other parameters match. Example is the record of subject No. 5 from 15.05.2013. During that experiment only 2 out of 3 periods are matching. The dark grey color indicates very weak match, i.e. the there is only one period of coincidence as for examples data received from subject No. 4 on 15.05.0213.

Conclusion

The pilot experiments revealed that the matches of the variations of heart rates and the variations of the horizontal component of the geomagnetic vector are observed not only in the North but also in the southern latitudes. The sample presented in this paper is not sufficient to make firm conclusion about the correlation between the trends in the variability of GMF vector and physiological parameters recorded. More extensive study is required. However, the results received demonstrate that it is worth dedicating efforts and time to study the above mentioned trend in more details as well as to expect strong correlation. Based on the results summarize in Table 1 the conclusion is that event in the available small sample size (5 subjects per 5 measures) 47,8% (grey color) of the data revealed fully matching of geophysical and physiological data. In additional 30,4% the variation trends of the physiological and geophysical parameters is high although not entirely identical (white color). Or, in 78,2% of the experimental data a similar patterns of variation of geophysical and heart rate variability is recorded.

Experiments, as those described in this paper, are important. The experiments discussed in the paper involved healthy volunteers, i.e. people that have good adaptation reserves, and the response to variation of GMF will not push them beyond the physiological norms. However, for people suffering from cardiovascular diseases such as instability of sinus node function, external factors affecting the generation of the cardiac impulse and controlling the heart rate may cause serious problems. The observed effect of synchronization of heart rate fluctuations of healthy subjects with

fluctuations in GMF may give us an effective tool to address further one of the most important tasks geliobiophysics – the revealing the mechanism of geomagnetic sensitivity.

References

1. H e n s h a w , D . The interaction of magnetic fields with biological systems – trying to understand the diversity of reported health effects, Paper presented at the Joint Annual Meeting of the Association for Radiation Research and The United Kingdom Environmental Mutagen Society, University of Nottingham, UK, June 29 - July 1, 2011, available at <http://www.electric-fields.bris.ac.uk>
2. J o r d a n o v a , M . e t a l . The influence of solar activity and meteorological factors on human cerebral pathology, Presentation at Space Weather Effects on Humans in Space and on Earth, June 4-8, 2012, Moscow, Russia, http://swh2012.cosmos.ru/sites/new.swh2012.cosmos.ru/files/presentations/SWH_2.21_Jorganova.pps
3. M i k u l e c k y , M . , S t ř e š t n ě k J . Cerebral Infarction vs. Solar and Geomagnetic Activity, IMAJ, 9, 2007, pp. 835–838
4. G r i g o r y e v , P . e t a l . Heliogeophysical factors as possible triggers of suicide terroristic acts; Health, 1, 4, 2009, 294-297
5. B e r k , M . e t a l . Do ambient electromagnetic fields affect behaviour? A demonstration of the relationship between geomagnetic storm activity and suicide, Bioelectromagnetics, 27, 2, 2006, 151-155
6. G u r f i n k e l , I u . E t a l . Assessment of the Effect of a Geomagnetic Storm on the Frequency of Appearance of Acute Cardiovascular Pathology, Biofizika, 43, 4, 1998, 654-658
7. G o r d o n , C . , B e r k M . The effect of geomagnetic storms on Suicide, South African Psychiatry Review, 6, 2003, 24-27
8. R a p o r t , S . I . , B r e u s T . K . Melatonin as a most important factor in the action of weak natural magnetic fields on patients with hypertensive disease and coronary heart disease. Клиническая медицина, 2011, 3, 9-14 and Vol. 4, 4-7
9. N e i l , C . Schumann Resonances, a plausible biophysical mechanism for the human health effects of Solar/Geomagnetic Activity, Natural Hazards 26, 2002, 279–331
10. К л e й м e н o в a , Н . Г . и д р . Сезонные вариации инфаркта миокарда и возможное биотропное влияние короткопериодных пульсаций геомагнитного поля на сердечно-сосудистую систему. Биофизика, 52, 2007, 6, 1122-1119
11. П o б a ч e н к o , С . В . и д р . Сопряженность параметров энцефалограммы мозга человека и электромагнитных полей шумановского резонатора по данным мониторинговых исследований, Биофизика, 51, 2006, 3, 534-538

12. M a x i m o v , A . L . e t a l . About Resonance Interaction of Schumann's Biospherical Frequencies And Human Brain Rhythms VI International Congress "The weak and super-weak fields and radiation in biology and medicine", St-Peterburg, June 2-6, 2012, 168, www.biophys.ru/archive/congress2012/proc-p168.pdf
13. Z e n c h e n k o , T . Synchronization of Human Cardiac Rhythm Indices and 0.3 – 3 MHz Geomagnetic Field Variations, Proceedings of International Conference "Space Weather Effect on Humans: in Space and on Earth", Moscow, June 4-8, 2012, 120-121.
14. Z e n c h e n k o , T . e t a l . Synchronization of Heart Rate Indices of Healthy People and 0.3 – 3 MHz Geomagnetic Field Variations, Paper presented at VI International Congress "The Weak and Super-Weak Fields and Radiation in Biology and Medicine", St-Peterburg, June 2-6, 2012, available at www.Biophys.Ru/Archive/Congress2012/Proc-P152.Pdf
15. П о с т н и к о в , Е . Б . Вейвлет-преобразование с вейвлетом Морле: методы расчета, основанные на решении диффузионных дифференциальных уравнений, Компьютерные исследования и моделирование, 1, 2009, 1, 5–12, available at <http://crm.ics.org.ru/uploads/kim1/crm09101.pdf>

СИНХРОНИЗАЦИЯ НА ВАРИАБИЛНОСТИТЕ НА СЪРДЕЧНИЯ РИТЪМ И ГЕОМАГНИТНОТО ПОЛЕ: ПИЛОТНО ПРОУЧВАНЕ

**Т. Зенченко, М. Йорданова, Л. Поскотинова, А. Медведева,
Т. Узунов, А. Аленкова, Т. Бреус**

Резюме

Проектът "Heliobiology" (2011 - 2015) отразява големия интерес към влиянието на слънчевата активност върху здравето на човека. Една от задачите му е да проучи предполагаемата връзка между геомагнитната активност и промените на вариабилността на сърдечната честота при здрави доброволци.

Статията представя първите резултати от 5 едновременни експерименти, извършени през 2013 г. в три различни географски ширини - София , Москва и Архангелск . Целта на експеримента е да се изследва степента на съответствие във вариабилността на сърдечната честота и вариации на геомагнитното поле.

За да се намали влиянието на редица странични фактори една и съща апаратура се използва за регистрация на сърдечните параметри и в трите града. Тава е ЕКГ холтер "Kardi -2" със софтуерен пакет е

"Екосан - 2007", разработени от " Медицински компютърни системи", Зеленгород, Русия. Продължителността на експериментите варира от 60 до 100 минути. Сравнението на динамиката на минутните промени в сърдечната честота с хоризонталната компонента на вектора на геомагнитното поле разкри синхронизация на изследваните параметри независимо от географската ширина. Допълнителни експерименти са планирани в следващите години, за да се потвърдят резултатите на по-голяма експериментална група.

DETECTION AND ASSESSMENT OF ABIOTIC STRESS OF CONIFEROUS LANDSCAPES CAUSED BY URANIUM MINING (USING HYPERSPECTRAL EO-1/HYPERION DATA)

Lachezar Filchev

*Space Research and Technology Institute – Bulgarian Academy of Sciences
e-mail: lachezarhf@space.bas.bg*

Abstract

*The paper presents the results from a study aiming at detecting and assessing abiotic stress in coniferous landscapes of Black pine monocultures (*Pinus nigra* L.) by using ground-based geochemical data, models of technogenic pollution, and satellite hyperspectral data from EO-1/Hyperion. Four vegetation indices (VIs), such as, MCARI, TCARI, MTVI 2, and PRI, as well as the shape and area attributes of the red-edge spectral features, have been studied in order to detect changes caused by the geochemical pollution. The analysis was performed on 4 test sites sized each 30m × 30 m, to correspond to EO-1/Hyperion pixel subspace, in homogenous coniferous landscapes in the Teyna River basin – a left tributary to Iskar River. In effect, the red-edge position index for unstressed coniferous landscapes (Black pine) was found to be at about $\lambda=683$ nm, whereas the stressed ones' red-edge position is at $\lambda=671$ nm. It was found that VIs, such as TCARI/MCARI and Z_c has highest correlation ($r^2=0.63$; F: 5.20 at F: <0.1), followed by MTVI 2 and Z_c ($r^2=0.42$; F: 2.48 at F: <0.21), and PRI and Z_c ($r^2=0.30$; F: 1.34 at F: <0.33). Subsequently, the four test sites chosen were subdivided in two pairs, corresponding to the modeled Z_c values after Inverse Multiquadratic Function (IMF) from the set of Radial Basis Function (RBF), into unstressed (test sites No. 2 and No. 5) and stressed coniferous landscapes (test sites No. 10 and No. 11). The hypothesis tested is that the clustering of EO-1/Hyperion VIs corresponds to Z_c clustering using hierarchical clustering method (Ward). As a result, the MTVI 2 and TCARI/MCARI values group their first cluster relatively farther than Z_c but the PRI does not reflect the Z_c clusters. This lead to the conclusion that the satellite hyperspectral narrowband VIs are still not sensitive enough to study the geochemical background and vegetation stress of geochemically stressed coniferous landscapes by uranium mining without a priori ground based data.*

1. Introduction

Nature features cannot be measured directly by remote sensing. Usually the reflectance in different spectral bands is correlated with ground-measured forest attributes (Dimitrov and Roumenina, 2012). By the incremental and non-specific changes in those forest characteristics it is possible to detect negative and positive changes. From botanist point of view it is accepted that plant stress is: “state in which increasing demands made upon a plant lead to an initial destabilization of functions, followed by normalization and improved resistance” (Lichtenthaler, 1996). Furthermore, “If the limits of tolerance are exceeded and the adaptive capacity is overworked, the result may be permanent damage or even death” (Larcher 1987; Lichtenthaler, 1996). The plant stress is further differentiated by its driving force, direction (positive or *eu-stress* and negative *dis-stress*), phases (*response*, *restitution*, *end*, and *regeneration* phase) and the scale of its impact (Lichtenthaler, 1996). A classification of the abiotic stressors and their impact on the spectral characteristics of coniferous vegetation at particular wavelengths of the spectrum has been done recently (Jones and Schofield, 2008). In present study the studied stress driving factors are: heavy metals and natural radionuclides. The possible use of hyperspectral satellite missions such as CHRIS/PROBA (ESA) and EO-1/Hyperion (NASA) for forest monitoring and chemical vegetation stress have been addressed in several publications recently (Peddle *et al*, 2008; Filchev, 2013; Filchev and Roumenina, 2013). However, the still experimental technology and the limited capabilities of the hardware, including telemetry, calibration, as well as the high volume of data coming from hyperspectral sensors, are still preventing the widespread use of hyperspectral data.

The motivation for the study is based on the fact that coniferous forests in Bulgaria cover over 1.2 million ha, which represents 31 % of the forested area (NSI, 2008; Dimitrov and Roumenina, 2012). Furthermore, during the past decade in Europe have been implemented a series of projects under FP6 and FP7 as well as on national levels which deal with the utilization of hyperspectral remote sensing data for detection of stress and monitoring of pollution in mining environments (Filchev and Roumenina, 2013). In Bulgaria the potential use of multispectral and hyperspectral Remote Sensing (RS) satellite and airborne data, for detection and assessment of pollution from mining, has been studied since the beginning of 80s of 20th century (Mishev *et al*, 1981, 1987; Roumenina, 1991; Spiridonov *et al*, 1992; Velikov *et al*, 1995). For studying the level and the

pathways of the pollution of the soil-vegetation system in the vicinity of former *Devnya* enterprise, *Kremikovtzi* metallurgic enterprise, and *Kardzhali* metallurgic enterprise were created landscape maps with the use of multispectral images from MKF-6M and panchromatic images from MRB, onboard of AN-30, as well as from the satellites ERTS, Landsat and Salut 4. In order to study the level of the anthropogenic load is used the coefficient of technogenic load or concentration - K_c , which is also used in present study. Later on, geoinformation technologies are used in ecological risk assessment and health assessment of the spruce forests of *Chuprene* Man And Biosphere (MAB) UNESCO reserve (Roumenina and Dimitrov, 2003; Roumenina *et al*, 2003). The interest in studying the effects from geochemical pollution had gained momentum and was continued and further developed by employing field spectrometry data in the works of (Nikolov *et al*, 2005; Kancheva and Borisova, 2005, 2007, 2008; Kancheva and Georgiev, 2012; Filchev and Roumenina, 2012, 2013).

The objective of the study is to detect and assess abiotic stress of coniferous landscapes, composed of monoculture European Black pine forests (*Pinus nigra L.*), caused by uranium mining by using hyper spectral Earth Observing (EO)-1/Hyperion satellite data and ground based geochemical data.

1.1. Study area

The study area comprises the river basin of the *Teyna* River. It is located between 42°50'N and 40°51'N latitude and 23°19'E and 23°20'E longitude and occupies an area of 4,775 km² with altitude varying from 500 m a.s.l. at the influx of the *Teyna* River into the *Iskur* River to 964 m a.s.l., i.e. the highest parts of the water-catchment (Filchev, 2009; Filchev and Yordanova, 2011; Filchev and Roumenina, 2013). The dominating vegetation type is presented by mono-culture plants of Scots pine (*Pinus sylvestris L.*) and European Black pine (*Pinus nigra L.*) in the place of the natural oak (*Quercus sp.*) (Bondev, 1991; Filchev and Roumenina, 2013).

Iskra uranium mining section:

The *Iskra* uranium mining section is located in the river basin of the *Teyna* River (area 4.87 ha) (Roumenina *et al*, 2007; Naydenova and Roumenina, 2009). Within the section were developed 12 embankments, 1 quarry, and 2 technological sludge pans. In 1956 after open-pit mining technique started the development of the deposit. The classical mining in the section ended in 1962. In 1984 geotechnological mining was started, and

was decommissioned in 1990. The technological liquidation, biological restoration, and reclamation started after 1994 based on Decree No.163/20.08.1992 of the Council of Ministers and Order No.56 of the Council of Ministers from 29.03.1994 (Simeonova, Ignatov, Mladenov, 1993; Banov and Hristov, 1996; Naydenova and Roumenina, 2009). The environmental conditions in the studied region were additionally complicated by the correction of the river bed which caused almost total draining of the surface waters through adits in the *Kisseloto ezero* (Filchev and Yordanova, 2011).

2. Materials and methods

2.1. Data

In this study two types of data are used – ground-based and satellite data.

Ground-based data:

During the ground-based studies conducted in 2010–2011 on the *Iskra* mining section, the following data were collected: GPS measurements for more accurate georeferencing of the satellite data. The test sites were sized 30m × 30m, which is the ground projection of EO-1/Hyperion pixel (Filchev and Roumenina, 2013). The assessment of the geo-chemical condition of the test area was based on an archive data and published articles, (Simeonova, Ignatov, Mladenov, 1993; Banov and Hristov, 1996; Georgiev and Grudev, 2003).

Satellite data:

One scene from the EO-1/Hyperion satellite spectroradiometer acquired in 21 August 2002 (ID EO1H1840302002233110PZ), distributed by the United States Geological Survey (USGS), was used. The EO-1/Hyperion data is distributed in Hierarchical Data Format (HDF) 4.1 (or 5 edition) or Geographic Tagged Image-File Format (GeoTIFF) recorded in band-interleaved-by-line (BIL) files. The data quantisation (digital numbers – DN) is 16 bits and the scene total width is 7.5 km and the length is 42 km. From 242 bands in the spectral region: (λ 357 ÷ 2576 nm), 220 are unique, i.e. they do not spectrally overlap. Fully calibrated are 198 bands but due to the overlap in the Visible and Near InfraRed (VNIR) their number is reduced to 196 bands. The calibrated bands are respectively, from 8th to 57th band in the VNIR and from 77th to 224th for the Shortwave InfraRed (SWIR). With the increase of the wavelength (λ) Signal-to-Noise Ratio (S/N Ratio) of the EO-1/Hyperion decreases from 190:1 to 40:1

(Pearlman, Segal et al. 2000). The scene under investigation represents the study area 10 years after uranium mine decommissioning. The satellite data and the vector layers used in the analysis were transformed into World Geodetic System (WGS 84) datum, Universal Transverse Mercator (UTM), Zone 35N projection. The 16-bit integer values of the .hdf files were converted into spectral radiances (Beck, 2003). This was followed by selection of EO-1/Hyperion spectral channels 6–57 and 77–92, which are calibrated and correspond to ASD HH FS Demo 1445 spectral range used in previous study of the authors (Filchev and Roumenina, 2013). The spectral resolution of EO-1/Hyperion in the VNIR part of the spectrum is 10 nm, which provides to derive information about the position of the red edge and narrow-band VIs. QUICK Atmospheric Correction (QUAC) algorithm was applied on the selected channels in the respective spectral range using the module QUAC in ENVI (Bernstein, Adler-Golden *et al.* 2005; ENVI Atmospheric Correction Module User's Guide, 2010).

2.2. Data processing and analysis

2.2.1. Aggregate pollution index Z_c

Forest maps from the regional forestry services of the town of *Novi Iskar* were used in order to establish the heavy metal, metalloids, and radionuclide pollution in the examined region (Filchev and Yordanova, 2011; Filchev and Roumenina, 2012; Filchev and Roumenina, 2013). In order to determine the test sites a stratified random sampling was made within European black pine forests (McCoy, 2005). This sampling resulted in the 15 randomly distributed test sites (Filchev and Yordanova, 2011; Filchev and Roumenina, 2013).

According to the developed model it is envisaged to perform a GIS analysis by integrating the results from the processing of the satellite images at test site level. The test sites are sized 30 m × 30 m, i.e. the same size as is the spatial resolution of 1 pixel from EO-1/Hyperion. The test sites were chosen within landscape units characterized with the exact composition of natural and semi-natural environmental features. Some biometric parameters of coniferous trees, such as: tree density, age, and height (derived from forestry maps) were chosen to be homogeneous within the landscape units in order to eliminate the bias in collecting the spectra from EO-1/Hyperion image. This provides for a selection of 4 out of 15 test sites for analysis. Furthermore, the four test sites were grouped in two pairs appeared to be more contrasting in terms of aggregate pollution index - Z_c values, and

hence under different stress conditions. This provides for the statistical representation of the integral assessment, as well as for the required spatial level of detail for analysis by additional ground-based data of the technogenic load of the examined region (Fig. 1).

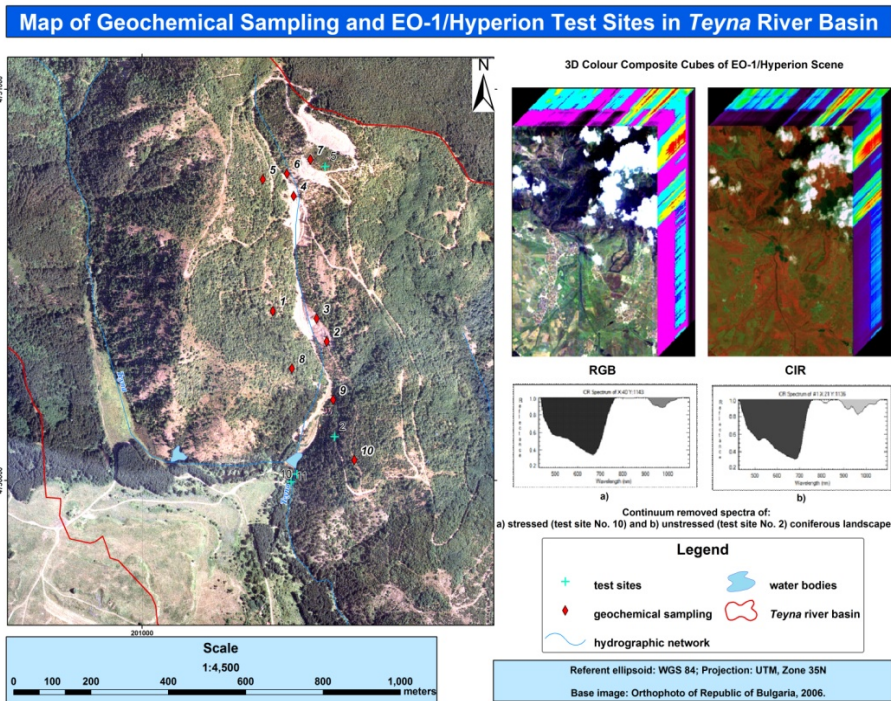


Fig. 1. Map of ground truthing and EO-1/Hyperion test sites in Teyna river basin

The assessment of the technogeochemical state of the examined coniferous landscapes for 1996 was made using the aggregate pollution index (Z_c), see equation 1, with respect to the background concentrations (Saet, Revich, Yanin, 1990; Vodyanitskii, 2010):

$$(1) \quad Z_c = \sum_{i=1}^n K_c - (n - 1) \quad .$$

where K_c is the technogenic concentration coefficient with $K_c > 1$ (or 1.5), representing the ratio of heavy metal and metalloids concentrations and/or the specific activities of natural radionuclides in the topsoil (0-20 cm) to the background concentrations and specific activities determined for the

examined region (Filchev and Yordanova, 2011; Filchev and Roumenina 2012; Filchev and Roumenina 2013):

$$(2) \quad K_c = \frac{C}{C_{background}} \quad .$$

The distribution fields of Z_c were made using Geostatistical Analyst Extension in ArcInfo/ArcGIS 9.2 (Academic license). The interpolation method used for calculating the K_c and Z_c was the Inverse Multiquadratic Function (IMF) from the set of the Radial Basis Functions (RBF), since the Root Mean Square Error (RMSE) has found to be the lowest compared to other interpolation methods during cross-validation of the resulting layers (Filchev and Yordanova, 2011; Filchev and Roumenina, 2013).

2.2.2. *Red-edge position*

For present study the red-edge position, depth, asymmetry and area were calculated after the linear red-edge reflectance model (Guyot, Baret, Major, 1988):

$$(3) \quad R_{red-edge} = \frac{(\rho_{670} - \rho_{780})}{2} \quad .$$

The position of the red-edge wavelength of the electromagnetic spectrum is given by (Van der Meer and De Jong, 2001):

$$(4) \quad \lambda_{red-edge} = 700 + 40 \left(\frac{(\rho_{red-edge} - \rho_{700})}{(\rho_{740} - \rho_{700})} \right) \quad .$$

2.2.3. *Vegetation indices*

The estimated and used four Vegetation Indices (VIs) in present study have exhibited higher correlation with the Z_c than the rest of the 30 VIs tested initially. Those VIs have proven to be good estimates of pigment content of the coniferous vegetation based on correlation between grounds measured chlorophyll and carotene as well as field spectrometry of the coniferous needles (Filchev and Roumenina, 2013). They are namely: Modified Chlorophyll Absorption in Reflectance Index (MCARI), Transformed CARI (TCARI), Modified Triangular Vegetation Index 2 (MTVI 2), Photochemical Reflectance Index 1 (PRI 1), (*Table 1*).

Table 1: EO-1/Hyperion VIs used for detection and assessment of the abiotic vegetation stress in coniferous landscapes

VIs	Equation	Source
MCARI	$MCARI = [(R_{700} - R_{670}) - 0.2 * (R_{700} - R_{550})] * (R_{700} / R_{670})$	(Daughtry <i>et al</i> , 1989)
TCARI	$TCARI = 3 * [((R_{700} - R_{670}) - 0.2 * (R_{700} - R_{550})) * (R_{700} / R_{670})]$	(Haboudane <i>et al</i> , 2002)
MTVI2		(Haboudane <i>et al</i> , 2004)
PRI 1	$PRI1 = (R_{528} - R_{567}) / (R_{528} + R_{567})$	(Gamon <i>et al</i> , 1992)

2.2.4. Statistical analysis

Pearson correlation (r) and regression (r^2) analyses between the EO-1/Hyperion VIs and Z_c values were carried out. A set of dendrograms (cluster analysis) were prepared according to the hierarchical clustering (Ward method) using the derived VIs from EO-1/Hyperion satellite data and Z_c .

2.2.5. Validation

To assess the accuracy of geostatistical models, cross validation procedure was used. For this purpose the models were assessed by leaving out of the model a small subset of data from the sample. The accuracy of the models was assessed by the Root Mean Square Error of estimate (RMSE).

3. Results and Discussions

3.1. Red-Edge Position and Depth from EO-1/Hyperion Data

The spectra, extracted from EO-1/Hyperion satellite data, shows a blue shift of the red edge. The EO-1/Hyperion bands complying with the calculated position of the red-edge are band No. 32 with central wavelength of $\lambda=671.02$ nm, and band No. 33 at $\lambda=681.20$ nm. Difference is also registered in the depth, area, and asymmetry between the two isolated groups of plants: stressed and unstressed (Table 4). However, the highest difference is exhibited at test site No. 2, which red-edge position; depth, area, and asymmetry are completely different from the others. This can be

explained with the fact that test site No. 2 is positioned on the left slope above the sludge pan. Hence, the geochemical leeching of the heavy metals and natural radionuclide is impossible. In this sense the test site No. 2 environmental conditions also can be assessed as closer to the background conditions than the rest of the test sites under investigation. This conclusion is supported also by the more recent investigation of the authors using field spectrometry measurements (Filchev and Roumenina, 2013). Conversely, the initially designated as most polluted test sites, i.e. test site 10 and 11, proved to be with close values of the red-edge position, depth, area and asymmetry. This similarity is supported not only by the background geochemistry but also by the relative closeness of the two test sites which are located tens to hundred meters down the stream after the technological sludge pan of *Teyna* River. The difference in the red-edge position between the test site No. 2 and test sites No. 10 and 11 is about 10 nm, which is within the bandwidth of available to the scientific community satellite hyperspectral systems such as EO-1/Hyperion and CHRIS/PROBA. Therefore, the detection capabilities of current satellite hyperspectral systems are very weak and need either higher spectral sampling rate at these zones of the spectrum or to look at different spectral derivatives for detection of chemical abiotic stress. Those distinctive features are obviously the depth, area and asymmetry of the red-edge feature which is not strictly bind to the limitations of spectral resolution of present satellite hyperspectral missions, (*Table 2*).

Table 2: Depth and position of the red-edge in the visible (VIS) part of the electromagnetic spectrum for EO-1/Hyperion data

Test site No.	Red-edge position λ (nm)	Depth	Area	Asymmetry
2	683.00	0.20	41.44	4.66
5	660.85	0.60	135.14	2.28
10	671.02	0.65	141.97	2.77
11	671.02	0.54	117.43	2.86

3.2. Statistical analysis

3.2.1. Correlation and regression analysis

The next step of the analysis is to perform a correlation between the grounds measured geochemical background expressed in modelled Z_c values and the VIs extracted from EO-1/Hyperion scene. It was found strong negative relationships between Z_c and TCARI and MCARI, and poor

direct relationship between Z_c and PRI, (*Table 3*). The correlation between Z_c and the VIs proved the initial hypothesis that VIs were affected by the background geochemistry. However, the high inverse correlation between MCARI and TCARI is also reported between pigment content (chlorophyll) and the VIs (Haboudane *et al*, 2002). Therefore, at the rates of geochemical pollution the higher the pollution is the higher is the chlorophyll content is registered in the studied test sites. This conclusion is supported by a recent work of the authors which uses field spectrometry and ground-based biogeochemical data (Filchev and Roumenina, 2013). It is to be noted that the VIs such as TCARI and MCARI are less sensitive to heavy metal pollution than to natural radionuclide pollution (*Table 5*). Contrarily, the MTVI 2 and PRI exhibit stronger relationships with heavy metals (metalloids) than with natural radionuclide. However, even they are more sensitive to the metalloids concentration in soils their correlation coefficient is not higher enough in order to use them to make geochemical predictions. The strongest positive correlation is for TCARI/MCARI and Z_c ($r^2=0.63$; F: 5.20 at F: <0.1). The lowest correlation is between MTVI 2 and Z_c ($r^2=0.42$; F: 2.48 at F: <0.21), and accordingly between PRI and Z_c ($r^2=0.30$; F: 1.34 at F: <0.33).

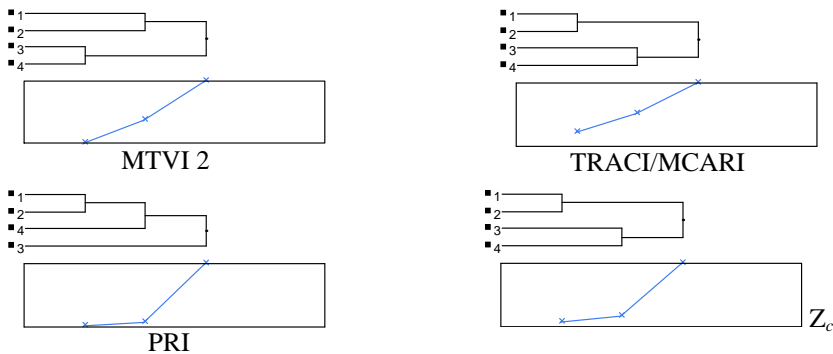
Table 3: Pearson correlation coefficient (r; $\alpha=0.05$) for Z_c and EO-1/Hyperion VIs.

Variable	Z_c	Z_c radionuclide	Z_c metalloids
TCARI	-0.80	-0.80	-0.71
MCARI	-0.80	-0.80	-0.71
MTVI 2	-0.67	-0.66	-0.73
PRI	0.56	0.52	0.74

3.2.2. Cluster analysis

The areas subject to technogenic geochemical pollution were delineated based on the Z_c . Coniferous landscapes subject to abiotic stress were reclassified into four classes according to the values of the Z_c : unstressed ($Z_c=0\div 10$), moderately stressed ($Z_c=10\div 20$), stressed ($Z_c=20\div 50$), and heavily stressed ($Z_c>50$) (Filchev and Roumenina, 2013). Within those areas only the test sites No. 2 and No. 5 (unstressed) and test sites No. 10 and No. 11 (stressed) were used in the cluster analysis in order to test whether the Z_c values group similarly to the VI_s values from EO-1/Hyperion. The results are represented on (*Figure 2*).

Fig. 2: Dendrograms of clustering of EO-1/Hyperion VIs and Z_c . The numbers on the figures correspond to: 1- test site No. 2; 2 – test site No. 5; 3 – test site No. 10; 4 – test site No. 11



On Fig. 2, MTVI 2 and TCARI/MCARI values group their first cluster relatively farther than Z_c . However, the PRI does not reflect the Z_c clusters. These results also support the conclusions for the VI's performances for abiotic stress detection drawn from visual comparison between dendrogrammes from field spectrometry data, although there only the first Principal Component of the VIs and field pigment data correspond to the Z_c groupings (Filchev and Roumenina, 2013).

4. Conclusions

Through the joint use of satellite spectrometry data and VIs from EO-1/Hyperion and ground-based geochemical data, it was established that coniferous forests are subject to abiotic stress caused by uranium mining. It was found that, in satellite spectra, the position of the red-edge with stressed trees is shifted slightly towards the orange and green part of the spectrum, i.e. the so called "blue shift". With healthy plants this shift is at $\lambda=683$ nm, while it is at about $\lambda=671$ nm for the stressed ones. Furthermore, the stressed coniferous plants feature a non-specific stress reaction or „exstress” or an increased chlorophyll and carotene content with increased levels of geochemical pollution - Z_c . It should be noted however, that the registered effects from geochemical pollution are specific to at a certain point after which the saturated geochemical background has an adverse impact on the vegetation expressed in chlorosis (yellowing) and die out of the coniferous trees.

It has also been found out that the VIs such as TCARI/MCARI and Z_c ($r^2=0.63$; F: 5.20 at F: <0.1) has the highest correlation followed by MTVI 2 and Z_c ($r^2=0.42$; F: 2.48 at F: <0.21), and PRI and Z_c ($r^2=0.30$; F: 1.34 at F: <0.33). Therefore, the space borne derived VIs from hyperspectral sensors at present level of technology development may be used as an indirect indicator neither of geochemical background stress nor for stress detection caused by uranium mining in coniferous landscapes due to the weak relationships between geochemical background and narrowband vegetation indices. However, the correlation between the four obtained VIs and Z_c led to the conclusion that most VIs, using chlorophyll absorption lines, shows a very strong inverse correlation relationship with the Z_c .

In conclusion, the study will continue with an investigation of the narrowband VIs which feature the most distinctive relationship between VIs and the modelled Z_c values. Those studies will benefit from employing rigorous and versatile models for pollutant distribution in soils and reclaimed lands.

References

1. B a n o v, M. and B. H r i s t o v. Investigation and recultivation of lands of the vicinity of the Town of Buhovo damaged by Uranium mining. *Problems of Geography*, 1, 1996, 78–86. (in Bulgarian)
2. B e r n s t e i n, L. S., A d l e r - G o l d e n, S. M. *et al.* Validation of the QUick Atmospheric Correction (QUAC) algorithm for VNIR-SWIR multi- and hyperspectral imagery. In: *SPIE Proceedings - Algorithms and Technologies for Multispectral, Hyperspectral, and Ultraspectral Imagery XI*, 2005. DOI: 10.1117/12.603359
3. B e c k, R. EO-1 User Guide ver. 2.3, (University of Cincinnati), 2003, 74 p.
4. B o n d e v, I. Vegetation of Bulgaria. Map in scale 1:600000 with a description text. Sofia University “St. Kliment Ohridski” Publishing House, Sofia, 1991, 183 p.
5. D a u g h t r y, C. S. T., L. L. B i e h l, K. J. R a n s o n. A new technique to measure the spectral properties of conifer needles. *Remote Sensing of Environment*, 27, 1989, 81–91. DOI: [http://dx.doi.org/10.1016/0034-4257\(89\)90039-4](http://dx.doi.org/10.1016/0034-4257(89)90039-4)
6. D i m i t r o v, P. and E. R o u m e n i n a. Studying the Relationship between Some Attributes of Coniferous Forests and Spectral Data from the Aster Satellite Sensor. *Aerospace Research in Bulgaria*, 24, 2012, 116–128.
7. ENVI Atmospheric Correction Module - User's Guide. ITT VIS Inc., 2009. http://www.exelisvis.com/portals/0/pdfs/envi/Flaash_Module.pdf (last date accessed: 10 June 2013).
8. FieldSpec UV/VNIR HandHeld Spectroradiometer User Guide, ASD Inc., 2003, 72 p.
9. F i l c h e v, L. Design of digital landscape model of the Teyna river watershed for the pur-poses of landscape-ecological planning. In: *Proceedings of 5th Scientific*

- Conference with International Participation Space, Ecology, Nanotechnology, Safety (SENS 2009)* (SRI-BAS, Bulgaria), 2009, 168–173. URL: <http://www.space.bas.bg/SENS2009/9-R.pdf>
10. Filchev, L. and I. Yordanova. Landscape-geochemical investigations of the consequences from uranium-ore extraction in taina river basin, *Ecological Engineering and Environment Protection (EEEEP)*, 4, 2011, 14–22. (in Bulgarian)
 11. Filchev, L. and E. Roumenina. Detection and Assessment of Abiotic Stress of Coniferous Landscapes Caused by Uranium Mining (Using Multitemporal High Resolution Landsat Data), *Geography, Environment, Sustainability*, 5(01), 2012, 52–67. M. V. Lomonosov Moscow State University URL: http://int.rgo.ru/wp-content/uploads/2012/03/GES_01_2012.pdf
 12. Filchev, L. and E. Roumenina. Model for detection and assessment of abiotic stress caused by uranium mining in European Black Pine landscapes. *EARS eProceedings*, 12(2), 2013, 124–135.
 13. Georgiev, P. and S. Grudev. Characteristic of Polluted Soils in the Uranium Mine section. *Annual of University of Mining and Geology St. Ivan Rilski*, 46, 2003, 243–248. (in Bulgarian)
 14. Guyot, G., F. Baret, D. J. Major. High spectral resolution: determination of spectral shifts between the red and near infrared. *International Archives of the Photogrammetry, Remote Sensing and Spatial Information Sciences*, 27, 1988, 750–760.
 15. Gamon, J. A., J. Penuelas, C. B. Field. A narrow-waveband spectral index that tracks diurnal changes in photosynthetic efficiency. *Remote Sensing of Environment*, 41, 1992, 35–44. DOI: [http://dx.doi.org/10.1016/0034-4257\(92\)90059-S](http://dx.doi.org/10.1016/0034-4257(92)90059-S)
 16. Houbandane, D., J. R. Miller, P. J. Zarco-Tejada, L. Dextraze. Integrated narrow-band vegetation indices for prediction of crop chlorophyll content for application to precision agriculture. *Remote Sensing of Environment*, 81, 2002, 416–426. DOI: [http://dx.doi.org/10.1016/S0034-4257\(02\)00018-4](http://dx.doi.org/10.1016/S0034-4257(02)00018-4)
 17. Houbandane, D., J. R. Miller, E. Patteny, P. J. Zarco-Tejada, I. B. Strachan. Hyperspectral vegetation indices and novel algorithms for predicting green LAI of crop canopies: Modeling and validation in the context of precision agriculture. *Remote Sensing of Environment*, 90, 2004, 337–352. DOI: <http://dx.doi.org/10.1016/j.rse.2003.12.013>
 18. Jones, H. G. and P. Schofield. Thermal and other remote sensing of plant stress. *General and Applied Plant Physiology*, 34, 2008, 19–32. URL: http://www.bio21.bas.bg/ipp/gapbfiles/v-34_pisa-08/08_pisa_1-2_19-32.pdf
 19. Kancheva, R. and D. Borisova. Vegetation Stress Indicators Derived from Multispectral and Multitemporal Data. *Space Technol.* 26(3), 2007, 1–8.
 20. Kancheva, R. and D. Borisova. Spectral Models for Crop State Assessment Considering Soil and Anthropogenic Impacts. In: *Proceedings of 31st International Symposium on Remote Sensing of Environment “Global Monitoring for Sustainability and Security”*, 20-24 June 2005, St. Petersburg, Russia. URL: <http://www.isprs.org/publications/related/ISRSE/html/papers/695.pdf>
 21. Kancheva, R. and D. Borisova. Colorimetric analysis in vegetation state assessment. In: *Proceedings of the 28th Symposium of the European Association of*

- Remote Sensing Laboratories “Remote Sensing for a Changing Europe”*, Istanbul, Turkey, 2–5 June 2008, 151 – 156. DOI: 10.3233/978-1-58603-986-8-151
22. K a n c h e v a, R. and G. G e o r g i e v. Spectrally based quantification of plant heavy metal-induced stress. In: *Proc. SPIE 8531, Remote Sensing for Agriculture, Ecosystems, and Hydrology XIV*, 85311D. DOI:10.1117/12.974533
 23. L a r c h e r, W. Streb bei Pflanzen. *Naturwissenschaften*, 74, 1987, 158–167.
 24. L i c h t e n t h a l e r, H. K. Vegetation Stress: an Introduction to the Stress Concept in Plants. *Journal of Plant Physiology*, 148, 1996, 4–14. DOI: [http://dx.doi.org/10.1016/S0176-1617\(96\)80287-2](http://dx.doi.org/10.1016/S0176-1617(96)80287-2)
 25. M i s h e v, D. *Spectral Characteristics of Natural Objects*, Publ. House Bulg. Acad. of Sci., Sofia, 1986, 150 p.
 26. M i s h e v, D., H. S p i r i d o n o v, V. V e l i k o v, E. R o u m e n i n a, V. P e t r o v a. An attempt of using scanner images for landscape mapping. *Problems of Geography*, 2, 1981, 25–36.
 27. M i s h e v, D., N. D o b r e v. *Remote Sensing in Geophysics and Geology – Aerospace Methods for Studying Earth Structure*. Sofia, Technika, 1987.
 28. M i s h e v, D., E. R o u m e n i n a, V. V e l i k o v, Determination of anthropogenic pollution in technogenically loaded region with landscape-geochemical and remote sensing methods. *Problems of Geography*, 2, 1987, 24–31.
 29. N a y d e n o v a, V. and E. R o u m e n i n a. Monitoring the mining effect at drainage basin level using geoinformation technologies. *Central European Journal of Geosciences*, 1, 2009, 318–339. DOI: 10.2478/v10085-009-0023-6
 30. N i k o l o v, H., D. B o r i s o v a, M. M i r c h e v a. Reclaimed Areas Mapping by Remotely Sensed Data, *The International Archives of the Photogrammetry, Remote Sensing and Spatial Information Sciences*, 34, XXXVI, Part 7, Paper ID: 095. <http://www.isprs.org/proceedings/XXXVI/part7/PDF/095.pdf>
 31. P e d d l e, D. R., R. B. B o u l t o n, N. P i l g e r, M. B e r g e r o n, A. H o l l i n g e r. Hyperspectral detection of chemical vegetation stress: evaluation for the Canadian HERO satellite mission. *Canadian Journal of Remote Sensing*, 34, 2008, S198–S216. DOI: 10.5589/m08-006
 32. P e a r l m a n, J., C. S e g a l, L. B. L i a o, S. L. C a r m a n, M. A. F o l k m a n, W. B r o w n e, L. O n g, S. G. U n g a r. Development and Operations of the EO-1 Hyperion Imaging Spectrometer. *SPIE 4135, Earth Observing Systems V*, 243, 2000, 11. DOI: 10.1117/12.494251
 33. R o u m e n i n a, E., N. P e l o v a, V. V e l i k o v, Aerospace Remote Sensing and Landscape Geochemical Methods of Observation of the Antropogenic Factor in the Devnja Region. In: *Proceedings of International Symposium on Hydro-and Aerodynamics in Marine Engineering. HADMAR '91*, Varna, 1991, 1: 42-1–42-3.
 34. R o u m e n i n a, E., V. D i m i t r o v, E. I v a n o v. Spatial Model of Ecosystem Changes in Chouprene Region, West Balkan Mountains. Bulgaria. *Journal of Balkan Ecology*, 6(1), 2003, 64–76.
 35. R o u m e n i n a, E., N. S i l l e o s, G. J e l e v, L. F i l c h e v, L. K r a l e v a. Designing a spatial model of land use impact dynamics caused by uranium mining using remote sensing and ground-based methods. In: *Proceedings of the 3rd Scientific Conference with International Participation „Space, Ecology, Nanotechnology, Safety“ (SENS) 2007*, (SRI-BAS, Varna, Bulgaria), 179–184.

36. S a e t, Y. E., B. A. R e v i c h, E. P. Y a n i n. Geochemistry of the Environment (Mir, Moscow, Russia), 335 p. (in Russian)
37. S i m e o n o v a, A., J. I g n a t o v, M. M l a d e n o v. Radiological Assessment of “Iskra” section at underground construction (DIAL Ltd. - Buhovo 1830), 1993, 77 p. (in Bulgarian)
38. S p i r i d o n o v, H., R o u m e n i n a, E., M i l e n o v a, L. Complex Investigation of a System “Industrial Site-Environment” Using Remote Sensing and Landscape-Geochemical Methods. In: *Proceedings of European ISY’92 Conference Environment Observation and Climate Modelling through International Space Projects*. Munich, 1992, 114–119.
39. Statistical Yearbook 2008. National Statistical Institute (NSI), Republic of Bulgaria, Sofia, 2009.
40. V a n d e r M e e r, F. and S. M. d e J o n g. Imaging Spectrometry: Basic Principles and Prospective Applications (Springer), 2001, 403 p.
41. V e l i k o v, V., D. M i s h e v, E. R o u m e n i n a. Space, Landscapes, Ecology. Sofia University “St. St. Cyril and Methodius” Publishing House, V. Tarnovo, 1995, 141 p.
42. V o d y a n i t s k i i, Yu. N. Equations for assessing the total contamination of soils with heavy metals and metalloids. *Eurasian Soil Science, Degradation, Rehabilitation, and Conservation of Soils*, 43, 2010, 1184–1188. DOI: 10.1134/S106422931010011X

ОТКРИВАНЕ И ОЦЕНКА НА АБИОТИЧЕН СТРЕС, ПРИЧИНЕН ОТ УРАНОДОБИВ, В ИГЛОЛИСТНИ ЛАНДШАФТИ (С ИЗПОЛЗВАНЕ НА СПЪТНИКОВИ СПЕКТРОМЕТРИЧНИ ДАННИ ОТ EO-1/HYPERION)

Л. Филчев

Резюме

В статията са представени резултатите от проведено изследване с цел откриване и оценка на абиотичен стрес в иглолистни ландшафти на черноборови монокултури (*Pinus nigra* L.) с помощта на геохимични наземни данни, модели на техногенно замърсяване, както и спътникови спектрометрични изображения от EO-1/Hyperion. Изследвани са вегетационните индекси (ВИ): MCARI, TCARI, MTVI 2, и PRI, както и атрибутите на червения ръб, с цел откриване на промени, причинени от геохимично замърсяване вследствие на уранодобив. Анализът е извършен на четири тестови участъка с размери всеки 30 m × 30 m, съответстващи на размера на подпикселното пространство на EO-1/Hyperion, заложени в хомогенни иглолистни ландшафти в

басейна на р. Тейна - ляв приток на река Искър. В резултат е установена позицията на червения ръб за нестресирани иглолистни ландшафти (черен бор) $\lambda=683$ nm, както и за стресирани иглолистни ландшафти $\lambda=671$ nm. Установено е, че вегетационните индекси, като TCARI / MCARI и сумарния коефициент на техногеохимично замърсяване - Z_c са силно корелирани ($r^2=0.63$; F: 5.20 на F:<0.1), последвани от MTVI 2 и Z_c ($r^2=0.42$; F: 2.48 на F:<0.21), и PRI и Z_c ($r^2=0.30$; F: 1.34 на F:<0.33). Тествана е хипотезата, че групирането на EO-1/Hyperion ВИ съответства на клъстеризацията на Z_c стойностите използвайки метода на йерархичната клъстеризация (по метода на Ward). За тази цел, избраните четири тестови участъка са разделени на две двойки съответстващи на моделните стойности на Z_c (използвайки инверсна мултиквадратна функция - IMF от множеството на радиално базираните функции - RBF): 1) нестресирани (тестови участъци № 2 и № 5) и 2) стресирани иглолистни ландшафти (тестови участъци № 10 и № 11). В резултат на това е установено, че групирането на стойностите на MTVI 2 и TCARI/MCARI на първия клъстер става сравнително подалече от първия клъстер на Z_c . Съответно клъстеризацията на PRI не отразява клъстерите Z_c . Това води до заключението, че спътниковите спектрометрични тесноканални ВИ получени от EO-1/Hyperion, не са достатъчно чувствителни, към геохимичния фон и абиотичния стрес на иглолистните ландшафти, причинен от геохимичните замърсявания от уранодобива.

CROP INVESTIGATION USING HIGH-RESOLUTION WORLDVIEW-1 AND QUICKBIRD-2 SATELLITE IMAGES ON A TEST SITE IN BULGARIA

Vassil Vassilev

*Space Research and Technology Institute – Bulgarian Academy of Sciences
e-mail: vassilev_vas@yahoo.com*

Abstract

The paper aims to investigate the capabilities of using high-resolution satellite images: panchromatic WorldView-1 satellite image acquired on 30/11/2011 and multispectral QuickBird-2 satellite image acquired on 31/05/2009 for crop analysis, which includes crop identification, crop condition assessment and crop area estimates applications in Bulgaria using the power and flexibility of ERDAS IMAGINE tools. The crop identification was accomplished using unsupervised and supervised classification processing techniques using as reference ground data. After the supervised classification, fuzzy convolution filter was applied to reduce the mixed pixels using ERDAS Imagine software. Accuracy totals, error matrix and kappa statistics were calculated using accuracy assessment tool in ERDAS Imagine to assess the quality of the classification process. Crop condition assessment was accomplished using the derived Normalized Difference Vegetation Index (NDVI) image from the QuickBird-2 image, which was reclassified and was given meaningful estimations on the crop condition. Crop area was estimated using pixel counting approach. Pixel counting methods are known for introducing bias to the crop area estimates but using the high Overall Accuracy of 90.86% and overall Kappa Statistics of 0.8538 for the classified QuickBird-2 image and Overall Accuracy of 86.71% and overall Kappa Statistics of 0.7721% for the classified WorldView-1 allows that option to be utilized according to (Gallego, 2004). As a conclusion it can be stated that using the benefits that high-resolution satellite images gives in combination with the power and flexibility of ERDAS Imagine tools, crop identification can be achieved more accurately by increasing the identification accuracy and also by having the necessary ground information for selecting appropriate training samples. Crop identification by applying an arable mask is better practice, because it is reducing the mixed pixels problem i.e. also known as “salt and pepper effect” (common for coarse and low resolution satellite images), As a result it is making the map products much more useful thus making more accurate crop area estimates when pixel counting methods are used.

1. Introduction

Accurately identifying crops using information derived from earth observation can contribute to improved use of resources and aids agricultural planning. On the other hand, using high-resolution satellite images is useful for delineation of crop fields and accurate crop area estimates. In the past, remote sensing has been shown to be a valuable tool in separate applications in agriculture. Remote sensing techniques have been successfully applied in classifications of arable crops and in quantification of vegetation characteristics at different spatial and temporal scales. The crop discrimination and mapping using space data is carried out either by visual or digital interpretation techniques. Visual techniques generally are based on standard FCC (False Color Composite) generated using green, red and near-IR bands assigned blue, green and red colors. The digital techniques are applied to each pixel and use full dynamic range of observations and are preferred for crop discrimination. The field size was shown to have a strong effect on classification accuracy with small fields tending to have lower accuracies even when the effect of mixed pixels was eliminated (Batista et al. 1985; Buechel et al. 1989). Medhavy et al. (1993) showed that when supervised classification is adopted, use of training strategy based on selection of isolated pixels has higher classification accuracy than selecting blocks of pixels as training set.

- Scope of the research

The agricultural land in Bulgaria in its majority is represented by small in size fields with mixed crops, which makes the crop identification process rather difficult by applying coarse and low resolution satellite images, caused by the mixed pixel occurrence. The current paper will apply high-resolution satellite images for investigation of crops. Utilizing the capabilities of high-resolution imagery will give opportunity to investigate the possibilities of crop identification, crop condition assessment and crop area estimates on a test site in Bulgaria. The QuickBird-2 satellite image gives a substantial opportunity of identifying crops and crop condition analysis with its spectral and spatial resolution and the WorldView-1 image for crop area estimates using its spatial resolution. Using high-resolution satellite images aids precision agriculture applications as well, which will be attempted in this paper. The RED and NIR bands have traditionally great application in crop conditions assessment by deriving Normalized

Difference Vegetation Index (NDVI) images (Rouse, 1973). The objectives of the present paper are highlighted below:

- Identifying appropriate sample fields and training samples for different crops like: winter wheat, winter rapeseed, grain maize and sunflower using collected ground truth data.
- Using one panchromatic WorldView-1 and one multispectral QuickBird-2 satellite images for crop identification and crop area estimation applications on a test site in Bulgaria.
- To classify the test site using unsupervised classifiers (ISODATA algorithm) and supervised (Maximum Likelihood classifier).
- Calculate the accuracy assessment of the classified images using accuracy assessment tool and evaluate the crop classes classified.
- Deriving conclusions for crop condition assessment and precision agriculture using multispectral QuickBird-2 satellite image and reclassified NDVI image.
- Assessing crop area estimates using the classified images by applying pixel counting methods.

- Study Area

The test area of Zhiten is one of the Bulgarian Aero-Space Test Sites (BASTS) and is associated with investigating agricultural applications using satellite images with different spatial, spectral and temporal resolution on the territory of Bulgaria (Figure 1.). The test site is located in Dobrich Region, North-East Bulgaria, and represents intensively cultivated area sowed mostly with cereals and sunflower. This territory is one of the main agricultural regions of the country. The geology is presented mainly by Miocene limestone, clay and marl covered subsequently by loess. The region is about 200 m a.s.l. Its relief is characterized by wide, flat ridges and steep-sided dry valleys. The area is part of the European-continental climatic province of the temperate climatic belt. Climate is moderately warm with no distinctive dry season. Mean annual air temperature is 10.2°C. Precipitation maximum is in June and minimum – in February. Overall annual precipitation is 540 mm. Due to the carbonate bedrock, i.e limestone, marl, the hydrographic network is represented by intermittent streams. The main soil types are chernozems from zonal ones and fluvisols from azonal ones.

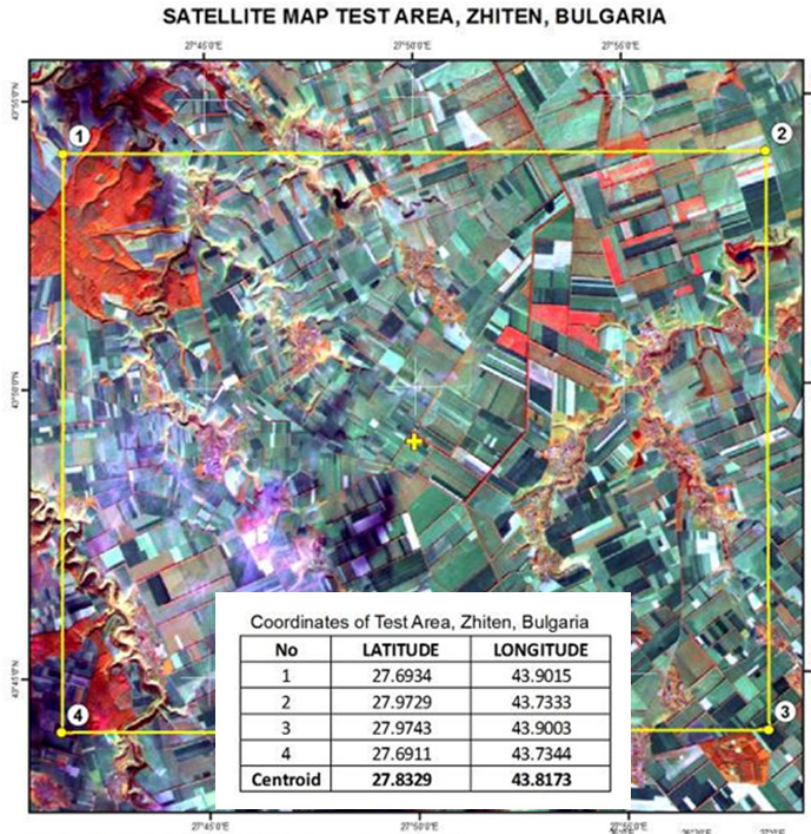


Fig. 1. Zhiten test site, Bulgaria

- Collection of field data and used satellite images

During the 2010-2011 agricultural season and in particular in the period between March–July 2011 four exhaustive field surveys were carried out and ground data was collected and organized in a geodatabase. Field data was collected in the framework of a project financed by the Belgian Federal Science Policy Office (BELSPO) under the PROBA-V Preparatory Programme, contract Ref. No CB/XX/16, with acronym – PROAGROBURO (<http://proagroburo.meteoromania.ro/>). The ground-truth data consists of descriptions of the LU/LC types, phenological stages and total projective cover (TPC) of crops, GPS measurements, and photos. The collected ground data will contribute of selecting appropriate training samples for the supervised classification on the chosen satellite images. Two

satellite images were used in this study: a WorldView-1 panchromatic satellite image with 0.50m spatial resolution, acquired on 30/11/2011 and QuickBird-2 multispectral (2.4m spatial resolution) and panchromatic image (with 0.60m spatial resolution), acquired on 31/05/2009 (Figure 2).

Used Satellite Images For The Test Site of Zhiten, Bulgaria

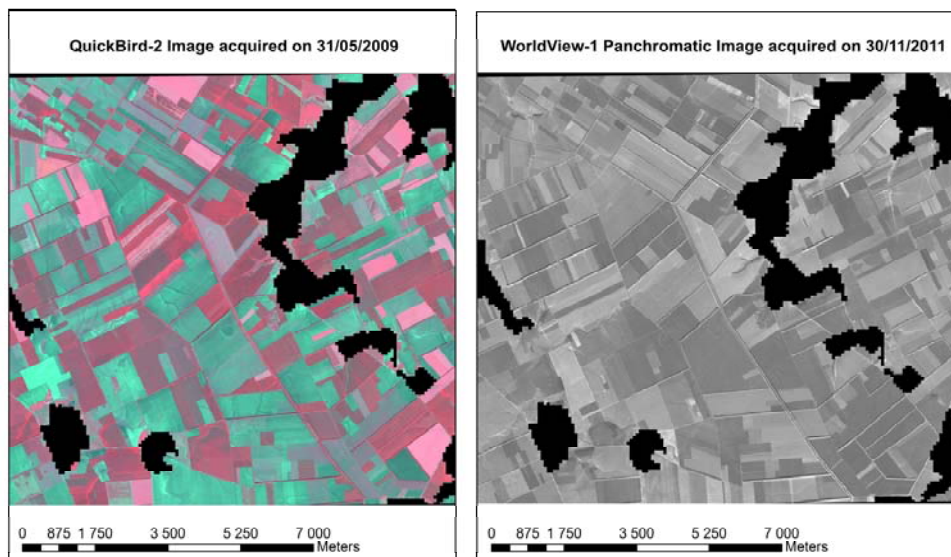


Fig. 2. Used satellite images

2. Methodology

An arable land mask using CORINE data was applied on the images used for the research in order to work only with the arable land. For the process of crop identification and crop area estimates, unsupervised and supervised classifications were used which is common method for mapping crops, utilizing also the ground information collected. Fuzzy convolution filter option was used to reduce the mixed pixel problem using ERDAS Imagine software. After applying the image classifications, accuracy assessment tool was used and the accuracy totals, error matrix and kappa statistics was calculated and the high overall accuracy assessment of the satellite images was used for crop area estimation applying pixel counting methods. Crop condition assessment was accomplished using the supervised classification

and also by composing an NDVI image from the QuickBird-2 image and reclassifying the image to differentiate between crops in good or bad vegetation status on the test site. All the benefits that these high-resolution satellite images give makes it possible to conduct rather quick and interesting research which provides without a doubt intriguing results concerning crop identification, crop condition assessment and crop area estimated using ERDAS Imagine software (Figure 3).

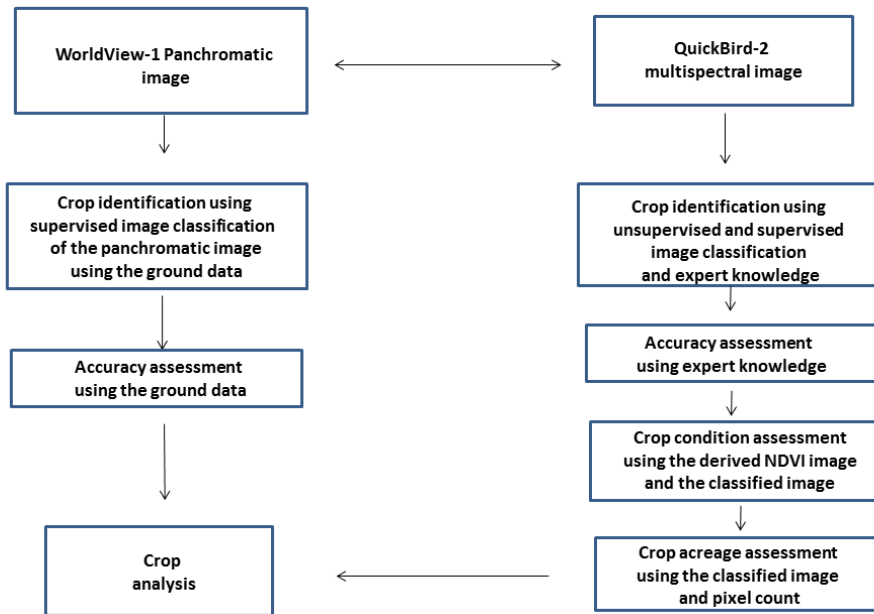


Fig. 3. Methodology of the research

3. Results and discussions

3.1. Crop identification by applying unsupervised and supervised classifications

An arable land mask using CORINE data was applied on the WorldView-1 and the QuickBird-2 images in order to classify only the arable land and reduce the occurrence of mixed pixels. The WorldView-1 image is acquired on 30/11/2011 and was used for delineation of crop fields using its spatial resolution and the fact that it is acquired in the year of the field data

collection surveys. The QuickBird-2 image is acquired on 31/05/2009 and although it does not coincide with the ground surveys of the territory of research that were undergone was used for crop analysis of the territory of research. The reason behind that decision was that the rate of land cover change in the test site is not great and the use of image from previous year can be used without introducing severe bias in the analysis. The crop identification process was accomplished firstly by conducting unsupervised classification (using ISODATA algorithm) with 4-5 classes for both the QuickBird-2 and WorldView-1 image and for the derived NDVI image from the QuickBird-2 satellite image. The purpose of that step is to use that spectral information derived as an indicator on which fields to use as training samples for the supervised classification in combination with the ground data. The unsupervised classification is traditionally the first step and is accommodating the interpreter to understand the image. Supervised classification using the Maximum Likelihood Classification (MLC) algorithm was applied to the arable land images (Figure 4 and 5). In the MLC procedure, a key concern is to collect a training set comprising of at least 10–30 independent training cases per class per discriminatory variable (e.g. band) to allow the formation of a representative description of the class, so that its mean and variance can be reasonably estimated (Piper, 1992; Mather, 2004). For example, the spectral response of an agricultural crop class in an image might vary as a function of variables, such as: the crops growth stage, topographic position, density of cover, health, impact of management activities, substrate conditions and instrument view angle (Foody, 2002). The gathered training set from the field data was good enough to make representative training samples for the arable land classes. The unsupervised classification in combination with the ground information and the derived NDVI image helped to choose and delineate appropriate training samples for the supervised classification of the QuickBird-2 image. The classes chosen for the QuickBird-2 image are: Stubble fields/bare soil, Spring Crops – Sunflower and Maize, Bad Status – Winter Wheat/Winter Rapeseed, Average Status – Winter Wheat/Winter Rapeseed and Good Status – Winter Wheat/ Rapeseed. From (Figure. 4) it can be seen that some fields are in bad vegetative status, this can be due to late planting or utilizing different types of winter crops seeds, which can result in late developing stage of winter wheat/rapeseed crops. Average status of winter wheat/rapeseed class can be explained with delayed cropping procedures, which outcomes in experiencing low vigor status. While the good status –

Winter wheat/rapeseed class is in the best vigor status for the period of acquisition of the satellite image – 31/05.2009. This is also proved by the NDVI image derived (Figure 8).

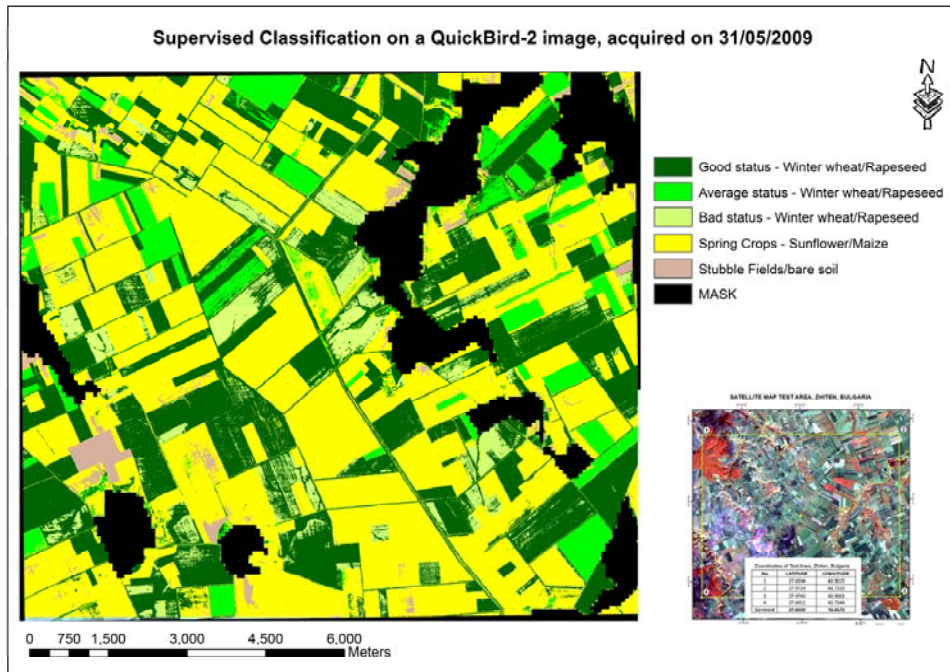


Fig. 4. Supervised classification on a QuickBird-2 image, acquired on 31/05/2009

Supervised classification was conducted on the panchromatic WorldView-1 image, acquired on 30/11/2011 as well (Figure 5). The classes that are classified are: Stubble fields, spring crops represented by sunflower and maize and the class winter crops, represented by winter wheat and winter rapeseed. For the panchromatic image classification the actual choice of training samples was marginally more difficult. For assessing the training samples a big effect played the ground data which helped point out appropriate training samples, although the ground surveys took place couple of months earlier. A rather important part of the study is that after the supervised classification a fuzzy convolution filter followed which was applied to the final resulted supervised classifications by using ERDAS Imagine software. The purpose was to smooth and try to reduce the mixed pixel effect on the classified images. As a result better cartographic product

was possible to be visualized and supports more accurate crop area estimates.

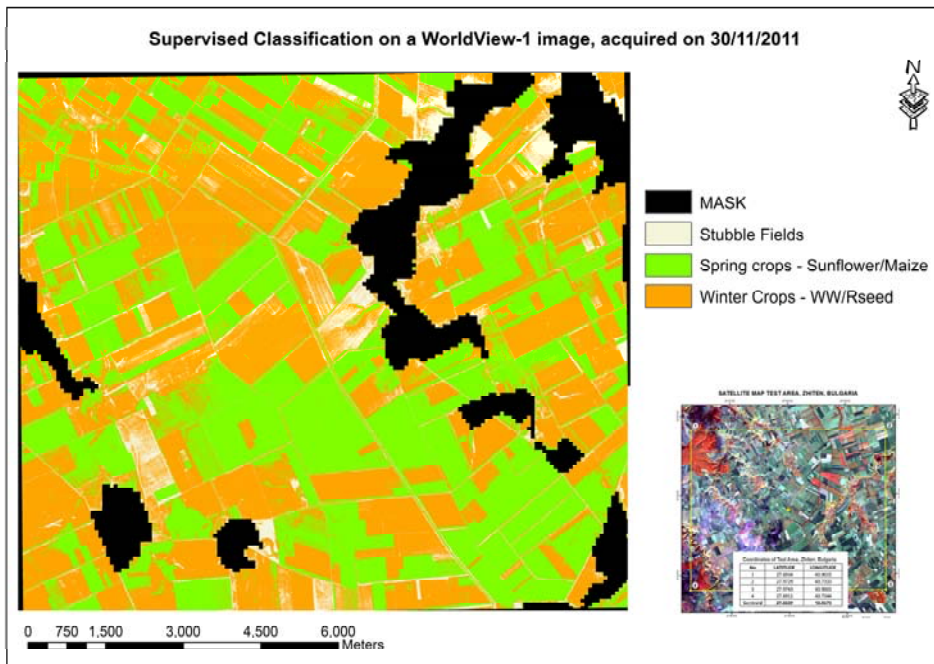


Fig. 5. Supervised classification on a WorldView-1 image, acquired on 30/11/2011

3.2. Accuracy Assessment

The accuracy assessment was accomplished using the fuzzy convolution classified images and the accuracy assessment tool in ERDAS Imagine software. Around 160-170 randomly distributed points were assessed for both classified images. Accuracy assessment was applied on the WorldView-1 classified image for crop identification using its high spatial resolution by applying visual interpretation on the panchromatic and both on the unsupervised and supervised classifications in combination with the ground data (Figure 6.). The accuracy totals show overall classification accuracy of 86.71% and overall kappa statistics of 0.7721 (Table 1.). The class stubble fields show high accuracy. This is due to the fact that the class is easily identified both on the unsupervised classification and on the panchromatic image. The choice of good and representative training sample was achieved by using visual interpretation techniques utilizing the high

spatial resolution. The actual strong point of this supervised classification on this panchromatic WorldView-1 satellite image is the other two classes – winter crops and spring crops.

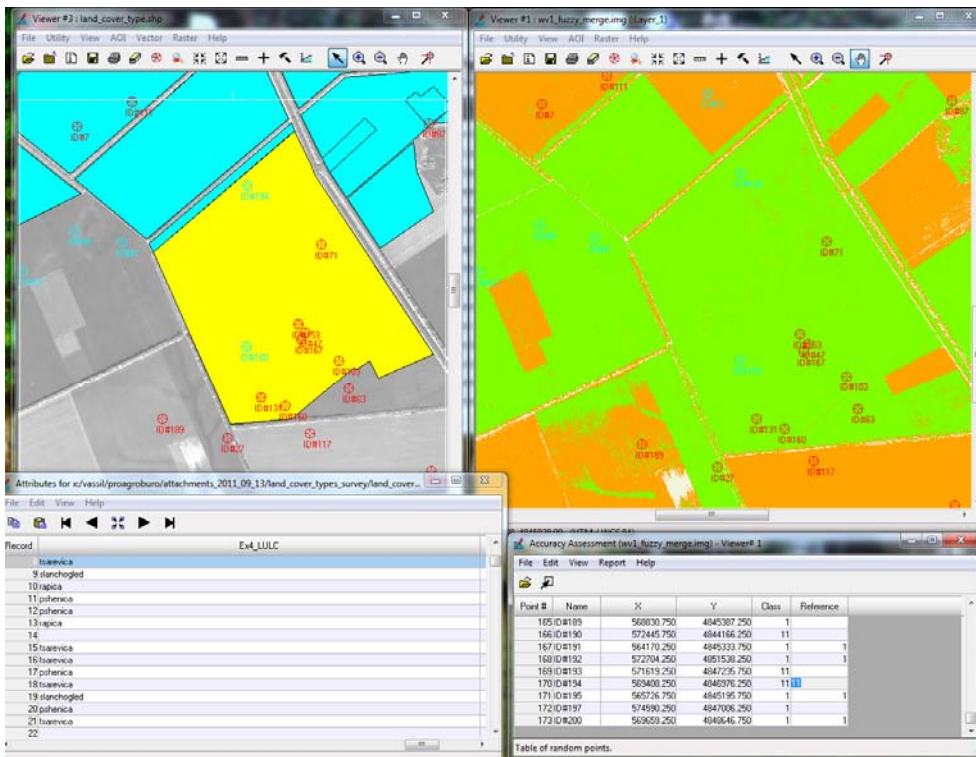


Fig. 6. Accuracy assessment on a WorldView-1 image

For both classes the producer and users accuracy is above 83%, which is quite a reasonable accuracy. For both classes the reference totals are more than 70 points, which makes the accuracy assessment process reliable. The high accuracy assessment is most likely due to the reference data used (unsupervised and supervised classification also with the ground data used) and the good choice of training samples, which is the most important thing for the classification process. It is not common practice to classify panchromatic images but nevertheless the high overall accuracy shows encouraging results.

Table 1. Accuracy totals for WorldView-1 image

Class name	Reference Totals	Classified Totals	Number Correct	Producer Accuracy	Users Accuracy
MASK	0	0	0	-	-
Stubble Fields	19	15	14	73.68%	93.33%
Winter Crops – winter wheat/Winter Rapeseed	73	77	64	87.67%	83.12%
Spring Crops – Sunflower/Maize	81	81	72	88.89%	88.89%
Totals	173	173	150	-	-

The accuracy assessment of the QuickBird-2 satellite image was accomplished using the fuzzy supervised classification and the accuracy assessment tool in ERDAS Imagine software (Figure 7). Randomly distributed 175 points were used (Table 2). The overall classification accuracy is 90.86% and overall kappa statistics is 0.8538. The class stubble field is with high accuracy, the reason is that the class is easily identified using the multispectral QuickBird-2 image. In this case the precise delineation of the training sample in ERDAS Imagine is the key for achieving high accuracy. The class spring crops, represented by sunflower and maize are with extremely high accuracy (Table 2.), with 90 reference points used for assessment of that class, which suggest that the accuracy assessment is reliable.

Considering the acquisition date of the QuickBird-2 image – 31/05/2009 the identification of spring crops is accomplished using the unsupervised classification in combination with the derived NDVI image. All this information accompanied with the ground surveys, although done 2 years later help the analyst. Thus some rotations of the crops is undergone this will inevitably help in assessing the accuracy of the supervised classification better. The class good status – winter wheat and winter rapeseed is with relatively high accuracy, with both the producer and users accuracy are above 85%. The high accuracy is due to the good information that was extracted from the derived NDVI image. The NDVI image was used to establish and to select good training samples for the supervised classification. A big advantage was also using the unsupervised classification, which in many cases gives the right set of mind in order to appoint appropriate training samples.

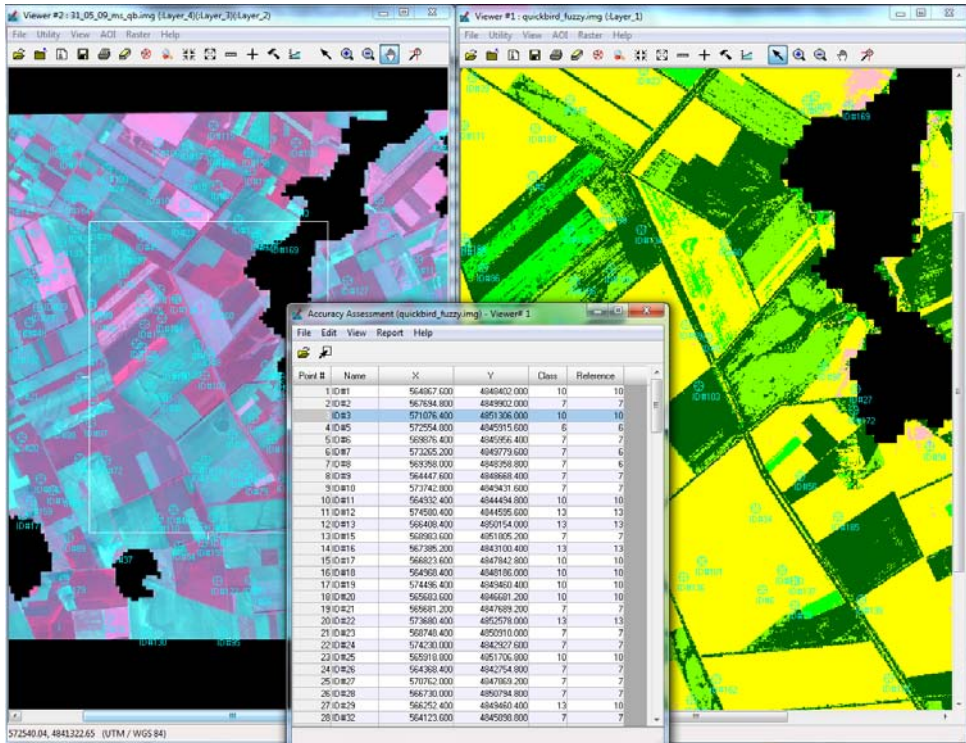


Fig. 7. Accuracy assessment on a QuickBird-2 image

Looking at the accuracy totals, the classes that are experiencing lower accuracies are the average status class and bad status class of winter wheat and winter rapeseed, with both of them having producers accuracy around 60%, although the users accuracy for both classes is above 90% (Table 2). The lower producers accuracy is probably due to the fact that these classes are representing different status of winter crops, which is always difficult to apply. The idea behind these two classes is indeed to try to identify different status of the winter wheat and winter rapeseed. The two classes are actually attempt to apply precision agriculture on the test site fields and identify where the winter crops are experiencing growth problems. This is very useful information if it can be delivered in real time or almost real time, so precision agriculture practices can be applied on specific places on the fields. For the time being this application is difficult to be put in practice considering the problems of high-resolution data acquisitions. But in the future this could be feasible.

Table 2. Accuracy totals for QuickBird-2 image

Class name	Reference Totals	Classified Totals	Number Correct	Producer Accuracy	Users Accuracy
MASK	0	0	0	-	-
Stubble Fields	6	5	5	83.33%	100.00%
Bad Status – winter crops	14	8	8	57.14%	100.00%
Average Status – winter crops	21	15	14	66.67%	93.33%
Good Status – winter crops	44	48	42	95.45%	87.50%
Spring Crops – Sunflower/ Maize	90	99	90	100.00%	90.91%
Totals	175	175	159	-	-

3.3. Crop condition assessment

The crop condition assessment was applied using the NDVI image derived from bands 3 and 4 of the QuickBird-2 image, representing RED and NIR spectral bands respectively. The Normalized Difference Vegetation Index (NDVI) is calculated as follows:

$$NDVI = \frac{(NIR - VIS)}{(NIR + VIS)}$$

where VIS and NIR stand for the spectral reflectance measurements acquired in the visible (RED) and near-infrared regions (NIR), respectively (Rouse, 1973).

The NDVI image was used to identify the main groups of crops based on the presence of vigor of green vegetation within the fields. Precision agriculture analysis is attempted using the high spatial resolution NDVI image. Considering the time of acquisition of the QuickBird-2 satellite image, a reclassification of the derived NDVI image was undergone in order to give reasonable meaning of the NDVI index and to try to establish differences between crops with good condition and these experiencing late

development or bad vigor status and map that crop condition for each crop field (Figure 8).

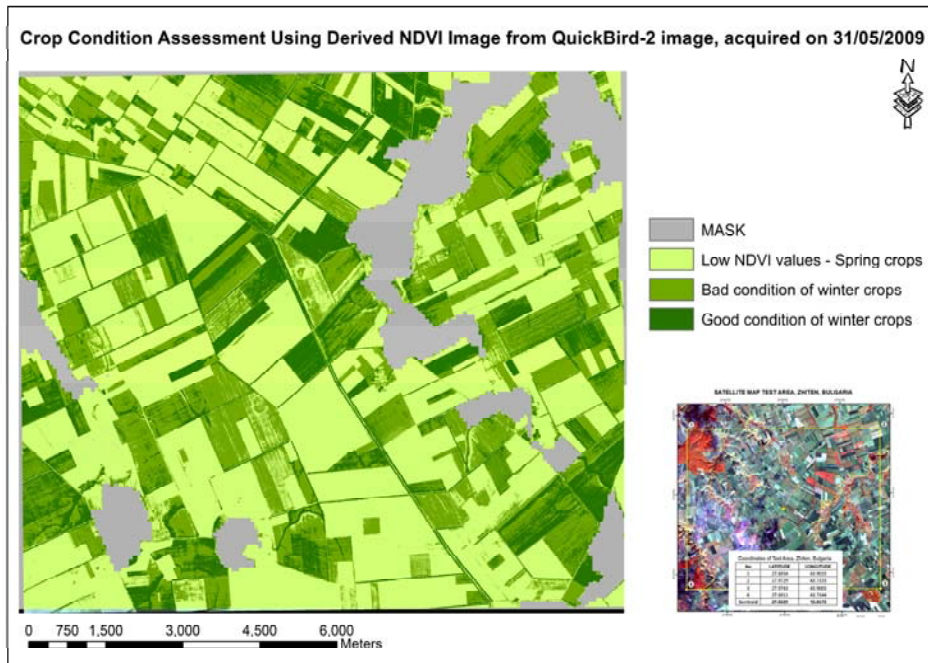


Fig. 8. Crop condition assessment using derived NDVI image from QuickBird-2 image

The NDVI image was reclassified using as reference the unsupervised and supervised classification and the histogram of the QuickBird-2 image. It was quite a challenge to establish reasonable thresholds for that matter. It was decided to divide the NDVI image in three classes – low NDVI, which in that acquisition date (31/05/2009) will represent the spring crops. The other two classes will be separated depending on their condition, which will be defined by either bad or good conditions. From the map it is quite easy to understand that the class spring crops is homogenous, which is due to the development stage of these crops and the NDVI doesn't separate them at the current stage. The conclusions that you can draw from that map can give some clear idea where the agronomical procedures were appropriate and as a result the crop status is good and where the agricultural practices were not so suitable, either not applied on appropriate date or using inappropriate

products for plant protection. Having that information in short time frame will really make a difference in all stages of crop development, where each agronomical practice should be carefully planned and accurately and precisely executed by the farmers.

3.4. Crop area estimation

The crop area estimates were calculated for both classified images WorldView-1 and QuickBird-2 using the fuzzy supervised classifications. The crop area estimates are calculated using the followed formula: number of pixels for each class of the classified image multiplied by the area represented by each pixel (Gallego, 2004). This method was selected because the overall classification accuracy was high enough to apply that method and in the same time not introducing bid bias. The crop area estimated for the WorldView-1 image show (Figure 9.) the following distribution: 36% class spring crops, 45% class winter crops and 6% of class Stubble fields. The mask class is 13% from the scene used.

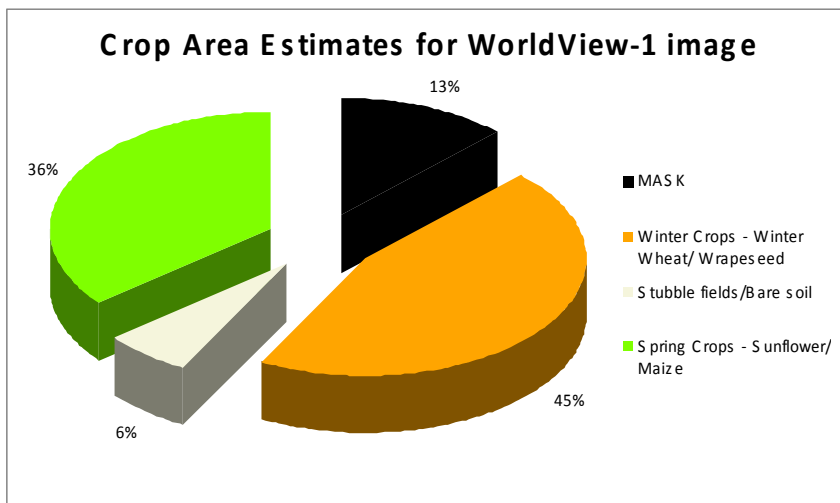


Fig. 9. Crop area estimates for WorldView-1 image

The crop area estimates for the QuickBird-2 classified image show the following figures (Figure 10): The class spring crops represents 43% of the studied territory. The sum of 42% is represented by winter crops, divided by status: 28% - good status, 8% - average status and 6% - bad status. Only 2%

represent stubble field class, which is reasonable having in mind the acquisition date of the satellite image – 31/05/2009. The stubble fields are the territories left for fallow lands for that agricultural year.

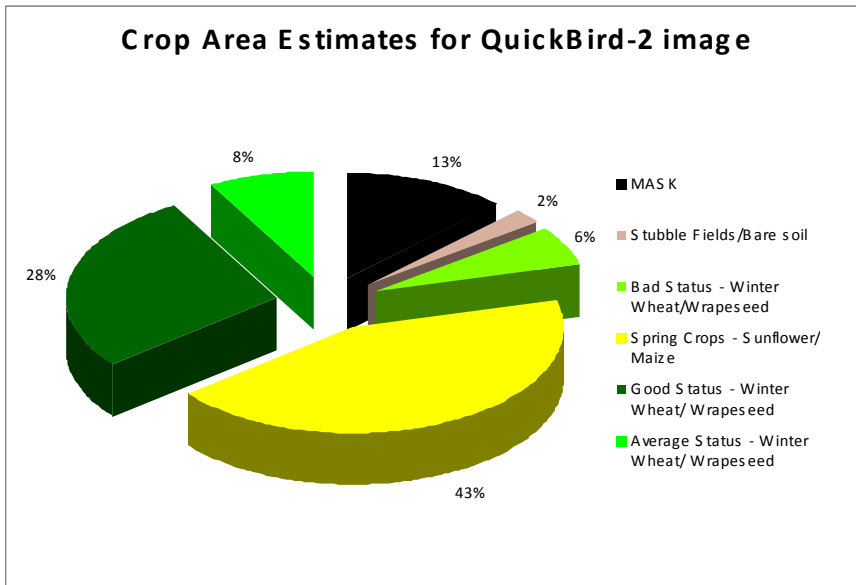


Fig. 10. Crop area estimates for QuickBird-2 image

4. Conclusions and future work

Using high-resolution satellite images in combination with ground data can be a strong combination for making crop analysis. High-resolution satellite images make it possible to accomplish accurate and precise crop identification on arable land. Thus, assessing crop condition and making some conclusions on crop status. Using NDVI as an indicator of crop condition is commonly used practice and is giving reliable results. The high accuracy assessment of both WorldView-1 and QuickBird-2 satellite images makes the crop area estimates as much as accurate as possible using the pixel counting approach. As a conclusion from the crop area estimated it can be highlighted that although the supervised classifications were applied on one panchromatic and one multispectral image, in different agricultural years, the results are almost identical (Figure 9 and 10). This can only be explained with the high accuracy of the research conducted and that the spatial distribution of winter crops and spring crops is well regulated on the

test site. Having good and reliable ground data has proven to be of great use together with expert knowledge from the analyst. This research is one of the first applying high-resolution satellite images on that test site. The encouraging results will be used for future work related with attempts of getting even more accurate estimates and applying coarse and low resolution satellite images on the same test site and using the achieved result from this research for validation of low-resolution vegetation products.

Acknowledgments

This work would not be possible without the support of ERDAS Geospatial Challenge contest, together with DigitalGlobe and Intergraph, which granted the satellite images after accepting a paper proposal.

This work is part of a PhD study from Assist. Prof. Vassil Vassilev done at the SPACE RESEARCH & TECHNOLOGIES INSTITUTE (SR&TI) at the Bulgarian Academy of Sciences, Sofia, Bulgaria (<http://www.space.bas.bg/Eng/Eng.html>)

References

1. B a t i s t a, G., M. H i x s o n & M. E. B a u e r. 1985. Landsat MSS crop classification performance as a function of scene characteristics. *International Journal of Remote Sensing* 6:1521-1533.
2. B u e c h e l, S. W., W. R. P h i l i p s o n & W. D. P h i l p o t. 1989. The effects of a complex environment on crop separability with Landsat TM. *Remote Sensing of Environment* 27: 261-272.
3. F o o d y, G. M., 2002. Status of land cover classification accuracy assessment. *Remote Sens. Environ.* 80, 185–201.
4. G a l l e g o (2004): Remote sensing and land cover area estimation, *International Journal of Remote Sensing*, 25:15, 3019-3047.
5. M a t h e r, P. M. (2004). *Computer processing of remotely sensed images* (3rd ed.). Chichester7 Wiley
6. M e d h a v y, T. T., T. S h a r m a, R. P. D u b e y, R. S. H o o d a, K. E. M o t h i k u m a r, M. Y a d a v, M. L. M a n c h a n d a, D. S. R u h a l, A. P. K h e r a & S. D. J a r w a l. 1993. Crop classification accuracy as influenced by training strategy, data transformations and spatial resolution of data. *Journal of Indian Society of Remote Sensing* 21: 21-28.
7. P i p e r, J. (1992). Variability and bias in experimentally measured classifier error rates. *Pattern Recognition Letters*, 13, 685–692.

8. Rouse, J. W., R. H. Haas, J. A. Schell, and D. W. Deering (1973) 'Monitoring vegetation systems in the Great Plains with ERTS', Third ERTS Symposium, NASA SP-351 I, 309-317

АНАЛИЗ НА ЗЕМЕДЕЛСКИТЕ КУЛТУРИ ПО СПЪТНИКОВИ ИЗОБРАЖЕНИЯ СЪС СВРЪХ-ВИСОКА ПРОСТРАНСТВЕНА РАЗДЕЛИТЕЛНА СПОСОБНОСТ ОТ WORLDVIEW-1 И QUICKBIRD-2 ЗА ТЕСТОВИ УЧАСТЪК НА ТЕРИТОРИЯТА НА БЪЛГАРИЯ

В. Василев

Резюме

Целта на настоящият доклад е да се изследват възможностите при спътникови изображения със свръх-висока пространствена разделителна способност от панхроматично изображение на WorldView-1 и многоканално изображение на QuickBird-2, заснети на 30.11.2011г. и 31.05.2009г. съответно за земеделски приложения, включващи разпознаване на земеделски посеви, оценка състоянието и оценка на площите. Разпознаването на земеделските посеви е извършено, чрез прилагане на неконтролирана и контролирана класификация. След контролираната класификация, фъзи филтър е приложен за да се ограничи проблема със смесените пиксели, използвайки програмния продукт ERDAS Imagine. Обща точност, матрица на грешките и капа статистика са изчислени при оценката на точността, с цел проверка на резултата от класификациите. Оценка състоянието на земеделските култури е извършена на базата на изчисление на Нормираният Разликов Вегетационен Индекс (NDVI) за изображението на QuickBird-2, което бе рекласифицирано на основата на хистограмата си. Оценка на площите е изчислена по принципа на (Gallego, 2004), където се преброяват класифицираните пиксели. Този подход не дава най-надеждни резултати, но при обща точност за изображението на QuickBird-2 от 90.86% и 86.71% за изображението на WorldView-1 дава възможност да се приложи. Прилагането на маска на обработваемите земи с цел разпознаване на земеделските култури е подобряващ подход, защото ограничава проблема със смесения пиксел.

CROP MONITORING USING SPOT-VGT NDVIs S10 TIME-SERIES PRODUCT FOR THE ARABLE LAND OF BULGARIA

Vassil Vassilev

*Space Research and Technology Institute – Bulgarian Academy of Sciences
e-mail: vassilev_vas@yahoo.com*

Abstract

The objects of investigation are the major crops in Bulgaria (winter wheat, winter barley, sunflower and maize). The purpose of this paper is to 1) identify major crops using satellite data with low spatial resolution of 1000 m using agro-phenological information; 2) monitoring based on NDVI time-series values for the years 2007, 2008 and 2010, where anomaly events occur based on the information in the National Institute of Meteorology and Hydrology at the Bulgarian Academy of Sciences (NIMH-BAS) agrometeorological monthly bulletins. The current paper shows the massive potential of using low spatial resolution satellite data in identifying crops and monitoring the development anomalies on crops. This research will contribute in applying and elaborating JRC MARS methodology in Bulgaria by using low resolution SPOT-VGT NDVIs S10 satellite product.

Introduction

Satellite remote sensing (RS) provides synoptic, objective and homogeneous data, which can be geographically and temporally registered, and therefore, could be an efficient tool for providing standard, high quality information on agriculture, evenly over the whole of Europe. The Monitoring Agriculture with Remote Sensing (MARS) project of the European Union was established in order to define and demonstrate how RS could be used operationally to supplement, interpret, and standartize agricultural statistical data provided by conventional techniques (Meyer-Roux and Vossen, 1994; de Winne, 2004). Satellite remote sensing techniques have proven to be effective and useful in broad-scale agricultural

surveys such as: large area crop inventory experiment (LACIE) in the USA and monitoring agriculture with remote sensing (MARS) in Europe (Cohen and Shoshany, 2002). Experiments such as Crop Identification Technology Assessment for Remote Sensing (CITARS) and Large Area Crop Inventory Experiment (LACIE) were conducted to demonstrate the capabilities of RS for crop inventory and forecasting (MacDonald, 1984; Blaes, 2005). Crop identification during the growing season is currently a major challenge for forecasting crop production as well as for controlling area-based subsidies (Blaes, 2005).

Materials and Methods

The whole arable territory of the Republic of Bulgaria was used for applying the proposed methodology. The most commonly used vegetation index for agricultural applications using RS data is the Normalized Difference Vegetation Index (NDVI), expressed with the following formula:

$$NDVI = \frac{(NIR - VIS)}{(NIR + VIS)},$$

where VIS and NIR stands for the spectral reflectance measurements acquired in the visible (RED) and near-infrared regions (NIR), respectively (Rouse et al., 1973).

Time-series of SPOT-VEGETATION NDVIs S10 smoothed actual product with spatial resolution of 1000 m. for three year (2007, 2008 and 2010), where anomaly events were observed, based on the information from the monthly bulletins from NIMH-BAS. Overall the used low-resolution satellite images for the study were 108.

The two major tasks are the following:

- 1) Identification of crops in the arable territory of Bulgaria, for the years 2007, 2008 and 2010, using the cluster analysis method upon a 10-day SPOT-VGT NDVIs S10 product by extracting agro-phenological information from the NIMH-BAS monthly bulletins;
- 2) Monitoring the NDVI time-series values for the years 2007, 2008 and 2010, where anomaly events occur based on the information of the NIMH-BAS monthly bulletins.

A complex approach has been undertaken in order to achieve the purpose of the study. The methodological scheme includes the sequence of the following working tasks Figure 1:

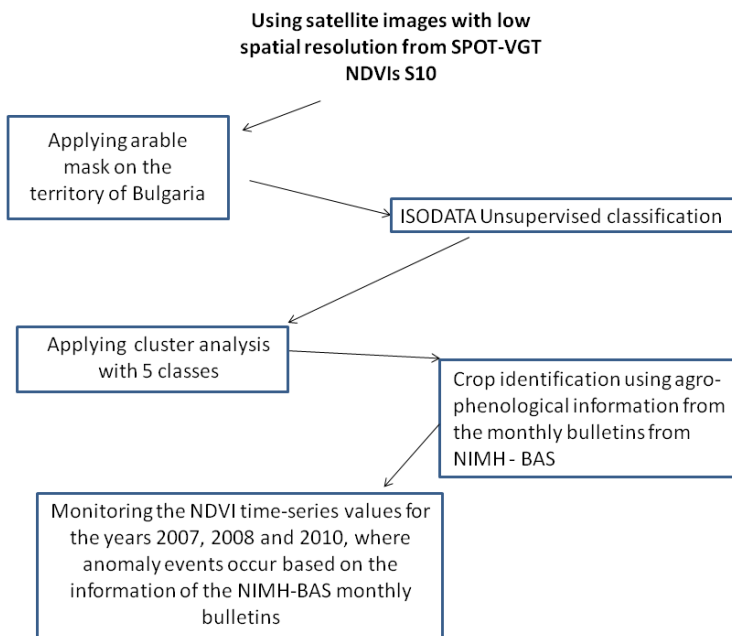


Fig. 1. Workflow of the study

Short description of the methodology

An arable mask was applied in order to extract only the arable land using information from CORINE 2000 database and then aggregated to the spatial resolution of the used SPOT-VGT NDVIs S10 product – 1000 m. The images were stacked on yearly basis (one file with 36 bands, representing the 36 decads of the year) in order to work with more concise data. Unsupervised ISODATA classification with five classes was used on the individual yearly stacked images in ERDAS Imagine software (Groom et al., 1996; Garcia-Consuerga and Cisneros, 1999; Yang et al., 1999). Using this method the arable territory of Bulgaria was divided into five clusters based on the differences of their spectral reflections. Following the classification, a cluster analysis was conducted, which extracts the mean NDVI values for each 10-day for every cluster separately. Using that information NDVI time-series profiles of the five clusters were created for

the period January 01 – December 31, for each year (2007, 2008 and 2010). The crop identification process was accomplished using a summary table derived from the agro-phenological montly bulletins of National Institute of Meteorology and Hydrology at Bulgarian Academy of Sciences (NIMH-BAS) at the following web site - <http://www.meteo.bg/>, where information for the specific growth stages (phenophase), agro-technical treatments throughtout the growing season and some experienced anomaly events for each 10-day is given. Monitoring of these three years for every 10-day period was initiated using SPOT-VGT NDVIs S10 product in order to investigate its capabilities to detect anomaly events. The data absolutely corresponds to the temporal resolution of the satellite data that was used. The time-series profiles were interpreted and the major crops were identified using the ground data summarized in the table for each 10-day period. The table includes the phonological stage and stage of deelopment for every 10-day periods of the year, information on the agronomical practices that are applied on the crops and if any anomaly events have accured during this period (Table 1). There is an example of crop growth stages for cereals: sowing, seedling growth, tillering, stem elongation, flowering, grain-filling periods (milk and dough development), ripening and harvest.

Table 1. NIMH-BAS agro-phenology summary table with an interpretation key

Месец	Януари	Февруари	Март	Април	Май	Юни	Юли	Август	Септ.	Октомври	-	-
Година	Януари	Февруари	Март	Април	Май	Юни	Юли	Август	Септ.	Октомври	-	-
2012	През период е: 6.8 и 25.27.1 се запази положителна, тенденцията на есенно-зимното влаготнапруване. Обилни валежи, вследствие е на наднормените топлинни условия през през първото десетдневие на месеца - стоплане на снежната покривка в равнините - четири	Интензивните валежи в края на януари и през първите две седмици на февруари - съществено увеличаване на запасите от влага в почвата (ППВ). През периода 1: 5: 8,8 , на много места паднаха обилни валежи, надхвърлили в Северна и Южна България месечните норми (над 79-142 l/m ² (Хасково 142 l/m ² , Кърджали 79 l/m ² , Пловдив 47 l/m ² , Благоевград 46 l/m ² , Пазарджик: 43 l/m ² , Сливен 40 l/m ² , Видин 33 l/m ²)	Падналите валежи близо под нормата . През 1 интензивното снеготопене ограничаваша възможностите за нормално провеждане на сезонните полски работи. 2 превалвания от дъжд. Това възпрепятства навременното азотно подхранване на есенниците и провеждането на механизирани почвообработки. На 17.03 началото на пролетния вегетационен период запасите от продуктивната влага в почвата	Валежите в част от Северна, Централна и Източна България количеството надхвърли нормите за месеца , докато в Южна България и Подбалканските полета сумата на априлските валежи бе едва 13-18 l/m ² , което е под 50% от месечната норма . 1 ниски нива на ППВ. 2 валежи повишиха стойностите на 80-85 % от ППВ. 3 малкото валежи доведоха до ряско снижаване на продуктивната влага (Дунавска равнина и Юните надбани) Май.	1 Задълбочаващо засушаване в (северозточни и южни райони 2 дъждовния наднормените валежи (с количества над 120-150 l/m ²) и градушките, ветрове - щети на част от земеделските култури. 1 високите темп. - рязко намаление на влагата в 20 и 50-сантиметровите почвени слоеве. Критично ниски посевите встъпили във фаза изкласване. 2 валежите отново бяха обилни и посевестни. 2 рязко повишение на ППВ в почвата. 3 влаготнапруване	Липса на валежи - през климатично най-дъждовния месец от годината, дефицитът на влага в почвата - Източна и Южна България. В края на месеца продуктивната влага в отделни части на Южна България (Костендил, Хасково, Кърджали) бе почти изчерпана. Проведеното на земеделските мероприятия бе силно затруднено. Понижението на водните запаси в края	Сухо време през коли задълбочи още повече сушата. Постепенно изчерпване на продуктивната влага както от горите, така и от дълбоките почвени хоризонти. Оцеляване само чрез напояване. Почти унищожен и пролетни култури на места при неполиване. Наднормен и температур и - съсьвяване на	Горещо и сухо време. 1 валежи в Западна Б-я, подобриха състоянието почвено влагосъдържане. Културите зависими от напояване (зеленци и овоши). 2:3 дефицит на почвена влага. Критично състояние на пролетни култури без напояване. 1 съсьвяване на	Топло за сезона време в полското район. Затрудняване на сезонните мероприятия. Ускорено развитие на късните земеделски култури. ППВ е осъдна. 1 ускори последните етапи на развитие на земеделските култури. Царевича - среднокъсна и - въсьчна зрелост, а късните - млечна зрелост. Узяване на	1 Драматично намаление и пълно изчерпване на запасите от влага в горите и дълбоките почвени слоеве. Исклучени я се наблюдаваха единствено в районите на Разград, Хасково и Чирпан. 2 Продуктивна влага около и под критичните граници. 1 Проведането на есенната септемна нампаяния и механизирани	-	-

Results and discussions

Cluster analysis

The following crops were identified for each cluster from (1-5) using as reference the summarized agro-phenological information and the cluster analysis: 1) mixed crops 2) winter wheat 3) winter barley 4) sunflower, and 5) maize.

Figures representing the spatial distribution of the cluster classes together with time-series profiles for the anomaly years (2007, 2008 and 2010) were prepared.

Analysis of 2007

The year 2007 was characterized as anomalous as the winter crops at the beginning of the year were ahead of their development by 45 days. In March they were already in heading phenophase. In May caused by bad agrometeorological conditions shortening of the phenophase periods were observed and as a result the collected yield from both winter crops and spring crops were small. The harvest of the late cultivars of maize was delayed due to intensive rainfall in the beginning of September.

The cluster map of actual NDVI values shows the spatial distribution of the identified crops. The classes' winter wheat and winter barley are distributed in the most common for them areas: Dobrudja plain and Upper-Tracian valley. The classes' sunflower and maize are distributed in the west part of the Danube plain (Figure 2a). Classes that were identified as winter wheat and winter barley were clearly separated, because since the first decade the NDVI values were above 0.38, which was a clear indication for winter crops (Figure 2b). The cultivars of winter wheat and winter barley reach their mean maximum NDVI values (0.67 and 0.63 respectively) at the end of April and at the middle of May when flowering and grain filling phenophases occur, and this corresponds to the information summarized from NIMH-BAS monthly bulletins. Winter wheat and winter barley are harvested during the first decade of June, and this can be observed in the time-series profiles where the NDVI values decrease to 0.35. Sunflower and maize cultivars reach their peak of NDVI values in June (0.69 and 0.78, respectively) when they are at flowering phenophase (Figure 2b).

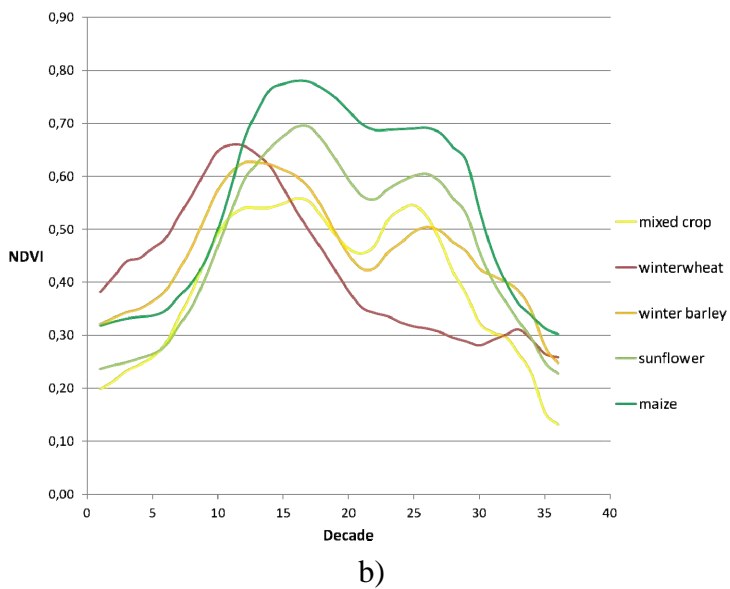
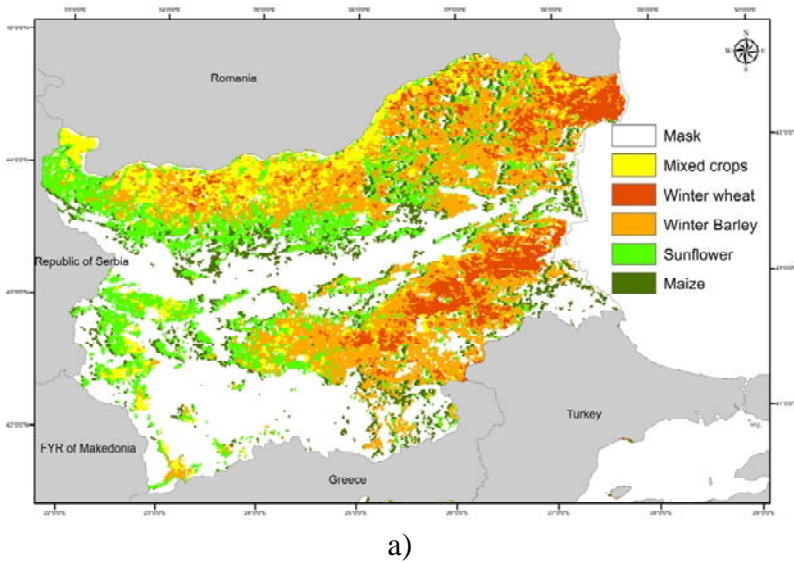


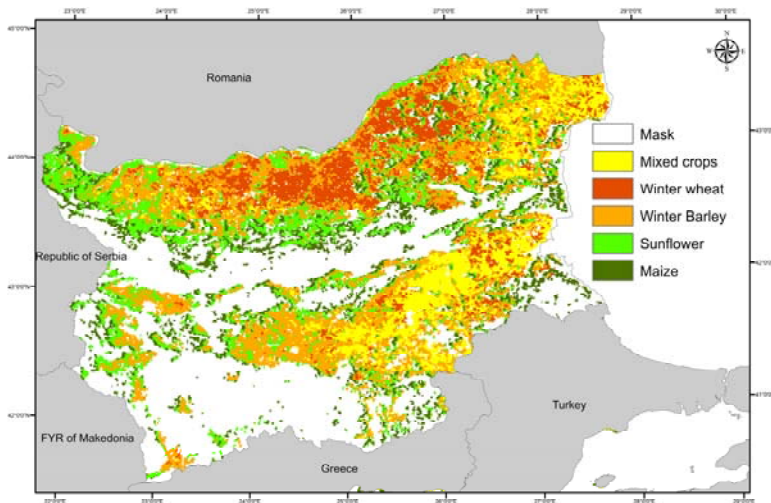
Fig. 2. a) Cluster map of actual NDVI values for 2007 b) NDVI cluster time-series profiles for 2007

Analysis of 2008

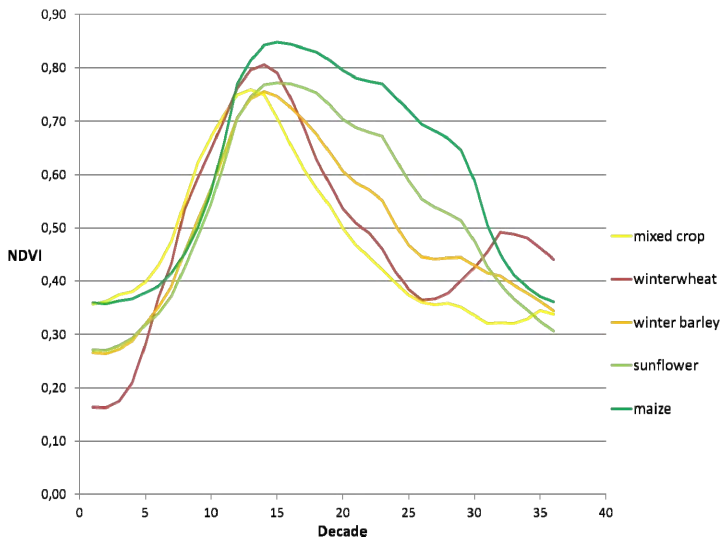
The year 2008 was characterized as anomalous year in terms of favourable agrometeorological conditions and in-time conducted agrotechnical procedures, which is having great impact on the achieved yield values.

The cluster map (Figure 3a) shows that the class mixed crops was situated in the northeast part of the country, whereas the cultivars of winter crops (winter wheat and winter barley) were located in the central north parts of Bulgaria.

The time-series profiles of the winter crops reflects very precisely the late onset of the tillering and heading phenophases, at the beginning of March due to the late snow melt reported in the NIMH-BAS monthly bulletins. The cultivars of winter wheat and winter barley reach their mean maximum NDVI figures at the end of May with very high values (0.81 and 0.76, respectively). Meanwhile, classes' sunflower and maize reach their peak of NDVI in June with exceptionally high values (0.77 and 0.85, respectively). This high NDVI values for the year 2008 corresponds to the official statistics where highest yields have been reached for the last 20 years (Figure 3b).



a)



b)

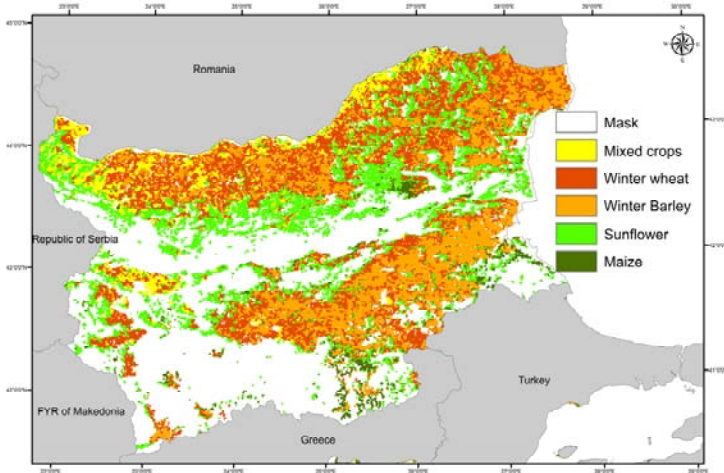
Fig. 3. a) Cluster map of actual NDVI values for 2008; b) NDVI cluster time-series profiles for 2008

Analysis of 2010

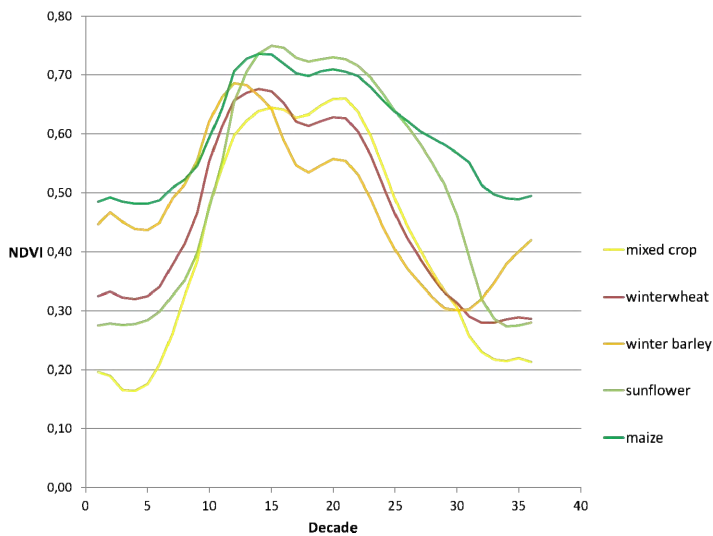
The agrometeorological conditions in 2010 regarding the crop condition can be summarized as unfavourable, which causes delay of the harvest and has negative impact on the achieved crop quality and yield figures.

The cluster map (Figure 4a) shows that classes' winter wheat and winter barley are located in Dobrudja plain and the Danube valley, as well as in the South-East part of Bulgaria (upper-Tracian plain), while sunflower and maize cultivars are distributed in western part of Danube plain. The NDVI values for every class in the beginning of the year experience a slight increase than usual due to the favourable conditions – high temperatures for January, which keeps the vegetative state of the winter crops. In the middle of the month the temperatures decrease rapidly, which returns the crops to dormancy. Nevertheless, this anomalies were clearly identified using the NDVI time-series profiles. It is recognizable from the time-series profiles that winter crops renew their vegetative stage with NDVI values between 0.35-0.43. They reach their mean maximum NDVI values in May and at the beginning of June when they are in grain filling and ripening phenophases,

while at the beginning of June winter barley is at maturity stage with NDVI values 0.69. In the end of June and July the spring crops (sunflower and maize) reach their mean maximum NDVI values accumulating to 0.75 and 0.74, respectively (Figure 4b).



a)



b)

Fig. 4. a) Cluster map of actual NDVI values for 2010; b) NDVI cluster time-series profiles for 2010

Conclusions

The possibility of identifying and monitoring the development of the major cultivated crops on the arable territory of Bulgaria using data from low spatial resolution satellite images from SPOT-Vegetation NDVIs S10 product combined with well organized ground data from NIMH-BAS was investigated in this paper. The applied methodology proves that the low resolution satellite images are an ideal solution for crop identification and monitoring on large arable territories; however they must always be supported by and used in combination with agro-phenological ground data. The monitoring analysis using cluster maps and time-series data from SPOT-VGT NDVIs S10 product shows great potential to follow the development of crop cultivars throught out the year. Using the agro-phenological monthly bulletins from NIMH-BAS together with the low resolution satellite images can be used operationally for detecting anomaly events as well as monitoring crop condition and development.

Acknowledgments

The study is part of the PhD thesis of the autor. The author would like to express his gratitude to the MARS Unit, Agri4cast action at the Joint Research Center (JRC) of the European Commision (EC) for supplying him with the satellite data from SPOT-Vegetation NDVIs S10 product.

References

1. M e y e r – R o u x, J., P. V o s s e n. The first phase of the MARS project, 1988–1993: overview, methods and results. In: Official Publications of the E.U., Luxembourg (Ed.), Report EUR 15599 EN, 1994. Conference on the MARS project: Overview and prospectives, Belgirate, pp. 33-79.
2. de W i n n e, P. Les Besoins de la Direction Generale VI: Agriculture. In: Office for official publications of the E.U., Luxembourg (Ed.), Report EUR 15599 EN, 2004. Conference on the MARS project: Overview and prospectives, Villa Carlotta, Belgirate, Lake Maggiore, Italy, pp. 17–22 (in French).
3. C o h e n, Y., M. S h o s h a n y. Int. J. Applied Earth Observation and Geoinformation, 4, 2002, No 1, pp. 75-87.
4. M a c D o n a l d, R. IEEE Transaction on Geoscience & Remote Sensing, 1984, GE-22: 473-481.
5. B l a e s. Efficiency of crop identification based on optical and SAR image time series. Remote Sensing of Environment, 2005, 96, pp. 352 – 365.

6. R o u s e, J., R. H a a s, J. S c h e l l, D. D e e r i n g. Monitoring vegetation systems in the Great Plains with ERTS. In: Third ERTS Symposium, 1973, NASA SP-351 I, 309-317.
7. G r o o m, B. G., F u l l e r, R. M., J o n e s, A. R. Contextual correction: techniques for improving land-cover from remotely sensed images. Int. J. Remote Sens. 1996, 17, pp. 69–89.
8. G a r c í a – C o n s u e g r a, J., C i s n e r o s, G. Establishing spatially continuous in a non-supervised way. In: Proceedings of the IEEE International Geoscience and Remote Sensing Symposium (IGARSS'99), 1999, Hamburg, Germany.
9. Y u a n, H., K h o r r a m, S., D a i, X. L. Applications of simulated annealing minimization technique to unsupervised classification of remotely sensed data. In: Proceedings of the IEEE International Geoscience and Remote Sensing Symposium (IGARSS'99), 1999, Hamburg, Germany.

МОНИТОРИНГ НА ЗЕМЕДЕЛСКИТЕ КУЛТУРИ ПО ВРЕМЕВИ СЕРИИ ОТ ВЕГЕТАЦИОНЕН ПРОДУКТ SPOT-VGT NDVIs S10 ВЪРХУ ОБРАБОТВАЕМАТА ТЕРИТОРИЯ НА Р. БЪЛГАРИЯ

В. Василев

Резюме

Обектът на изследване в настоящата статия са основните за България земеделски култури (зимна пшеница, зимен ечемик, слънчоглед и царевица), а целта е да се извършат следните задачи: 1) идентифициране на основните за България земеделски култури чрез прилагането на спътников продукт с ниска пространствена разделителна способност от 1000 м. от SPOT-Vegetation NDVIs S10 с помощта на информация от месечните агрометеорологични бюлетини на Националния Институт по Метеорология и Хидрология към Българската Академия на Науките (НИМХ-БАН); 2) провеждане на мониторинг по NDVI времеви серии от данни от продукт SPOT-Vegetation NDVIs S10 за календарните 2007, 2008, 2010 години, които се считат за аномални по своите агрометеорологични условия, съдейки по месечните бюлетини на НИМХ-БАН. Настоящата статия показва огромния потенциал при използването на спътникови продукти с ниска пространствена разделителна способност при идентифицирането и мониторинг развитието на земеделските култури върху обработваемата територия на България. Това изследване ще допринесе с прилагането на JRC MARS методологията за мониторинг на земеделските култури в България.

LANDFORM CLASSIFICATION USING ASTER GDEM AND OPTICAL HIGH RESOLUTION SATELLITE IMAGES OF SOFIA CITY DISTRICT

Vanya Naydenova, Stefan Stamenov

*Space Research and Technology Institute – Bulgarian Academy of Sciences
e-mail: vnaydenova@gmail.com*

Abstract

The morphologic and morphometric landform information plays a significant role in the spatial and temporal analysis and modeling of the landscape and affects the course of the natural processes. The geoinformation technologies provide for performing digital terrain analysis and extraction of a series of morphometric parameters and landform elements. The compound geomorphologic analysis and interpretation can be performed through various algorithms incorporated in the GIS software product. The objective of the present study was to classify the landform elements and to describe landform complexity of Sofia City District based on ASTER GDEM and satellite images. TPI-based algorithm for landform classification will be applied and the terrain heterogeneity of the study area will be assessed. As a result of the performed spatial analysis maps of the topographic position index and landform classification map were elaborated.

Introduction

Relief is one of the major components of each landscape, which plays an important role in the spatial distribution of the surface water runoff and determines the exogenic processes (denudation, accumulation, erosion, etc.). The landform information is essential for the modeling and understanding of many physical processes [1]. The term *landform* is defined as “*any physical feature of the Earth’s surface having a characteristic, recognizable shape*” [2]. From the geomorphometric point of view a landform is “*a terrain unit created by natural processes in such a way that it may be recognized and described in terms of typical attributes where ever it may occur*” [3], [4].

Digital terrain modeling, also known as geomorphometry, integrates methods from earth sciences, geoinformatics and geostatistics. It studies the quantitative and qualitative description and measurement of landform [5], [6] using various approaches, including classification of morphometric parameters, filter techniques, cluster analysis, and multivariate statistics. Terrain analysis for landform classification has been applied by many authors dating back to 50-ties of the XXth century [7]. A large number of automated techniques and algorithms for DEM/DTM processing and extraction of landform elements has been developed and applied [8], [9], [10], [11], [12]. Many of these algorithms has been implemented into GIS software (e.g ESRI and the open source products such as SAGA, GRASS, gvSIG, etc.), whereas others were developed as stand-alone programs and software packages (MICRODEM [13], LandSerf [10], TAPES set [12], DiGeM [14] [15], TAS GIS [3], etc.)

The landscape differentiation can be performed by extraction of different landform elements through parameterization of digital elevation model (DEM). Various classifications of landforms have been proposed according to the morphometric variables which are used as a basis for their characterization and description. Among the well known algorithms are those developed by Hammond, Wood, Conrad, etc [15], [10], [16], [17]. The object-oriented approach for landform classification has been applied for territories with different relief types [18], [19], [20], [21], [22].

Objective

The objective of this study was to classify the landform elements and to describe landform complexity of Sofia Municipality based on ASTER GDEM and satellite images. We apply and test the TPI-based (topographic position index) algorithm for landform classification developed by Conrad and assess the terrain heterogeneity of Sofia City District.

Study area

The Sofia (Metropolitan) Municipality, which in the term of territorial scope is identical with the Sofia City District, is located in Western Bulgaria. It includes 38 settlements - 1 city (Sofia), 3 towns (Bankya, Novi Iskar and Buhovo) and 34 villages. According to the data obtained from CORINE land cover 2006, its territory is occupied by urbanized territories (13.5%), agricultural land (37%), forest areas (30%), scrubs and open spaces with little or no vegetation (9.4%), mining and quarry areas (1.6%), transport and infrastructure facilities (5.5%) and water areas (3%). From the point of view of physical geography its location is analyzed with respect to the main

morphological structures (structural units). Sofia Municipality occupies part of the Sofia hollow (field), and parts of the surrounding mountains - Mala and Sofia Mountains in the northern part, and Vitosha, Plana, Lyulin and Lozenska Mountains in its southern part (Fig.1). The landscape of Sofia Municipality is characterized by varied relief and relatively mild climate, part of the moderate-continental climatic region of Bulgaria. The relief is represented by flat areas, foothills, valleys and mountain areas, which are changing from mountain areas in north to flat areas in the middle of territory and again mountain areas in the southern part. The average altitude of Sofia hollow is approximately 550 m a.s.l. and in its periphery the elevation rises gradually. The average altitude for the whole municipality is calculated to 1386 m, while the maximum and minimum elevation values vary from 450 to 2241 m. Due to the high rate of urbanization, the natural relief is significantly complemented and transformed by the anthropogenic factor as a result of which a number of anthropogenic landforms have been created - artificial reservoirs (such as Iskar Dam, Pancherevo Dam, Passarel Dam), transport and industrial infrastructure, quarries, embankments, etc.

The available geological information and the studies conducted over the years by Kamenov, Georgiev, Frangov on the area of Sofia Municipality show that the Sofia hollow is young, Neogene-Quaternary tectonically active graben structure [23], [24], [25], [26]. Detailed geomorphologic studies of Sofia region including surrounding mountains have been conducted by Hristov, Georgiev, Kanev ([27], [28], [29], [30], [31], [32]), and the anthropogenic relief has been discussed by Vlaskov and Simeonov in 1992 [33]. Digital terrain analysis of the relief for geocological studies of Sofia Municipality has been performed by Choleev and Popov in 2005 [34].

The main elements of the hydrographic network in Sofia Municipality are the rivers and water reservoirs and lakes. The main drainage artery is the river Iskar with its asymmetrical tributary network, represented mainly by short tributaries. Most of them are left-handed, which spring from from Vitosha Mountains (the river Bistritsa, Perlovska, Vladayska) and from Lyulin Mountains (e.g. river Suhodolska), as well as the river Blato. The most significant right-hand tributary of Iskur river is Lesnovska (as known as Stari Iskur). Based on the landscape diversity (determined by the natural characteristics of the territory) and the altitude-based zoning the natural landscapes of Sofia Municipality can be divided into three major types: Mountain landscapes, Foot-hill landscapes, Plane landscapes.

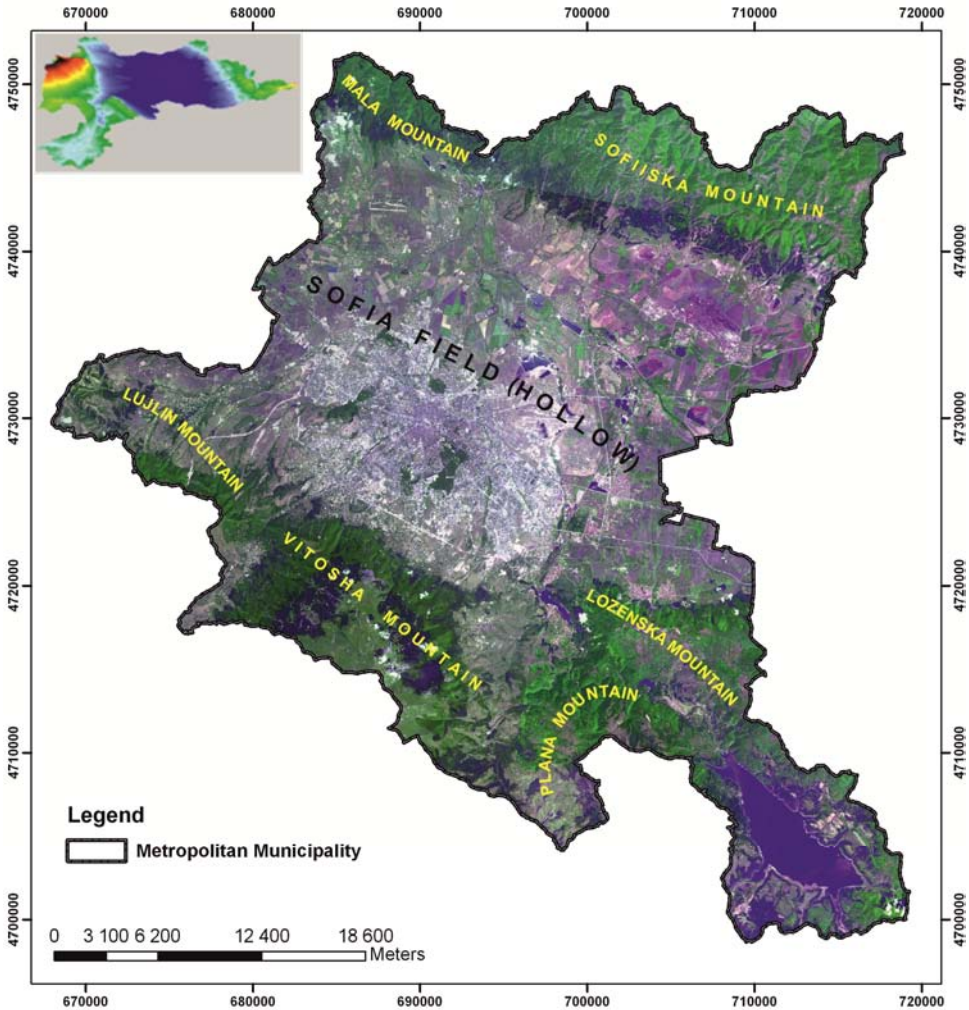


Fig. 1. Overview of Sofia City District (Metropolitan Municipality)

Methodology

Data sources

The main data source for the present study is ASTER GDEM (ASTER Global DEM) with resolution 30 m. ASTER GDEM is a satellite product provided by METI and NASA and download by WIST web portal of NASA. The missing data and error of the DEM was filled through spatial analyst tools of ArcGIS, and then converted in ascii grid file.

Digital terrain analysis

The present work is focused on some morphometric parameters and derivatives. The chosen morphometric parameters for characterization of the structural elements of the relief are the topographic position (TPI) and topographic ruggedness indexes (TRI), the Multi-resolution index of valley bottom flatness and TPI-based landform classification. The calculations were performed using SAGA GIS modules and algorithms for terrain analysis, developed by Conrad [35] (table 1).

The **TRI** reveals the terrain roughness and serves as an objective measure of the topographic heterogeneity and diversity [36]. It is calculated for every grid based on the change of the elevation and the mean of the elevation for the neighboring cells within 3x3 pixel grid.

The **TPI** is defined as a difference between the elevation of a specific cell and the average elevation of the neighboring grid cells. It compares the elevation of each cell in a DEM compared to the mean elevation of a specified neighborhood around that cell.

The multi-resolution index of valley bottom flatness calculates two morphometric parameters - multi-resolution index of valley bottom flatness (MRVBF) and multi-resolution index of the ridge top flatness (MRRTF). The first of them classifies valley bottoms as flat, low areas using slope and elevation (DEM), while the second index uses the opposite algorithm for identification the ridge tops [37].

The classification approach which is applied in the present study is known as TPI-Based Landform Classification, developed by O. Conrad (2011).

Table.1. Morphometric parameters and indexes applied for the territory of Sofia City District

Morphometric parameter/index	Input data	Algorithm author/references
MRVBF	DEM	<i>Algorithm: O. Conrad (2006)</i>
MRRTF	DEM	
TRI	DEM	<i>Algorithm: O. Conrad (2010)</i>
TPI	DEM	<i>Algorithm: O. Conrad (2010)</i>
Landform Classification	DEM	<i>Algorithm: O. Conrad (2011)</i>

Results

Maps of the morphometric parameters and landforms of the Sofia City District were elaborated. The result were correlated and compared to ASTER satellite image of the Sofia Municipality with spatial resolution 18 m.

The valley bottoms of Sofia City District were classified through the multi-resolution index of valley bottom flatness, where the highest value indicates the low flat areas (Fig. 2). The lowest part of the Sofia hollow is well distinguished and it coincides with the valleys of Iskur river, Blato and Leskovska.

Fig. 2. Map of the multi-resolution index of valley bottom flatness (MRVBF) of Sofia City District

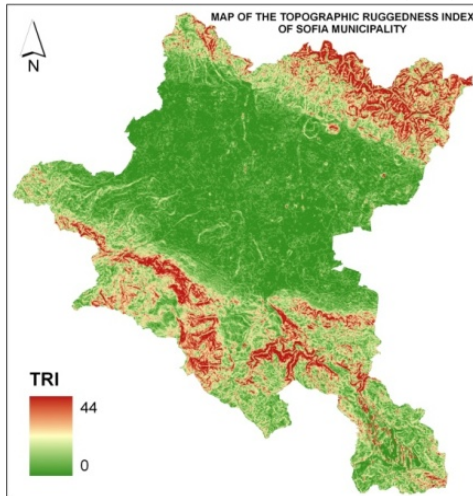
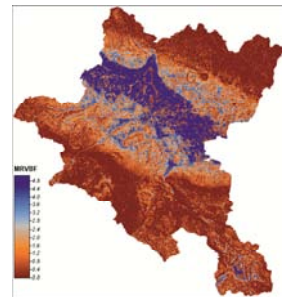


Fig. 3

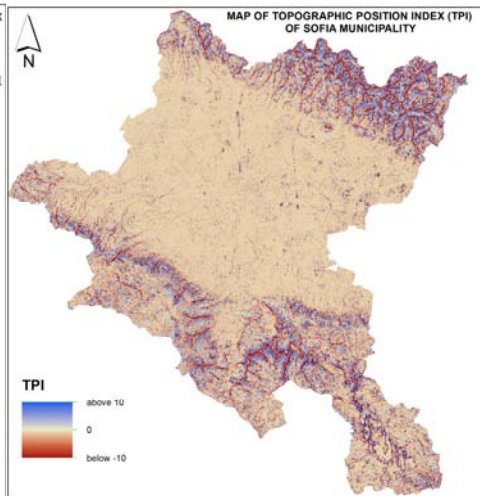


Fig.4

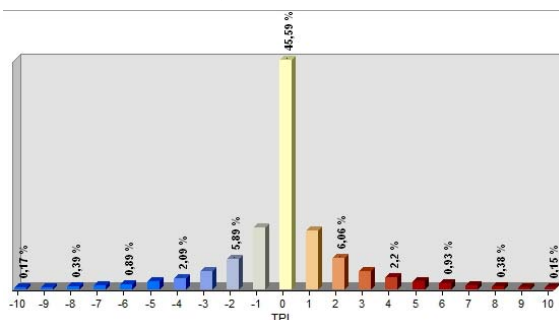


Fig. 5. Histogram of the TPI values for the territory of Sofia City District

The areas with most fluctuations of the elevation correspond to the areas of highest values of TRI. The lowest TRI values are observed in the Sofia hollow and in some areas in the southern part of the Sofia City District – Vitoshka plateau and parts of Lozenska and Plana mountains. The highest rate of heterogeneity is registered in the mountainous areas in the northern and southern part of the District (Fig. 3). The terrain heterogeneity is an

important morphometric parameter and variable for analyzing the landscape heterogeneity and diversity.

The TPI values for the territory of Sofia vary between minus 10 to plus 10 (Fig.4 and 5). The positive TPI values are associated with locations that are higher than the average of their neighborhood surroundings and they are defined as ridges, while the negative represent locations that are assigned with values lower than their surroundings and are classified as valleys. The flat areas are calculated with values near zero, whereas when the slopes are greater than zero. Almost 50% of the territory of Sofia City District has TPI value 0, and is classified as flat areas.

The topographic position index is used for differentiation of the main landform classes. The calculations are performed in SAGA GIS environment using the TPI-based algorithm.

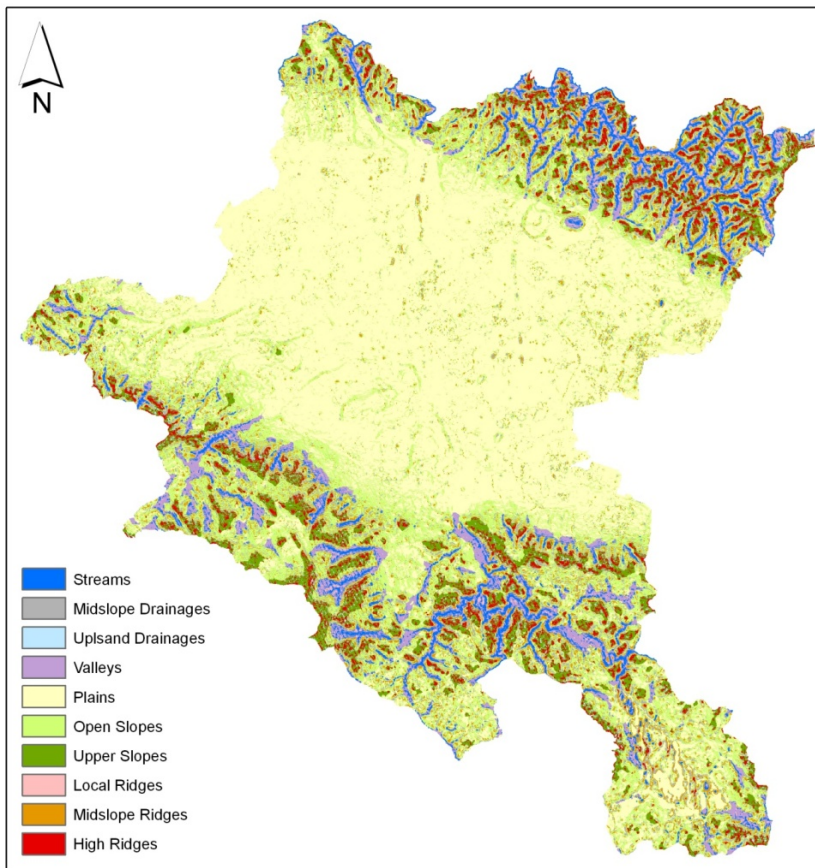


Fig. 5. Landform map of the Sofia Municipality using the TPI-based landform classification algorithm

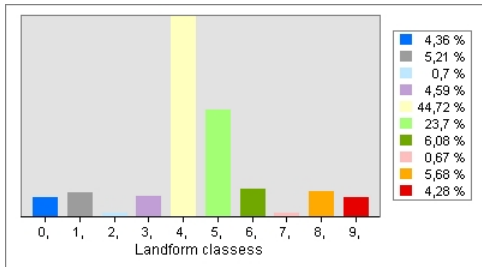


Fig. 6. Histogram of the landform classes of the Sofia City District, calculated in percent

The main landform classes for the study area are the plains and the slopes, respectively with 45% and 30% (Fig. 5 and 6). The ridges and the valleys are presented almost equally and they are distributed mainly in the northern and southern part of the study area.

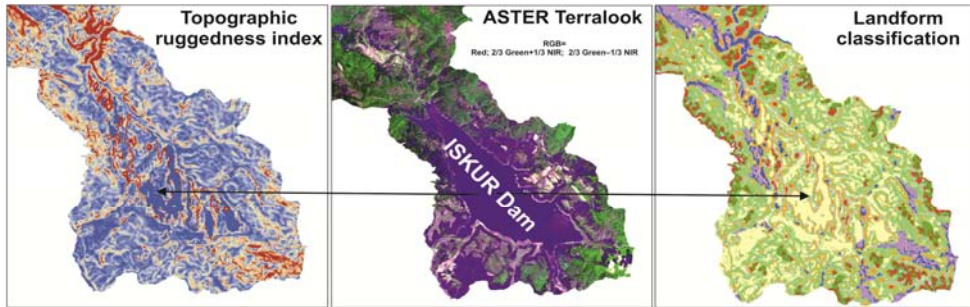


Fig. 7. Anomalies in ASTER GDEM

Some discrepancies and visual anomalies in the ASTER GDEM are observed in water bodies (Fig. 7). The anomalies in the water bodies of the ASTER GDEM are described also by Guth, who assess and compare the geomorphometric characteristics of ASTER GDEM to SRTM DEM [38].

Conclusions

The present study attempts to describe and classify the landforms of the Sofia City District using remote sensing data and GIS technologies. The obtained results will be further analyzed and compared to the outputs from the same classification procedure using various data sources (SRTM DEM and DEM from topographic maps). The data will be used also for landscape planning of the territory.

References

1. Blaschke, T., Strobl, J. Defining landscape units through integrated morphometric characteristics. In: Buhmann, E., Ervin, S. (Eds.), *Landscape Modeling: Digital Techniques for Landscape Architecture*. Wichmann-Verlag, 2003, 104–113.

2. B a t e s, R. L., and J a c k s o n, J. A. (ed) Glossary of geology, 3rd Ed. American Geological Institute, Alexandria, VA., 1987, 788 p.
3. L e i g h t y, R. D., Automated IFSAR Terrain Analysis System: Final Report. U.S. Army Aviation & Missile Command, Defense Advanced Research Projects Agency (DoD) Information Sciences Office, Arlington, VA, 2001, 59 p.
4. M a c M i l l a n, R. A. and P. A. S h a r y. Chapter 9 Landforms and Landform Elements in Geomorphometry. In T. Hengl and H. I. Reuter, editors, *Geomorphometry: Concepts, Software, Applications*, vol. 33 of Developments in Soil Science, Elsevier, Amsterdam, 2009, 227–254.
5. P i k e, R. J. Geomorphometry: diversity in quantitative surface analysis. *Prog. Phys. Geogr.* 24 (1), 2000, 1 – 20.
6. P i k e, R. J., D i k a u, R. Advances in geomorphometry. *Z. Geomorphol.*, N.F. Suppl. Bd. 101, 1995, 238.
7. E v a n s, I. S., General geomorphology, derivatives of altitude and descriptive statistics. In: Chorley, R.J. (Ed.), *Spatial Analysis in Geomorphology*. Harper and Row, NY, 1972, 17–90.
8. B u r r o u g h, P. A., v a n G a a n s, P. F., M a c M i l l a n, R. A., 2000. High resolution landform classification using fuzzy *k*-means. *Fuzzy Sets and Systems* 113 (1), 37–52.
9. M a c M i l l a n, R. A., P e t t a p i e c e, W. W., N o l a n, S. C., G o d d a r d, T. W., A generic procedure for automatically segmenting landforms into landform elements using DEMs, heuristic rules and fuzzy logic. *Fuzzy Sets and Systems* 113, 2000. 81–109.
10. W o o d, J. D. The geomorphologic characterization of digital elevation models. PhD Dissertation, University of Leicester, UK, 1996.
11. D i k a u, R., The application of a digital relief model to landform analysis in geomorphology. In: Raper, J. (Ed.), *Three Dimensional Applications in Geographical Information Systems*. Taylor and Francis, London, 1989, 51–77.
12. W i l s o n, J. P., G a l l a n t, J. C. (Eds.), *Terrain Analysis: Principles and Applications*. Wiley, New York, 2000, 303 p.
13. G u t h, P. L., Slope and aspect calculations on gridded digital elevation models: examples from a geomorphometric toolbox for personal computers. *Zeitschrift für Geomorphologie* 101, 1995, 31–52.
14. C o n r a d, O. Die Ableitung hydrologisch relevanter Reliefparameter am Beispiel des Einzugsgebiets Linnengrund. – 89 pp. 1998, [Geogr. Inst. Univ. Göttingen, diploma thesis.
15. C o n r a d, O. DiGeM – A Program for Digital Terrain Analysis, 2001.
16. G a l l a n t, A. L., D. D. B r o w n, and R. M. H o f f e r. Automated Mapping of Hammond's Landforms. *IEEE Geoscience and Remote Sensing Letters*, Vol. 2, No. 4, 2005.
17. M o r g a n et al. Developing Landform Maps Using ESRI's ModelBuilder, *ESRI User Conference Proceedings*, 2005, 11 p.
18. A l e - E b r a h i m, S. Landform classification from a digital elevation model and satellite imagery, *Geomorphology*, Vol. 100, 3–4, 2008, 453-464, ISSN 0169-555X.

19. J a s i e w i c z, J., T. F. S t e p i n s k i. Geomorphons — a pattern recognition approach to classification and mapping of landforms, *Geomorphology*, Vol. 182, 2013, 147-156, ISSN 0169-555X.
20. D r ä g u t, L., T. B l a s c h k e. Automated classification of landform elements using object-based image analysis. *Geomorphology*, Vol. 81, 3–4, 2006, 330-344, ISSN 0169-555X
21. S a h a, K., N. A. W e l l s, M. M u n r o – S t a s i u k. An object-oriented approach to automated landform mapping: A case study of drumlins. *Computers & Geosciences*, Vol. 37, 9, 2011, 1324-1336, ISSN 0098-3004.
22. B o l o n g a r o - C r e v e n n a, A., V. T o r r e s - R o d r í g u e z, V. S o r a n i, D. F r a m e, M. A. O r t i z, Geomorphometric analysis for characterizing landforms in Morelos State, Mexico. *Geomorphology*, Vo. 67, Issues 3–4, 2005, pp. 407-422, ISSN 0169-555X
23. К а м е н о в, В л. The Pliocene-Pleistocene Boundary in the Sofia Hollow. *Journal of the Bulgarian Geological Society*, vol.26, book 1, BAS, Sofia, 1965, 112-114 (in Bulgarian).
24. К а м е н о в, В л., С о h e n Е l. Notes on the Geology of the Sofia Young Tertiary Basin, Sofia, *Annual of the Chief Directorate of Geologic and Mining Prospecting*, Sect.A, vol.V, 1952 (in Bulgarian).
25. Г е о р г и е в, М. (Georgiev, M.) По някои въпроси относно морфотектонското развитие на Софийската котловина – *Год. на СУ, ГГФ*, 61, 1968, №2, 71-80.
26. F r a n g o v, G. Basic Regularities in the Distribution of Technogenic Landslides in Bulgaria, *Journal of the Bulgarian Geological Society*, vol. LI, book 1, BAS, Sofia, 1990, 112-114 (in Bulgarian).
27. Х р и с т о в, Р. (Hristov, R.) Геоложки и геоморфоложки изследвания на Витоша планина – *Год. на МГИ*, 5, 1958, 2 част
28. Г е о р г и е в, М. (Georgiev, M.) Геоморфология на Искърския пролом между Плана планина и Лозенска планина. – *Год. на СУ, БГГФ*, 55, 1962, 51-94
29. Г е о р г и е в, М. (Georgiev, M.) Геоморфология на източния склон на Витоша – *Год. на СУ, БГГФ*, 56, 1963, №3, 48
30. Г е о р г и е в, М. (Georgiev, M.) Геоморфология на северния и северозападния склон на Витоша – *Год. на СУ, ГГФ*, 58, 1965, №2, 13-53
31. К а н е в, Д. (Kanев D.) Относно влиянието на ерозионния базис върху разнообразието в югоизточната част на Софийското поле - *Год. на СУ, БГГФ*, 55, 1962, №3, 97-114
32. К а н е в, Д. (Kanев D.) Куриловският праг през кватернера. – *Год. СУ, Геол.-геогр. Фак.*, 2 – Геогр. 58, 2, 1965, 1–9.
33. В л а с к о в, В л., Й. С и м е о н о в. (Vlaskov, Vl. And Simeonov, J.). Антропогенен релеф в Софийската котловина. *Проблеми на географията*, БАН 3, 1992, 33–39.
34. Ч о л е е в, И., А. П о п о в. (Choleev, I., A. Popov). Геоecологичен анализ на релефа на територията на Софийска голяма община. *Сб. Доклади “Международна научна конференция ПМФ`2005”*, Благоевград, 2005, 213-221.

35. C o n r a d, O. SAGA-Program Structure and Current State of Implementation. In: Böhner, J., McCloy, K.R. & Strobl, J. [Hrsg.]: *SAGA-Analysis and Modeling Applications*. Göttinger Geographische Abhandlungen, Bd.115, 2006, 39-5.
36. R i l e y, S. J., S. D. D e G l o r i a, E l l i o t, R. A Terrain Ruggedness that Quantifies Topographic Heterogeneity. *Intermountain Journal of Science*, Vol.5, No.1-4, 1999, 23-27.
37. G a l l a n t, J. C., D o w l i n g, T. I. A multiresolution index of valley bottom flatness for mapping depositional areas. *Water Resources Research*, 39(12), 2003, 1347 - 1359.
38. G u t h, P. L. Geomorphometric comparison of ASTER GDEM and SRTM, ASPRS/CaGIS 2010 Fall Specialty Conference, Orlando,FL, 2010.

**КЛАСИФИКАЦИЯ НА ФОРМИТЕ НА ЗЕМНАТА
ПОВЪРХНОСТ С ИЗПОЛЗВАНЕ НА ЦИФРОВ МОДЕЛ НА
РЕЛЕФА ASTER GDEM И САТЕЛИТНИ ИЗОБРАЖЕНИЯ С
ВИСОКА ПРОСТРАНСТВЕНА РАЗДЕЛИТЕЛНА СПСОБНОСТ
ЗА РАЙОНА НА ОБЛАСТ СОФИЯ ГРАД**

В. Найденова, Ст. Стаменов

Резюме

Морфологичната и морфометрична информация за формите на земната повърхност играят важна роля в пространствения и времеви анализ и моделиране на ландшафта и оказва влияние върху хода на протичане на природните процеси. Геоинформационните технологии дават възможност за извършване на цифров анализ на терена и извличане на серия от морфометрични параметри и елементи на формите на земната повърхност. Геоморфоложкият анализ и интерпретация могат да бъдат извършени чрез различни алгоритми, интегрирани в ГИС софтуерните продукти. Целта на настоящето изследване е да се извърши класификация на формите на земната повърхност и да се опише тяхната хетерогенност за територията на област София-град на базата на цифров модел на релефа ASTER GDEM и сателитни изображения. Приложена е ТРІ-базирана класификация на формите на земната повърхност и е оценена хетерогенността на терена за изучаваната територия. В резултат на извършените пространствени анализи са съставени морфометрични карти и карта на класовете форми на земната повърхност.

APPLICATION OF AEROSPACE METHODS FOR MONITORING OF FOREST FIRES AND EVALUATION OF BURNED AREA IN HASKOVO REGION IN THE SUMMER OF 2011

Maria Dimitrova, Iva Ivanova, Mariana Zaharinova, Roumen Nedkov

*Space Research and Technology Institute – Bulgarian Academy of Sciences
e-mail: asic@space.bas.bg*

Abstract

The most significant forest and field fires in Haskovo region in the summer of 2011 are looked through. Information about physico-geographic characteristics of the area, land cover, etc. are gathered and analyzed in GIS. The location and the area affected by the largest fire are being determined based on satellite data. An analysis of the affected area is done.

Introduction

Haskovo region is situated in the East part of South Bulgaria. It has an area of 5534 km² that is 5% of the country area. In the region there are 261 urban places, arranged in 11 municipalities - Haskovo, Dimitrovgrad, Svilengrad, Lyubimets, Harmanli, Madzharovo, Simeonovgrad, Ivaylovgrad Topolovgrad, Mineral Baths and Stambolovo. The municipality borders are: the districts of Plovdiv, Stara Zagora, Yambol, Kardzhali. In the South-East region it borders with Greece and Turkey. The region is crossed by the railway line Sofia - Istanbul and the highway "Trakia".

The territory of Haskovo region covers the southwestern ridges of the Sakar Mountain and the northern parts of the Eastern Rhodopes. Though the region flow the rivers Maritsa, Arda and Sazliyka. There are hot springs and balneological resorts in the area of Haskovski Mineral Baths and Merichleri, in Simeonovgrad and Dolno Botevo.

The terrain is hilly. As a northern extension of the Eastern Rhodopes the area was named the Eastern Rhodopes foothills step or Haskovo hilly area. The highest point is Mechkovets - height 860 m asl. The region offers good conditions for the development of cultural, rural and eco-tourism.

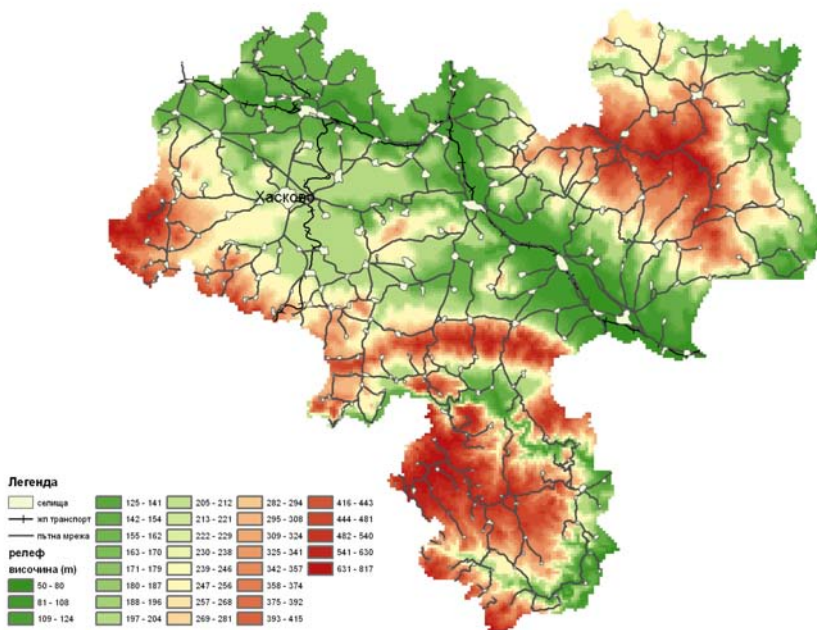


Fig. 1. Thematic map of the terrain and road network of Haskovo

The climate in the municipality is temperate continental with a strong Mediterranean influence. That influence results in higher average annual temperatures and causes a significant shift of the main precipitation minima and maxima. The absolute value of the maximum temperature is considered to be one of the most generous in the country.

The average annual temperature in the valley and lowland areas is 12 °C and in the Eastern Rhodopes is 13 °C.

The biodiversity within the region is extremely rich. The Eastern Rhodopes are notorious for many protected areas inhabited by rare animal and plant species and is recognized as an Important Bird Area and an area with the highest biodiversity (such as types and numbers) in Europe. There were registered 25 species of orchids and more than 300 species of birds.

Here is one of the three natural breeding colonies of vultures in Europe and the largest number of breeding pairs of black storks.

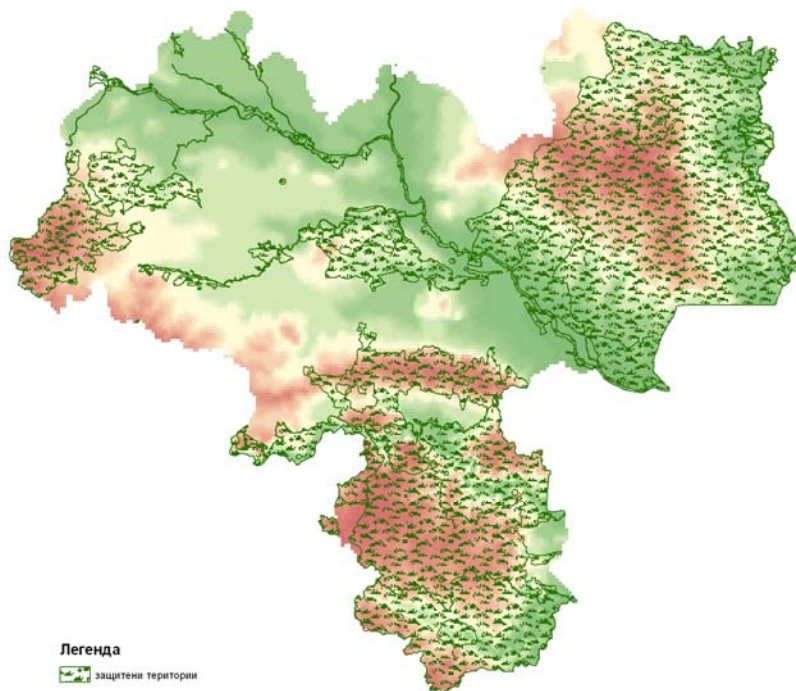


Fig. 2. Thematic map of the protected areas in Haskovo

According to the Law for the Protection of Nature in the territory of Haskovo region there are the following categories of protected natural areas: 1 reserve, 1 maintained reserve, 24 historic places, 28 natural monuments, 21 protected areas; 119 old trees.

This area includes 25 zones of the European ecological network NATURA 2000.

The number of fires and the scale of the destroyed areas in recent years have reached critical levels and have no equivalent in the history of forestry in Bulgaria. The data show that in regard to the indicators of traditional possibility of forest fires in Bulgaria the rates have reached and even exceeded many times the average level, typical for the Mediterranean region. For example, in the year 2000 the area of the burned territory is about 100 times greater than that in the early 90's.

The largest fire in recent years in Bulgaria is that on August 2007, in municipalities Topolovgrad and Svilengrad. The fire began on August 25 between the village of Srem and Ustrem and destroyed 15000 hectares of forest area. The fire passed through the villages Radovets, Prisadets, Varnik and Filipovo.

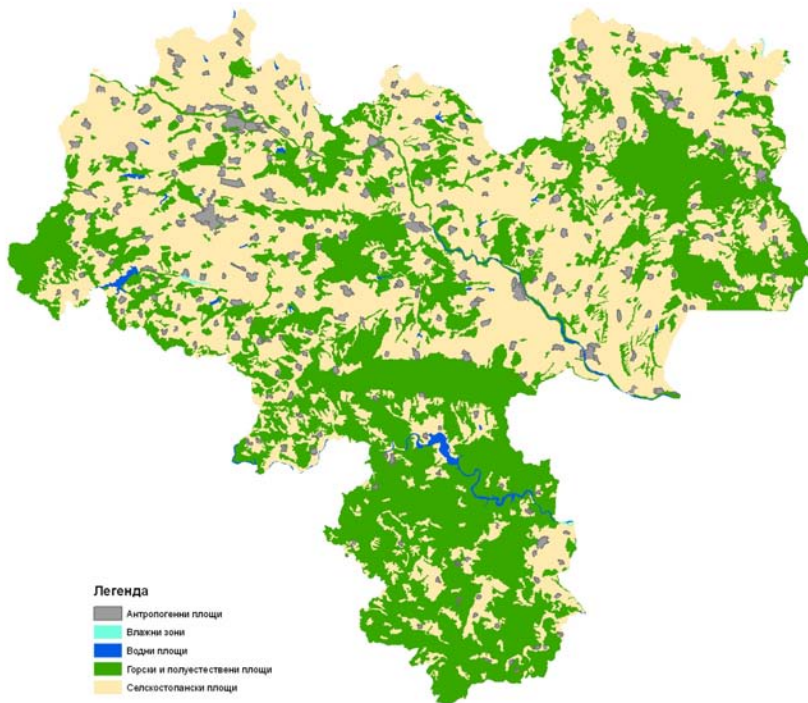


Fig. 3. Thematic map of land cover in Haskovo

Methodology for studying the dynamics of fires based on satellite data

The fire detection is performed using spectral channels of MODIS (4-11 μm) of temperature brightness. The fire detection procedure is based on absolute fire detection, if it is strong enough, or on detection of objects close to the fire, which is associated with changes in the surface temperature. To improve the visual images they are presented in pseudo colors.

Aqua and Terra satellites provide 4 images for 24 hours. Data from MODIS can be used to monitor the burning stubble, specify the type and

condition of the vegetation, the smoke aerosols, water vapor and clouds, which serves as a comprehensive monitoring of the fire development and its impact on ecosystems, the atmosphere and climate.

This information can be used to monitor the spatial and temporal distribution of the fires in different ecosystems, detect changes in their distribution and determine their new boundaries and intensity.

The described methodology is based on satellite data from the system MODIS, that have high spectral, temporal and radiometric resolution, and meet the requirements of objective and accurate assessment of fire dynamics. The satellite data parameters of MODIS system are:

- temporal resolution – 2 times in 24 hours for each satellite;
- spatial resolution – 250–2000 m;
- spectral resolution – obtaining hyperspectral data from 36 spectral ranges;
- radiometric resolution – 12 bits.

For processing of forest and field fires in Haskovo region in the summer of 2011 in GIS environment layers are created, that contain:

- Digital Elevation Model
- Urban areas
- Road Network
- River Network
- Vegetation Index
- Protected Areas
- Fires Location

Two satellite images are presented for each moment. The first image is entirely in the visible range (channels 143) and the second one is a combination of channels in the visible and infrared range (channels 721).

In the first satellite image is better to observe the area covered by the smoke and its density, and in the second image type is seen the outbreak of the fire and also the already burned areas. The spreading smoke is less visible, because in the higher atmosphere layers it cools and is not visible in the infrared channels.

The darker and in brown colored spots are already burnt areas and their size can be measured.

Forest and field fires in Haskovo region in the summer of 2011

Code red, which is the highest level of risk for the occurrence of forest and field fires was announced from 12.07.2011 in Haskovo. The decision is related to the permanent increase in the temperatures over 35 degrees.

The largest fire in the country for that summer is the one of 14 September 2011 between the villages Vaskovo, Oryahovo and Georgi Dobrev in Haskovo region, and it was spread to over 9000 acres.

That summer from all the fires in the area were affected more than 25000 acres of forest, shrub and farmland.

Table 1 lists the ten most significant fires during the summer of 2011. Fig. 4 shows their distribution in the observed area.

Tab. 1. List of the ten most significant fires in Haskovo region in the summer of 2011

date	Area (acres)	Type area affected	Urban Place
16.07	1 000	Dried grasses, shrubs and deciduous forests	Podkrepa
17.07	2000	deciduous forest	Mineralni bani
20.07	1 500	grass and shrubs	Garvanovo
26.08	50	grass	Lyubimec
27.08	100	60 - deciduous forest 40 - grass and shrubs	Hlyabovo
29.08	1 000	270 - deciduous forest	Dimitrovgrad, Merichleri
15.09	3000	Not forest land	Tatarevo, Garvanovo
	5000	farmland	Vaskovo, Oryahovo, Georgi Dobrev
	500	100 - forest	Kostilkovo, Meden buk
Общо 15.09	12 000	grasses, shrubs and forests	
18.09	70	mixed forest	Bogomil
Full affected area		Over 25 000 acres	

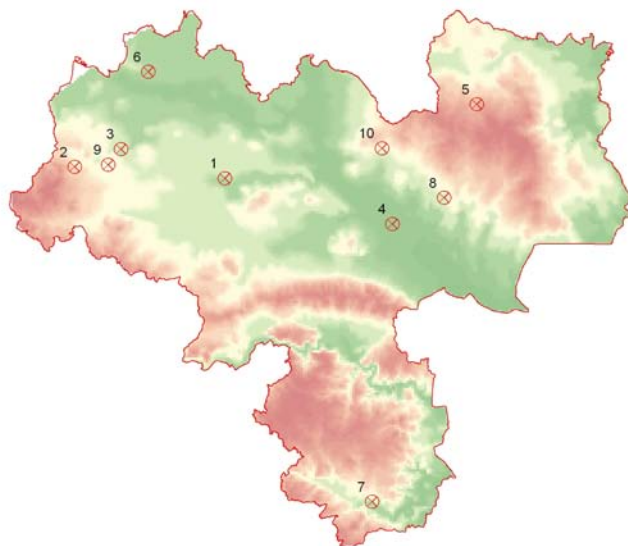


Fig. 4. Distribution of a major fire in 2011 on the territory of Haskovo

The fire from 14.09.2011 was traced through aerospace images from the satellites Terra and Aqua and they are presented in Figures 5, 6 and 7.

Figure 8 shows the completely destroyed area by the fire. Its size is shown.

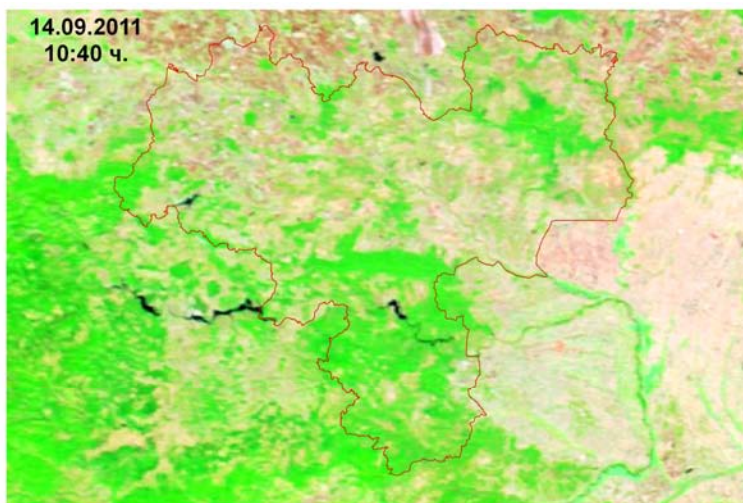


Fig. 5. Image in spectral channels 721 from Terra satellite - 14.09.2011 before the fire

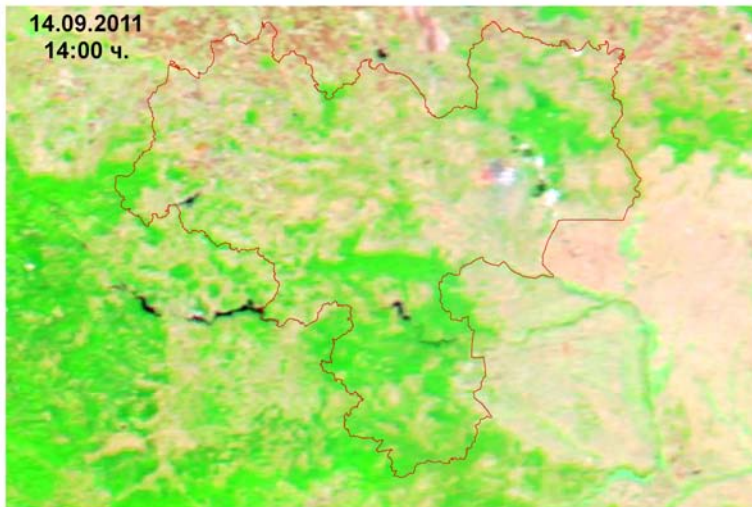


Fig. 6. Image in spectral channels 721 from Aqua satellite - 14.09.2011 before the fire



Fig 7. Image in spectral channels 143 form Terra satellite on 14.09.2011, include two existing fires

Figure 5 shows the territory of Haskovo before the fire on the day it arises – September 14, 2011. The image is in the visible range of the spectrum.

In Fig. 6 can be detected the flame of the fire, visible on the image of the spectral channels 721 of the Aqua satellite on 14.09.2011.



Fig. 8. Thematic map of the area completely burnt in the fire area of 721 spectral channels from the Aqua satellite

Fig. 7 shows an image in the visible spectrum range from the satellite Terra from 14.09.2011. The smoke from the existing fires is to be seen.

Fig. 8 shows already burnt area a day after the fire - 15.09.2011- in the spectral 721 channels from the satellite Aqua. Its size is calculated.

Analysis of the fire affected area on 14.09.2011

The fire near the village Vaskovo is a result from a thrown not doused cigarette.

The completely burnt area, determined by satellite images, is 8682 sq.km. It borders the territory of the village Vaskovo.

Mainly affected are agricultural areas, as shown in Fig. 9.

Fig. 10 presents a thematic map of protected habitats, on which territory is the burnt spot.

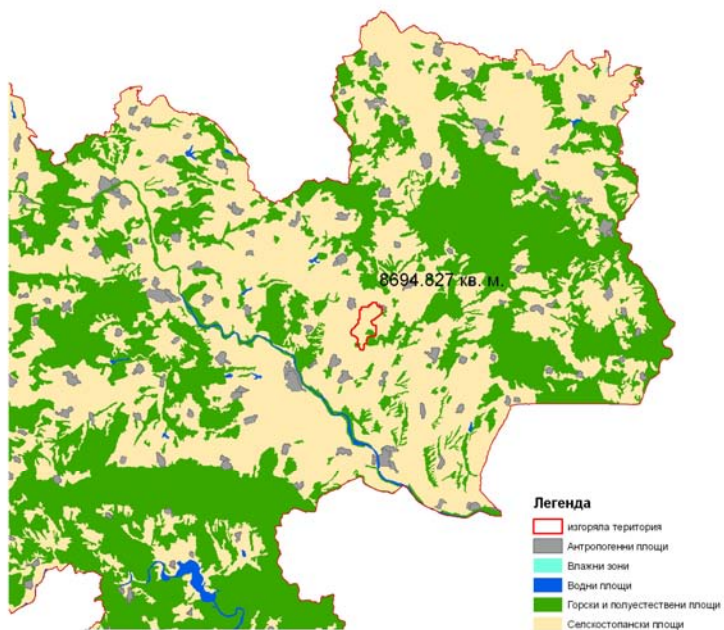


Fig. 9. Nine thematic maps of land cover affected by the fire at 14.09.2011

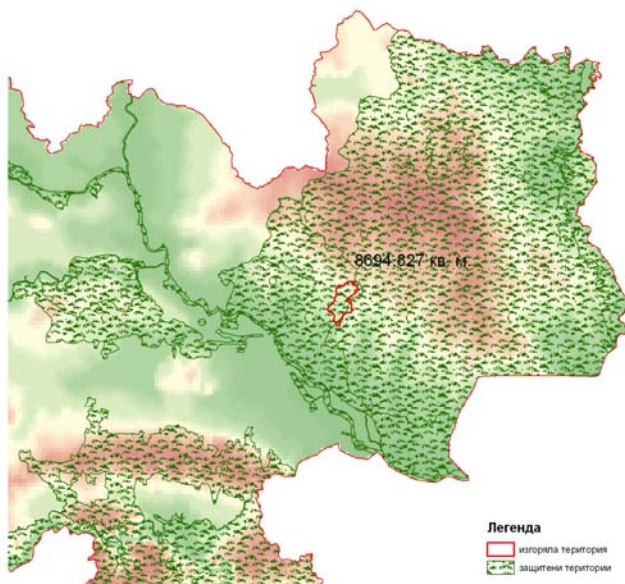


Fig. 10. Thematic map of the protected area affected by the fire at 14:09

Conclusions

Analysing the results, based on the proposed methodology for monitoring of the fire dynamics and development, the following conclusions can be made:

- The methodology used is applicable to study the dynamics of fire;
- Despite the short fire duration the induced negative effect associated with the environment is significant

Fires can cause long lasting disturbances in the ecological balance for the recovery of which decades are needed.

The problem of the occurrence of summer forest and field fires, especially due to human negligence, and their consequences should be treated with appropriate seriousness.

Due to the aerospace methods and technical equipment it is possible to trace the occurrence, development and impact of fires on the environment by making analysis and evaluation of the burnt areas and the occurred damages in time, close to real one.

References

1. Pavlova, A., R. Nedkov. Remote Sensing Based Forest Fire Monitoring In Different Seasons,WDS'06, 2006, Prague,pp 163-167
2. Nedkov, R., M.Dimitrova, M. Zaharinoва, I.Ivanova. Web-based monitoring of the fires in the Balkan using satellite data during July and August 2007, vol.1/2008, Ecological Engineering and Environment Protection, pg.13-20
3. Мардиросян, Г. Природни екокатастрофи и тяхното дистанционно аерокосмическо изучаване, "Проф.М.Дринов" - БАН 2007 г.
4. Web-based monitoring of fires at the Balkans region - <http://195.96.250.235/BG-Fires/index.html>

**ПРИЛОЖЕНИЕ НА АЕРОКОСМИЧЕСКИТЕ МЕТОДИ ЗА
ПРОСЛЕДЯВАНЕ НА ГОРСКИ И ПОЛСКИ ПОЖАРИ И
ОЦЕНКА НА ИЗГОРЕЛИТЕ ПЛОЩИ В ОБЛАСТ ХАСКОВО
ПРЕЗ ЛЯТОТО НА 2011 г.**

М. Димитрова, И. Иванова, М. Захарина, Р. Недков

Резюме

Разгледани са по-значителните горски и полски пожари в област Хасково през лятото на 2011 година. В GIS среда е събрана и анализирана информация за физикогеографските характеристики на областта, растителна покривка и др. На базата на сателитни данни са определена местоположението и площта на засегнатата от най-големия пожар територия. Направен е анализ на засегнатата от него област.

MODELING OF THE HUMAN – OPERATOR IN A COMPLEX SYSTEM FUNCTIONING UNDER EXTREME CONDITIONS*

Peter Getzov, Zoia Hubenova, Dimitar Yordanov, Wiliam Popov

*Space Research and Technology Institute – Bulgarian Academy of Sciences
e-mail: director@space.bas.bg*

Abstract

Problems, related to the explication of sophisticated control systems of objects, operating under extreme conditions, have been examined and the impact of the effectiveness of the operator's activity on the systems as a whole. The necessity of creation of complex simulation models, reflecting operator's activity, is discussed. Organizational and technical system of an unmanned aviation complex is described as a sophisticated ergatic system. Computer realization of main subsystems of algorithmic system of the man as a controlling system is implemented and specialized software for data processing and analysis is developed. An original computer model of a Man as a tracking system has been implemented. Model of unmanned complex for operators training and formation of a mental model in emergency situation, implemented in "matlab-simulink" environment, has been synthesized. As a unit of the control loop, the pilot (operator) is simplified viewed as an autocontrol system consisting of three main interconnected subsystems: sensitive organs (perception sensors); central nervous system; executive organs (muscles of the arms, legs, back). Theoretical-data model of prediction the level of operator's information load in ergatic systems is proposed. It allows the assessment and prediction of the effectiveness of a real working operator. Simulation model of operator's activity in takeoff based on the Petri nets has been synthesized.

Introduction

Human activity under the conditions of space flight is a specific type of labour, carried out in unusual and sophisticated conditions, requiring high activity, readiness for reaction to sudden vague situations and ability to bear

* Results under Contract DTK 02/59 of FNI

loads, weightlessness, isolation, and possession of a particular system of knowledge, skills and habits. He/she performs various functions – piloting, monitoring, communication, repair, ergatic reserve, etc., which require high creativity, purposefulness and efficiency. Routine and smooth reactions of human-operator (HO) after failure of technical equipment give way to sometimes forgotten, unusual and rare operations that has to be carried out in extreme situation and deficit of time and with consequences for the safety of humans, transport vehicles, material and natural values.

The formalization, modelling and analysis of the man in the sophisticated ergatic systems (ES) in that regard turns out to be *important interdisciplinary scientific problem*, requiring the use of theory and methods in many branches of science: the Cybernetics, Physiology, Ergonomics, Mathematics (fuzzy sets, mathematical linguistics, semi-markov processes, etc.), system analysis, biomechanics, computer sciences etc. [1-6]. When analysing the function of such sophisticated systems, it becomes increasingly evident, that reliable results cannot be obtained without taking into account the human factor, because a person is an active part in them, who defines to a large extent the achievement of its objectives in its operation and development. The man, as an element of the control, participates in every stage of its formation – perception, recognition, prediction, adoption of a decision and implementation [7].

Problem Formulation

Research and experimental work on the creation of unmanned aerial vehicles (UAV) in the 21st century has become a priority topic for the aviation and in particular – for military aviation and services for public protection from accidents and natural disasters. Due to the large number of such aircrafts, the preparation for UAV pilots became a separate problem. It takes special equipment, separate airbases for pilot's training and special control systems for control of UAV. The airspace is one for everyone and the air traffic control assumes new dimensions and philosophy.

HO is separated from the machine not only in functional (as in the case with supervisory control, e.g. during piloting Airbus), but in literal sense: he has not direct contact with the machine, there is no additional sensory information from the flight's point function, he is “out” of it, and in this sense the “dimensionality” of his sensory space decreases. UAV pilot is immersed and works in a new virtual environment and in a sense he

practices his profession in a virtual workplace. All these new circumstances put many new challenges to researchers and designers of ergatic control systems and to the modelling of HO, now as a man as a control system (MCS).

In the specialized literature the concepts UAV (Unmanned Aerial Vehicle) and RPV (Remotely Piloted Vehicle) are distinguished. Unmanned aerial complex (UAC) or the system (UAS) consists of UAV and ground control station – the radiotechnical system, compulsory elements on which are radio channel to transmit current target information and the ground control station in control radio channel for control of RPV and its service load. Exactly in the interaction of RPV with the ground control station and its main element – human-operator, the main feature of RPV – the interactive control is realized [8, 9, 10]. In such a way, RPV is an automated interactive drone, capable to perform flight on a preset route and to maintain its orientation in the space without human intervention, but at the same time is ready to respond to the controlling impact of human-operator. As a rule, UAV performs a flight under program set into its onboard control complex, with receipt or transmission of target information on the customers radio channel. Moreover, the multifunctional and intellectual nature of such technical complexes provide for change of the flight's program in a real time scale. The availability of automatic pilot of UAV, along with remote control devices outside of the area for visual or radiotechnical visibility, distinguishes it from the simple sport aeromodels.

Considering the system approach, the structure of organisational-technical system of unmanned aviation can be represented as a three level's hierarchy (Fig. 1). The complex technical systems with UAV are on the first (lowest) level, the unmanned aerial complex (UAC) is on the second level and on the third – the technical unit combines with ergatic. Besides UAV, the structure of UAC consists of the devices for: communication and control, the aircraft ground handling, launching, landing, saving, transportation and storage. This representation of the unmanned aviation's structure allows the treatment of different concepts and their component elements of common positions by seeking their interconnection.

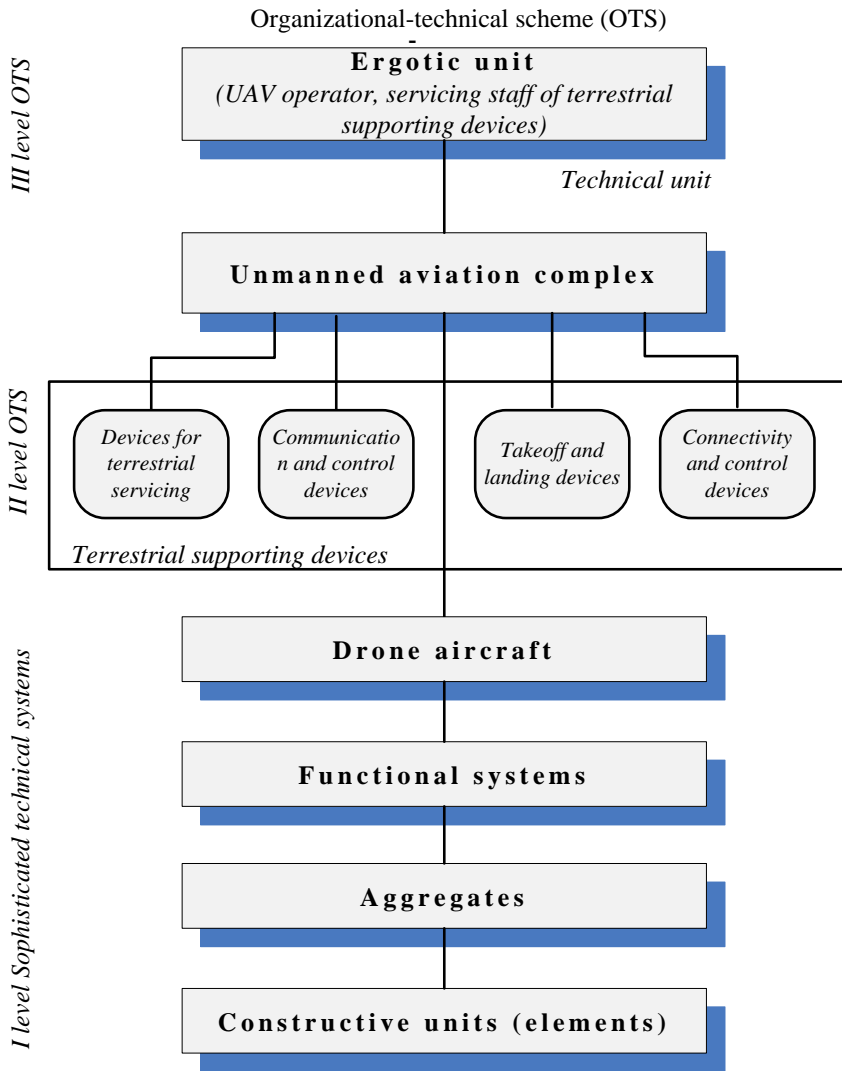


Fig.1. UAC organizational-technical scheme

Main purpose of the intelligent onboard systems is the collection and processing of data coming from technical devices and the creation of models of the process in real time. In general, the formation of the control model and its display on screens is implemented in the following order:

- data collection from peripheral sources and processing by the system;

- creation of models of the controlled process based on incoming information;
- representation of invented models in a form, convenient for perception and highlighting of the most significant risk events [11].

The indicated sequence of actions shows that the system creates a base of knowledge for monitoring and control which is initial for control activity of the operator. This is the reason the “UAV – operator/s” system to be considered as a class ergatic system.

Modelling of the man in ergatic system

Researches on the human brain activity are focusing on the fact that a reasonable person copes with unfamiliar situations and makes rational decisions because he can extract new knowledge from existing experience and can consider the consequences of those decisions. People analyse not only accurate, predefined data, but also incomplete information which often has not a numeric expression. This means that a person meets challenges of unstructured type with non algorithmic solution on daily basis; the quantities he operates with cannot be set in numerical form; their solution requires processing of information which is ambiguous and changes dynamically; purposes of the mathematical problem cannot be expressed by exact objective function.

The human intellect is complex biological phenomenon and it is not limited only to problem solving, structured or unstructured. But in the present level of knowledge and instrumentation not all types of human reasoning are well studied and therefore it is impossible to be modelled (for instance like creativity, intuition, imagination).

Conceptual and computer model of the Man as control system (MCS) and his subsystems

The man as a control system (MCS) is complex multi-parametric and multilayer system and can be seen, formalised and modelled in different sections (in different qualities and parameters). With a high degree of abstraction, MCS can be seen as a hierarchical system of three levels: mechanics, control, intellect, united into one conceptual model (Fig. 2). Each subsystem and the system as a whole has two faces, two areas of functioning and manifestation: internal and external [12,13,14].

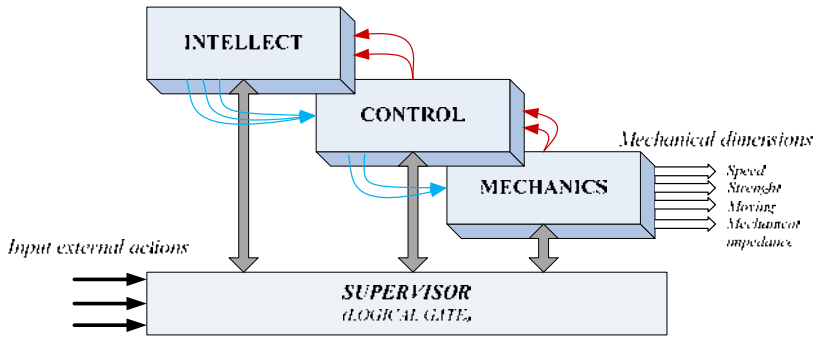


Fig. 2. Systematical representation of MCS

Level *mechanics* of high degree of abstraction can be defined as a sophisticated mechanical system of solid bodies with a large number of mobility degrees. The executive human organs are determined, i.e. they have as a rule more than necessary degrees of freedom to perform a movement. This enables alternative selections, great flexibility and thereby –optimization in the organization and control of each motion. This subset of mechanical system’s elements defines efferent (executive) organs of MCS.

Mechanical human system becomes vital due to a *level of management*, containing a range of different programming modules, functionally organized in two levels:

- Local subsystems – closed systems to control the mutual position of a group of solid bodies (bones) with their own autonomous endo sensors, regulators (nerve ganglia) and efferent executive organs (muscles). Each subsystem has channels of communication with the upper level;

- Central subsystems – for coordinated control of ensembles of local subsystems. Regulators of this level are located in the central nervous system. There are located “the libraries” of standard motor programs for coordinated control of the local systems and implementation of various structural and functional compositions from them.

While the first level (mechanics) is a “hardware”, the intelligence level is “software” or “bio-software”. In this sense it is “the most hidden” level and can be summarized as an capability to receive, preserve and process a database – an information processing; capability to receive, preserve and process a knowledge base – knowledge processing; capabilities to create of mental (reflective) models (MM); capability of internal off-line reflective analysis of MM’s functioning and performance of adjustments to

them based on the stored results from real human actions; opportunities for mental operational and long-term prognosis and evaluation of the results of the scheduled upcoming action; opportunity of criteria adjustment of the lower control level; opportunity to control the strategy choice (risk level); opportunity of self-regulation of the internal information processes (informative regulator) depending on the uncertainty, danger, responsibility of the upcoming action.

Software “MATLAB –Simulink” is used for computer realization of the algorithmic models and it is suitable for formal presentation and modelling of cognitive activity of Man as a control system, as well as Fuzzy Logic environment for modelling of fuzzy systems [15].

Models of the following subsystems were developed and experimented: subsystem for fuzzy evaluation of the input signals by triple overlapping of triangular membership functions (MF) as an example for fuzzification and fuzzy logic; subsystem input signals – perception of position, velocity and acceleration from MCS; a subsystem for switching of various generators for input stimuli; subsystem for interval estimation of input signals, comprised of 25 blocks in 5 subsystem levels; “Training” subsystem – model of “variable (stochastic) conduction” in a knot of self-learning matrix; “Exit” subsystem – model of fuzzy-exit of MCS of stochastic type, comprised of 14 three-level subsystems.

Models are implemented in an accelerated time scale. Real time step depends on the hardware platform. However, it does not affect the dynamic characteristics, logical and numerical results, as they are scaled accordingly and on the graphs, as time functions are read real units (to man) – usually seconds.

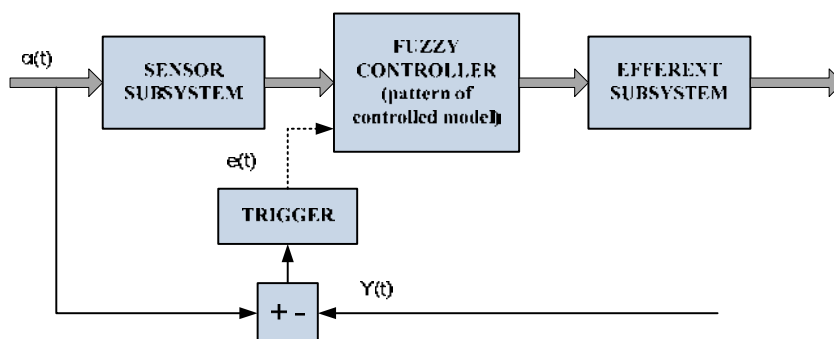


Fig. 3. Conception model of MCS

An original computer model of a Man as a tracking system (MTS) is also implemented in one-dimensional mode of accompanying tracking (fig. 3). Synthesized model of MTS has multi-layer structure, implemented and tested on Simulink by MATLAB (fig. 4). Models are synthesized in heuristic way. In systematic aspect Simulink environment is virtually the laboratory and experimental environment in which the system as a whole and its various subsystems are built and verified:

- sensor subsystem;
- subsystem subjective evaluation of target's dynamic. The subsystem consists of 11 subsystems for each channel for random interval evaluation, each of which – by another subsystem of third line;
- model of the central subsystem of PTS in an accompanying tracking mode;
- subsystem for generating random sequences with uniform and Gaussian distribution.

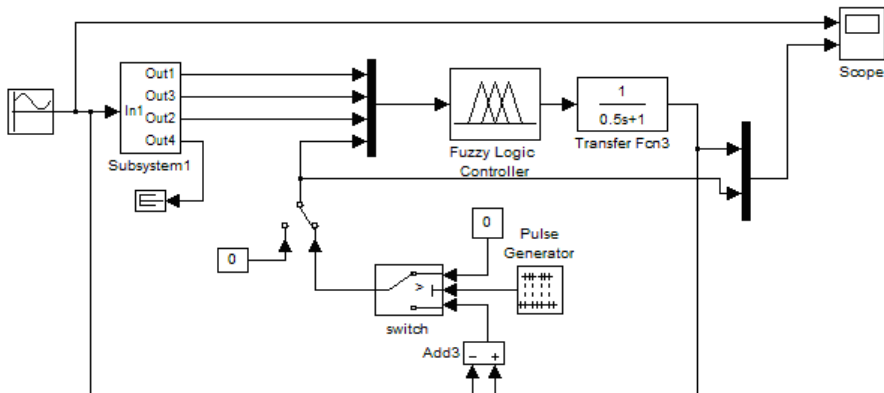


Fig. 4. Computer model of MTS

Subsystems are working and are synthesized with existence of a large number of parameters which can be set to different values and a very large number of experiments (virtual) can be produced. Results can be used for data verification from experimental researches of real operators. Synthesized computer models can be build with subsystems of higher grade

and can be modelled MTS systems with possession of part of “human” qualities and capabilities.

In Fig. 4 is shown the computer model of a man as tracking system in a concomitant track. Visual information for tracking object – *the target* enters at the inlet.

Subsystem has four outputs – target position (S), moving speed of the target (V), acceleration of moving (a) and direction of moving sign. Four signals entry as four input values in the Fuzzy Controller Fuzzy Logic Controller, the action and set value of which are described above. In this case the object of control (tracked object – *the cursor*) is represented as an inertial unit of first tier [16].

3.2. Model of unmanned complex for training of operators and formation of a mental model of emergency situation

Operator’s work in the control loop of unmanned complex differs from the work of the pilot in a real aircraft, in the manner of determining the position of the aircraft in space. Operator, especially in absence of direct visibility of the aircraft (in autonomous flight outside the field of vision) works on the device’s data in the control panel. Based on the indication of the complex of devices, he forms mental image of flight (also called “mental” model) and monitors it by comparing this picture with indications of the devices. When this is fixed mode in the performance of type programmed mission, this process usually does not pose much difficulty and is learned relatively successful after a cycle of trainings and piloting of real flights. The situation is completely different with the formation of mental picture on the aircraft behaviour after failures – in an emergency situation.

Countering of failures in control system of a drone is practically fruitless task, although for some retarded situations after passive failures it is possible (according to data modelling) to respond promptly and to attempt to save the aircraft. As a rule, after emergency identification the pilot should activate the emergency rescue system in order to avoid the aircraft’s destruction, as well as objects on the route of collision. The only reliable method with a minimum research costs for the behaviour of the aircraft, its trajectory and continuation of the situation, and the operator’s capabilities in the conditions of time shortage is the development of computer models, visualization of the flight on simulative device’s panel and its multiple repetition with monitoring of the situation on the devices [17]. For the research of formation process of imaginary (mental) picture (IP) of

emergency was developed pattern, reflecting the specific features of the drone with capabilities for modelling different types of failures in the control system with the help of program product “Simulink”.

In the basis of the *flight model* development are subsystems of lateral and longitudinal motion and connections between them, model of the control system with automatic pilot and manual mode for adjustments (i.e. combined mode) [18,19]. Upon active failure of the ailerons the motion loses stability, resulting in vigorous rotation around the longitudinal and transverse axes. The reason for this is the work of the steering wheel after the ailerons active failure. Before the intervention of the pilot-operator to shut off the automatic pilot in third second, the aircraft is on the critical angles of attack (over 200) due to the deflection of steering wheel for height in end position «on toss bombing» from the working pitch channel of the automatic pilot and has significant sliding to the right. The spatial position of the drone in runoff auger is – the aircraft is on its back, but with supercritical angle of attack. The available time for the operator is very short ($t_{av} \leq 2$ s). If the operator succeeds to turn off the automatic pilot during this time and auger does not occur, the aircraft performs spiral motion to the right with drooping down nose. This is an adverse failure with a very high probability of an unfavourable outcome. From a practical point of view, it cannot be averted during a flight outside the field of vision. At sufficient flight height a parachute system could save the drone from destruction. The destruction is possible even before the fall of the aircraft due to the high values of normal overload even in the first 5 - 10s if the operator does not intervene.

If the device readings by emergency situation could be visualized the picture will show the following: the aviation horizon rotates and fluctuates by pitch in the zone of negative pitch angles. Iteration of the modelled situation forms a flight's image in the operator's mind of the type “monitoring of the aircraft from the ground”, which is necessary for quick identification of the situation and activation of the emergency parachute system.

Model of the pilot. During a flight every crew member performs the tasks, appointed to him by the flight's program, but in the loop for direct piloting of the aircraft, constantly in a manual mode of piloting is included the aviator – pilot. Various mathematical models are used for his actions with controls in the cockpit during the study of closed loop.

As a unit of the control loop, the aviator can be seen simplified as a system for automatic adjustment, comprising of three basic, interconnected subsystems: sensitive organs (perceiving sensors); central nervous system; executive organs (muscles of the arms, legs, back). The central nervous system (CNS) is a base of knowledge and behaviour models in each particular situation. As a result of training and drills there are created and maintained the ideas of pilot for correct and safe flight (mental models). Function of information processing and decision making resulting from a comparison of real flight parameters to the mental images of pilot for the flight is performed in the central nervous system. Movements of the executive organs and the efforts, developed by them, are an output signals in the control loop. Through motive (kinaesthetic) receptors the information about the muscles action is transmitted back to the central nervous system. Thus are formed internal connections in the organism, similar to the reverse connections in the automatic adjustment systems. Thanks to these reverse connections, the aviator can dose the control levers motion, as according to effort and displacement.

Modification in an effort are better felt than moving of the control levers and accuracy of dosing according to efforts is bigger than in moving, therefore among the features of controllability of the aircraft, priority have those in efforts. If the pilot does not feel the changes of efforts in moving the control levers, he deprives himself of a very important part of information and this leads to large mistakes in piloting even to complete loss of stability of the control loop.

Modelling program for takeoff and the pilot's actions in implementing of the program through motions of the control lever in this case is an imaginary (mental) model of the pilot for takeoff, realized by Simulink's devices. The most important features of pilot's MM are safe takeoff (observing of the aircraft's limitations, defined by its aerodynamics and a short distance and profile of the flight after detachment which ensures the passing over the obstacle at a safe height (min 50 m above it)).

These particulars are developed in the process of flight preparation on the basis of knowledge of aerodynamic characteristics of the aircraft, which are studied by the pilots on theory [20].

Block "Step input Programme_pitch 110 s_1-0" eliminates the mental model of takeoff and prepares the model of pilot for implementation of the horizontal flight and landing.

Modelling of pilot's work in control loop during takeoff and landing. Flight program is modelled by considering an aircraft type with following characteristics: mass = 10252 kg; area of the wing $S_w = 34 \text{ m}^2$;

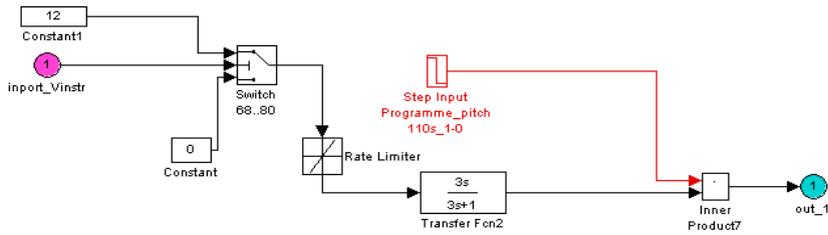


Fig. 5. MM of the pilot in detachment of the aircraft from the runway

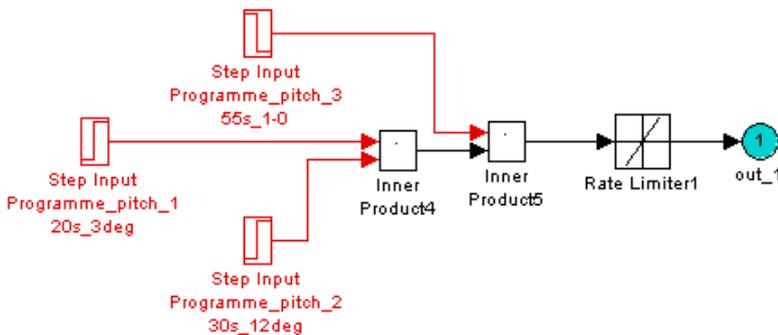


Fig. 6. MM of the pilot on the phase of initial climb

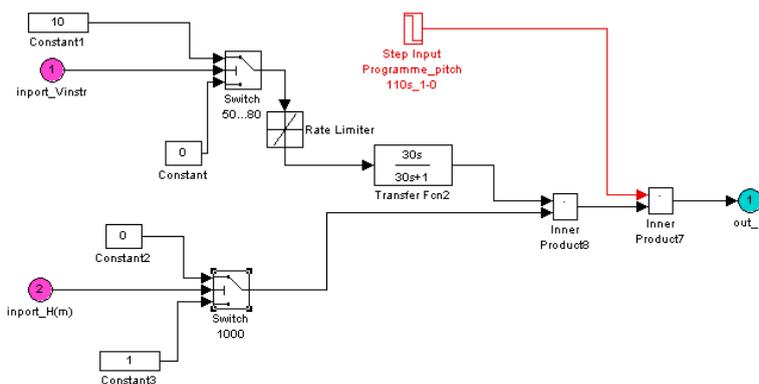


Fig. 7. Detachment of the aircraft from the runway and the initial climb are connected

average aerodynamic chord $b_a = 4.16$ m; wingspan $l_w = 9.3$ m; body length $L_m = 10$ m; inertia moment about the axis OZ (for pitch control) $I_z = 111593$ kgm²; coefficient characterizing the efficiency of controllable horizontal stabilizer $m_z^\phi = -0.91$; range of deviation of controllable horizontal stabilizer “on toss bombing” $\phi_{bomb} = -150$; maximum coefficient of elevating force $C_{y_{max}} = 1.2$ (without flaps); increase in coefficient of elevating force from flaps $C_y = 0.5$ (flaps).

Model of closed loop illustrates the capabilities of “Simulink” product for simulating of sensomotoric activity in single-channel control by pitch. The operation of closed loop is presented by the devices of “Simulink” based on three main hypotheses. The first one – in takeoff and landing the pilot works by pitch because the speed pressure is low and the reaction of the aircraft in deviation of control means is more sensitive to the angles and angular velocity of pitch and lower on normal overloading.

This fact is well-known and is established by engineering-psychological research and flight tests and it is attached as a key hypothesis in the work of the pilot. Another hypothesis which is ground the work of the pilot to be simulated through model, are known facts and research of the methods for building of mental model for the development of the flight in the future, which in the control loop is the flight’s program.

Logical operations for the beginning and the end of different phases of the control process (point of support) and the assessment of impedance mismatching between set and actual value of monitored parameter are carried out in it. The third hypothesis is from the information theory: if a constantly varying value (e.g. pitch) is observed with discreet perceptions (alternating phases of observation and breaks between them), then the operator (pilot) by the discreet perceptions under certain conditions may form the mental model of constantly varying parameter.

Modelling results indicate that the pilot’s model performs the flight program safe in compliance with the basic restrictions imposed by the characteristics of the object for control. The object for control is a manoeuvrable aircraft with resistance and navigable characteristics which under the conditions of time and space scarcity can provoke emergency and catastrophic development of flight situation as a result of pilot’s errors.

The model of pitch control developed by the pilot implements the mental models set in the program for the flight and landing. The typical stages in observance of safe flight conditions are reflected.

3.3. Modelling of information interaction of human-operator in an ergatic system

Terrestrial information systems are this part of equipment with which the UAV's operator directly interacts. Based on the information received, he creates a mental model of the control process he uses his activity. That is why the effective implementation of such systems is impossible without detailed analysis of relations in examined complex "man – machine" (in this case "HO/pilot – aircraft").

Increasing the efficiency and throughput capacity of the interface is particularly important task, related with the modification of the human component on the one side, which is more difficult, and of the other – by adapting and improving to HO of the second component – the information system. In this case it is necessary the capabilities and limitations of the pilot to be known, as well as the conditions of his work to be taken into account.

Relations "pilot – information system" are part of the broader and general relations "pilot – aircraft", including, if necessary, the UAV control, and of the other – the informing of the pilot about the condition of the object for control and the surrounding environment by the on-board information systems (generally accepted term is pilot-vehicle interface) [9, 10].

Theoretical-data model of the operator activity. As we noted so far, the operator's activity differs from the other type of activity with this that he resolves issues on control, management, transmission or transformation of information, interacting with the external environment or technical devices not directly, but by the assistance of various means to display the information and by the relevant control authorities. General characteristics of the activity of all operators is the collection, evaluation and processing of information for technical equipment, technological and other processes, dynamic objects; taking the relevant operator's decisions based on the evaluation of information; actions on their implementation; monitoring of the effectiveness.

In the proposed model, in which the operator monitors several devices simultaneously, the viewer is represented as a non-stationary discrete communication channel with discrete time.

It is appropriate to assume that in the operational and long-term memory of the operator is stored information about the purposes of functioning and quality assessment of the activity, i.e. there is a certain "instruction" and setting for the task implementation.

In the general case, the tasks of human-operator (HO) are presented as prescribed image of the area of input impacts L_x on the space of the acceptable responses L_y . Thus in set or known characteristics of the permissible ability of the operator in terms of sensor input and motor output the actual and perfect information load of the operator must be assessed. This problem cannot be solved by conventional methods of information theory, since the properties of the operator in resolving of specified tasks are non-stationary in the usual sense. Multiple data from the area of general and experimental psychology for cognitive processes, results of psychophysiological experiments and modern theoretical understanding of the structure of sensory-perceptual processes convincingly confirm the specified status.

In order of the evaluation of work characteristic of the operator upon receipt and processing of the information, has been introduced the concept model unit of functioning of the operator (MUF). Under this concept is understood all the operations and activities of operator, related to search, finding and knowledge of a certain signal – element of L_x , and also its logical processing and formation of response reaction – element of L_y . Essentially, MUF can be regarded as some elementary unit of the operator's activity, with a limited spatial and time duration. In terms of quality it is natural for MUF to be characterized firstly by ultimate continuity in time and secondly with certain information, i.e. with this amount of information, processed by the operator in its implementation [21].

Using MUF in such a manner, the operator's functioning as a process is described as stochastic sequence of disjoint unit of functioning. Then each final time interval of operator's functioning can be represented as a total sum of incidental number incidental augends, corresponding to discrete time intervals of MUF implementation in order of their following, starting from $t = 0$.

Based on the accepted limits and the examined structure the mathematical model of the operator's activity is described for unspecified MUF $_{\nu}$:

$$(1) \quad P(Y; \nu) = \Psi[P(X; \nu), \nu],$$

where Ψ in general case is a symbol of non-stationary transformation of discrete sequences of distinct states of the information panel (elements of space L_x) in a discrete sequence of the recognizable for the object

controlling impacts of the operator (elements of space L_y). Physical meaning of this transformation is that in the absence of errors in formation and implementation of the controlling impact, the operator is obliged in response to every x_j state of the information panel with probability one to realize the set the corresponding control action y_j . On the basis of this functional dependence of MUF's number arises an opportunity for reading of such specific operator characteristics as adaptation to situations, adapting to work, tiredness, ability for improving the activities in the learning process, etc.

$$(2) \quad P(Y; \upsilon) = P(x; \upsilon) M(\upsilon) ,$$

where $M(\upsilon)$ is the matrix of conditional probabilities with dimension $N \times N$, satisfying all conditions of stochastic matrix, since all its elements are non-negative, does not exceed one and the elements sum in each row is equal to one. This matrix is specific for each operator in a sense that it reflects his individual characteristics associated with the intake and processing of information within the examined structure of activity.

The proposed theoretical-data model allows selection of basis for comparison of real operators with the perfect one according to matrices type $M(\upsilon)$ and assessment of work quality by comparison of the matrixes $M(\upsilon)$. Thus, a summary model which reflects the integral characteristics of the operator's activity can be used for normative assessment of both operators and information models in systems for control and managing of complex objects.

Perspective opportunities for application of the proposed approach presumes further development and application of the method for integrated data assessments with subsequent complication of the communication channel, inclusion of the memory and after-effect in the channel. This method provides an opportunity to be built a satisfactory description of the reliability and efficiency of operator's work in the real control and management systems; and to provide comparable descriptions of the functioning of the "human" and "technical" part of the entire system.

In the presence of sufficiently complete empirical material – engineering-psychological and experimental-psychological data on the operator's work in receiving and processing of signalling information, the

method set forth herein provides an opportunity for effective prognosis of the actual information loads of operator in the systems.

An algorithmic model of operator activity is formalized and studied. The model of the process is set by the interaction of three structures (Fig. 8), which may be described, respectively, graph of the objectives, graph of operations and graph of indicators

The objectives are divided into final, characterized the results of the activities described in the working procedures and intermediate, which are stages upon reaching of the main ones.

The indicators contain assessments of various aspects of the operator's activity in the process of reaching of the final objective, set by the procedure.

When modelling with Petri nets a graph of indicators can be formed, in which transitions have certain weight factors. For the time parameter the summary coefficient at any point is equal to the time of achieving the task [22, 23].

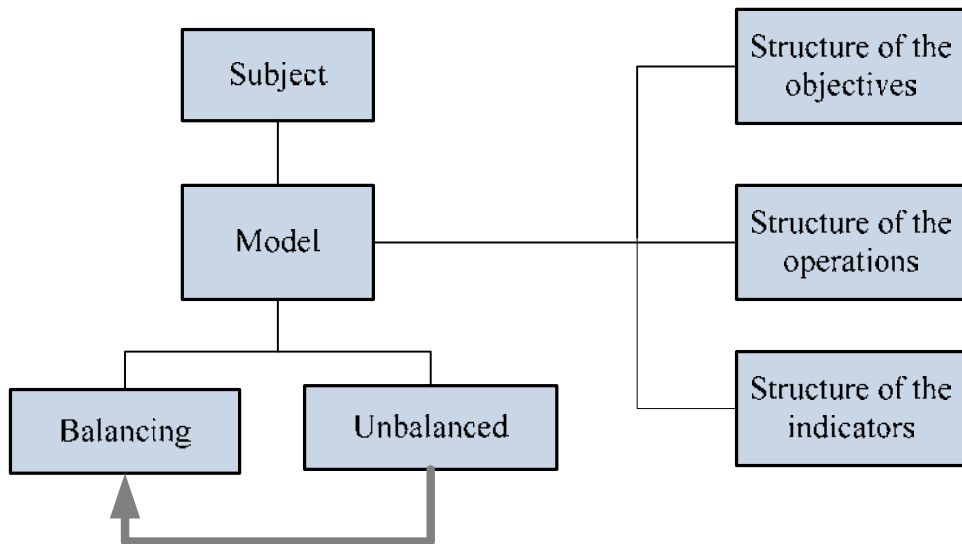


Fig. 8. Process model

The algorithmic model for actions of the operator is developed and it is presented with two graphs with Petri nets – graph of the objectives and graph of the operations, as it is accepted that each objective ends with

operation to implement the taken decision. Graph of objectives describes the structure of sequential actions in time, oriented to achievement of the final objective.

Implementation of the model of procedure with graph of objectives is formalized in the theory of Petri's nets as a script (fig. 9).

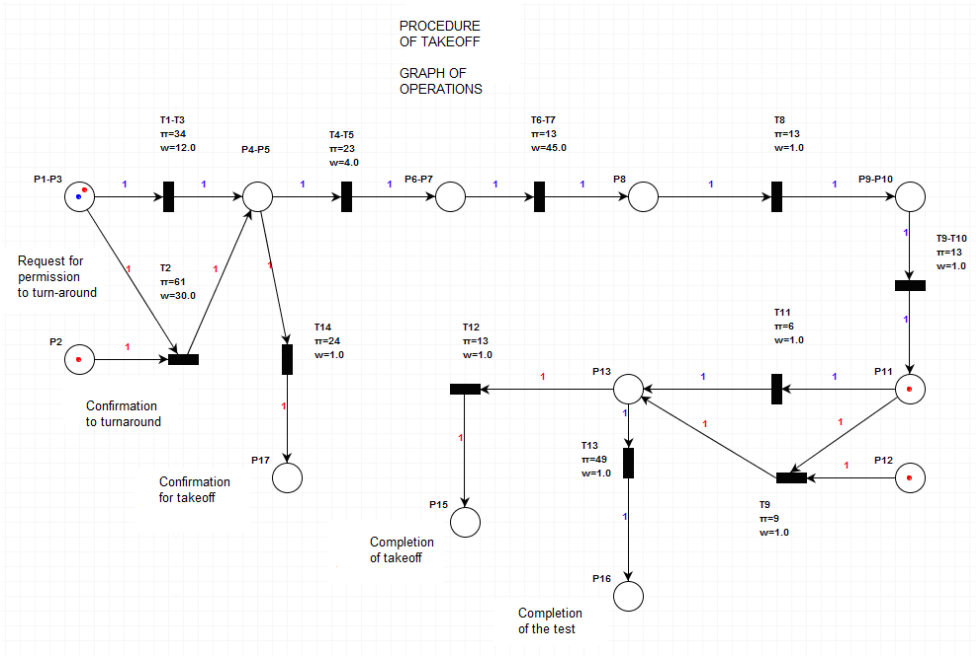


Fig. 9. Operations graph

The model of operation includes a graph with Petri nets with the sequence of actions (operations), performed by the operator. In practice the target model's development precedes the development of model for the operations and they are created independently of one another. In this graph the positions corresponds to the operations and for each point of the graph is drawn a table with description of the achieved objectives and current status of the indicators. Current indicators in the case are the time, necessary for performance of certain operation, reducing the working capacity of the operator, alteration of technical parameters of the flight (speed, altitude, fuel consumption).

Conclusion

Within the framework of the implemented project of FNI DTK 02-59/1913 “Study of the functional efficiency of man under work in extreme conditions”, Contract DTK 02/59 (2009-2013) were developed a concept and methodology for assessing of man in the structure of ergatic systems. Computer models of human-operator with possibility of different applications have been implemented.

Algorithmic model of MCS is synthesized, which is considered as a complex hierarchically organized control system at three levels: mechanics, control, intelligence. Organizational-technical system of the unmanned aircraft complex as sophisticated ergatic system has been described.

Computer realization of the main modules of the algorithmic model of the man as a control system has been implemented and software for data processing and analysis has been developed, including: 1) Model of unmanned training complex of operators and formation of the mental model in an emergency situation, implemented in “Simulink”. This model reflects the specific features of the drone aircraft and has the capacity to model different types of failures in the control system. 2) Flight model.

At the base of development of the model stand subsystems of lateral and longitudinal motion and connections between them, model of the control system with automatic pilot and manual adjustments mode (i.e. “combined mode”). Modelling has been done for specifically adopted characteristics of small drone. 3) Pilot’s models. As a unit of the control loop, the pilot (operator) is simplified viewed as an autocontrol system consisting of three main interconnected subsystems: sensitive organs (perception sensors); central nervous system; executive organs (muscles of the arms, legs, back).

Models of the system aircraft-operator-automatic pilot under different modes of operation are presented in detail. Operation of the pilot in closed loop during takeoff and landing in “matlab-simulink” environment is modelled. Results of the modelling of flight with takeoff, horizontal flight and landing are shown. Characteristic stages in observance of safe flight conditions are presented.

Theoretical-data model for prediction of the level of operator’s information load in erratic systems is proposed. It allows the assessment and prediction of the effectiveness of a real working operator. Simulation model of operator’s activity is synthesized based on the Petri nets. The sequence of the actions of HO are given by the algorithm of activity, including

consecutively performance of elementary operations to solve of the given task.

References

1. K a n t o w i t z, B. H. and R. D. S o r k i n. Human factors: understanding people-systemrelationship. N.Y.: Wiley, 1983.
2. L e f e b v e r, V. A. The Formula of Man an outline of Fundamental Psychology, University of California q Irvine,1991
3. M e s a r o v i c , M . D . , D . M a c k o , Y . T a k a h a r a . Theory of Hierarchical Multilevel Systems. Academic Dress, New York, 1970.
4. L i n d s a y, P., D o n a l d H. N o r m a n A. Human Information Processing, by Academic Press Inc.,U.S, 1972.
5. S o l s o, R o b e r t L.,COGNITIVE PSYCHOLOGY, 6-th edition, Allyn and Bacon, 2006.
6. Г е ц о в, П., Й о с и л и я н и, Х а с а м б е е в, Р а д к о в с к и. Оценка и прогнозирование психической работоспособности советско – болгарского экипажа на борту орбитальной станции “Мир” XXII съвещание на постоянно действащата работна група по космическа медицина и биология, стр. 102, Варна, 1989 г.
7. Н u b e n o v a , Z . Method of information assurance operators’ activities during control processes within complex ergatic systems, 20th International Scientific Conference, Academic journal “Mechanics, Transport, Communications”, Issue 3/2011, p.VIII-76-83, ISSN 1312-3823.
8. Р о с т о п ч и н , В . В . Беспилотные авиационные системы, www.avia.ru.
9. Flight Control Systems, Switzerland, <http://www.wecontrol.ch/Fixed-Wings-UAV/card-ch.html>
10. The Simlat UAS SPOT, Simlat Ltd., Israel, www.simlat.com
- 11.Беспилотные авиационные системы (БАС), Циркуляр 328 ИКАО, Международной Организацией Гражданской Авиации, University Street, Montréal, Quebec, Canada, ИКАО, 2011.
12. Г е ц о в, П., В. П о п о в, К. С т о я н о в. Параметричен модел на човек като управляваща система. Параметричен модел на човешка дейност. Юбилейна научна сесия “30 години Институт за космически изследвания”, с. 259 – 261, 1999.
13. V a s s i l e v a , T . , W . P o p o v . Algorithmic model of human as a ruling system”, WDS`03 Proceedings of contributed papers, part I, Mathematics and Computer sciences, Charles University, Prage, 2003, 243–247.
14. V a s s i l e v a , T . , W . P o p o v . Down – Up Model of Human as a Control System, WDS`04 Proceedings of contributed papers, part I, Mathematics and Computer sciences, Charles University, Prage, 2004, 218–222.
15. "MATLAB Programming Language". Altius Directory. Retrieved 2010-12-17.

16. Ц и б у л е в с к и й , И . Е . Ч е л о в е к к а к з в е н о с л е д я щ е й с и с т е м ы . М .
Наука, 1981. 288 с.
17. Д е н и с о в , В . Г . , В . Ф . О н и щ е н к о . И н ж е н е р н а я п с и х о л о г и я в а в и а ц и и и
космонавтике изд. "Машиностроение", Москва, 1972.
18. J o r d a n o v , D . , P . G e s o v . Unmanned aircraft – modelling and control ,Third
Scientific Conference with International Participation SPACE, ECOLOGY,
NANOTECHNOLOGY, SAFETY 27–29 June 2007, Varna, Bulgaria.
19. Й о р д а н о в , Д . В . К о м п ю т ъ р н и м о д е л и н а с и с т е м и з а у п р а в л е н и е н а с а м о л е т и и
хеликоптери, МП И-во на ТУ- София - първа част 2004г, втора част 2005.
20. Л е б е д е в , А . А . , Ч е р н о б р о в к и н Л . С . Д и н а м и к а п о л е т а б е с п и л о т н ы х
летательных аппаратов, Машиностроение, 1973.
21. H u b e n o v a , Z . Methodological Approaches Toward the Problem of Estimating
Information Load Exerted on the Man – Operator Within an Ergatic System, ,
Sixth Scientific Conference with International Participation SPACE, ECOLOGY,
SAFETY, 2010, 2011. p. 186-194.
22. P e t r i , C . A . Kommunikation mit Automaten, Institut für Instrumentelle Mathematik,
Schriften des ИМ Nr.2, Bonn, 1962.
23. Handbook of Human Factors, edited by G. Salvendy, in 6 volumes, Purdue University.
1998.

МОДЕЛИРАНЕ НА ЧОВЕКА – ОПЕРАТОР В СЛОЖНА СИСТЕМА, ФУНКЦИОНИРАЩА В ЕКСТРЕМНИ УСЛОВИЯ

П. Гецов, З. Хубенова, Д. Йорданов, В. Попов

Резюме

Разглеждат се проблеми, свързани с експликацията на сложни системи на управление на обекти, работещи в екстремни условия, както и влиянието на ефективността на операторската дейност върху системата като цяло. Обоснована е необходимостта от създаването на комплексни имитационни модели, отразяващи операторската дейност. Описана е организационно-техническата система на безпилотен авиационен комплекс, като сложна ергатична система. Осъществена е компютърна реализация на основните подсистеми на алгоритмичния модел на човека като управляваща система и е разработен специализиран софтуер за обработка и анализ на данните. Реализиран е изследван оригинален компютърен модел на Човек като следяща система. Синтезиран е модел на безпилотен комплекс за тренировка на оператори и формиране на менталният модел на аварийна ситуация, реализиран в "matlab-simulink" среда. Като звено от контура за управление, летецът (операторът) е разгледан опростено като система за автоматично регулиране състояща се от три основни, свързани помежду си

подсистеми: чувствителни органи (възприемащи датчици); централна нервна система; изпълнителни органи (мускули на ръцете, краката, гърба). Предложен е теоретико-информационен модел за прогнозиране на нивото на информационното натоварване на оператора в ергатични системи, който позволява да се оцени и прогнозира ефективността на реално работещ оператор. На база мрежите на Петри е синтезиран информационен имитационен модел на операторска дейност при излитане.

NEW CONSTRUCTION KU-BAND ANTENNA WITH IMPROVED RADIATION DIAGRAM FOR SATELLITE BROADCASTING RECEIVING EARTH STATION

Peter Petkov¹, Elissaveta Alexandrova²

¹Technical University

²Bulgarian Astronautical Society

e-mail: e_alexandr@mail.bg

Abstract

The development of a new design small offset antenna with elliptical aperture equivalent to about 60 cm circular aperture intended for receiving earth stations in the band 11.7÷12.5 GHz of Broadcasting Satellite Service (BSS) is reported in the paper. The antenna mechanical and electrical characteristics are presented. The main antenna feature is the improved antenna radiation pattern in the plane of the geostationary satellite orbit (GSO) compared to the reference antenna pattern of BSS receiving earth stations in Annex 5 of Appendix 30 of the Radio Regulations (RR) that will contribute to less interference impact between real BSS systems in Ku-band especially systems with satellites located at comparatively closely situated GSO positions. The antenna parameters values achieved in this project are in support of the idea to improve the reference antenna pattern of the BSS earth stations that will contribute to more efficient use of the frequency spectrum-orbital resources in this band corresponding to the wording of Article 44 of the Constitution of the International Telecommunication Union (ITU) and the main principle of the RR for equitable access to frequency spectrum and GSO.

1. Introduction

The World Radiocommunication Conference 2000 (WRC-2000) adopted the international Plan for GSO BSS systems with national coverage based on a completely digital technology for television programs transmissions for Regions 1 and 3 countries (Europe, Africa, Asia and Australia). The down-link protection criteria in this BSS Plan are based on

the 60 cm reference antenna radiation pattern for the BSS receiving earth stations taken from ITU-R Recommendation BO.1213 with a half power beamwidth of almost 3° (2.86°) and included in Annex 5 of RR Appendix 30 (Fig.7bis) [1]. According to this reference radiation pattern at 3° orbital separation between BSS satellites positions on GSO discrimination of the co-channel co-polar Adjacent Satellite Interference (ASI) is about 13 dB and 18 dB for cross-polar applicable to BSS channels with circular polarization and 27 MHz BSS channel bandwidth. In the operational BSS systems the circular polarization has no popularity from the very beginning. By the time it is becoming more and more impossible circular polarization to be used, because of the numerous filings for additional use of the BSS band resources under the provisions of Article 4 of RR Appendix 30 intended to use BSS channels with linear polarization and especially with the preferred 33 MHz BSS channel bandwidth. The cross-polar discrimination for linear polarized signals according to the reference BSS receiving earth stations antenna pattern is decreasing up to 1 dB at around 3° off axis angles, because of the offset BSS channels arrangement and the use of 33 MHz BSS channel bandwidth. This circumstance makes completely impossible polarization reuse and reduces the opportunity to obtain coordination agreement for additional uses BSS systems and this creates difficulties for their implementation, as well as for the systems in the BSS Plan.

During the year 2012 „Bulgaria Sat” AD was awarded by the national regulatory authority CRC (Commission for regulation in communications) with permission to use GSO position 1.9°E for BSS system in case of successful coordination. At about 3° from both sides of this position the satellites of other countries BSS systems in operation are positioned. The analyses carried out showed that the three systems can operate at equal EIRP values without any perceptible mutual interference, however the existing coordination provisions [1] requires higher carrier-to-interference ratios than the actually needed. These provisions predetermined the WRC-12 decision on the Bulgarian proposal [2] the BSS channels in the lower part of the BSS band to be allowed for use from position 1.9° , however with quite low EIRP [3]. This Conference decision showed the need of a new antenna design for BSS receiving earth stations with improved electrical parameters: some higher maximum gain and improved radiation pattern particularly around 3° off-axis angle and better polarization discrimination.

2. Construction of the BSS receiving earth station antenna accordance

The proposed BSS receiving earth station antenna (elliptical offset) is designed in accordance with the recommendations in [4, 5]. The antenna reflector with aperture dimensions of 70 x 50 cm with elliptical rim (Fig.1) in a manner placing the feed out of the main beam of antenna pattern (Fig.2). The shift of the mechanical antenna axis from the electrical one (offset angle) is 30° . The antenna feed is a conical horn with an elliptical aperture complemented by choke (Fig.3) and dimensioned for achieving pattern symmetry and best possible maximum match with the feed waveguide in the full DTH TV band ($10.7 \div 12.75$ GHz) (Fig. 4).

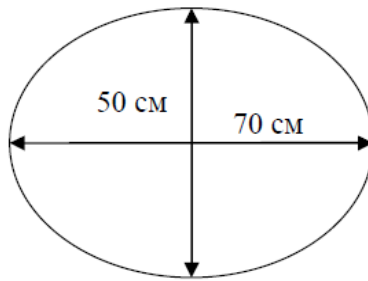


Fig. 1. Shape and size of antenna aperture

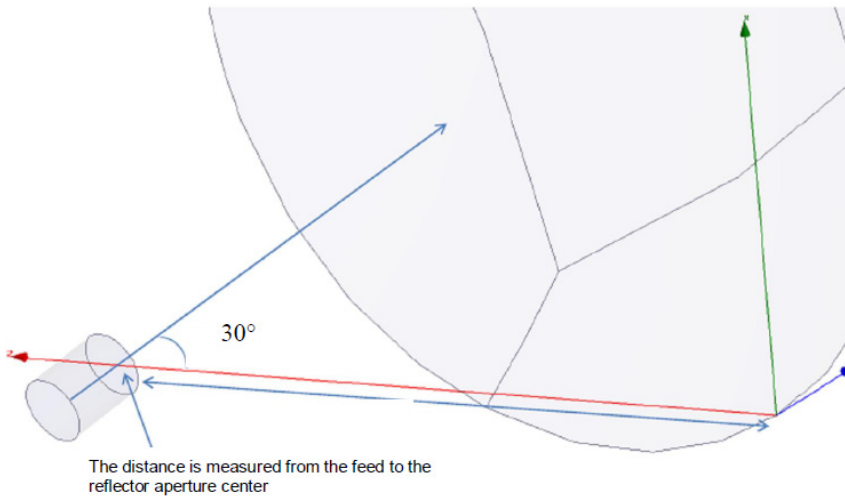


Fig. 2. Alignment the antenna feed

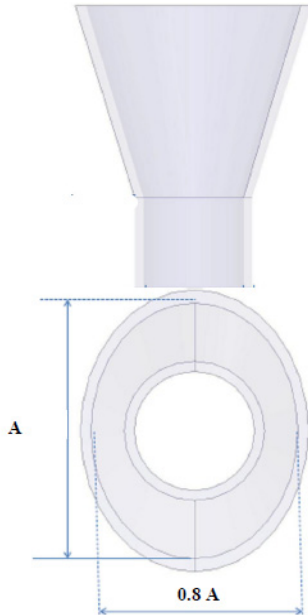


Fig. 3. Dimensioning of the antenna feed

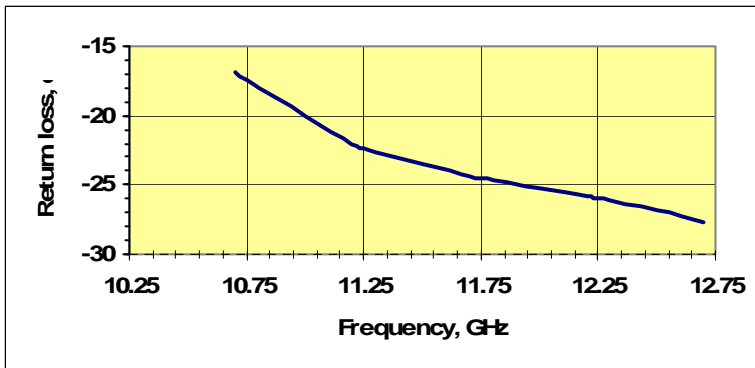


Fig. 4. Return loss of the antenna feed

3. Electrical characteristics of the new design BSS receiving earth station antenna

Theoretically determined maximum directivity of the new design BSS receiving earth station antenna at the BSS band middle frequency 12.2 GHz is over 36 dBi and the maximum cross-polar discrimination is over

30 dB in the cone of the co-polar component relative gain of -0.25 dB. Directivity values vs. frequency in the antenna operating band are summarized in Table 1.

The improvement of the new design BSS receiving earth station antenna radiation pattern in the GSO plane (horizontal plane) compared to the existing reference Regions 1 and 3 antenna radiation pattern for the receiving BSS earth stations in Annex 5 of RR Appendix 30 can be expressed by the following points (**Annex 1**):

1. Off-axis co-polar discrimination in the off-axis angle sector of 2.5° ÷ 3.5° is higher than 20 dB including 0.5 dB antenna mispointing error.
2. Cross-polarization discrimination is above 10 dB in the off-axis angle sector of 2.5° ÷ 3.5° including 0.5 dB antenna mispointing error.

It wasn't observed any perceivable variation of the main components of the new design BSS receiving earth station antenna radiation pattern in the off axis angles sector of $\pm 10^{\circ}$ throughout the whole BSS band and even throughout the whole antenna operating frequency band 10.7-12.5 GHz (**Annex 1**).

4. Tolerance analysis of the proposed new design BSS receiving earth stations antenna parameters

The expected decrease of the main beam antenna gain for the feed horn shift from the antenna focus along the three axis (Fig.5) is presented on Fig.6. It is evident that 1 cm shift of the antenna feed phase center from the focus of the parabolic reflector along each axis causes the maximum antenna gain decrease of less than 0.1 dB. The gain is most susceptible to a shift of the antenna feed phase center along the paraboloid axis; 0.5 dB decrease of the gain corresponds to 2 cm shift from the antenna focus. The antenna gain is substantially more tolerable to the feed twist around its own axes in the horizontal and vertical planes (Fig.7) than the cross-polarization discrimination; when the feed is twisted around the antenna vertical axis (elevation) with more than 3° the cross-polarization discrimination value falls below 20 dB, while the gain decreases with less than 0.04 dB.

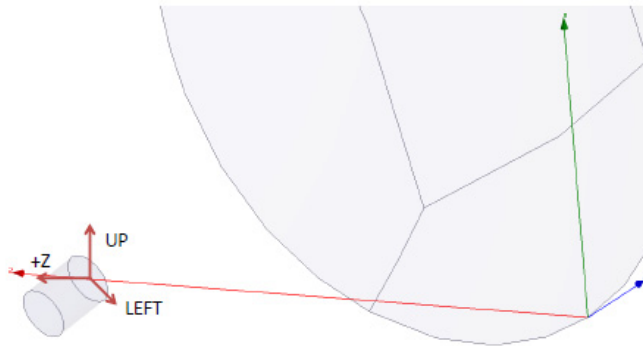


Fig. 5. Positioning of the antenna feed

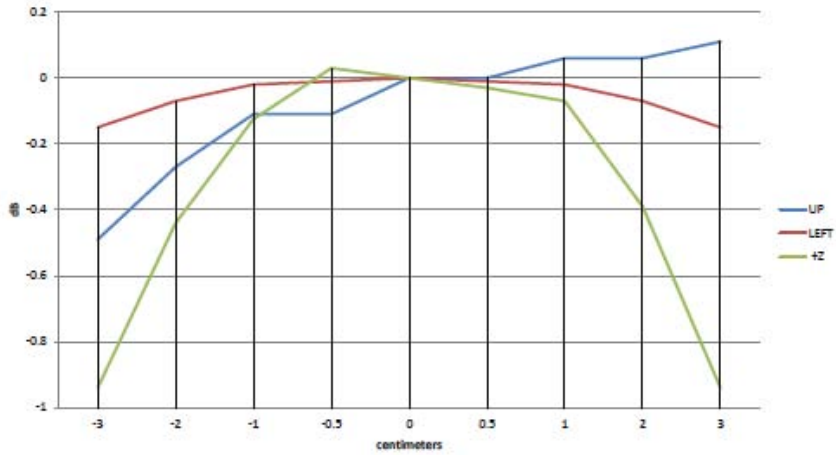


Fig. 6. Gain loss due to feed displacement (shift) from the parabolic reflector focus (Directions as per Fig. 5)

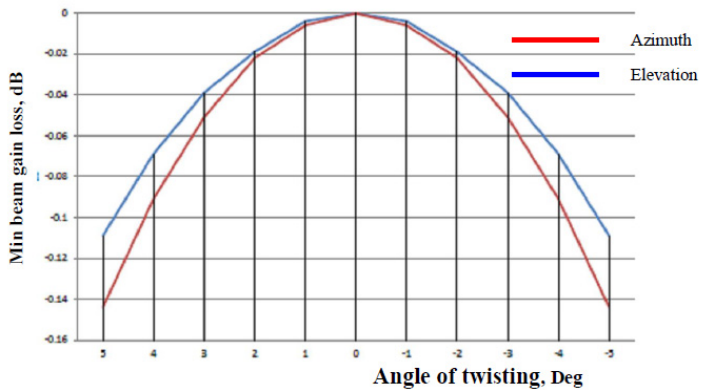


Fig. 7. Gain loss in case of feed twist around its axes

The impact of the root-mean-square (r.m.s.) deviation of the antenna reflector surface from the ideal paraboloid was analyzed at frequency 12.0 GHz which falls in the middle of the antenna operating frequency band and the results are presented here below:

r.m.s. deviation, mm	0	0.047	0.094	0.235	0.47	0.705	0.94	1.175	1.41
Gmax, dBi	36.2	36.199	36.194	36.154	36.011	35.773	35.44	34.99	34.45
Gmax decrease, dB	0	0.001	0.006	0.046	0.189	0.427	0.76	1.21	1.75

The deviation from the parabolic surface of the mass production small aperture antennas is typically less than 0.5 mm r.m.s. It results less than 0.2 dB decrease of the antenna gain theoretical value.

The values of the main beam antenna gain (Gmax) of the new design BSS receiving earth station antenna accounting for the losses due to the manufacturing allowances are summarized in Table 1. It can be seen that Gmax is apparently higher than 35.5 dBi at the mid BSS band frequency 12.2 GHz with aperture efficiency of 70 %.

Table 1.

Frequency, GHz	Polarization	Directivity, dBi	Feed shift loss, dB	Surface error loss, dB	Other losses, dB	Gmax, dBi
10.7	Vertical	34.98	0.2	0.19	0.25	34.34
10.7	Horizontal	34.87	0.2	0.19	0.25	34.23
11.725	Vertical	36.03	0.2	0.19	0.25	35.39
11.725	Horizontal	35.95	0.2	0.19	0.25	35.31
12.0	Vertical	36.25	0.2	0.19	0.25	35.61
12.0	Horizontal	36.15	0.2	0.19	0.25	35.51
12.75	Vertical	36.4	0.2	0.19	0.25	35.76
12.75	Horizontal	36.87	0.2	0.19	0.25	36.23

The losses due to finite conductivity of the reflector surface, antenna feed and waveguide are negligible, as well as the return loss (better than -18dB over the band of operation). They are summarized in the column “Other losses”, forming a significant safety margin of about 0.25 dB.

5. Preconditions for and expected results from the introduction of a new reference BSS receiving earth station antenna radiation pattern

The results from a comparative analysis were presented in [6] in which the potentially affected BSS systems and administrations by the Bulgarian BSS satellite system submitted at GSO position 1.9°E under the provisions of the Appendix 30 criteria for down-link direction based on the existing reference BSS receiving earth station antenna pattern were identified and compared with those obtained by applying the antenna pattern with steeper slopes like the presented above new design of BSS receiving earth station antenna. The analysis based on the narrower antenna pattern of the BSS receiving earth stations keeping all other conditions unchanged showed reduction of the number of the affected BSS systems and the number of administrations with which the coordination agreement have to be obtained was also reduced [6].

There are a number of BSS satellite systems submissions in ITU Region 1 at positions which fall in the BSS receiving earth stations antenna beam off-axis angle sector of 2.5°÷3.5° [6] of other BSS systems previously submitted to the ITU Radiocommunication Bureau (ITU-BR) and that's why having priority. The later submissions seem to be impossible to be brought into use, because of serious difficulties for notifying administrations to obtain coordination agreements due to usually quite great number of identified as affected ones. The reason for that is in a great extent the theoretically defined interference impact based on the use of the existing reference antenna pattern of BSS receiving earth stations. Observing the applicable protection ratios and the reference antenna pattern of the Regions 1 and 3 BSS receiving earth stations [1] even BSS systems at GSO positions separated with 6°÷7° are identified as affected. However, to obtain coordination agreement even in such cases is equally labor-consumption and expense-consumption and some times even impossible for non-technical reasons. Unnecessarily large number of systems and administrations with which agreements have to be sought is a barrier to successful coordination and recording of new BSS systems for additional uses of the BSS band in the Master International Frequency Register (MIFR) and impedes providing finances for their implementation. At the same time the ITU Region 2 BSS Plan (North and Sought America) is based on the reference antenna pattern of BSS receiving earth stations with comparatively narrower beam and antenna design independent. Such an approach leads to more effective use of the Region 2 BSS frequency-orbital resources than the corresponding for

the Regions 1 and 3. From the other side tightening of the reference antenna pattern defining in a great extent the access to and the effective use of GSO to the specific antenna dimension is not a perspective approach because the antenna technologies are continuously improving. The small Ku-band antenna manufacturing companies currently demonstrate achievement of much better antenna pattern discrimination in the vicinity of 3° off axis angle even for the same antenna size.

Making the reference antenna pattern of the Region 1 and 3 BSS receiving earth stations in Annex 5 to RR Appendix 30 (Fig.7bis) narrower especially in off axis angle region from 2.5° to 3.5° will ease the coordination procedure because the identification of the need for coordination is based on it and the number of the potentially affected BSS systems and administrations identified by the ITU-BR will be reduced. As a result much more BSS systems can be successfully coordinated and implemented at conditions of closely located positions of the BSS systems in the Plan and the submitted under RR Appendix 30 Article 4 [1].

6. Conclusion

The goals set forth the design of the new BSS receiving earth station antenna are achieved:

- the maximum gain is higher than 35.5 dBi @ mid frequency (BSS);
- the ASI suppression in a cone of 3° from the antenna main beam axis is over 15 dB throughout the BSS band;
- no perceptible change of the antenna radiation pattern throughout the BSS band is observed in the off-axis angle sector of ±10 degrees.

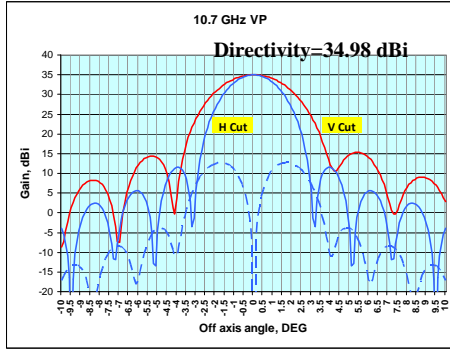
Having in mind the considerable margins demonstrated in the antenna gain analysis the presented new design antenna for BSS receiving earth stations will be suitable for mass production even with limited control over dimensions tolerances.

There is a trend of increasing of the number of the submitted to the ITU-BR RR Appendix 30 Annex 4 BSS systems and consequently decreasing of the orbital separation between the filed GSO positions that leads to less opportunity for successful coordination and as a result to ineffective use of the BSS frequency spectrum-orbital resources and the access of new satellite operators to them. This situation might be resolved based on the results of the new design BSS receiving earth station antenna demonstrating the feasibility to improve the reference antenna pattern of BSS Region 1 and 3 receiving earth stations and through its improvement to

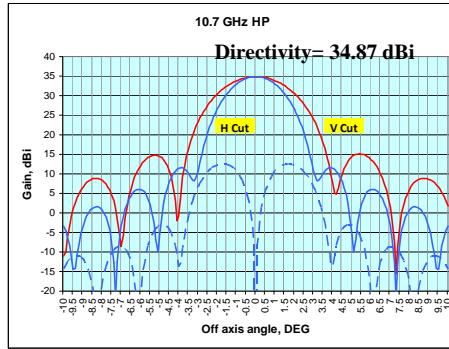
facilitate the coordination procedure and the access to GSO for Region 1 and 3 countries.

Annex 1

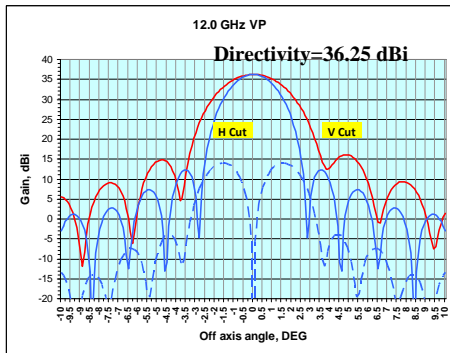
Radiation patterns at both polarizations (V and H) in both orthogonal planes at 12 GHz and at both edge frequencies of the new BSS receiving antenna design frequency band



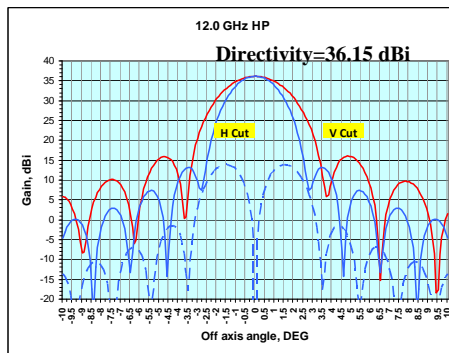
Off axis angle (θ), Deg



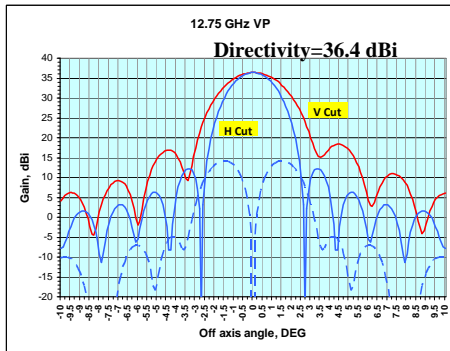
Off axis angle (θ), Deg



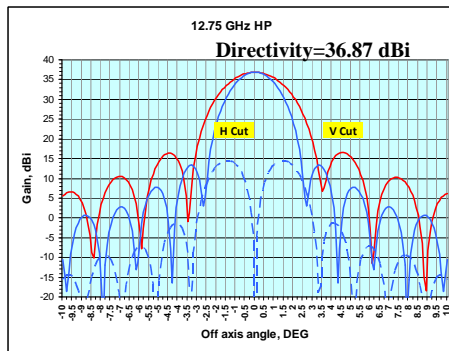
Off axis angle (θ), Deg



Off axis angle (θ), Deg



Off axis angle (θ), Deg



Off axis angle (θ), Deg

V Cut – in vertical plane (elevation), **H Cut** – in horizontal plane (azimuth)

References

1. Appendix 30 of the Radio Regulations, Edition of 2008.
2. Document 58 (Add.3), Bulgaria (Republic of), Proposal for the work of the Conference, World Radiocommunication Conference (Geneva, 23 January – 17 February 2012).
3. Document 517-E, 14 February 2012, Chairman of Committee 5, Six report from Committee 5 to the Plenary meeting, Agenda Item 7, World Radiocommunication Conference (Geneva, 23 January – 17 February 2012).
4. R u d g e, A. W., K. M i l n e, A. D. O l v e r and P. K n i g h t. The Handbook of Antenna Design, Peter Peregrinus Ltd, London, UK, 1982.
5. Antenna Handbook, Vol.2, Y.Lo & S.Lee, Eds., Van Nostrand Reinhold, New York, 1993.
6. Document 4A/43-E, 23 May 2012, Bulgaria (Republic of), Improvement of the RR Appendix 30 BSS receiving stations reference antenna pattern for Regions 1 and 3 as an opportunity for more efficient use of the spectrum/orbit resources for BSS systems and facilitation of the access to these resources by new comers, ITU-R Working Party 4A Meeting (Geneva, 30 May – 06 June 2012).

НОВА КОНСТРУКЦИЯ НА АНТЕНА ЗА ПРИЕМНА СТАНЦИЯ ЗА СПЪТНИКОВО ТЕЛЕВИЗИОННО РАЗПРЪСКВАНЕ В КУ-ОБХВАТА С ПОДОБРЕНА ДИАГРАМА НА ИЗЛЪЧВАНЕ

П. Петков, Е. Александрова

Резюме

В статията е представена разработката на нова конструкция на малка офсет антена с елиптична апертура, еквивалентна на кръгла апертура с диаметър около 60 см, предназначена за приемни земни станции в обхвата 11.7-12.5 GHz за спътниково телевизионно разпръскване (BSS). Представени са механичните и електрически характеристики на антената. Основното качество на антената е подобрената диаграма на излъчване в равнината на геостационарната спътникова орбита (GSO) в сравнение с еталонната диаграма на излъчване на антени за BSS приемни станции в Допълнение 5 на Приложение 30 на Международния радиорегламент (RR). По-добрата диаграма на излъчване ще допринесе за намаляване на влиянието на смущенията между спътници на сравнително близки GSO позиции. Стойностите на параметрите на антената, постигнати в този проект, са в подкрепа на идеята за подобряване на еталонната диаграма на антени за BSS приемни земни станции, което ще повиши ефективността при използване на честотно-орбиталните ресурси в този обхват, напълно в съответствие с призива в Член 44 на Конституцията на Международния съюз по далекосъобщения (ITU) и с основния принцип на RR за равноправен достъп до честотния спектър и геостационарната орбита.

FUNCTIONAL TESTING OF THE CAMERA WITH ACTUATOR FOR THE EXPERIMENTAL DETERMINATION OF THE POLARIZATION OF LIGHT BY MEASURING THE STOKES PARAMETERS

*Zhivko Zhelezov², Roumen Nedkov¹, Dimitar Teodosiev¹,
Maria Bivolarska², Neven Georgiev², Ivo Lilov², Georgi Chamov²,
Spaska Yaneva³*

¹*Space Research and Technology Institute – Bulgarian Academy of Sciences*

²*Space Research Ltd, Sofia, Bulgaria*

³*University of Chemical Technology and Metallurgy, Sofia, Bulgaria
e-mail: rnedkov@space.bas.bg*

Abstract

The article presents the results from the functional tests of cameras with actuator for determining of Stokes parameters. The aim of the tests is to investigate the possibility for the cameras in question to work in the space. Positive results are obtained, which allow the cameras to be used for measurements in free space.

Introduction

The polarization of light is a process that occurs in interaction of light waves with matter. According to Maxwell's electromagnetic theory light waves are electromagnetic (EM) transverse wave: the vibration of the electric and magnetic vector is carried out in directions perpendicular to the direction of propagation of light.

The light can be considered as electromagnetic radiation from a large number of atoms belonging to a given source. Since every atom of the source emits vibrations independently of the other, in total EM radiation is characterized by the kinds of equally possible orientations of the electric vector \vec{E} , which is also called a light vector.

In the radiation from majority of sources the direction of the electric vector is in general not defined but changes continuously and randomly over extremely short time intervals. Such radiation is called unpolarized or natural light.

If the light reflected or passed through the dielectric, the electric vector of light waves can vibrate only in one plane – the so-called full or linear polarization plate, or, due to a more complex interaction with the substance, the electric vector vibrates in a sequence that can be illustrated with a vector rotating spiral with "step" equal to the wavelength λ . If during this rotation the amplitude of the electric field is kept constant in all directions perpendicular to the direction of propagation, the polarization is circular. If the amplitude is changed and is different in two orthogonal directions, the tip of the vector will describe an ellipse and the polarization is elliptical [1], [2].

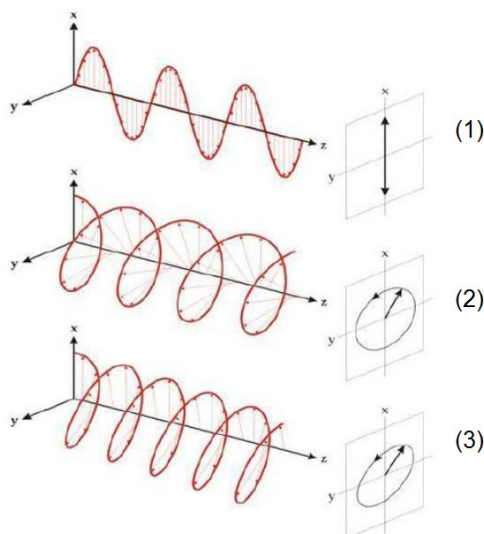


Fig. 1. Schematic representation of a linearly (1), a circularly (2) and an elliptically (3) polarized light

The state of polarization of light is described completely by the four Stokes parameters, which contain complete information on the intensity, the extent, and the form of polarization of light. They are real numbers with dimension of intensity and can be expressed by the Cartesian components of the electric field (E_x и E_y) by the following equations [3]:

- (1) $\mathbf{I} = S_0 = I(0^\circ) + I(90^\circ) = \langle |E_x|^2 \rangle + \langle |E_y|^2 \rangle$
- (2) $\mathbf{Q} = S_1 = I(0^\circ) - I(90^\circ) = \langle |E_x|^2 \rangle - \langle |E_y|^2 \rangle$
- (3) $\mathbf{U} = S_2 = I(45^\circ) - I(135^\circ) = \text{Re}\langle E_x E_y \rangle$
- (4) $\mathbf{V} = S_3 = I_{\text{RHC}} - I_{\text{LHC}} = \text{Im}\langle E_x E_y \rangle$

Where the brackets “ $\langle \rangle$ ” indicate averaging over a long time.

The first parameter S_0 gives us the total light intensity; S_1 indicates the difference between the components of the wave which is horizontally (+) or vertically (–) polarized; S_2 indicates the difference between the components of the wave which is polarized at -45 and $+45$ degrees; S_3 gives the difference between the circular components with intensities I_{RHC} and I_{LHC} of right and left rotating polarization.

The polarization state is completely determined by the three ratios known as relative Stokes parameters:

- (5) $P_1 = S_1/S_0$
- (6) $P_2 = S_2/S_0$
- (7) $P_3 = S_3/S_0$

They have possible values between (-1) and $(+1)$.

The following equations are used to calculate the degree of polarization – the ratio of the polarized light to the total intensity.

Degree of polarization P :

$$(8) \quad P = \text{sqrt}(S_1^2 + S_2^2 + S_3^2) / S_0$$

Degree of linear polarization P_L :

$$(9) \quad P_L = \text{sqrt}(S_1^2 + S_2^2) / S_0$$

Degree of circular polarization P_C :

$$(10) \quad P_C = S_3 / S_0$$

P_C is positive for right-handed circular polarization and negative for left-handed circular polarization.

Experimental measurements and results

The aim of the experimental measurements is the determination of Stokes parameters and the state of polarization of a light source by using photodiode and a prototype of the onboard camera.

A *He-Ne laser* with a wavelength of 633 nm and an output of 5 mW is used as a light source. A linear polarizer is utilized for the determination of Stokes parameters and the rotating of the plane of polarization, and a photodiode and a camera – for measurement the signal. The silica photodiode with active area size 2.5 x 2.5 mm is mounted in a metal protective housing and connected to an amplifier. The black/white camera is selected with high light sensitivity (4.8 V/lux.s), dynamic range >110 dB and relatively high resolution (752 x 480). It also has the property to average by hardware (as analogue level) pixels in areas up to 4 x 4 in the whole frame, which additionally increase the signal to noise ratio.

In order to determine Stokes parameters, a certain sequence of steps is followed. First, the linear polarizer has to be placed in front of the photodiode/camera. By rotating of the position of the polarizer at 0 and 180 degrees, the intensity has to be measured and the result to be averaged. Similar measurements have to be made at 90 and 270 degrees. By these measurements S_0 and S_1 will be determined. The averaging of the readings will give a more accurate value. In a similar manner S_2 has to be determined with the polarizer at 45 and 135 degrees. By equations (1–4) Stokes parameters can be calculated.

Three series of measurements were made. Images of the experimental setup of the first series are shown in Figure 2.

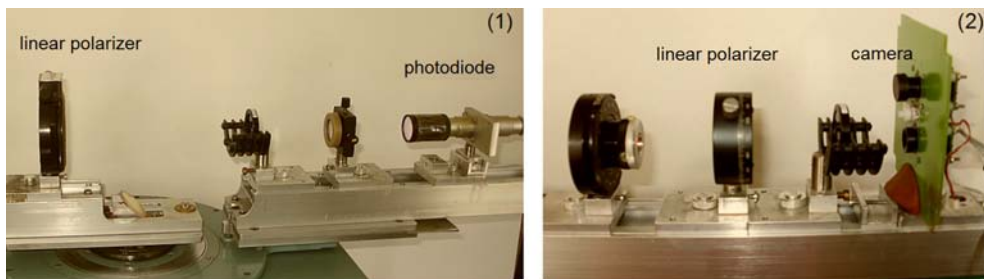


Fig. 2. Experimental setup for measurement Stokes parameters by using He-Ne laser as a light source

In this series of experiments, a difficulty in measuring the signal with the camera occurs. In spite of the use of attenuators, the signal from the laser was outside the dynamic range of the camera, which prevents the measurement. This required a change of the light source.

The second series of experiments aimed assembling a setup with a source light-emitting diode (LED), which emits unpolarized light in the red range of spectrum and is fitted with a potentiometer for adjusting the brightness of the light. The experimental setup is shown in Figure 3.

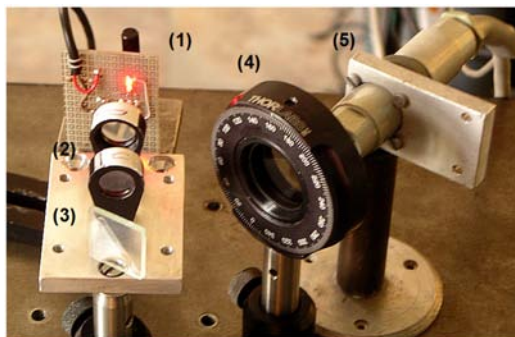


Fig. 3. Experimental setup for measurement Stokes parameters by LED as a light source: 1) LED, 2) lens system, 3) glass plate, 4) polarizer, 5) photodiode chip

The light from the LED passes through a lens system and reaches the glass plate. The reflected light is polarized, and the state of polarization depends on the angle of incidence and, respectively, on the angle of reflection from the plate. [4] After reflection from the plate, the light passes through a polarizer and falls on the photodiode chip.

The aim of the third series of experiments is to determine Stokes parameters by LED as a light source and to compare the measurement results of the camera with those of photodiodes. The following pictures show the configuration of the experimental setup with a photodiode and a camera.

In this series of experiments, measurements were divided into several groups depending on:

- the angle of incidence/reflection of light from the glass plate – 30 and 40 degrees;
- the step of rotating the position of the polarizer – in our case 30 and 45 degrees.

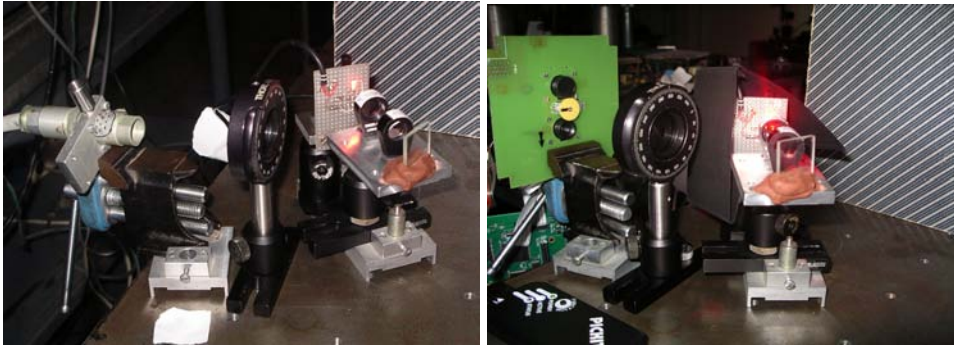


Fig. 4. Pictures of the experimental setup for measurement of Stokes parameters by a photodiode (left side) and a camera (right side) in source LED

The normalized results from measurements of light intensity using a photodiode and a prototype of the onboard camera are presented in the following tables. They are received in a step of rotating the position of the polarizer 30 degrees (Table 1) and 45 degrees (Table 2) and a reflection angle of the glass plate 30 degrees.

Table 1. Results of measurements of the intensity of light: step of rotating the position of the polarizer 30 degree; reflection angle of the glass plate 30 degrees

Experiment 1		
deg	camera	photodiode
30	0.686	0.725
60	0.971	0.992
90	0.948	0.950
120	0.656	0.658
150	0.401	0.400
180	0.425	0.442
210	0.686	0.725
240	0.971	0.992
270	0.948	0.950
300	0.656	0.658
330	0.401	0.400
0	0.425	0.442

Table 2. Results of measurements of the intensity of light: step of rotating the position of the polarizer 45 degree; reflection angle of the glass plate 30 degrees

Experiment 1		
deg	camera	photodiode
0	0.640	0.675
45	1.000	1.000
90	0.712	0.700
135	0.365	0.367
180	0.640	0.675
225	1.000	1.000
270	0.712	0.700
315	0.365	0.367

The diagrams below (Figure 5) present the state of polarization of light by comparing the results of the first two experiments.

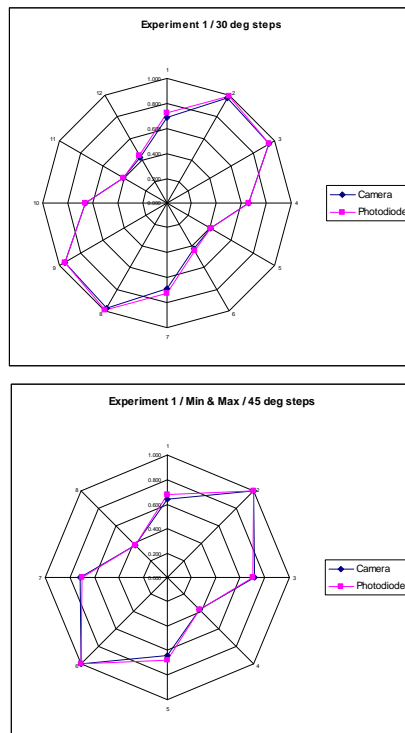


Fig. 5. Diagram of the state of polarization at step 30 degrees and 45 degrees and a reflection angle of the glass plate 30 degrees

The normalized results of the measurements of the light intensity at a reflection angle of the glass plate 40 degrees are shown in the following tables. They are received in the step of rotating the position of the polarizer 30 degrees (Table 3) and 45 degrees (Table 4).

Table 3. Results of measurements of the intensity of light: step of rotating the position of the polarizer 30 degree; reflection angle of the glass plate 40 degrees

Experiment 2		
deg	camera	photodiode
30	0.757	0.753
60	0.941	0.955
90	1.000	0.981
120	0.815	0.801
150	0.617	0.592
180	0.595	0.573
210	0.757	0.753
240	0.941	0.955
270	1.000	0.981
300	0.815	0.801
330	0.617	0.592
0	0.595	0.573

Table 4. Results of measurements of the intensity of light: step of rotating the position of the polarizer 45 degree; reflection angle of the glass plate 30 degrees

Experiment 2		
deg	camera	photodiode
0	0.722	0.715
45	0.982	1.000
90	0.825	0.820
135	0.585	0.554
180	0.722	0.715
225	0.982	1.000
270	0.825	0.820
315	0.585	0.554

The following diagrams (Figure 6) present the state of polarization of light by comparing the results of the last two experiments.

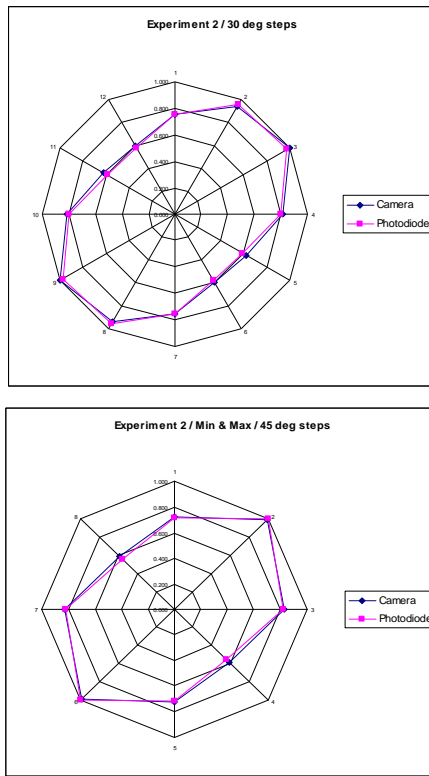


Fig. 6. Diagram of the state of polarization at step 30 degrees and 45 degrees and a reflection angle of the glass plate 40 degrees

Using the experimental results and formulas (1–7) given in the theoretical part, Stokes parameters S_0 , S_1 and S_2 are calculated. Calculations are made with normalized intensity values. The results are presented in the following tables. The *Experiment 1* corresponds to the case of the reflection angle of the glass plate 30 degrees and the *Experiment 2* – to the case of the reflection angle of the glass plate 45 degrees.

Table 5. Measurement results and calculated Stokes parameters using a photodiode

No	$I(0^\circ)$	$I(90^\circ)$	$I(45^\circ)$	$I(135^\circ)$	S_0	S_1	S_2	P_1	P_2
Exp. 1	0.675	0.700	1.000	0.367	1.375	-0.025	0.633	-0.018	0.460
Exp. 2	0.715	0.820	1.000	0.554	1.535	-0.105	0.446	-0.068	0.291

Table 6. Measurement results and calculated Stokes parameters using a camera

No	I(0°)	I(90°)	I(45°)	I(135°)	S ₀	S ₁	S ₂	P ₁	P ₂
Exp. 1	0.640	0.712	1.000	0.365	1.352	-0.072	0.635	-0.053	0.469
Exp..2	0.722	0.825	0.982	0.585	1.547	-0.103	0.397	-0.067	0.257

The percentage difference between the readings of the photodiode and a Δk camera is calculated on the basis of the data from two different measurements. The normalized results of the first calculation are shown in Table 7.

Table 7. Difference between the readings of the camera and the photodiode from the first measurement

angle	camera	photodiode	difference (%)
0	0.414	0.442	-6.180
30	0.686	0.725	-5.408
60	0.971	0.992	-2.083
90	0.948	0.950	-0.249
120	0.656	0.658	-0.324
150	0.401	0.400	0.358
180	0.425	0.442	-3.797

A difference between the readings of the camera and those of the photodiode for angles from 0 to 180 degrees is given in the last column of Table 7.

The percentage difference Δk is given by the formula:

$$(11) \quad \Delta k = (I_{\max} - I_{\min})/2$$

In this case, after the due calculations, we obtain 3.27% for Δk.

The results of the second test are shown in Table 8.

In this case we obtain Δk = 3.46% after calculations.

We can conclude from them that the results received by the camera coincide with those obtained by photodiode with an accuracy of about 3.5%, which is evident from the diagrams given in Figures 5 and 6.

Table 8. Difference between the readings of the camera and the photodiode from the second measurement

angle	camera	photodiode	difference (%)
0	0.604	0.573	5.455
30	0.757	0.753	0.503
60	0.941	0.955	-1.464
90	1.000	0.981	1.908
120	0.815	0.801	1.684
150	0.617	0.592	4.194
180	0.595	0.573	3.759

Illustration of the results from the camera – the change in the intensity as a function of the angular position of the polarizer (from 0 to 180 degrees) is shown in Figure 7.

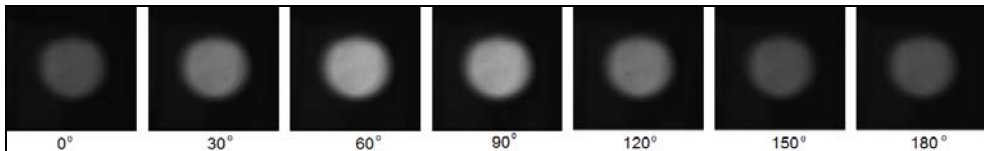


Fig. 7. Change in intensity of light as a function of the angular position of the polarizer

We can conclude from the calculations of Stokes parameters (Table 5 and 6), the diagrams in Figure 5 and 6, and the photos from Figure 7, that the tested light is elliptically polarized.

Sources of errors in measurements

The magnitude of the error in the experimental measurements depends both on the accuracy of the instrument and the natural fluctuations in the values, which can be a result from accidental causes.

Errors in the performed experimental measurements can accumulate each element presented in the setup: LED, the polarizer, the photodiode and the camera.

The change of LED's power can be a source of error. To account this change, the power was repeatedly measured as a function of time. The power changed by less than 1% within 120 minutes, which has no significant influence on the measurements.

The accuracy of measurement of the polarization depends on the smallest division of the holder, in which the polarizer is placed and by

which the plane of polarization of the light can be changed. In our case, it is 2 degrees and hence the measurement error is $\pm 2^\circ$.

The smallest change in measuring by photodiode signal is 0,001 V. Therefore, the error that can occur is $\pm 0,001$ V. The average dark signal is 0,000 V.

Testing of the camera with actuator in a vacuum. Incorporation of the equipment for 30 min in a vacuum – $2 \cdot 10^{-3}$ mbar

Upon reaching a vacuum value of $2 \cdot 10^{-3}$ mbar (Figure 8), the equipment was turned on for checking of its functionality. Deflection in the power supply and in the operating mode as well as a mechanical displacement of the cameras were not found.



Fig. 8. Incorporation of the equipment for 30 min in a vacuum - $2 \cdot 10^{-3}$ mbar

The captured test images show the normal functioning of both cameras (Figure 9 and 10).

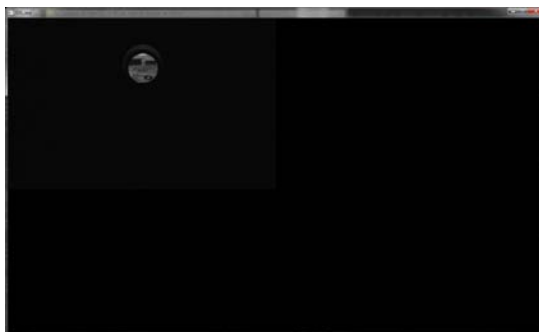


Fig. 9. Test image in vacuum at $2 \cdot 10^{-3}$ mbar captured without outside backlight conditions



Fig. 10. Test image in vacuum at 2.10^{-3} mbar captured with outside backlight condition.

Turning on the equipment for 10 min in a vacuum at $9,4.10^{-6}$ mbar (Figure 3, 4, 5).

After the completion of the tests described above, the equipment was turned off without being removed from the thermo-vacuum chamber. The thermo-vacuum chamber reached a values $9,4.10^{-6}$ mbar for 40 min. After reaching the maximum values, the equipment was turned on, in order to explore its functionality. Deflection in the power supply and in the operating mode as well as a mechanical displacement of the cameras were not found.

The captured test images show the normal functioning of both cameras (Figure 11, 12, 13).



Fig. 11. Reaching the values $9,4.10^{-6}$ mbar of vacuum thermo chamber

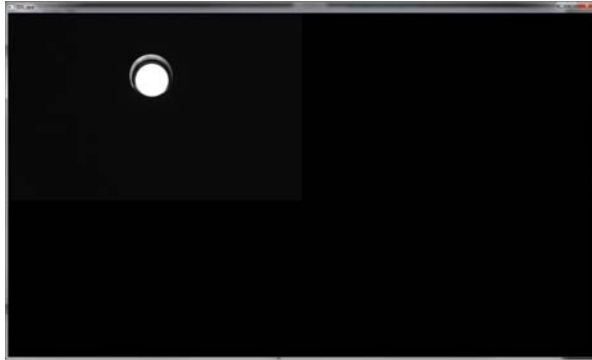


Fig. 12. Test image in vacuum at $9,4 \cdot 10^{-6}$ mbar captured with outside backlight conditions



Fig. 13. Test image in vacuum at $9,4 \cdot 10^{-6}$ mbar captured with outside backlight conditions

Conclusion

On the basis of the results obtained from the thermo- and vacuum tests of the equipment, it can be concluded that it meets the general technical requirements for operation in a vacuum of a value of $9,4 \cdot 10^{-6}$ mbar.

Acknowledgements

The present work was supported by project FFNNIPO_12_01654 FUND “Scientific Investigations”, Ministry of Education and Science, Bulgaria.

References

1. H u a r d, S., Polarization of Light, Wiley (1997)
2. C o l l e t t, E. Field Guide to Polarization, SPIE (2005)
3. B e r r y, H. G., G. G a b r i e l s e, A. E. L i v i n g s t o n. Measurement of the Stokes Parameters of Light, Applied Optics, Vol. 16, No 12, December (1977)
4. H a l l i d a y, D., R. R e s n i c k, J. W a l k e r, Fundamentals of Physics, 6th edition, Wiley (2000).

ФУНКЦИОНАЛНО ТЕСТВАНЕ НА КАМЕРА СЪС ЗАДВИЖВАНЕ ЗА ЕКСПЕРИМЕНТАЛНО ОПРЕДЕЛЯНЕ НА ПОЛЯРИЗАЦИЯТА НА СВЕТЛИНАТА ЧРЕЗ ИЗМЕРВАНЕ НА ПАРАМЕТРИТЕ НА СТОКС

*Ж. Железов, Р. Недков, Д. Теодосиев, М. Биволарска,
Н. Георгиев, И. Лилов, Г. Чамов, С. Янева*

Резюме

В настоящата работа са представени резултати от проведени функционални тестове на камери със задвижване, с помощта на които се определят параметрите на Стокс. Целта на тестовете е да се изследва възможността за работа на камерите в условията на открития космос. Получените резултати са положителни, което дава възможност те да бъдат използвани при измервания в условия на открит космос.

In memoriam

80th Anniversary of the birth and 10th death anniversary of acad. Dimitar Mishev



Academician prof. Dimitar Mishev was one of the most distinguished Bulgarian world acknowledged scientists. He was renowned both as one of the creators of Bulgarian TV network and as a pioneer of space research and initiator of remote sensing in Bulgaria.

Professor Mishev contributed significantly to the development of different fields of space researches in Bulgaria, including image processing, remote sensing of the Earth, investigation of spectral characteristics of natural formations, sensors and systems for remote sensing of the Earth and planets, telecommunication systems.

A person with international reputation, Dimitar Mishev was promoting every kind of international cooperation with exceptional enthusiasm.

Dimitar Mishev authored and co-authored more than 300 publications in scientific journals and 35 books, dictionaries and manuals. He was holder of 66 Bulgarian, French and Russian patents.

He was a member of the Bulgarian Academy of Sciences, International Academy of Astronautics, Scientific Council of the Nansen International Environmental Remote Sensing Center, International EuroAsien Academy of Sciences, International Engineering Academy, and member of many scientific councils in Bulgaria.

He was editor or chief or member of the editorial board of many scientific journals, including "Aerospace Research in Bulgaria".

He was teaching in four Bulgarian universities, a tutor and supervisor of 22 Ph.D. students and over 150 Sc. students.

In 1990 Professor Mishev founded the Solar-Terrestrial Influences Laboratory at the Bulgarian Academy of Sciences and was its Director till his unforeseen death.

Dimitar Mishev was holder of the highest Bulgarian medal for science - "Cyril and Methodius 1"; award of the International Academy of Astronautics Section 1 "Basic Sciences"; the biggest Bulgarian Academy of Sciences award for 1998 for his book "Television in Bulgaria - Facts and Documents"; the basic sciences award "For Significant and Lasting Contributions to the Advancement of the Astronautical Sciences", International Academy of Sciences, Toulouse, France 2001; First annual award of the Ministry of Education and Science "For outstanding science contribution", Sofia, December 2002.

He made many friends during his career. He put a deep imprint on the lives of those who were lucky to work with him. We greatly miss his bright intellect and warm spirit.